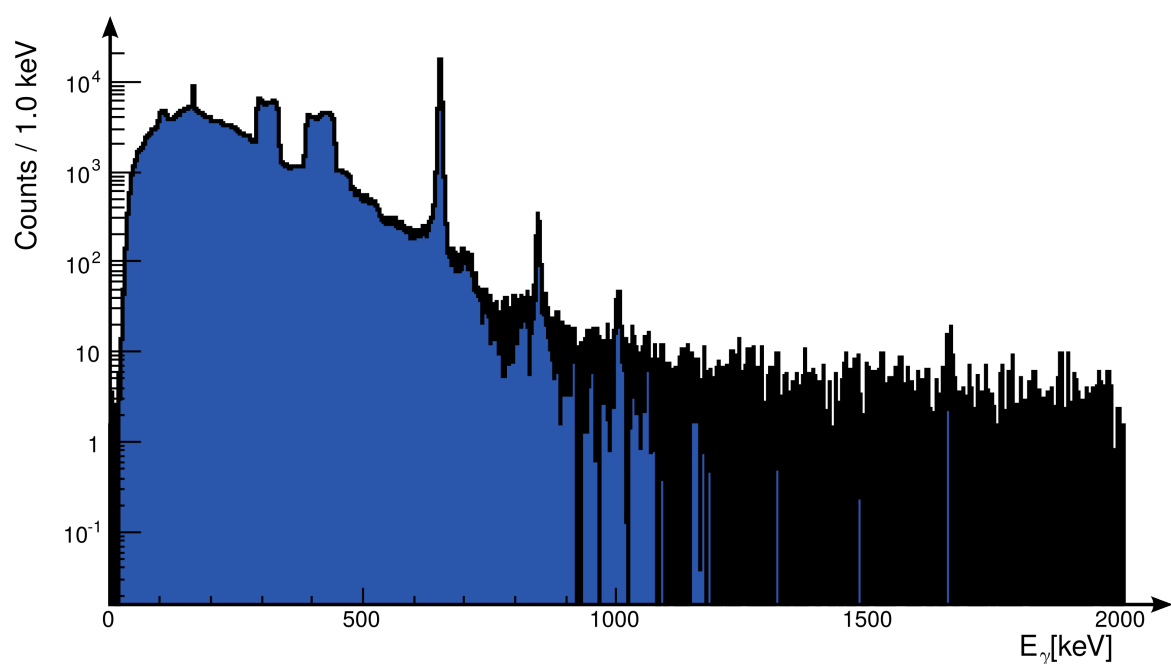Physik - Department der Technischen Universität München
Lehrstuhl E12 für Experimentalphysik, Physik der Hadronen und Kerne

Probing Nuclear Shell Structure beyond the $N = 40$ Subshell using Multiple Coulomb Excitation and Transfer Experiments

Dissertation von Stefanie Christine Hellgartner

Technische Universität München
Physik-Department
Lehrstuhl E12 für Experimentalphysik, Physik der Hadronen und Kerne

Probing Nuclear Shell Structure beyond the $N = 40$ Subshell using Multiple Coulomb Excitation and Transfer Experiments

Stefanie Christine Hellgartner

Vollständiger Abdruck der von der Fakultät für Physik der Technischen Universität München zur Erlangung des akademischen Grades eines

Doktors der Naturwissenschaften (Dr. rer. nat.)

genehmigten Dissertation.

Vorsitzender: apl. Prof. Dr. Norbert Kaiser

Prüfer der Dissertation:

                          1. Univ.-Prof. Dr. Reiner Krücken

                          2. Univ.-Prof. Dr. Lothar Oberauer

Abstract

In the last decades, enormous efforts have been made to study the evolution of nuclear shell structure going from the valley of stability towards exotic nuclei. Modern experiments at the newly developed radioactive beam facilities revealed that some of the classical magic numbers have to be replaced by new magic numbers going to the drip lines. For this thesis, the subshell closure at the neutron number $N = 40$ is of particular interest. It mimics a magic behavior, especially for ^{68}Ni which features in addition a magic proton shell ($Z = 28$). However, the magic properties are very localized since the neighboring zinc isotopes ($Z = 30$) already show collective features. As, additionally, there is strong tension in the available experimental data, the nature of the zinc isotopes is addressed in this thesis with two complementary experimental methods: Transfer reactions and multiple Coulomb excitation. Both experiments were performed with a radioactive ^{72}Zn beam provided by the REX-ISOLDE accelerator at CERN.

In a transfer experiment, a ^{72}Zn beam ($E_{beam} = 2.7$ MeV/u) was impinging on a radioactive tritium target to study the two-neutron transfer reaction t(^{72}Zn, p)^{74}Zn and the one-neutron transfer reaction t(^{72}Zn, d)^{73}Zn simultaneously. To disentangle the reaction channels, the light transfer products p and d were identified with the ΔE-E telescopes of the nearly 4π silicon detector array T-REX. From the energy and the position information of the detected particles, excitation energy spectra of the states populated in ^{73,74}Zn were obtained. Additionally, the characteristic γ-rays of the zinc nuclei were detected with the European γ-ray spectrometer MINIBALL to unambiguously identify the reaction channel and the populated states. Combing the information of both detector arrays, differential cross sections were extracted. In case of the two-neutron transfer, the differential cross sections of the ^{74}Zn ground state and its first excited 2^+ state were determined and compared to FRESCO calculations. For the ^{74}Zn ground state the two neutrons are transferred dominantly to the $1g_{9/2}$ shell above $N = 40$. The cross section of the 2_1^+ state could be reproduced by FRESCO only if the $2d_{5/2}$ shell above the magic $N = 50$ shell gap is included in the shell model calculation. This might indicate a weakening of the $N = 50$ shell gap for nuclei with $Z \approx 28$ and $N > 40$. Moreover, an upper limit of the cross section for the population of the currently unknown 0_2^+ state was obtained. In the one-neutron transfer reaction t(^{72}Zn, d)^{73}Zn, two new levels in ^{73}Zn were discovered and the corresponding differential cross sections were determined.

The multiple Coulomb excitation (Coulex) experiment was performed with a ^{72}Zn REX-ISOLDE beam ($E_{beam} = 2.85$ MeV/u) impinging on a 1.17 mg/cm^2 thick ^{109}Ag target. The scattered ^{72}Zn and ^{109}Ag particles were detected with the C-REX silicon array which was designed and build in the framework of this thesis. C-REX features a large angular coverage which allows to measure the angular dependency of the Coulex cross sections. Compared to previous experiments, it is especially sensitive to multi-step Coulomb excitations which occur dominantly at backward center-of-mass scattering angles. Again, the particle information was complemented by the simultaneous detection of γ-rays from either ejectile or target with MINIBALL. To obtain a high γ-ray energy resolution, the Doppler correction capabilities of MINIBALL were significantly improved using, for the fist time, a new data-driven technique. The achieved resolution of $\Delta E = 6.4$ keV (FWHM) at $E_\gamma = 653$ keV allowed to clearly separate even close lying γ-ray transitions such as the $4_1^+ \to 2_1^+$ and the $0_2^+ \to 2_1^+$ transition in ^{72}Zn. Fitting calculated γ-ray yields from different Coulex codes (CLX/DCY, GOSIA and GOSIA2) to the experimental data resulted in a consistent set of nine ^{72}Zn matrix elements. Thanks to the newly developed, nearly 4π C-REX setup in combination with the highly efficient MINIBALL γ-ray spectrometer, this marks one the first measurements of such a large set of matrix elements for a radioactive isotope. In addition, the large Coulex data set of 110 γ-ray transitions from the stable target allowed to extract 26 electric and magnetic ^{109}Ag matrix elements at unprecedented precision. In the future, this high-precision set of ^{109}Ag matrix elements can be used to obtain a more accurate

normalization for upcoming Coulex experiments.

The nine determined ^{72}Zn matrix elements correspond to six reduced transition strengths ($B(E2)$ values) connecting the 0^+_1, 2^+_1, 4^+_1, 0^+_2 and 2^+_2 states of ^{72}Zn and three quadrupole moments of the 2^+_1, 4^+_1 and 2^+_2 states. The $B(E2; 2^+_1 \rightarrow 0^+_1) = (20.2 \pm 2.3)$ W.u. strength is in excellent agreement with previous Coulex and lifetime measurements. The larger $B(E2; 4^+_1 \rightarrow 2^+_1) = (28.9 \pm 3.5)$ W.u. is moderately collective, which coincides with the results from previous Coulex measurements, but is in tension to the lifetime measurements which propose a much smaller, non-collective value. Furthermore, the $B(E2)$ values of the $2^+_2 \rightarrow 2^+_1$ and $0^+_2 \rightarrow 2^+_1$ transitions have been measured for the first time in the radioactive zinc chain. Their comparably small reduced transition strengths $B(E2; 2^+_2 \rightarrow 2^+_1) = 11.5 \pm 2.3$ W.u. and $B(E2; 0^+_2 \rightarrow 2^+_1) = 11.0 \pm 5.4$ W.u. indicate a different structure of the 0^+_2 and the 2^+_2 state in ^{72}Zn compared to the 0^+_1, 2^+_1 and the 4^+_1 states of the yrast band, as proposed by two shell model calculation using the jj4c and the JUN45 interaction. Similar to ^{70}Zn, the 0^+_2 state in ^{72}Zn is predicted to feature a higher fraction of the closed $N = 40$ configuration in its neutron wave function than the ground state. The quadrupole moments of the 2^+_1, 4^+_1 and 2^+_2, which have been derived for the first time, provide additional insights about the shapes of the nuclei: The 2^+_1 and the 4^+_1 state of ^{72}Zn feature negative quadrupole moments $Q_s(2^+_1) = (-24 \pm 4)$ efm^2 and $Q_s(4^+_1) = (-27 \pm 8)$ efm^2, respectively, which are in accordance with a prolate shape. The 2^+_2 state, in contrast, features a positive quadrupole moment $Q_s(2^+_2) = (+39 \pm 6)$ efm^2 which corresponds to an oblate shape. Furthermore, by applying quadrupole sum rules a moderately deformed and almost triaxial character of the 0^+_1 ground state in ^{72}Zn was found.

In summary, the moderately collective $B(E2)$ values and the moderate deformed shapes of the yrast states of ^{72}Zn, determined in this thesis, indicate that the $N = 40$ subshell closure is not strong enough to stabilize the nearly spherical shape of the nucleus as expected close to magic nuclei. Instead, it has been shown experimentally that $^{72}_{30}$Zn is in the transitional region between $^{70}_{28}$Ni with a (nearly) spherical ground state and the collective $^{74}_{32}$Ge nucleus featuring a deformed ground state.

Zusammenfassung

In den letzten Jahrzehnten gab es große Anstrengungen die Entwicklung der Schalenstruktur von stabilen bis hin zu exotischen Atomkernen zu verstehen. Experimente an den neu entwickelten Beschleunigeranlagen für radioaktive Ionenstrahlen zeigten, dass einige klassische magische Zahlen jenseits des Tals der Stabilität ihre Gültigkeit verlieren und sich stattdessen neue magische Zahlen herausbilden. In dieser Arbeit wird der Unterschalenabschluss $N = 40$ genauer beleuchtet. Die Neutronenzahl $N = 40$ zeigt ein magisches Verhalten, vor allem im Kern ^{68}Ni, der zusätzlich noch eine magische Protonenzahl ($Z = 28$) besitzt. Jedoch treten die magischen Eigenschaften von $N = 40$ nur sehr lokal auf, da bereits die benachbarten Zink-Isotope ($Z = 30$) ein kollektives Verhalten aufweisen. Da die experimentelle Datenlage derzeit widersprüchlich ist, wurden die neutronenreichen Zink-Kerne in dieser Arbeit mit zwei komplementären Methoden untersucht: Transferreaktionen und Coulomb-Anregung. Beide Experimente wurden mit einem radioaktiven ^{72}Zn Strahl an der ISOLDE Beschleunigeranlage am CERN durchgeführt.

In dem Transferexperiment wurde der ^{72}Zn Strahl mit einer kinetischen Energie von $E_{beam} = 2.7$MeV/u auf ein radioaktives Tritium-Target geschossen. Somit konnte die Zwei-Neutronen-Transferreaktion t(^{72}Zn, p)^{74}Zn und die Ein-Neutronen-Transferreaktion t(^{72}Zn, d)^{73}Zn gleichzeitig untersucht werden. Um beide Reaktionskanäle voneinander zu trennen, wurden die entstandenen Transfer-Protonen und Deuteronen mittels der ΔE-E Teleskope des nahezu 4π Silizium-Detektorarrays T-REX identifiziert. Aus der Energie- und Ortsinformation der detektierten Teilchen wurden Anregungsenergie-Spektren der ^{73,74}Zn Kerne berechnet. Zusätzlich wurden die emittierten γ-Quanten mit dem Europäischen Germanium-Spektrometer MINIBALL nachgewiesen, um eindeutig den Reaktionskanal und den bevölkerten Zustand zu identifizieren. Kombiniert man die Informationen aus beiden Detektorarrays, so lassen sich differenzielle Wirkungsquerschnitte bestimmen. Im Fall der Zwei-Neutronen-Transferreaktion konnte der Wirkungsquerschnitt vom Grundzustand und vom 2_1^+ Zustand von ^{74}Zn extrahiert und mit FRESCO Rechnungen verglichen werden. Daraus lässt sich folgern, dass bei der Bevölkerung des ^{74}Zn Grundzustands die Neutronen hauptsächlich in das $1g_{9/2}$ Orbital jenseits der $N = 40$ Schalenlücke transferiert werden. Der experimentelle Wirkungsquerschnitt des 2_1^+ Zustands in ^{74}Zn konnte nur reproduziert werden, wenn in der Rechnung zusätzlich das $2d_{5/2}$ Orbital jenseits der magischen Zahl $N = 50$ berücksichtigt wird. Dies könnte darauf hindeuten, dass die $N = 50$ Schalenlücke für Kerne mit $Z \approx 28$ und $N > 40$ geschwächt ist. Außerdem wurde eine obere Grenze für den Wirkungsquerschnitt des bisher unbekannten 0_2^+ Zustands aus den experimentellen Daten bestimmt. Im Kanal der Ein-Neutronen-Transferreaktion wurden zwei neue Zustände in ^{73}Zn entdeckt, sowie deren differenzielle Wirkungsquerschnitte extrahiert.

Die mehrfache Coulomb-Anregung (Coulex) von ^{72}Zn wurde mit einem radioaktiven ^{72}Zn REX-ISOLDE Strahl ($E_{beam} = 2.85$ MeV/u) durchgeführt, der auf ein reines 1.17 mg/cm^2 dickes ^{109}Ag Target geschossen wurde. Die gestreuten ^{72}Zn und ^{109}Ag Kerne wurden mit dem C-REX Aufbau nachgewiesen, der im Rahmen dieser Arbeit entwickelt wurde. Er verfügt über eine große Raumwinkelabdeckung, die es erlaubt die Winkelabhängigkeit der Coulex-Wirkungsquerschnitte zu messen. Im Vergleich zu bisherigen Experimenten ist C-REX besonders sensitiv auf die mehrfache Coulomb-Anregung, die vor allem bei großen Streuwinkeln im Schwerpunktsystem auftritt. Die Teilcheninformation aus C-REX wird ergänzt durch den gleichzeitigen Nachweis, der von den angeregten ^{72}Zn und ^{109}Ag Kernen emittierten γ-Quanten in MINIBALL. Um eine hohe Energieauflösung in den Doppler-korrigierten γ-Spektren zu erzielen, wurde das Potential der Dopplerkorrektur mit MINIBALL durch die Entwicklung einer neuen, auf Daten basierenden Methode deutlich verbessert. Die erreichte Energieauflösung von $\Delta E = 6.4$keV (FWHM) bei $E_\gamma = 653$keV erlaubt es, auch energetisch naheliegende γ-Übergänge, wie die Übergänge $4_1^+ \rightarrow 2_1^+$ und $0_2^+ \rightarrow 2_1^+$ in ^{72}Zn, klar zu trennen. Durch einen Fit der berechnete Zählraten von verschiedenen Coulex-Programmen (CLX/DCY, GOSIA und GOSIA2) an

die experimentell bestimmten Zählraten der Doppler-korrigieren Peaks ergaben sich neun elektromagnetische Matrixelemente für ^{72}Zn. Diese große Anzahl an experimentell bestimmten Matrixelementen ist bemerkenswert für einen radioaktiven Strahl und ist dem neuen C-REX Aufbau in Kombination mit dem hochauflösenden und effizienten MINIBALL γ-ray Spektrometer zu verdanken. Zusätzlich erlaubt es der große Coulex-Datensatz bestehend aus 110 Zählraten von 11 verschiedenen γ-Übergängen des stabilen Targets, 26 elektrische und magnetische Matrixelemente von ^{109}Ag mit einer bisher unerreichten Genauigkeit zu bestimmen. Diese hochpräzisen ^{109}Ag Daten liefern eine deutlich genauere Normierung für zukünftige Coulex-Experimente.

Die neun experimentell bestimmten ^{72}Zn Matrixelemente entsprechen insgesamt sechs reduzierten Übergangswahrscheinlichkeiten ($B(E2)$-Werte), die die Zustände 0_1^+, 2_1^+, 4_1^+, 0_2^+ und 2_2^+ in ^{72}Zn verbinden, sowie drei Quadrupolmomenten der Zustände 2_1^+, 4_1^+ und 2_2^+. Die gemessene Übergangsstärke $B(E2; 2_1^+ \rightarrow 0_1^+) = (20.2 \pm 2.3)$ W.u. ist in sehr guter Übereinstimmung mit dem vorangegangen Coulex-Experimenten und Lebensdauermessungen. Die höhere, mäßig kollektive Übergangsstärke $B(E2; 4_1^+ \rightarrow 2_1^+) = (28.0 \pm 3.5)$ W.u. ist im Einklang mit vorherigen Coulex-Messungen, aber steht im Widerspruch zu den bisherigen Lebensdauermessungen, die ein nicht-kollektives Verhalten vorhersagen. Außerdem wurden zum ersten Mal die $B(E2)$-Werte des $2_2^+ \rightarrow 2_1^+$ und des $0_2^+ \rightarrow 2_1^+$ Übergangs in den radioaktiven, neutronenreichen Zink-Isotopen gemessen. Ihre niedrigen reduzierten Übergangsstärken $B(E2; 2_2^+ \rightarrow 2_1^+) = 11.5 \pm 2.3$ W.u. und $B(E2; 0_2^+ \rightarrow 2_1^+) = 11.0 \pm 5.4$ W.u. weisen auf eine andere Struktur des 2_2^+ und des 0_2^+ Zustands im Vergleich zu den Yrast-Zuständen 0_1^+, 2_1^+ und 4_1^+ hin. Dies wird auch von zwei Schalenmodell-Rechnungen mit der jj4c und der JUN45 Wechselwirkung bestätigt: Ähnlich zu ^{70}Zn, weist der 0_2^+ Zustand in ^{72}Zn einen höheren Anteil der geschlossenen $N = 40$ Konfiguration in seiner Neutronen-Wellenfunktion auf als der Grundzustand. Die spektroskopischen Quadrupolmomente der Zustände 2_1^+, 4_1^+ und 2_2^+ wurden das erste Mal bestimmt und ermöglichen einen zusätzlichen Einblick in die Form des Kerns: Der 2_1^+ und der 4_1^+ Zustand in ^{72}Zn besitzen negative Quadrupolmomente $Q_s(2_1^+) = (-24 \pm 4)\,\mathrm{efm}^2$ und $Q_s(4_1^+) = (-27 \pm 8)\,\mathrm{efm}^2$, die einer prolaten Form entsprechen. Im Gegensatz dazu besitzt der 2_2^+ Zustand ein positives Quadrupolmoment $Q_s(2_2^+) = (+39 \pm 6)\,\mathrm{efm}^2$, das mit einer oblaten Deformation einhergeht. Außerdem konnte durch die Anwendung von Quadrupol-Summen-Regeln gezeigt werden, dass der ^{72}Zn Grundzustand mäßig deformiert und triaxial ist.

Die mäßig deformierten Zustände in der ^{72}Zn Yrast-Bande weisen darauf hin, dass der $N = 40$ Unterschalenabschluss nicht stark genug ist, um die sphärische Form zu stabilisieren, die nahe von doppelt magischen Kernen erwartet wird. Stattdessen wurde in dieser Arbeit experimentell gezeigt, dass sich $^{72}_{30}$Zn in einer Übergangsregion von $^{70}_{28}$Ni mit einem (nahezu) sphärischen Grundzustand und dem kollektiven $^{74}_{32}$Ge Kern mit einem deformierten Grundzustand liegt.

Contents

1

Motivation

Despite many experimental and theoretical efforts in the last decades, no unique theoretical description of nuclei exists which is applicable for the whole nuclear landscape. This is due to the complex nature of the nuclear interaction which features many degrees of freedom. Hence, depending on the region of interest on the nuclear chart and on the observed phenomena, different models are used to gain insight into the nuclear structure:

One of the most successful description of nuclei is the classical shell model, which especially characterizes the single particle properties of nuclei. Assuming a realistic mean-field potential, such as a Woods-Saxon potential, and by including the spin-orbit interaction of the nucleons, the shell model predicts correctly the experimentally found energy levels of (stable) nuclei [1, 2, 3, 4]. They are quantized like the energy levels of the electrons in the atomic shells. Large energy gaps between the shells indicate particularly stable configurations, similar to the noble gases in atomic physics. They occur at proton and neutron numbers 2, 8, 20, 28, 50, 82 and 126, respectively [1]. In nuclear physics, these closed shell configurations are called "magic numbers".

Complementary to the classical shell model, collective models allow to understand nuclear excitations in which many nucleons are involved [1, 5]. The most popular collective excitations are nuclear surface vibrations and rotations of deformed nuclei.

Shell Evolution of Exotic Nuclei

Originally, the shell model and the collective models have been developed for stable nuclei in the valley of stability. However, in the last decades, the development of radioactive beam facilities has allowed to study nuclei away from the valley of stability. It has been shown in many experiments that shell structure can change dramatically [6]: Going to exotic nuclei, the "classical" magic numbers can vanish and new magic numbers can appear. An early discovery of a new magic number near the neutron drip line was found in the oxygen isotopes: ^{24}O ($N = 16$) has a doubly magic nature, while ^{28}O ($N = 20$) is unbound [7, 8, 9]. These significant changes in nuclear shell evolution result from the residual interaction term[1] of the Hamilton operator of the nucleus. It can be treated as a small perturbation close to the valley of stability, but it plays a crucial role going towards the proton and neutron drip lines.

One important residual interaction, which can explain the changing of the shell sequence in many areas of the nuclear landscape, is the monopole part[2] of the tensor term of the nuclear force [10]. Following Otsuka et. al. [10], it depends on the relative alignment of the spin $\vec{s}$ and the angular momentum $\vec{l}$ of the nucleons. If $\vec{s}$ and $\vec{l}$ are parallel a nucleon occupies a $j_> = l + s$ orbit. Contrary, if $\vec{s}$ and $\vec{l}$ are aligned anti-parallel the nucleon resides in a $j_< = l - s$ orbit. The calculation of Otsuka shows that the tensor force between two nucleons works attractively if one nucleon occupies a $j_>$ orbit and the other a $j'_<$ orbit or vice versa [10]. Hence, filling more neutrons in a $j'_<$ orbit results in stronger bound protons in $j_<$ orbits, which corresponds to a lowering of the effective single particle energy of this proton orbit relative to the neutron orbit $j'_<$ (c.f. fig. 1.1). Contrary, the tensor force is repulsive if protons are in $j_>$ ($j_<$) and neutrons in $j'_>$ ($j'_<$). Hence, if more neutrons are filled into a $j'_>$ orbit, protons in a $j_>$ orbit feel a repulsive interaction. Thus, the protons are less strongly bound and their effective single particle

---

[1]The residual interaction term of the Hamiltonian corresponds to the difference between the mean field potential and the true potential of the nucleus.

[2]The residual interaction can be decomposed using a multipole expansion with a dominating monopole term [6].
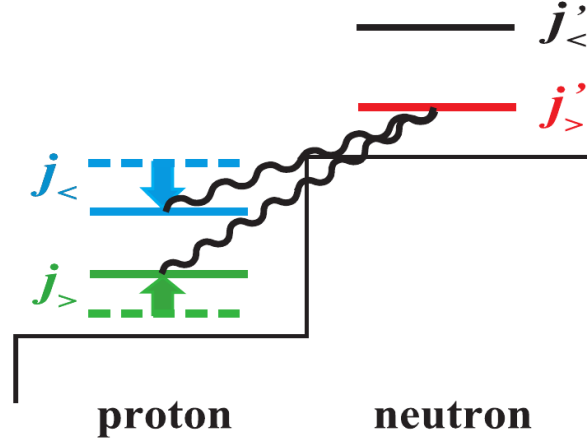
Fig. 1.1: A schematic figure showing the interaction between protons and neutrons due to the monopole part of the tensor force [10]. The tensor force works attractively between protons in a $j_< = l - s$ ($j_> = l + s$) orbit and neutrons in a $j'_> = l + s$ ($j'_< = l - s$) orbit. Contrary, the tensor force is repulsive if protons and neutrons occupy both $j_>$ or both $j_<$ orbits. Hence, the tensor force can change the size of the relative energy splitting between the orbits j and j'. Picture adapted from [10].
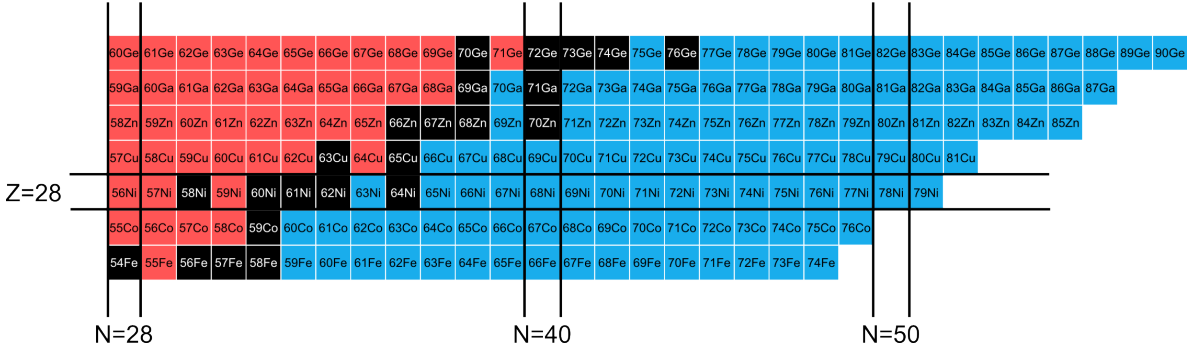
Fig. 1.2: An excerpt of the nuclear chart. Only atomic numbers between $Z = 26$ and $Z = 32$, as well as neutron numbers $N > 28$ are shown. The classical magic numbers $N = Z = 28$, $N = 50$ and the harmonic subshell closure $N = 40$ are highlighted.

energy is increased relative to the neutron orbit $j'_>$ (c.f. fig. 1.1).

Nuclear Structure around $Z = 28$ and $N = 40 - 50$

In this thesis, the neutron-rich nuclei near the classical magic proton number $Z = 28$ are investigated. On the neutron side, three shell closures play a crucial role: The harmonic subshell at $N = 40$ as well as the classical neutron magic numbers $N = 28$ and $N = 50$ (c.f. fig. 1.2). Despite many experimental and theoretical efforts, the evolution of the nuclear shells in this region is still under discussion. Especially, the experimentally found doubly-magic characteristics of ^{68}Ni ($Z = 28$, $N = 40$) have been studied in a large number of experiments (c.f. sec. 1.1). Furthermore, the stability of the doubly magicity of ^{78}Ni ($Z = 28$, $N = 50$) is of great importance, as ^{78}Ni is a weighting point nucleus in the astrophysical rapid neutron-capture process (r-process) [11]. To understand the evolution of the shell structure in this region, also the neighboring isotopes should be studied. As the $Z = 30$ neutron-rich zinc isotopes are experimentally well accessible with radioactive beam facilities [12], they allow a detailed investigation of this region with relative high statistics. In the scope of this thesis, the neutron-rich zinc isotopes are studied with two complementary methods: First, the single-particle properties are investigated using one- and two-neutron transfer reactions. Second, the collective properties of the neutron-rich zinc isotopes are analyzed by studying the multiple Coulomb excitation of ^{72}Zn.
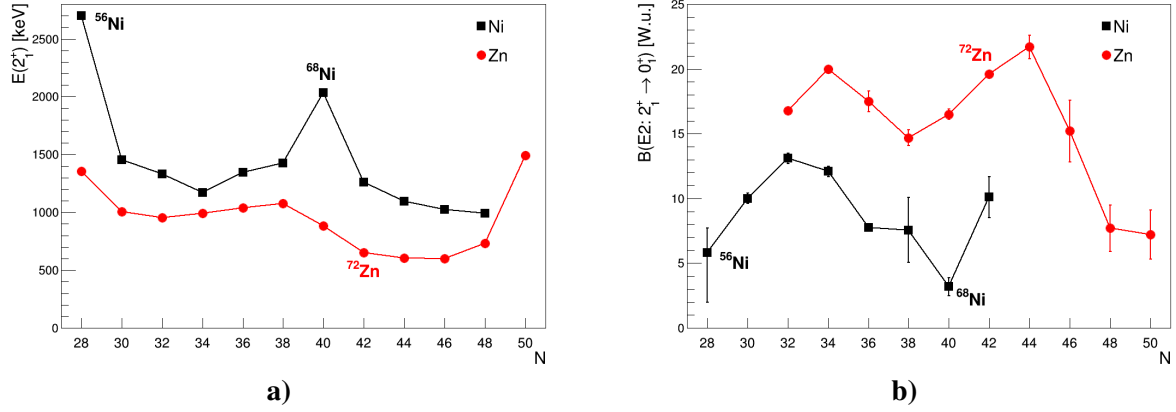
Fig. 1.3: The systematics of the energies of the first excited 2_1^+ state (**a**)) and of the reduced transition probabilities $B(E2; 2_1^+ \rightarrow 0_1^+)$ (**b**)) in the nickel and the zinc isotopic chain [13]. The connection lines are only included to guide the eye.

Thesis Overview

At the beginning of this chapter, a short introduction into nuclear models and the shell evolution beyond the valley of stability is given. The remainder of this chapter focuses on the nuclei of interest of this thesis, which are the neutron-rich nickel and zinc isotopes. The local doubly magicity of ^{68}Ni is discussed in sec. 1.1. Successively, sec. 1.2 presents the today's experimental status of the neutron-rich zinc isotopes. As the current experimental data does not provide a consistent picture yet, these measurements have been complemented in this thesis with two additional experiments using a radioactive ^{72}Zn ISOLDE beam: the study of one- and two-neutron transfer reactions and a multiple Coulomb excitation experiment. The used experimental setups T-REX and C-REX are detailed in chap. 3. Chap. 4 presents the used calibration procedures as well as the newly developed Doppler correction methods which are crucial for the success of the experiments. The analysis techniques and the obtained results are discussed in the two following chapters 5 and 6, respectively. Finally, chap. 7 gives a summary and provides an outlook on future experiments at HIE-ISOLDE dealing in the same nuclear region.

1.1 The Local Doubly Magicity of ^{68}Ni

The key nucleus in the region to which ^{72}Zn belongs is ^{68}Ni, that has a magic proton shell $Z = 28$ and a possible harmonic subshell closure at its neutron number $N = 40$. In the last decades, the ^{68}Ni nucleus was thoroughly investigated both experimentally and theoretically, since it has features which are characteristic for doubly magic nuclei (c.f. fig. 1.3): A high excitation energy $E(2_1^+) = 2034$keV for its 2_1^+ state [14], a low reduced transition probability $B(E2; 2_1^+ \rightarrow 0_1^+)$ (for its definition c.f. sec. 2.3.1) [15, 16] and a low lying 0_2^+ state [17]. Contrary, the two-neutron separation energies (i.e. mass measurements), which are the most sensitive and direct evidence for a doubly magic nucleus, do not show a pronounced shell closure at $N = 40$ [18, 19]. Today, explanations for this partial doubly magicity of ^{68}Ni exist: Assuming a close $Z = 28$ shell, the high 2_1^+ energy and the low $B(E2; 2_1^+ \rightarrow 0_1^+)$ value can be understood, as parity conserving quadrupole excitations from the 0_1^+ ground state to the 2_1^+ state are hindered due to the different parity of the fully-occupied fp-orbitals (negative parity) and the empty $1g_{9/2}$ (positive parity) neutron orbital (c.f. fig. 1.4). Hence, due to parity conservation, only a neutron pair can be scattered across the $N = 40$ gap to excite the 2_1^+ state [15]. Furthermore, since neutrons are chargeless, they cannot contribute directly to the $B(E2)$ value. Instead, favored e.g. by the tensor force, they induce proton-core polarizations, i.e. proton excitations from the $\pi f_{7/2}$ orbit across $Z = 28$ [15]. Therefore, the interplay between the protons and neutrons plays a crucial role.

Fig. 1.4: The shell model orbitals which are relevant in the neutron-rich nickel and zinc isotopes. The occupation number of ^{68}Ni, which is predicted by the classical shell model is shown.

Shape Coexistence

One tool to study of the proton-neutron interaction in a nucleus from the experimental and the theoretical point of view, is the presence of shape coexistence[3]. Shape coexistence in even-even nuclei is likely to occur if there is at least one low lying 0^+ state besides the ground state [20]. These excited 0^+ states can be interpreted as additional "ground states" featuring different nuclear shapes. In the nickel isotope chain there is strong evidence that shape coexistence appears in ^{68,70}Ni: For ^{68}Ni Monte Carlo shell-model calculations in the full $pfg_{9/2}d_{5/2}$ model space indicate a spherical ground state, a moderate oblate 0_2^+ state and a prolate 0_3^+ state [21, 22]. The 0_2^+ state is dominated by 2p-2h[4] neutron excitations from the νfp-shell to the $\nu 1g_{9/2}$ orbit [23], while the 0_3^+ state is dominated by 2p-2h proton excitations across $Z = 28$ [24, 25]. These configurations have also been confirmed by a large scale shell model calculation using a ^{48}Ca core, the full fp-shell for protons and the $f_{5/2}pg_{9/2}d_{5/2}$ shell for neutrons as well as the LNPS interaction [26]. Additionally, the structure of these states has been verified by the two-neutron transfer experiment t(^{66}Ni, p)^{68}Ni which was conducted at ISOLDE, CERN [27], [28]. Furthermore, there is a strong evidence from Monte Carlo shell-model calculations that also ^{70}Ni features shape coexistence with (nearly) spherical, oblate and prolate shapes [29]. However, the prolate structure of ^{70}Ni occurs at lower energies than prolate structure of ^{68}Ni as the tensor force between $1g_{9/2}$ neutrons and the protons is stronger due to the two additional neutrons in ^{70}Ni [29]. Thus, the $Z = 28$ shell-gap is reduced which favors 2p-2h excitations across $Z = 28$ (c.f. fig. 1.4).

Neighboring Isotopes of the Neutron-Rich Nickel Chain

Besides studying ^{68}Ni directly, a deeper insight into the proton-neutron interaction and the shell evolution in the nuclear region around ^{68}Ni can be gained by exploring the neighboring isotopes. Adding or removing a few protons of $Z = 28$ results in a rapid increase in collectivity: ^{67}Co which is one proton below ^{68}Ni is a deformed nucleus [30]. Removing another proton ^{66}Fe is reached which is deformed, too [31, 32, 33]. If a proton is added to ^{68}Ni, ^{69}Cu is reached whose first excited state corresponds to a single proton $1f_{5/2}$ configuration [34]. Furthermore, two protons above ^{68}Ni, ^{70}Zn shows a collective behavior especially in its level scheme. In conclusion, the $N = 40$ subshell closure is very localized. Therefore, the large variations of the nuclear structure in this region of the nuclear landscape is a good testing ground for theoretical models.

1.2   The Neutron-Rich Zinc Isotopes

Despite many investigations of ^{68}Ni and its neighbors, the interplay between the protons and neutrons is not understood in detail. An ideal system to study the complex proton-neutron interaction in this region represents the even-even nucleus ^{72}Zn. In a simple picture, ^{72}Zn can be interpreted as ^{68}Ni to

---

[3]A nucleus features shape coexistence if it assumes different geometrical shapes in states lying close in energy.
[4]two-particle-two-hole

which a pair of two protons and a pair of two neutrons is coupled. In the following, the systematics of the the neutron-rich zinc isotopes are discussed under the aspect of adding more neutrons to the simple system.

The evolution of the energies of their first excited 2_1^+ states and the reduced transition probabilities $B(E2; 2_1^+ \rightarrow 0_1^+)$ are compared in fig. 1.3 to the previously discussed nickel isotopes (c.f. sec. 1.1). In general, the zinc 2_1^+ energies are always smaller than the nickel 2_1^+ energies and the zinc $B(E2; 2_1^+ \rightarrow 0_1^+)$ values are always larger than the nickel $B(E2; 2_1^+ \rightarrow 0_1^+)$ values. This indicates a certain amount of collectivity in the zinc isotopes which clearly is induced by adding two protons and thus enlarging the proton-neutron interaction around $N = 40$. The evolution of the 2_1^+ energy in the zinc chain does not show a sign for a possible subshell closures at $N = 40$, since it even further decreases approaching $N = 40$. However, the $B(E2)$ values feature their minimum around $N = 40$, but the effect is less pronounced than in the nickel isotopes.

Contradictory Lifetime Measurements and Coulex Experiments

As the evolution of the $B(E2)$ values is ideal to study the collectivity, their precise determination is essential. This is especially important for the region around $N = 40$, since the underlying nuclear structure changes rapidly while adding or removing a few nucleons to ^{68}Ni. However, in the neutron-rich zinc chain, large discrepancies between Coulex experiments and lifetime measurements exit (c.f. fig. 1.5):

The reduced transition probabilities $B(E2)$ are directly linked to the lifetime of the excited state (c.f. eq. (2.25)). The expected lifetimes of the 2_1^+ states in the even-even zinc isotopes are in the order of picoseconds. Therefore, two techniques to measure the lifetime are applicable: First, the Doppler Shift Attenuation Method (DSAM) and second, the Recoil Distance Doppler Shift method (RDDS). The DSAM technique extracts the lifetime from the line shape of the Doppler shifted γ-ray peak which depends on the velocity of the de-accelerating nucleus in the used thick target, i.e. on the lifetime of the nuclear state. For ^{70}Zn a DSAM measurement was conducted which yielded a collective $B(E2; 4_1^+ \rightarrow 2_1^+)$ value proposing a structural change while passing $N = 40$ [35, 36] (c.f. fig. 1.5 b)). All other lifetime measurements in the neutron-rich zinc chain (^{70,72,74}Zn) were conducted with the Recoil Distance Doppler Shift method (RDDS) using the differential Cologne plunger device [37]. The Cologne plunger features a degrader foil which can be installed with various, but precisely known distances after the target. Depending on the lifetime of the excited state, the nucleus deexcites before the degrader foil or after the degrader foil. Since the velocity of the nucleus and thus the Doppler shift of the emitted γ-ray before and after the degrader foil is different, two γ-ray peaks appear in the γ-ray spectrum. From their intensity ratio, the lifetime of the state can be extracted. In general, the measurement is done using different degrader distances to eliminate systematic errors. In total, three Cologne plunger experiments have been performed in the neutron-rich zinc chain: One experiment has been conducted at the INFN Laboratory of Legnaro with the AGATA demonstrator and the PRISMA magnetic spectrometer [38]. Apart from that, two experiments at GANIL have been done using both the EXOGAM Ge clover detectors coupled to the VAMOS spectrometer [39] and the LISE fragment separator [40], respectively. The results[5] of all plunger measurements are summarized in fig. 1.5. Although all lifetimes have been determined using different production mechanisms of the zinc isotopes, all plunger experiments coincide well. Furthermore, they are in good agreement with all other experimentally obtained $B(E2; 2_1^+ \rightarrow 0_1^+)$ values, determined mainly by Coulex experiments (c.f. fig. 1.5 a)). However, a large discrepancy between the plunger experiments and the Coulex experiments is present for the $B(E2; 4_1^+ \rightarrow 2_1^+)$ values. The lifetime measurements suggest low $B(E2; 4_1^+ \rightarrow 2_1^+)$ strengths. This corresponds to a non-collective behavior which is expected close to magic numbers. Hence, this would indicate that the stability of the $N = 40$ shell-gap of the nickel isotopes is still present in the zinc isotopes. Contrary, the Coulex experiments predict more collectivity which supports the very localized $N = 40$ subshell closure. To solve this discrepancy an additional experiment

---

[5]Additionally, the obtained lifetimes of ^{72}Zn of all three plunger experiments are summarized in tab. 6.2.
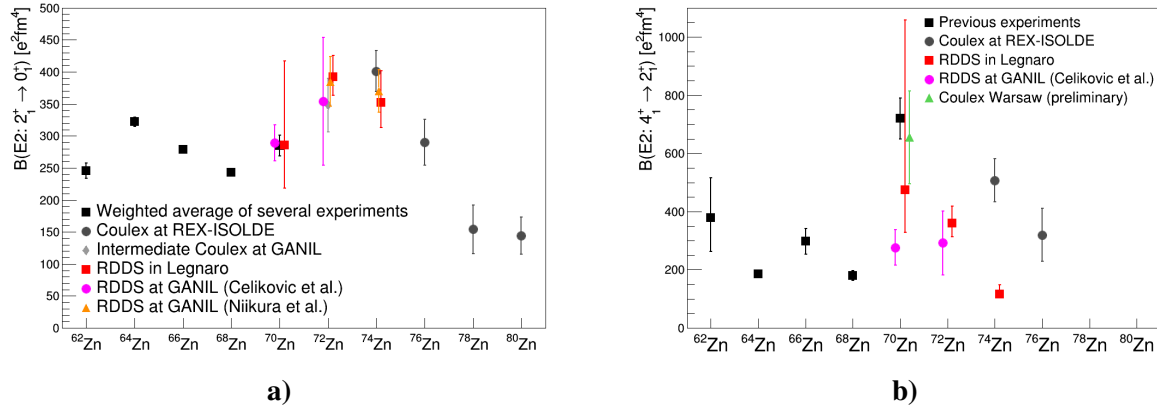
Fig. 1.5: The measured $B(E2)$ values of the neutron-rich zinc isotopes. The dark gray dots represent Coulex experiments which were performed at ISOLDE [41]. The black squares for ^{70}Zn correspond to a DSAM measurement [35, 36]. In addition, lifetime measurements using the Recoil Distance Doppler Shift method (RDDS) are shown: The red squares are the results from a plunger measurement with AGATA in Legnaro [38], the orange triangles and magenta dots are lifetime measurements at GANIL from [39] and [40], respectively. For details see text. Fig. **a)** shows the $B(E2; 2_1^+ \rightarrow 0_1^+)$ values which are in good agreement between all measurements. Fig. **b)** displays the $B(E2; 4_1^+ \rightarrow 2_1^+)$ values which feature discrepancies between the lifetime measurements and the Coulex experiments. With a green upper triangle a preliminary ^{70}Zn Coulex measurement at HIL Warsaw is visualized [42].

has been performed in the course of this thesis: the multiple Coulomb excitation of ^{72}Zn. It will be shown in chap. 6 that the statistics of the experiment is high enough to extract all $B(E2)$ values and quadrupole moments of the energetically low lying states in ^{72}Zn at high precision. This is of great importance, as the Coulex yields depend on the $B(E2)$ value and on the quadrupole moment. In the Coulex analysis of the more exotic zinc isotopes $^{74-80}$Zn, the influence of the quadrupole moment could only be roughly estimated due to low statistics. However, the $B(E2; 4_1^+ \rightarrow 2_1^+)$ value determined in the ^{74,76}Zn Coulex analysis changes only by about 6% assuming a quadrupole moment of $Q(4_1^+) = \pm 0.38$ ebarn [41]. Therefore, the large disagreement between Coulex and lifetime measurements cannot be explained solely with the influence of the quadrupole moment. Lifetime measurements have the advantage that they are only sensitive to the $B(E2)$ value and completely independent of the quadrupole moment. On the other hand, the big challenge of lifetime experiments is to treat the feeding from higher lying states correctly. In the lifetime analysis of [38], feeding contributions to the 4_1^+ state were taken into account. Furthermore, superimposed γ-ray transitions have to be identified and considered, which is especially challenging in the lifetime analysis, since each γ-ray transition features two peaks in the γ-ray spectrum. For a detailed discussion of the discrepancy see sec. 6.4.1.

Comparison to Simple Geometrical Collective Models

According to the 2_1^+ energies and $B(E2; 2_1^+ \rightarrow 0_1^+)$ values (c.f. fig. 1.3), the zinc isotopes are more collective than the nickel isotopes. In the following two geometrical collective models for the neutron-rich zinc isotopes are discussed: One collective model which can be used for the neutron-rich zinc isotopes is the vibrational model, since it describes a spherical nucleus with only a few nucleons outside a closed-shell ($Z = 28$, $N = 40$) via surface vibrations [5]. Second, the Wilets-Jean model describing a complete γ-soft nucleus is investigated, as especially the neighboring ^{72}Ge nucleus was found to be γ-soft [43].

The expected level scheme of a vibrational nucleus including the predicted $B(E2)$ values is shown in fig. 1.6 a). Comparing its level scheme to the level scheme of the zinc chain in fig. 1.7, it can be concluded that the zinc isotopes generally follow the predictions of the vibrational model, especially as in reality typical vibrational nuclei feature $E(4_1^+, 2_2^+, 0_2^+)/E(2_1^+)$ ratios between 2.0 and 2.4 (c.f. fig.
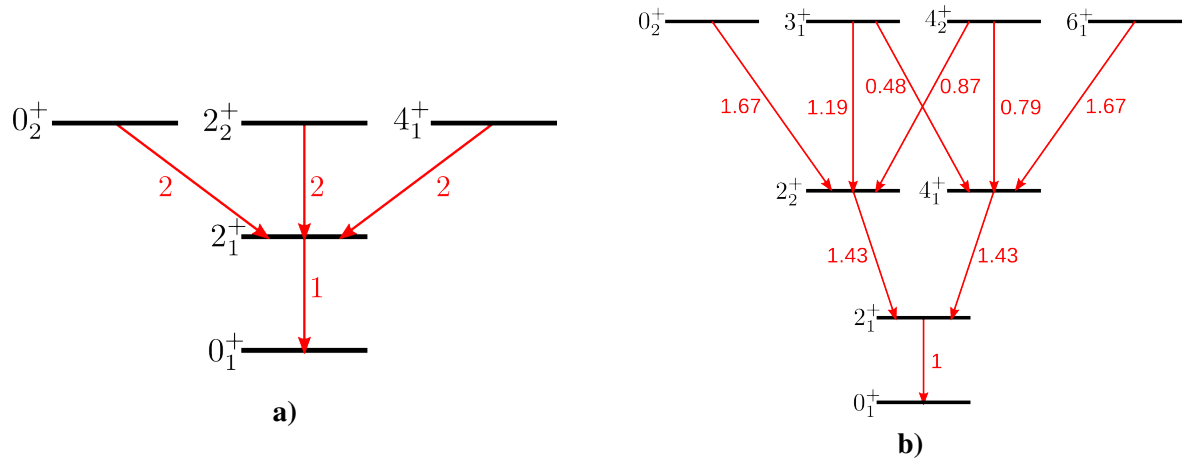
Fig. 1.6: a) A schematic picture of the level scheme of a vibrational nucleus. In the vibrational model, the first and most important vibrational mode is the quadrupole mode $\lambda = 2$, which is modeled in the second quantization by phonon excitations [1]. Starting e.g. from a 0_1^+ ground state of an even-even nucleus, a single $\lambda = 2$ phonon can excite the first excited 2_1^+ state. Two $\lambda = 2$ phonons can couple to the states 0_2^+, 2_2^+ and 4_1^+. The equidistant energy of the levels is given by the eigenvalues of a harmonic oscillator as it can be assumed that the vibrational amplitudes are small. The deexcitation of the excited levels in the vibrational model is realized solely by γ-ray emission with multipolarity $E2$ which follows the selection rule $\Delta N_{ph} = \pm 1$ with N_{ph} being the number of phonons. The reduced transition probabilities $B(E2; N_{ph} + 1 \rightarrow N_{ph})$ (shown with red arrows) are given by the number of phonons in the initial state and the number of possibilities for the final state according to the $E2$ selection rules [1]. Hence, $B(E2; 2_2^+, 0_2^+, 4_1^+ \rightarrow 2_1^+)$ is twice as big as $B(E2; 2_1^+ \rightarrow 0_1^+)$ as the $N_{ph} = 2$ states 0_2^+, 2_2^+ and 4_1^+ provide two phonons which can be destroyed to reach the $N_{ph} = 1$ state 2_1^+. In the picture all $B(E2)$ values are normalized to $B(E2; 2_1^+ \rightarrow 0_1^+)$. Adapted from [1]. **b)** A schematic picture of the level scheme of a γ-soft nucleus in the Wilets-Jean model. It is used to describe deformed nuclei which are free to vibrate in the triaxiality parameter γ, i.e. their potential surface has its minimum at a finite deformation parameter β, but it is completely flat in the γ-parameter [1, 44]. Hence, the nucleus oscillates between a prolate shape ($\gamma = 0$) and an oblate shape ($\gamma = 60°$). In the picture, all $B(E2)$ values (shown with red arrows) are normalized to $B(E2; 2_1^+ \rightarrow 0_1^+)$. Adapted from [44].
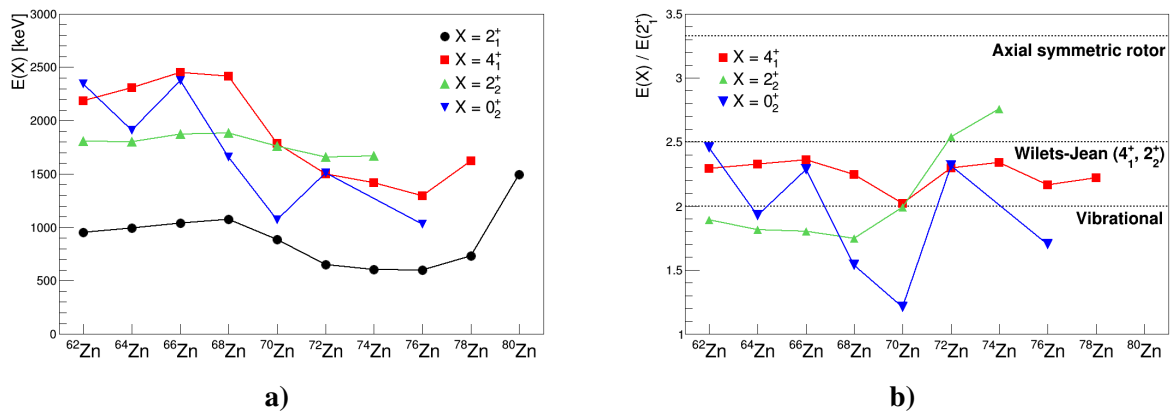
Fig. 1.7: a) The first excited states of the neutron-rich zinc isotopes. Values taken from [13] and picture adapted from [45]. Note, that the spin of the 0_2^+ state in ^{76}Zn was assigned using only the systematics of even-even isotopes. **b)** Energy ratios between the $4_1^+, 2_2^+, 0_2^+$ state and the 2_1^+ state. For comparison the expected ratios of simple collective models are shown. The 0_2^+ state features the largest deviations from the model predictions. The connection lines are only included to guide the eye.

Fig. 1.8: a) The measured ratios $B(E2; 4_1^+ \to 2_1^+)/B(E2; 2_1^+ \to 0_1^+)$ of the neutron-rich zinc isotopes. The dark gray dots represent Coulex experiments which were performed at ISOLDE [41]. The black square for ^{70}Zn corresponds to a DSAM measurement [35, 36]. In addition, lifetime measurements using the Recoil Distance Doppler Shift method (RDDS) are shown: The red squares are the results from a plunger measurement with AGATA in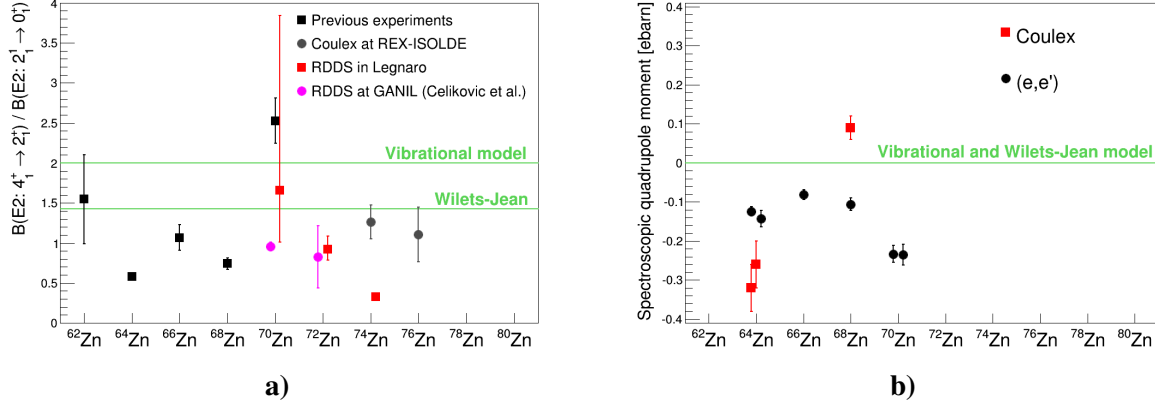 Legnaro [38] and magenta dots correspond to lifetime measurements at GANIL [40]. Additionally, the expectation of simple collective models are shown. In general, the neutron-rich zinc isotopes feature a lower collectivity than the than the vibrational model but are close to the Wilets-Jean model. **b)** Spectroscopic quadrupole moments of the 2_1^+ states of the neutron-rich zinc isotopes measured with (e,e') scattering and with Coulomb excitation. Values taken from [47] and [48]. Generally, negative spectroscopic quadrupole moments, i.e. weakly deformed prolate shapes are preferred in the zinc chain. Additionally, the Coulomb excitation of ^{74}Zn slightly favors a prolate shape for the 2_1^+ state [49].

1.7 b)) [1]. However, the evolution of the 0_2^+ state shows discrepancies, particularly the low lying 0_2^+ state in ^{70}Zn. It is further addressed with the performed experiments in this thesis using two-neutron transfer reactions as well as multiple Coulomb excitation. Apart from that, the measured g-factors support the vibrational model as they are in agreement with a collective value of $g = Z/A$ for all measured g-factors from ^{64}Zn to ^{72}Zn [46]. This indicates that the $N = 40$ shell-gap does not persist any more in the zinc isotopes. Nevertheless, deviations from the vibrational model are observed in the reduced transition strengths: The ratio $B_{42} = B(E2; 4_1^+ \to 2_1^+)/B(E2; 2_1^+ \to 0_1^+)$ is often around 1.0 in the neutron-rich zinc isotopes (c.f. fig. 1.5 and fig. 1.8 a)), i.e. far below the expectation $B_{42} = 2$ of the vibrational model. This low collectivity can correspond to the fact that the zinc isotopes are close to the closed-shell nickel isotopes. Furthermore, as the vibrational model describes spherical nuclei, vanishing quadrupole moments are expected. However, the zinc isotopes prefer dominantly prolate shapes (negative spectroscopic quadrupole moments) instead of spherical shapes (c.f. fig. 1.8 b)). Apart from that, the $2_2^+ \to 0_1^+$ transition is expected to be hindered for vibrational nuclei (c.f. fig. 1.6 a)). With $B(E2; 2_2^+ \to 0_1^+) < 1$ W.u., this is fulfilled for the stable zinc isotopes ^{62,64,66,68,70}Zn [50]. But, today there is no data for the radioactive zinc isotopes available. Hence, measuring the $B(E2; 2_2^+ \to 0_1^+)$ strength in the ^{72}Zn Coulex experiment gives an additional insight into their collective structure beyond $N = 40$ (c.f. chap. 6).

Contrary to the vibrational model, the collective γ-soft model of Wilets-Jean (c.f. fig. 1.6 b)) does reproduce the B_{42} better, as it predicts a lower B_{42} ratio of $10/7 \approx 1.43$ [44]. Additionally, the expected ratio $E(4_1^+, 2_2^+)/E(2_1^+) = 2.5$ of a completely γ-soft nucleus is in agreement for the neutron-rich zinc isotopes beyond $N = 40$. Therefore and due to the systematics in the neighboring Ge and Se nuclei, [39] suggests in the zinc isotopes a "transition from a spherical oscillator at $N = 40$ to a complete γ-softness at $N = 42$". However, similar to the vibrational model, the 0_2^+ state do not follow the expectation of a γ-soft nuclei, which indicates that the 0_2^+ state has a different nuclear structure than the other low lying states in the zinc chain (c.f. chap. 6). Apart from that, in the Wilets-Jean model all quadrupole moments are zero, which is in disagreement with the measured prolate shapes in the zinc chain (c.f. fig. 1.8 b)).
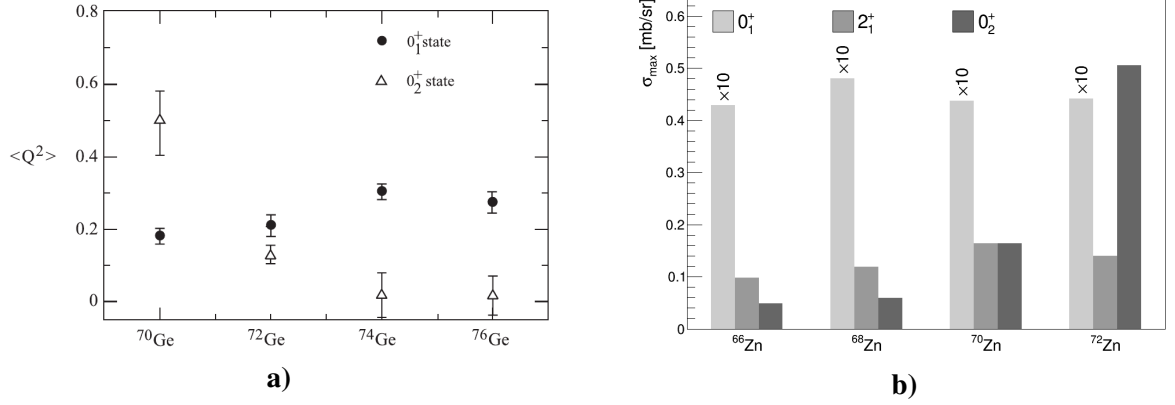
Fig. 1.9: a) The rotational invariant parameter $\langle Q^2 \rangle$ in e^2barn^2 of the 0_1^+ ground state and the 0_2^+ state of the even germanium isotopes $^{70-76}$Ge. A large $\langle Q^2 \rangle$ value corresponds to a deformed shape, while values close to zero represents a spherical shape. Both shapes coexist in $^{70-76}$Ge. The $\langle Q^2 \rangle$ values were determined using the $E2$ rotational invariants sum rules applied on the $B(E2)$ values extracted from a Coulomb excitation experiment (c.f. sec. 6.4.2). Adapted from [51]. **b)** The maximum of the cross sections of the ^{64,66,68,70}Zn(t,p)^{66,68,70,72}Zn reactions populating the ground state, the 2_1^+ state and the 0_2^+ state. While the cross section of the ground state and the 2_1^+ state is constant for the different isotopes, the transfer cross section to the 0_2^+ state increases dramatically. For details see text. Values taken from [52].

In summary, both simple models are not able to describe all observed quantities of the neutron-rich zinc isotopes. Instead, they feature a much more complex structure which needs more advanced models: A modern triaxial beyond mean field calculation, which is in good agreement with the measured g-factors [46], proposes triaxial shapes for at $N = 40$ (^{70}Zn) and a trend to more prolate shapes with increasing neutron number [46] (c.f. fig. 6.31). This is also consistent with the slightly favored prolate shape of ^{74}Zn by the Coulex experiment [49] and generally follows much better the systematics of the zinc spectroscopic quadrupole moment (c.f. fig. 1.8 b)).

Structure of 0^+ States

The microscopic nuclear structure of 0^+ states of nuclei close to the magic number $Z = 28$ and the harmonic subshell closure $N = 40$ is of particular interest: As pointed out in sec. 1.1, there are strong experimental and theoretical indications that the 0_1^+ ground state and the excited 0_2^+ and 0_3^+ states of ^{68}Ni ($Z = 28$) feature shape coexistence with spherical, oblate and prolate deformation, respectively. Apart from that, shape coexistence was experimentally proven in the stable germanium isotopes $^{70-76}$Ge ($Z = 32$) (c.f. fig. 1.9 a)): Going from ^{70}Ge to ^{76}Ge, the shape of the germanium ground states features an evolution from a weakly deformed to a deformed configuration, while the 0_2^+ state features a transition from a strongly deformed to a spherical configuration [20, 51]. Thus, the $Z = 30$ zinc chain is enclosed by nuclei featuring shape coexistence. Additionally, the 0_2^+ energies of the zinc isotopes show the strongest discrepancies from simple collective models (c.f. fig. 1.7). Hence, a further investigation of the 0^+ states in neutron-rich zinc isotopes allows a deeper insight into the nuclear structure around $N = 40$. A good tool to study 0^+ states are two-neutron (2n) transfer reactions which has been successfully demonstrated in previous 2n transfer experiments [27, 53, 54, 55] at the ISOLDE facility, CERN. The first 2n transfer experiments in the zinc chain address the stable zinc isotopes: [52] investigates the ^{64,66,68,70}Zn(t,p)^{66,68,70,72}Zn reactions with a 12 MeV triton beam provided by the Aldermaston tandem Van de Graaff accelerator. The tritons impinged on enriched zinc ^{64,66,68,70}Zn targets. The outgoing ^{66,68,70,72}Zn nuclei were detected with a multigap spectrograph. Fig. 1.9 b) shows the maximum values of the measured 2n transfer cross sections for the ground state, the 2_1^+ state and the 0_2^+ state of the produced zinc nuclei. Similar to the energy of the 0_2^+ state, the 0_2^+ cross section differs from the other states: It features an abrupt increase from ^{70}Zn ($N = 40$) to ^{72}Zn

($N = 42$), i.e. when crossing the harmonic oscillator shell-gap $N = 40$. Hence, to study the unusual evolution of the 0_2^+ state in the neutron-rich zinc isotopes, the 2n transfer reaction from ^{72}Zn to ^{74}Zn is investigated in the course of this thesis (c.f. chap. 5). Its main goal is to identify the currently unknown 0_2^+ state in ^{74}Zn as well as to determine its cross section after 2n transfer. This allows to gain a deeper insight into the structure of 0_2^+ states in the zinc chain, which plays a crucial role to understand the complex proton-neutron interaction in the region of ^{68}Ni.

Summary

The $N = 40$ harmonic subshell closure around ^{68}Ni has been extensively discussed in the last decades from the experimental and theoretical point of view. This indicates the complexity of this region on the nuclear landscape, but makes it also a good testing ground for theoretical models. To analyze the robustness of the $N = 40$ shell-gap not only ^{68}Ni directly, but also the properties of its neighboring isotopes play a crucial role. Removing two protons from nickel, iron is reached which shows much stronger deformation than expected in the vicinity of a good shell closure. Furthermore, despite many investigations, a conclusive picture about the collective structure of the neutron-rich zinc isotopes, which have only two protons more than the nickel isotopes, is not reached yet: Lifetime measurements predict a small collectivity which is consistent with a $N = 40$ shell-closure, while Coulomb excitation experiments show an increased collectivity of the 4_1^+ state. Furthermore, the 0_2^+ states in the zinc chain are of particular interest, as they show the strongest deviation from simple collective models, which is not fully understood. In order to shed more light on the microscopic structure of these nuclei, two complementary experiments with a ^{72}Zn ISOLDE beam have been performed in the course of this thesis: First, the two-neutron transfer experiment t(^{72}Zn, p)^{74}Zn which especially addresses the unusual behavior of the 0_2^+ states in the zinc chain. It allows to determine the content of the wave function of the populated states. In the past, 2n transfer reaction experiments proved to be an appropriate tool to study 0^+ states, as these states can be populated directly with zero angular momentum transfer of the two neutrons [27, 53, 55]. Second, the multiple Coulomb excitation of ^{72}Zn is studied. Hence, the electromagnetic transition strengths of all low lying ^{72}Zn states were extracted for the first time. This offers additional information on the inconsistencies of the collectivity of the 4_1^+ state and the nature of the 0_2^+ state. Furthermore, measuring differential Coulomb excitation cross sections allows to determine the shapes of the ^{72}Zn 2_1^+, 4_1^+ and the 2_2^+ state which complement the discussion about the shape coexistence in this region. Apart from that, a complete set of relative transition probabilities ($B(E2)$ values) of low lying states allows a more sensitive evaluation of theoretical models than using only the $B(E2; 2_1^+ \rightarrow 0_1^+)$ strength.

2

Reaction Theory

In this thesis, the neutron-rich zinc isotopes are studied with two complementary experimental techniques: One- and two-neutron transfer reactions and multiple Coulomb excitation (Coulex). In the following, these two methods are introduced. Sec. 2.1 deals with the treatment of elastic cross sections in the framework of the Optical Model. Based on this, sec. 2.2 provides an insight into the calculation of transfer cross sections and their comparison to experimental data. Sec. 2.3 gives an overview of the most important features of Coulomb excitation processes and illustrates their power to extract nuclear structure information from measured Coulex cross sections.

2.1 The Optical Model of Elastic Scattering

The Optical Model (OM) was introduced to determine elastic scattering cross sections, especially of light projectiles such as protons, deuterons, ^{3}He and α-particles on a target nucleus [56]. As the interaction between these light projectiles and the target is too complicated to directly calculate the cross section, it is replaced by a phenomenological effective complex potential $U(\vec{R})$, with $\vec{R}$ being the connection vector between the projectile and the target. The real part of the potential $U(\vec{R})$ describes the elastic scattering, whereas its imaginary component takes inelastic and reaction channels into account[1]. Nevertheless, the imaginary part of $U(\vec{R})$ does not specify the nature of these non-elastic channels. Instead, it only considers the flux removed from the elastic channel. [56]

The Hamiltonian in the OM (after separating the internal degrees of freedom of the target and the projectile) is written as

$$[\hat{T} + U(\vec{R}) - E]\chi(\vec{R}) = 0 \quad \text{with} \quad E = \frac{\hbar^2 K^2}{2\mu}, \tag{2.1}$$

with E and $\hat{T}$ being the kinetic energy and its operator. The Schrödinger equation can be solved if the effective potential U only depends on the distance $R = |\vec{R}|$ between the projectile and the target: $U(\vec{R}) = U(R)$. Hence, a partial wave decomposition is performed which factorizes the so called distorted wave function $\chi(\vec{R})$ in a radial and an angular part.

Traditionally, a phenomenological parametrization of the potential $U(R)$ is used (for details c.f. [57]). It contains a set of parameters which depends on the incident projectile energy as well as on the masses and charges of the projectile and target nuclei. These parameters are extracted from a wide range of elastic scattering experiments. Usually, $U(R)$ is parameterized in the following way:

$$U(R) = U_C(R) + U_R(R) + U_I(R) + U_D(R) + U_S(R) \quad \text{with}$$

$$U_C(R) = \begin{cases} \frac{Z_p Z_t e^2}{2R_C}\left(3 - \frac{R^2}{R_C^2}\right) & \text{if } R \leqslant R_C \\ \frac{Z_p Z_t e^2}{R} & \text{if } R > R_C \end{cases}$$

$$U_R(R) = -Vf(R, R_V, a_V) \quad \text{with} \quad f(R, R_V, a_V) = [1 + \exp{(R - R_V)}/a_V]^{-1}$$

$$U_I(R) = -iWf(R, R_W, a_W)$$

---

[1]The introduction of a complex potential is similar to the approach in optics where a complex index of refraction is used to account for scattering and absorption of light in a medium. Thus, the name Optical Model originates.
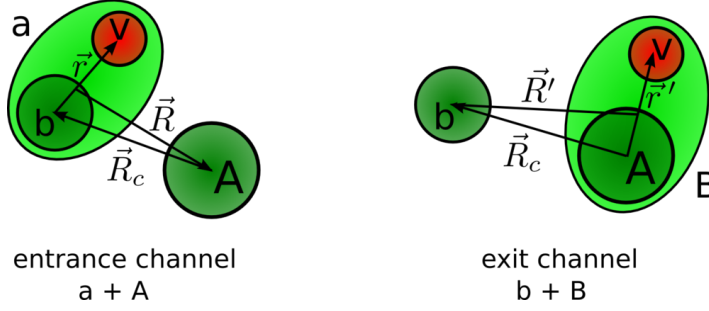
Fig. 2.1: Schematic representation of the transfer reaction $A(a, b)B$. The cluster v is stripped from the nucleus a and picked up by the nucleus A forming the nucleus B.

$$U_D(R) = 4iW_D \frac{d}{dR} f(R, R_W, a_W)$$

$$U_S(R) = \vec{s} \cdot \vec{l} \, V_S \frac{1}{R} \frac{d}{dR} f(R, R_S, a_S). \tag{2.2}$$

U_C represents a real Coulomb potential of a homogeneously charged sphere with radius R_C. $U_R(R)$ describes the real effective potential of the nuclear force with a typical Woods-Saxon form factor featuring a depth V, a radius R_V and a parameter a_V for the diffuseness. $U_I(R)$ is a complex volume potential and $U_D(R)$ a complex surface potential. $U_S(R)$ represents a spin-orbit interaction term.

2.2 Transfer Reactions

After presenting the treatment of the elastic scattering in the framework of the OM in sec. 2.1, more complex reactions such as transfer reactions are considered in this section. A more detailed discussion can be found in [58].

2.2.1 Ingredients for Transfer Cross Sections

Fig. 2.1 depicts a typical transfer reaction $A(a, b)B$. In the entrance channel, the projectile nucleus a forms a bound system of the core b and the valence cluster (or valence nucleon) v: $a = b + v$. In the exit channel, the cluster v is transferred to the target nucleus A forming the nucleus B: $B = A + v$. Thus, the outgoing projectile-like nucleus corresponds only to the core b.

Using the coordinates from fig. 2.1 the Hamilton operator of this system reads

$$H = \hat{T}_{\vec{r}} + \hat{T}_{\vec{R}} + V_{vb} + V_{bA} + V_{vA}, \tag{2.3}$$

where the sum $\hat{T}_{\vec{r}} + \hat{T}_{\vec{R}}$ represents the total kinetic energy and $V_{vb} + V_{bA} + V_{vA}$ considers the inter-nucleus interaction[2] of all three nuclei b, A and v. Considering that $a = b + v$ is a bound nucleus in the entrance channel and $B = v + A$ in the exit channel of the transfer reaction, the Hamiltonian can be rewritten as

$$H = \hat{T}_{\vec{r}} + \hat{T}_{\vec{R}} + V_a(\vec{r}) + U_{cc'}(\vec{R}_c) + V_B(\vec{r'}), \tag{2.4}$$

with $U_{cc'}(\vec{R}_c)$ being the core-core interaction of the cores b and A. The potentials V_a and V_B are the binding potentials of the initial and the final bound states, respectively. The Schrödinger equations of the bound states in the incoming and outgoing channel of the transfer reactions are:

$$[H_a - \epsilon_a]\phi_a(\vec{r}) \quad \text{with} \quad H_a = T_{\vec{r}} + V_a(\vec{r}) \tag{2.5}$$

$$[H_B - \epsilon_B]\phi_B(\vec{r'}) \quad \text{with} \quad H_B = T_{\vec{r'}} + V_B(\vec{r'}). \tag{2.6}$$

---

[2]The effects of three-body interactions are absorbed in the effective parametrization of the OM.

The eigenvalues ϵ_a and ϵ_B represent the binding energies of the valence cluster to the core. E.g. in the case that the bound system a is a deuteron, its binding energy is $\epsilon_a = -2.225\,\text{MeV}$. Using (2.5), the Hamiltonian H of eq. (2.4) can be written as [58]

$$
\begin{aligned}
H &= \hat{T}_{\vec{R}} + H_a + U_i(R) - U_i(R) + U_{cc'}(\vec{R}_c) + V_B(\vec{r'}) \\
&= \hat{T}_{\vec{R}} + H_a + U_i(R) + \mathcal{V}_i(\vec{R}, \vec{r'}) \quad \text{with} \quad \mathcal{V}_i(\vec{R}, \vec{r'}) = V_B(\vec{r'}) + U_{cc'}(\vec{R}_c) - U_i(R).
\end{aligned}
\tag{2.7}
$$

Here, the initial optical potential $U_i(R)$ between the projectile a and the target A is introduced (c.f. sec. 2.1). Thus, the Hamiltonian H consists of three parts which are interpreted in the following: The term $\hat{T}_{\vec{R}} + U_i(R)$ describes the motion of the projectile a and the target A in a common optical potential $U_i(R)$. The summand $H_a(\vec{r})$ considers the internal structure of the projectile $a = b + v$, i.e. the binding of the cluster v to the core b. Finally, the interaction term $\mathcal{V}_i(\vec{R}, \vec{r})$ causes the transfer reaction, i.e. it is responsible for the transfer of the cluster v from the core b to the core A.

However, the Schrödinger equation with the Hamilton operator H from eq. (2.7) cannot be solved analytically. Therefore, the Distorted Wave Born Approximation (DWBA) is used. In first order DWBA, the transition matrix (T-matrix) causing the transfer reaction reads [58]

$$
\mathcal{T}^{DWBA} \approx \langle \phi_B(\vec{r'}) \cdot \chi_f(\vec{R'}) | \mathcal{V}_i | \phi_a(\vec{r}) \cdot \chi_i(\vec{R}) \rangle,
\tag{2.8}
$$

with $\chi_i(\vec{R})$ and $\chi_f(\vec{R'})$ being the distorted wave functions of the optical potentials $U_i(\vec{R})$ and $U_f(\vec{R'})$ (c.f. eq. (2.1)) in the initial and final state of the transfer reaction, respectively. Finally, the cross section of the transfer reaction is given by [58]

$$
\left(\frac{d\sigma}{d\Omega}\right)^{DWBA}_{\text{transfer}} = \frac{\mu_\alpha \mu_\beta}{(2\pi\hbar^2)^2} \frac{K_\beta}{K_\alpha} |\mathcal{T}^{DWBA}|^2,
\tag{2.9}
$$

with $\alpha = a + A$ being the mass partition in the initial channel and $\beta = b + B$ the mass partition in the final channel. $\mu_{\alpha,\beta}$ and $K_{\alpha,\beta}$ are their reduced masses and their wave vectors, respectively.

In summary, the following physical inputs are necessary to calculate transfer cross sections in first order DWBA (c.f. eq. (2.7) and eq. (2.8)):

- The optical potentials U_i and U_f for the incoming and outgoing distorted waves χ_i and χ_f (c.f. sec. 2.1).

- The so-called overlap functions ϕ_a and ϕ_B describing the internal bound states of the cluster nucleus v to the core nucleus in the initial and in the final channel. They are calculated from the binding potentials V_a and V_B. It is convenient to parameterize V_a and V_B with a Woods-Saxon potential. Its depth is adapted to reproduce the binding energy of the cluster v to the core.

- The core-core interaction potential $U_{cc'}$.

Spectroscopic Factors

The overlap functions ϕ_a and ϕ_B play a crucial role in the calculation of transfer cross sections. E.g. ϕ_B describes how the valence cluster v (spin s, angular momentum l and total spin j) is bound to the core A with total spin I_A. Thus, the cluster v and the core A form the composite B with the total spin I_B. In general, there is more than one possibility to bind the cluster v to the core. Therefore, the spectroscopic factor $S_{lsj}^{jI_AI_B}$ is introduced which corresponds to the probability that a core A is left in state I_A if the valence cluster v with quantum numbers s, l and j is removed from the composite B with total spin I_B. It holds the relation [58]

$$
\sum_{lsjI_A} S_{lsj}^{jI_AI_B} = 1.
\tag{2.10}
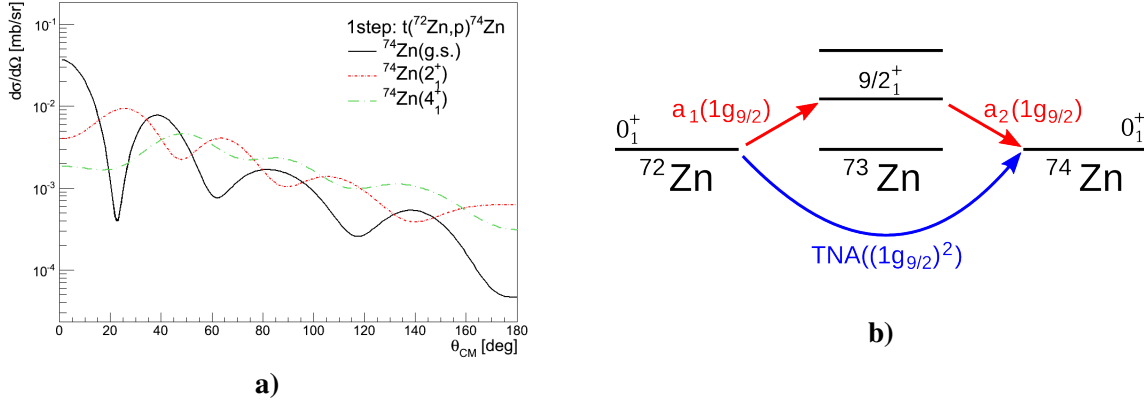$$

Fig. 2.2: a) A calculation of the two-neutron transfer reaction cross section t(^{72}Zn, p)^{74}Zn in inverse kinematics (E_{beam} = 2.7 MeV/u.). For all final states of ^{74}Zn it is assumed that the two neutrons are both transferred simultaneously in the $1g_{9/2}$ orbit. The used two neutron amplitudes (*TNA*) are all set to 1. The strong dependence of the shape of the cross section on the momentum transfer l allows to assign the spins in the final states of ^{74}Zn. **b)** A sketch of sequential and simultaneous transfer from the ^{72}Zn ground state to the ^{74}Zn ground state. As an example, it is assumed that both neutrons occupy the $1g_{9/2}$ orbit in ^{74}Zn. Of course other configurations such as the $(2p_{3/2})^2$, the $(2f_{5/2})^2$ or the $(2p_{1/2})^2$ configuration are also possible which all feature a different intermediate level in ^{73}Zn in the case of the sequential transfer.

However, in literature, even for one-neutron transfer reactions, spectroscopic factors can be larger than one, which is not compatible with the probability interpretation [59]. But, as protons and neutrons are not distinguishable and are generally described by anti-symmetric wave functions, the spectroscopic factor is multiplied by the number of possibilities to select the transferred nucleon from all valence nucleons in the orbit [58]. Furthermore, in case of pick-up reactions, such as (d,p) reactions, an additional spin-factor has to be included in the spectroscopic factor [60].

2.2.2 Comparison of Calculated Transfer Cross Sections to Experiment

As a consequence of sec. 2.2.1, the cross section of the transfer reaction A(a,b)B (c.f. fig. 2.1) consists of two parts:

$$\left(\frac{d\sigma}{d\Omega}\right)_{transfer} = S \cdot \left(\frac{d\sigma}{d\Omega}\right)_{DWBA}. \tag{2.11}$$

First, the term $(d\sigma/d\Omega)_{DWBA}$ comprises the kinematics of the transfer reaction which can be calculated with a DWBA code for different configurations of the transfered cluster v in the final nucleus B. Second, the spectroscopic factor S contains information about the initial and final nuclear wave function. It is related to the probability for a specific cluster configuration in the nucleus B. The goal of transfer experiments is to measure the differential cross section and subsequently to compare it to a DWBA calculation. This comparison allows to extract spectroscopic factors. Especially one-nucleon transfer reactions are an ideal tool to directly study single-particle properties as their cross sections are directly linked to the single-particle configuration of the transfered nucleon[3].
Furthermore, the shape of the differential cross section $(d\sigma/d\Omega)_{DWBA}$ is characteristic for the angular momentum l which is transferred by the cluster v: Zero angular momentum transfer $l = 0$ features a peak in the cross section at $\theta_{CM} = 0$. With increasing angular momentum l the first maximum of the cross section is shifting towards higher scattering angles θ_{CM} in the center-of-mass frame (c.f. fig. 2.2 a)). This strong dependence of the cross section of the angular momentum allows to determine the spin of the populated state in the final nucleus B.

---

[3]A pure single particle state occurs if only one valence nucleon or valence hole is outside an inert core. Thus, this valence particle defines the quantum numbers of the nucleus.

Apart from that, the cross section depends on the Q-value of the reaction. It is strongest for $Q = 0$ as here the momenta in the entrance and in the exit channel match best (Q-value matching) [58]. Hence, the t(^{72}Zn,p)^{74}Zn reaction, which is discussed in this thesis, populates dominantly states close to 5 MeV as $Q = 5.24$ MeV.

2.2.3 Sequential and Simultaneous Transfer of Two Neutrons

The transfer experiment, which is investigated in this work, is the two-neutron transfer reaction from ^{72}Zn to ^{74}Zn: t(^{72}Zn, p)^{74}Zn. In principle, there are two possible ways to transfer the two neutrons: simultaneously in one step or sequentially in two steps via an intermediate state of ^{73}Zn (c.f. fig. 2.2 b)). Therefore, two-neutron transfer reactions are suitable to study pairing correlations. However, the analysis of the measured experimental two-neutron transfer cross sections is challenging as there can be a large number of different dominating sequential and simultaneous paths which can strongly interfere with each other. Even for the theoretical calculation and the interpretation of the two-neutron transfer from the ^{72}Zn ground state to the ^{74}Zn ground state, a lot of spectroscopic information has to be included: In the sequential path all possible intermediate states including their spectroscopic amplitudes[4] have to be taken into account. Even if both neutrons are transfered simultaneously, all possible configurations of the two neutrons in the final nucleus ^{74}Zn have to be considered. The corresponding quantity to the spectroscopic amplitude a of a one-neutron transfer channel, is the two-nucleon spectroscopic amplitudes (TNA) in the simultaneous two-neutron transfer. The TNA is a measure of the probability that the two neutrons occupy a specific configuration in ^{74}Zn.

2.3 Coulomb Excitation

As described in the previous sections, transfer reactions are suited to study the single-particle properties of nuclei. A complementary method to gain nuclear structure information are Coulomb excitation reactions which address the collective properties of nuclei. A brief introduction to the basic principles of Coulomb excitation is given in this section.

Coulomb excitation (Coulex) is an inelastic scattering process between two charged nuclei. During the collision there is a probability that at least one nucleus is excited due to its interaction with the electromagnetic field between both reaction partners. This reaction type only allows for internal excitations of the projectile and / or the target particle. Thus, contrary to transfer reactions, in Coulex reactions the nuclei keep their identity. Typically, vibrational or rotational states of nuclei are excited in Coulex experiments. Since excited levels are populated from below, there is no difference between the population of yrast and non-yrast states: The population pattern is governed by transition probabilities and level energies only.

Safe Coulomb Excitation

If the two particles are always well separated during the reaction, only the electromagnetic interaction is important and the effect of the strong force can be neglected. This case is called "safe Coulomb excitation". It is a preferred experimental tool to study nuclear structure as the electromagnetic interaction, in contrast to the nuclear interaction, is well known. Thus, a model independent analysis is possible. The influence of the strong interaction can be ignored ($< 0.1\,\%$) if the distance of closest approach d_{min} of the two nuclei fulfills the condition [61]

$$d_{min} > [1.25(A_p^{1/3} + A_T^{1/3}) + 5]\,\text{fm}, \qquad (2.12)$$

with $1.25(A_p^{1/3} + A_T^{1/3})$ being the sum of the projectile and the target nuclear radii and the 5 fm represents an additional safety distance between the surfaces of the two nuclei. This condition can be translated

---

[4]The absolute square of the spectroscopic amplitude is the spectroscopic factor.
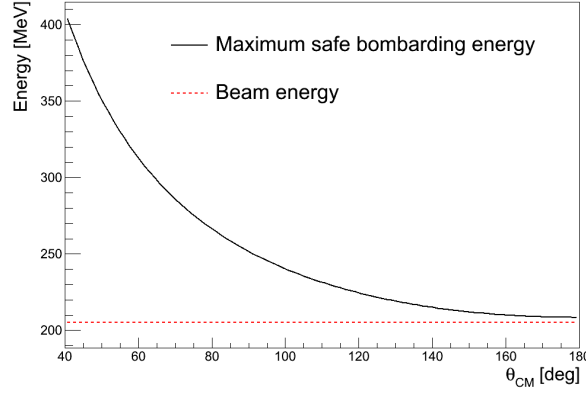
Fig. 2.3: Save Coulex criterion for the bombarding energy for the case of a ^{72}Zn projectile and a ^{109}Ag target. Additionally, with the red dashed line the beam energy $E_{beam} = 2.85$ MeV/u $= 205$ MeV used in the MINIBALL experiment at REX-ISOLDE 2012 is shown. The criterion is fulfilled for all scattering angles up to 180°.

to a more practical constraint for the beam energy E_{beam}:

$$E_{beam} < 0.72 \cdot \frac{A_p + A_T}{A_T} \cdot \frac{Z_P Z_T}{1.25(A_p^{1/3} + A_T^{1/3}) + 5} \cdot \left[1 + \frac{1}{\sin(\theta_{CM}/2)} \right] \text{MeV}. \qquad (2.13)$$

To fulfill this criterion for safe Coulomb excitation, it is, depending on the projectile and the target, necessary to measure with low beam energies or only at forward angles. In the case of the Coulomb excitation of a 205 MeV ^{72}Zn beam impinging on a ^{109}Ag target, which is studied in this thesis, the Coulex reaction is safe for the whole range of scattering angles θ (c.f. fig. 2.3).

2.3.1   One Step Coulomb Excitation

In a naive approach, one may calculate Coulomb excitation cross section fully quantum-mechanically using the partial wave decomposition, similar to the calculation of elastic scattering (c.f. sec. 2.1) or transfer (c.f. sec. 2.2) cross sections. However, due to the long range of the Coulomb force, a large number of partial waves l is necessary for a calculation with an accurate precision. Furthermore, the relevant states are strongly coupled. As a result, the evaluation of the cross section is very time-consuming and thus impracticable [61, 62]. Therefore, a semi-classical description of the Coulomb excitation is commonly used. It was first introduced by K. Alder and A. Winther in 1966 [63]. In the semi-classical model of Coulex reactions, the particle trajectories are treated classically, whereas the electromagnetic transitions in the nuclei are treated quantum-mechanically[5]. Hence, the Coulex cross section is given by the product of the elastic Rutherford cross section and the excitation probability $P_{i \to f}$ for exciting an initial state i to a final state f [60]:

$$\frac{d\sigma}{d\Omega} = \left(\frac{d\sigma}{d\Omega} \right)_{Rutherford} \cdot P_{i \to f}. \qquad (2.14)$$

The excitation probability $P_{i \to f}$ is calculated using the time-dependent perturbation theory of quantum mechanics. In first order perturbation theory $P_{i \to f}$ is expressed with the excitation amplitude a_{fi}:

$$P_{i \to f} = |a_{fi}(t)|^2 \quad \text{with} \quad a_{fi}(t) \approx -\frac{i}{\hbar} \int dt \, \langle f|V(t)|i \rangle \, e^{-\frac{i}{\hbar}(E_i - E_f)t}, \qquad (2.15)$$

---

[5]It is expected that the semi-classical approximation deviates from the full-quantum-mechanical description by less than a factor of $1/v$, where v is the Sommerfeld parameter [63, 64]. This approximation is the largest source of systematic errors in Coulex analysis [65, 66] (c.f. chap. 6).

with $V(t)$ being the time-dependent electromagnetic field of the projectile which is expanded into multipoles [60]. If only the dominating electric multipole moments $\mathcal{M}(E\lambda)$ of the order λ are used, the transition probability for the target excitation can be written as[6] [60]

$$P_{J_i \to J_f} = \left(\frac{4\pi Z_T e}{\hbar}\right)^2 \sum_{\lambda > 0} \frac{B(E\lambda; J_i \to J_f)}{(2\lambda + 1)^3} \sum_\mu |I_{\lambda\mu}(\omega_{fi})|^2 \quad \text{with} \quad \hbar\omega_{fi} = E_f - E_i. \tag{2.16}$$

The first sum runs over all electric multipoles of order λ and the second sum runs over all magnetic substates $\mu = -\lambda, \ldots, \lambda$. The quantity $I_{\lambda\mu}(\omega_{fi})$ is given by

$$I_{\lambda\mu}(\omega_{fi}) = \int_{-\infty}^{\infty} dt \, \frac{1}{r^{\lambda+1}(t)} \, Y_{\lambda\mu}(\vec{r}(t)) \, e^{i\omega_{fi}t}, \tag{2.17}$$

with $Y_{\lambda\mu}$ being the spherical harmonics. Generally, this integral is just a time-integral over the Rutherford trajectory $\vec{r}(t)$ and is completely independent of the nuclear structure. Instead, all nuclear structure information is contained in the $B(E\lambda; J_i \to J_f)$ value. This quantity is also called the "reduced transition probability".

The Reduced Transition Probability

The reduced transition probability $B(\pi\lambda; J_i \to J_f)$ is one of the main quantities which is determined in Coulomb excitation experiments. It depends on the initial and final wave function, i.e. on the nuclear structure of the excited nucleus. These wave functions are linked with the well-known electric or magnetic multipole operators $\mathcal{M}(E\lambda)$ and $\mathcal{M}(M\lambda)$, respectively:

$$B(\pi\lambda; J_i \to J_f) = \frac{1}{2J_i + 1} \sum_{M_i M_f} |\langle J_i, M_i | \mathcal{M}(\pi\lambda, \mu) | J_f, M_f \rangle|^2$$

$$= \frac{1}{2J_i + 1} |\langle J_i \| \mathcal{M}(\pi\lambda) \| J_f \rangle|^2, \tag{2.18}$$

with $\pi \in \{E, M\}$ indicating the electric and magnetic multipoles.

Due to its wave function dependence, the $B(\pi\lambda)$ value also contains information about the nature of the transition. To be more precise, it is a measure how many nucleons are involved in the excitation process. For a descriptive quantitative investigation a new unit, the "Weisskopf unit" (W.u.), was introduced which is as common as the standard SI-units $e^2\text{fm}^{2\lambda}$ for $B(E\lambda)$ values and $\mu_N\text{fm}^{2\lambda-2}$ for $B(M\lambda)$ values, respectively[7]. One W.u. is defined as [67]

$$1\,\text{W.u.} \stackrel{\triangle}{=} \frac{1}{4\pi}\left(\frac{3}{\lambda+3}\right)^2 (1.2A^{1/3})^{2\lambda} \; e^2\text{fm}^{2\lambda} \quad \text{for} \quad B(E\lambda) \text{ values}$$

$$1\,\text{W.u.} \stackrel{\triangle}{=} \frac{10}{\pi}\left(\frac{3}{\lambda+3}\right)^2 (1.2A^{1/3})^{2\lambda-2} \; \mu_N^2\text{fm}^{2\lambda-2} \quad \text{for} \quad B(M\lambda) \text{ values.} \tag{2.19}$$

If the reduced transition probability is around one W.u. than the transition has single-particle character with only one nucleon involved. Contrary, if $B(\pi\lambda) \sim 10 - 50\,\text{W.u.}$ a collective state with many participating nucleons has been excited.

2.3.2   Multiple Coulomb Excitation and the Quadrupole Moment

Up to now, the Coulomb excitation cross section was calculated in first order perturbation theory, i.e. only direct excitations from an initial state i to a final state f have been considered (c.f. fig. 2.4).
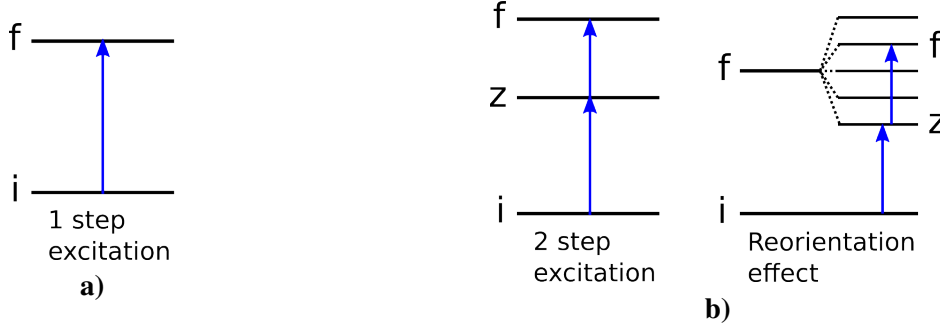
Fig. 2.4: a) The one step Coulomb excitation in from an initial state i to a final state f. This process can be described in first order perturbation theory. **b)** Two scenarios of multiple Coulomb excitations via an intermediate state z are sketched. For their theoretical calculation, also the second order terms of the perturbation theory have to be included. The image on the left shows a two step excitation, e.g. $0_1^+ \rightarrow 2_1^+ \rightarrow 4_1^+$. On the right, the reorientation effect is displayed which corresponds to transitions between magnetic substates of the same state of the nucleus.

However, in many Coulex experiments the influence of higher orders cannot be neglected. In the second order, the final state f is not excited directly, but via an intermediate state z (c.f. fig. 2.4). In this case, the excitation amplitude $a_{fi}^{(2)}$ is written as

$$a_{fi}^{(2)} = a_{fi}^{(1)} + \sum_z a_{fzi} \quad \text{with}$$

$$a_{fzi} = \frac{1}{(\hbar)^2} \int_{-\infty}^{\infty} dt \, \langle f|V(t)|z\rangle \, e^{-\frac{i}{\hbar}(E_z - E_f)t} \cdot \int_{-\infty}^{t} dt' \, \langle z|V(t)|i\rangle \, e^{-\frac{i}{\hbar}(E_i - E_z)t}. \tag{2.20}$$

The square of the absolute value of the total excitation amplitude $a_{fi}^{(2)}$ gives the excitation probability. Hence, is does not only contain quadratic terms but also interference terms. Therefore, the relative sign of the single excitation amplitudes, i.e. the relative sign of the matrix elements are important in Coulomb excitation processes involving more than one excited state. In the following, the two main second order processes are introduced, i.e. the multiple Coulomb excitation in two steps and the reorientation effect. Both processes are shown schematically in fig. 2.4.

Two Step Excitations to Higher Lying States
For near-vibrational even-even nuclei considered in this work, one of the most dominant multiple Coulomb excitation process is the two step excitation from the ground state to the first excited 4_1^+ state via the intermediate 2_1^+ state. Both excitation steps have $E2$ character, whereas a direct excitation from the ground state to the 4_1^+ state via an $E4$ transition is negligible in most cases. The small influence of the direct $E4$ excitation is given by

$$\frac{\sigma(E2, E2)}{\sigma(E4)} = 2.1 \frac{A_T Z_T^2}{E_{beam} \, [\text{MeV}]} \frac{B(E2; 0 \rightarrow 2)\,[e^2\text{fm}^4] \cdot B(E2; 2 \rightarrow 4)\,[e^2\text{fm}^4]}{e^2 B(E4; 0 \rightarrow 4)\,[e^2\text{fm}^8]}, \tag{2.21}$$

with A_T and Z_T being the mass number and the proton number of the target which excites the projectile of interest [64]. As a result, for the Coulomb excitation experiment which is discussed in this thesis, i.e. a ^{72}Zn beam ($E_{beam} = 2.85$ MeV/u) impinging on a ^{109}Ag target, $E4$ transitions in ^{72}Zn are suppressed by a factor of $10^3 \approx 2.1 \frac{109 \cdot 47^2}{205.2}$.

---

[6]An analogue expression can be given for magnetic multipoles. However, in the low energy regime which is discussed in this thesis (^{72}Zn beam with $E_{beam} = 2.85$MeV/u) the magnetic excitations are hindered by a factor of $(v/c)^2 \approx 0.07^2 = 0.005$, with v being the relative velocity of the projectile and the target.

[7]The quantity $\mu_N = \frac{e\hbar}{2m_p} = 0.105$ efm is the nuclear magneton.
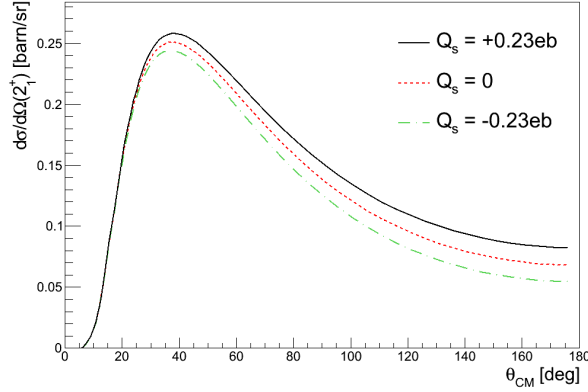
Fig. 2.5: The influence of the spectroscopic quadrupole moment $Q_s(2_1^+)$ on the excitation cross section of the 2_1^+ state of ^{72}Zn. The calculations of the 2_1^+ cross section are done with the CLX code [69, 70] assuming the same $B(E2; 2_1^+ \rightarrow 0_1^+) = 370\,e^2$fm^4 value for all stated quadrupole moments.

The Reorientation Effect and the Spectroscopic Quadrupole Moment

Another important aspect of second order perturbation theory is the reorientation effect [68], which occurs if a transition between two magnetic substates of the final state f happens. It deals with the interaction of the spectroscopic moment (i.e. the quadrupole moment in the laboratory frame) with the strong time-dependent electric field gradient during the electromagnetic collision of the projectile with the target. As the impact of the field gradient is strongest at small distances, the quadrupole moment has the highest influence at large backscattering angles. Whether the Coulex cross section is increased or decreased by the reorientation effects depends on the sign of the quadrupole moment of the state. For positive spectroscopic quadrupole moments the energy of the populated magnetic substates is increased whereas negative spectroscopic quadrupole moments lower the energy of these substates. As the Coulex excitation probability is enhanced for low lying final state energies, positive spectroscopic quadrupole moments increase the cross section, whereas negative spectroscopic quadrupole moments lead to a reduction of the cross section. For studied Coulomb excitation of ^{72}Zn, this effect is visualized in fig. 2.5.

Since the spectroscopic quadrupole moment ($\lambda = 2$) deals with the magnetic substates of the same state with spin J, it can be described with the diagonal matrix element $\langle J \| \mathcal{M}(E2) \| J \rangle$ of the state J

$$Q_s(J) = \sqrt{\frac{16\pi}{5}} \frac{\langle JJ20|JJ \rangle}{\sqrt{2J+1}} \langle J \| \mathcal{M}(E2) \| J \rangle, \qquad (2.22)$$

with the Clebsch–Gordan coefficient $\langle JJ20|JJ \rangle = \langle j_1 m_1 j_2 m_2|jm \rangle$ [71]. Thus, the spectroscopic quadrupole moment is, like the $B(E2)$ values, connected to the nuclear wave functions, which makes it a powerful quantity to study nuclear structure. In addition, it also contains information about the shape of the nucleus in the state J: A non-vanishing quadrupole moment corresponds to a deviation of the spherical charge distribution which is related to a deformed shape of the nucleus. It can be shown that a negative spectroscopic quadrupole moment describes a prolate shape, whereas a positive spectroscopic quadrupole moment is linked to an oblate shape.

2.3.3 Deexcitation via γ-ray Decay

The time scale for the Coulomb excitation from the ground state to higher lying states is about 10^{-21} s, whereas the time scale for the deexcitation is typically much longer with about $10^{-13} - 10^{-12}$s. Thus, the excitation and the deexcitation can be treated as two independent processes [65]. The radiative deexcitation of excited states to lower lying states is induced by the same multipole operators $\mathcal{M}(E\lambda)$ and $\mathcal{M}(M\lambda)$ as the Coulomb excitation. Therefore, the reduced transition probability $B(\pi\lambda; J_f \rightarrow J_i)$

for the decay is calculated directly from the $B(\pi\lambda; J_i \to J_f)$ value of the excitation

$$B(\pi\lambda; J_f \to J_i) = \frac{2J_i + 1}{2J_f + 1} B(\pi\lambda; J_i \to J_f). \tag{2.23}$$

All electromagnetic transitions between nuclear states have to fulfill angular momentum and parity conservation. The following selection rules apply [60]:

$$|J_i - J_f| \leqslant \lambda \leqslant J_i + J_f, \quad \text{but} \quad 0^+ \nrightarrow 0^+$$

$$P_i \cdot P_f = (-1)^\lambda \quad \text{for} \quad E\lambda \text{ transitions} \quad \text{and} \quad P_i \cdot P_f = (-1)^{\lambda+1} \quad \text{for} \quad M\lambda \text{ transitions} \tag{2.24}$$

with P_i and P_f being the parity of the initial and final nuclear state.

Moreover, the reduced transition probability $B(\pi\lambda; J_f \to J_i)$ for the radiative decay with a multipolarity $\pi\lambda$ from an initial state i to a final state f is directly connected to the decay probability[8] $P_{i \to f}(\pi\lambda)$ and the partial lifetime $\tau_{i \to f}(\pi\lambda)$ of the state i [60]

$$P_{i \to f}(\pi\lambda) = \tau_{i \to f}^{-1}(\pi\lambda) = \frac{8\pi}{\hbar} \frac{\lambda + 1}{\lambda[(2\lambda + 1)!!]^2} \left(\frac{E_f - E_i}{\hbar c}\right)^{2\lambda+1} B(\pi\lambda; J_i \to J_f). \tag{2.25}$$

From this equation it can be concluded that low multipole orders are preferred in the deexcitation process as higher multipoles are suppressed by a factor of at least $\left(\frac{E_f - E_i}{\hbar c/\text{fm}}\right)^{2\lambda+1} \approx \left(\frac{\sim 1\,\text{MeV}}{197\,\text{MeV}}\right)^{2\lambda+1}$. However, in contrast to the low energy electromagnetic excitation, magnetic multipoles can have a comparable influence to electric multipoles. This is e.g. expressed in the multipole mixing ratio $\delta(E2/M1)$ of a $E2$ and a $M1$ transition [72]

$$\delta(E2/M1) = 0.835 \cdot E_\gamma \frac{\langle J_f \| \mathcal{M}(E2) \| J_i \rangle}{\langle J_f \| \mathcal{M}(M1) \| J_i \rangle}, \tag{2.26}$$

with E_γ being the γ-ray energy of the $J_i \to J_f$ transition. The matrix elements $\langle J_f \| \mathcal{M}(E2) \| J_i \rangle$ and $\langle J_f \| \mathcal{M}(M1) \| J_i \rangle$ are given in the units eb and μ_N, respectively. In most cases $\delta(E2/M1)$ including its phase is determined with angular distribution measurements. Hence, also the sign between the two matrix elements can be observed. Moreover, following eq. (2.25) and eq. (2.26) yields

$$\delta^2(E2/M1) = \frac{P_{i \to f}(E2)}{P_{i \to f}(M1)} = \frac{\tau_{i \to f}^{-1}(E2)}{\tau_{i \to f}^{-1}(M1)} = 1.43 \cdot 10^{-6} A^{4/3} \cdot (E_\gamma(E2)[\text{MeV}])^2 \cdot \frac{B(E2)[\text{W.u.}]}{B(M1)[\text{W.u.}]}. \tag{2.27}$$

Another important quantity in γ-ray spectroscopy is the branching ratio BR of a decay which features more than one decay channel. Assuming that two decay channels 1 and 2 are involved, it is defined by

$$BR = \frac{\sum_{\pi\lambda} P_2(\pi\lambda)}{\sum_{\pi\lambda} P_1(\pi\lambda)}, \tag{2.28}$$

with $P_i(\pi\lambda)$ being the probability that channel i decays by emitting a γ-ray with multipolarity $\pi\lambda$. The most important BR, which is discussed in this thesis, is the branching ratio of the 2_2^+ state in ^{72}Zn. The 2_2^+ state can decay via $E2$ or $M1$ transition into the 2_1^+ state of ^{72}Zn (channel 1) or directly into the ground state (channel 2). Hence, the branching ratio reads

$$BR = \frac{P_2(E2)}{P_1(E2) + P_1(M1)}. \tag{2.29}$$

Using eq. (2.25) the branching ratio can be related to the reduced transition probabilities

$$BR = \left(\frac{E_{\gamma_2}}{E_{\gamma_1}}\right)^5 \frac{B_2(E2)}{B_1(E2) + \frac{100}{3}\left(\frac{\hbar c}{E_{\gamma_1}}\right)^2 B_1(M1)}. \tag{2.30}$$

Hence, branching ratios can be determined directly by measuring the γ-ray intensities of all decay channels or by measuring all involved $B(\pi\lambda)$ values.

---

[8]Note that the decay probability is actually a decay probability per unit time.

3

Experimental Setups

In this thesis, the neutron-rich Zn isotopes are studied in more detail with a ^{72}Zn beam using two different methods: First, a neutron-transfer experiment was conducted in 2011. In 2012, it was complemented by the study of the multiple Coulomb excitation of ^{72}Zn. Both experiments were performed at the radioactive beam facility ISOLDE, CERN. The production of the radioactive ^{72}Zn beam at ISOLDE is explained in sec. 3.1. The following sections describe the experimental setup of the transfer and the Coulomb excitation experiment: Sec. 3.2 deals with a short description of the European γ-ray spectrometer MINIBALL which detected the emitted γ-rays resulting from the deexcitation of the outgoing nuclei in both experiments. In the center of MINIBALL an array of silicon detectors was positioned around the target to detect the outgoing particles. For the neutron transfer experiment the nearly 4π T-REX silicon array was used which is detailed in sec. 3.3. Subsequently, in sec. 3.4 a new, modified T-REX setup, the C-REX silicon array, is introduced which was designed to study the multiple Coulomb excitation of high intense radioactive beams such as the ^{72}Zn beam.

3.1 Radioactive Beams at ISOLDE

In modern nuclear physics, the exploration of nuclei far off the valley of stability, such as the neutron-rich Zn isotopes, is of great interest. However, the half lives quickly decrease going away from the stable isotopes to very neutron-deficient or neutron-rich isotopes. Therefore, it is not possible to produce targets out of exotic nuclei. To study these rare isotopes, nowadays enormous efforts are made to deliver radioactive beams of exotic nuclei. During the last decades, two techniques for Radioactive Ion Beam (RIB) production have been well established: the Projectile Fragmentation method and the Isotope Separation On Line (ISOL) technique. In this thesis, the used ^{72}Zn beam was produced at the ISOL facility ISOLDE at CERN in Geneva, Switzerland which is explained in more detail in this section.

3.1.1 Production of a ^{72}Zn REX-ISOLDE Beam

The most important components of the ISOLDE facility are sketched in fig. 3.1. More information about ISOLDE can be found in [74].

Production of Neutral Radioactive Isotopes
The ISOL method operates a light beam which is shot on a thick, heavy target inducing target fragmentation, spallation and fission reactions. At ISOLDE a 1.4 GeV proton beam from the PS booster[1] with a mean beam intensity of up to 2μA is impinging in multiples of 1.2 s on an ISOLDE production target[2] (c.f. fig. 3.2 a)). A common target which was also used for producing the ^{72}Zn beam is a solid uranium carbide (UC$_x$) target. The UC$_x$ target consists of a mixture of UO_2 and carbon powder which is pressed into pills (c.f. fig. 3.2 b)). Due to its porous structure and due to the heating of the UC$_x$

---

[1]Proton Synchrotron booster

[2]ISOLDE has a lot of different target materials including solid metals, molten metals, oxides and carbides to reach the highest possible yield for the desired radioactive isotope [74].
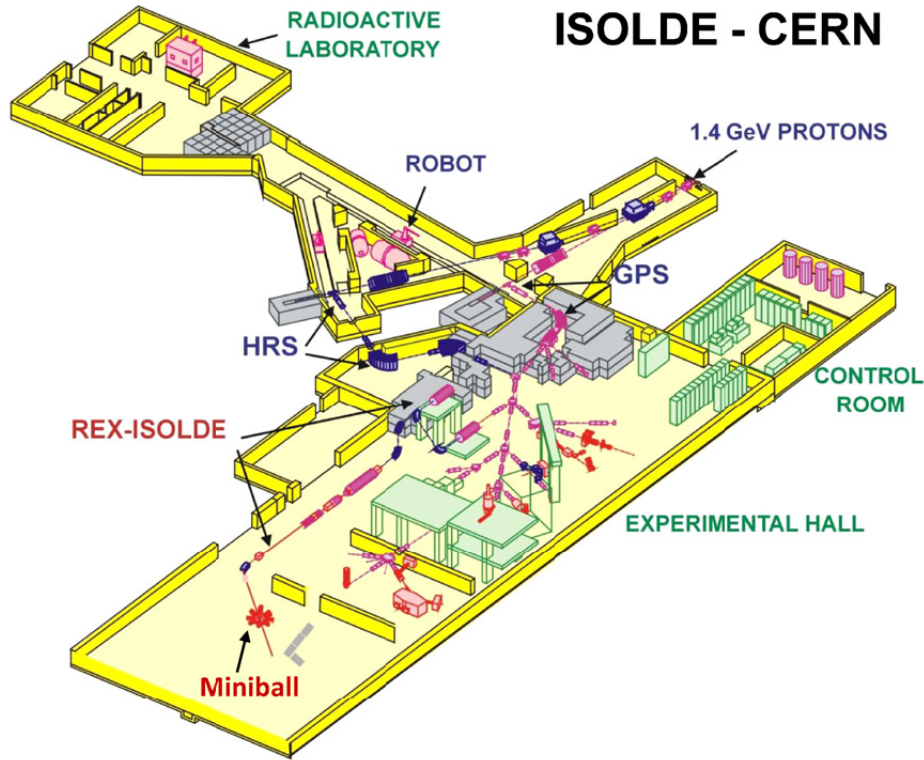
Fig. 3.1: Schematic overview of the ISOLDE facility at CERN in Geneva, Switzerland. A 1.4 GeV proton beam impinges on an ISOL target producing a huge amount of radioactive isotopes. These neutral radioactive elements diffuse and effuse out of the production target into an ion source where the element of interest is ionized. The resulting 1^+ ions are separated by the General Purpose Separator GPS or by the High Resolution Separator HRS to reach a higher beam purity. Subsequently, the ISOLDE beam can be post-accelerated with the REX-ISOLDE linac. Finally, the beam can be delivered to the MINIBALL target position. The picture was taken from [73].
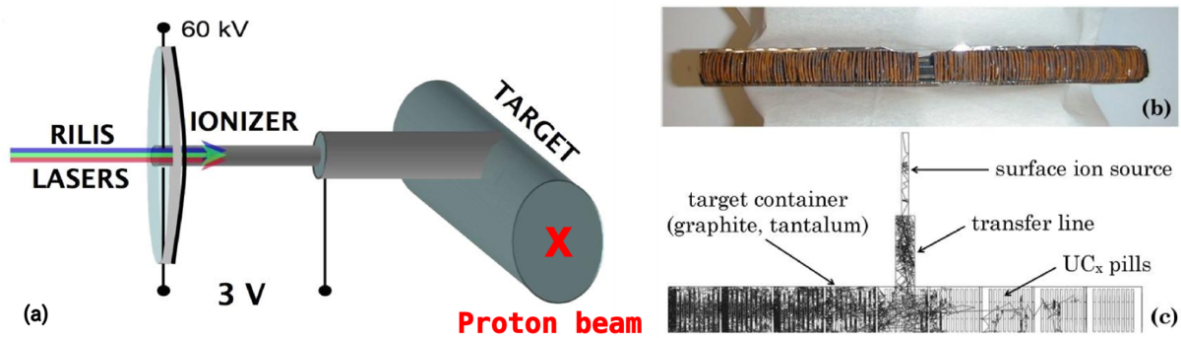
Fig. 3.2: a) A sketch of the ISOLDE production target in which radioactive elements are produced by the interaction of the proton beam with the heavy target material. Finally, the radioactive elements diffuse out of the target into the laser ionization source RILIS which only ionizes the element of interest. Finally, the singly charged beam is accelerated to 60 keV. **b)** A photograph of an UC_x target which consists of pressed pills of UO_2 and carbon powder. **c)** A simulation of the effusion and the diffusion processes in an UC_x target. In this picture the beam enters the target tube from the left. The pictures were adapted from [75] and [76].
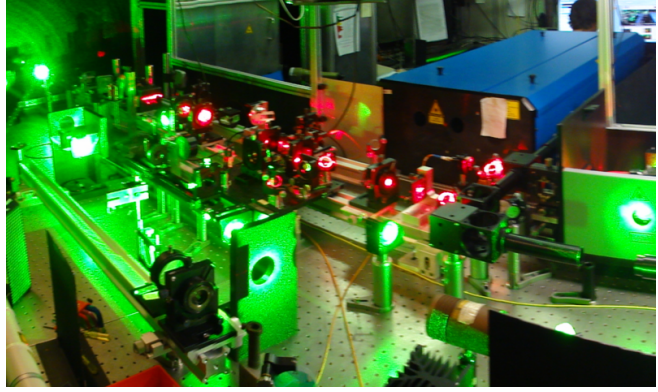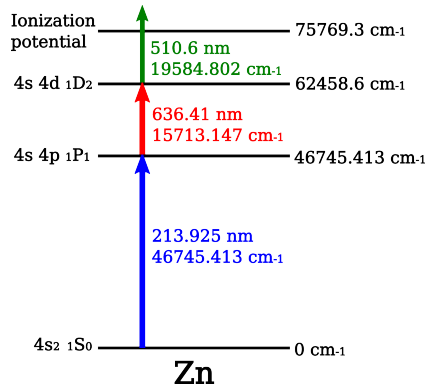
Fig. 3.3: On the left the 3-step ionization scheme for Zn is shown which is exploited by the RILIS ion source. The right picture shows a photograph of the RILIS laser system. The pictures were adapted from [79] and [78].

target to about 2000°C, the produced radioactive isotopes effuse[3] and diffuse out of the target through the transfer line into the ion source (c.f. fig. 3.2 c)) [77].

Ionization of the Neutral Radioactive Isotopes to 1^+ Ions
ISOLDE provides three different types of ion sources to produce 1^+ ions from the neutral radioactive atoms: surface ion sources, plasma ion sources, and laser ion sources. For the production of the ^{72}Zn beam, the Resonant Ionization Laser Ion Source RILIS is used [78]. The RILIS laser system (c.f. fig. 3.3 right) is tuned to the strongest atomic transitions of Zn to obtain 1^+ Zn ions. The used ionization scheme is shown in fig. 3.3 on the left. Due to the unique atomic shell structure of each element, the big advantage of the laser ion source is that only the element of interest is ionized. Thus, pure beams are achieved. However, a contamination of the RIB can result from the thermal surface ionization which occurs when neutral atoms loose an electron at the heated laser ionization cavity. Hence, Zn beams always features a small Ga contamination due to its low ionization potential (c.f. sec. 5.1.3 and sec. 6.1.6). After the ionization, the ions are accelerated to 60 keV.

Mass Separation: GPS or HRS
Finally, the singly charged ions have to pass the General Purpose mass Separator GPS or the High Resolution mass Separator HRS to achieve pure isobaric beams. The GPS features one bending magnet, whereas the HRS has two bending magnets resulting in a mass resolving power of $\Delta M/M > 5000$ [74]. For both, the Coulex and the transfer ^{72}Zn experiment, the HRS was used. Afterwards, the continuous RIB can be guided to the various low energy ISOLDE experiments or it can be post-accelerated with the REX-ISOLDE linac to be finally send to the MINIBALL setup.

Post-Acceleration with REX-ISOLDE
To perform Coulomb excitation and transfer experiments with MINIBALL a higher energetic RIB is mandatory as the reaction cross sections strongly increase with the beam energy. The linear accelerator REX[4] provides such beams with energies up to $E_{beam} = 3$ MeV/u. For an efficient post-acceleration the singly charged ions have to be ionized into a higher charge state. This charge-state breeding is done in two steps which are schematically shown in fig. 3.4: First, the continuous ISOLDE beam is accumulated and cooled in the Penning trap REXTRAP. The cooling is achieved through collisions of the RIB with the buffer gas in the REXTRAP. Subsequently, the RIB is send in bunches to the REX-

---

[3]In the effusion process the radioactive products move through holes of the molecular lattice of the UC$_x$ target. Contrary, diffusion give rise to a complete mixture of two substances.

[4]REX: Radioactive EXperiment
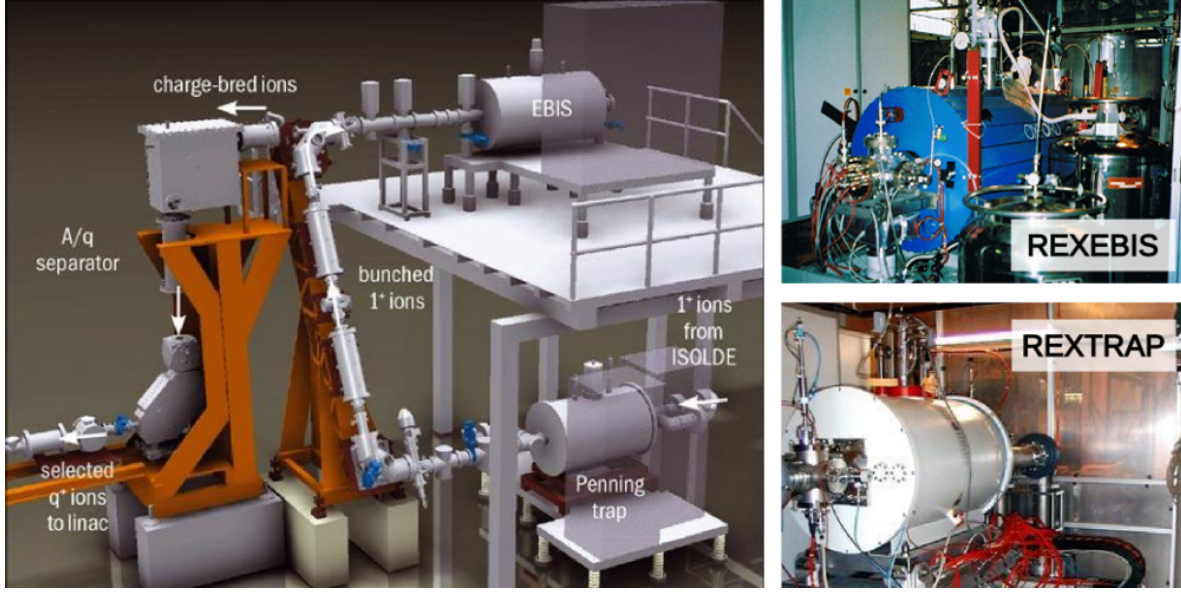
Fig. 3.4: The REX-ISOLDE charge breeder. The singly charged ions are first bunched in the Penning trap REXTRAP. Finally, these bunches are send to the REXEBIS for charge breeding with a highly intense electron beam. The pictures were adapted from [73].
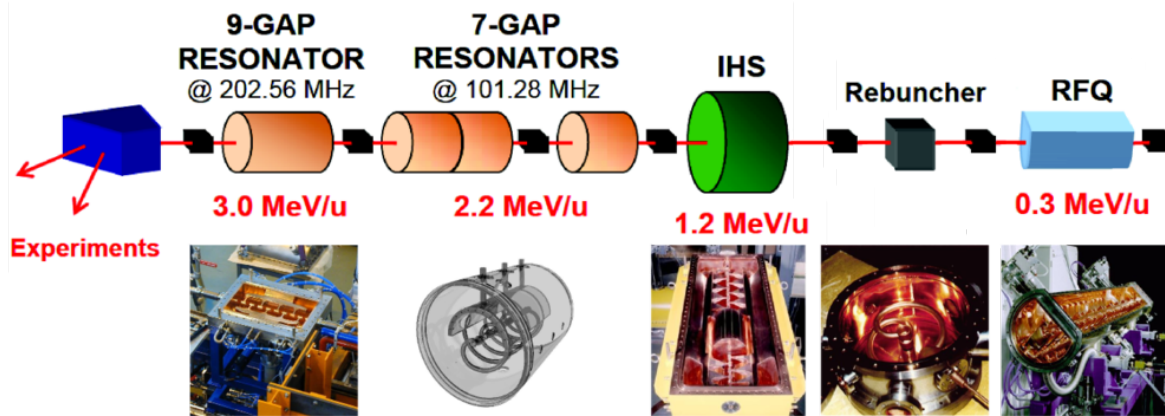
Fig. 3.5: The REX-ISOLDE room-temperature linac which post-accelerates the charge-bred q^+ ions using a RFQ component, a IH structure, a 7-gap and a 9-gap resonator to energies up to $E_{beam} = 3\,\mathrm{MeV/u}$. The beam enters the linac from the right. The pictures were adapted from [74] and [73].

EBIS[5] where a highly intense electron beam ionizes the single charged ions until the desired charge state is reached. The charge state q must fulfill the condition $A/q < 4.5$ which is a prerequisite of the subsequent REX linac. Depending on the isotope, the charge state and the breeding time are optimized to receive the highest yield. For the ^{72}Zn experiments the ^{72}Zn^{20+} charge state ($A/q = 3.6$) is chosen with breeding times of 68 ms (in 2011) and 78 ms (in 2012). After the charge breeding, the RIB has to be purified again from the residual gas of the REXTRAP using a mass separator. It consists of an electrostatic 90° cylinder deflector and a 90° magnetic bender [74]. In the case of the ^{72}Zn experiment, it selects only ions having the right $A/q = 3.6$ ratio.

In a final step, the RIB is post-accelerated with the room-temperature REX linac (c.f. fig. 3.5). The low-energy section of the REX linac starts with a RFQ[6] component which accelerates the ions from

---

[5]EBIS: Electron Beam Ion Source
[6]Radio FreQuency component

Parameter	Transfer experiment 20th-24th Oct. 2011	Coulex experiment 16th-20th Oct. 2012
Beam energy	2.7 MeV/u	2.85 MeV / u
Mean intensity	$(5.4 \pm 0.7) \cdot 10^6$ pps	$(3.5 \pm 0.3) \cdot 10^7$ pps
Instantaneous intensity	$(3.6 \pm 0.4) \cdot 10^8$ pps	$(2.7 \pm 0.3) \cdot 10^9$ pps
Run time with good RIB	72.5 h	66 h
EBIS breeding time	68 ms	78 ms

Tab. 3.1: Summary of the most important beam parameters for the transfer experiment in 2011 and the Coulomb excitation experiment in 2012 with a ^{72}Zn^{20+} REX-ISOLDE beam.

about E_{beam} = 5 keV/u to E_{beam} = 300 keV/u. Afterwards, the RIB passes a rebuncher and IH[7] structure which increase the beam energy to E_{beam} = 1.2 MeV/u. Subsequently, in the high energy section of the linac the beam is further accelerated to E_{beam} = 2.2 MeV/u with three 7-gap resonators. Finally, in 2004 a 9-gap resonator was installed to reach the maximal beam energy of E_{beam} = 3 MeV/u. In a last step, the final beam is guided with a bending magnet to the MINIBALL target position. [73]

3.1.2 Characteristics of ^{72}Zn REX-ISOLDE Beams

In the following the most important features of the two ^{72}Zn REX-ISOLDE beams, provided for the transfer experiment in 2011 and the Coulomb excitation experiment in 2012, are discussed. The relevant beam parameters are listed in tab. 3.1.

^{72}Zn Beam Intensities
Compared to other nuclei the ^{72}Zn beam can be produced at high intensities since ^{72}Zn is only two neutrons away from the stable ^{70}Zn isotope. The instantaneous beam intensity is larger due to the pulsed structure of the REX-ISOLDE beam, i.e. the whole ^{72}Zn ions which are trapped for 68 ms (in 2011) and 78 ms (in 2012) in the EBIS for the charge-breeding, are delivered to MINIBALL in a single much shorter EBIS pulse. Hence, due to the expected high beam intensities, in both experiments the slow extraction mode of the EBIS is used, i.e. the EBIS pulse is extended to its maximum length, which is 1 ms (c.f. fig. 3.6 a)). The advantage of the pulsed beam is, that background radiation e.g. from the β-decay of the beam and from natural sources can be subtracted easily.

Dependence of the Beam Purity on the Time Structure of the REX-ISOLDE Beam
By exploiting the time structure of the beam, the beam purity can be controlled to a certain extend: Due to the production mechanism of the RIB at ISOLDE each isotope has its specific time structure. The most important time quantities are the time since the last proton pulse and the time since the start of the last EBIS pulse:
Due to the different chemical properties of the produced radioactive atoms, their diffusion and effusion processes out of the ISOL production target occur on different time scales. E.g. fig. 3.6 b) shows that zinc leaves the target much faster than its beam contaminant gallium [80]. Hence, the gallium contamination can be suppressed by imposing a cut on the time difference between the proton pulse (given by the T1 signal) and the time signal of the particle detection. Apart from that, the different release time structure of the elements from the ISOLDE primary target can be exploited to determine the beam composition.
A second time structure which is element-selective is the EBIS release curve. The rest gas of the REXTRAP can have a different extraction time from the EBIS than the desired RIB. Therefore, a cut on the EBIS time pulse can improve the beam purity.

---

[7]Interdigital H-mode structure
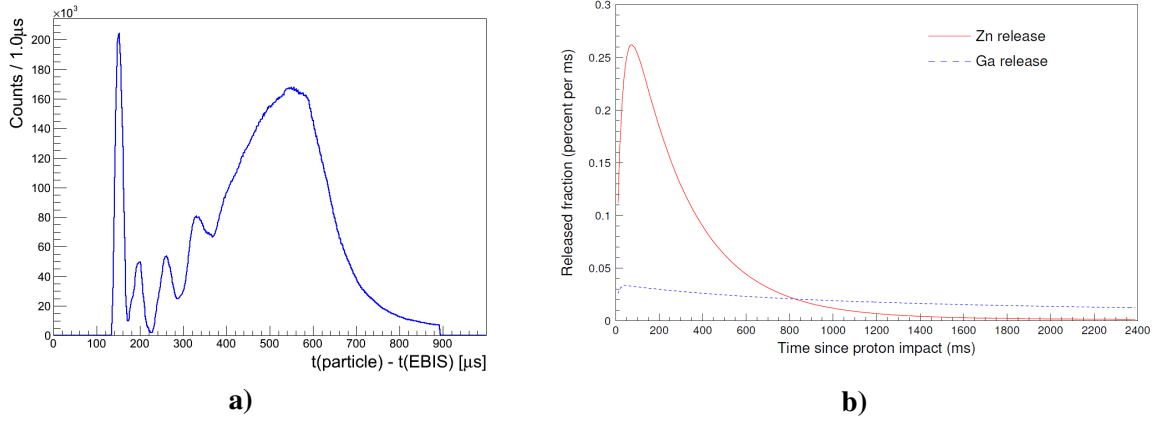
Fig. 3.6: a) The time profile of the ^{72}Zn beam intensity at the MINIBALL target position. It corresponds to the release curve of the EBIS. Due to the high beam intensities, the slow extraction mode of the EBIS pulse is used, i.e. the pulse is extended to 1 ms. **b)** An example for a release curve of zinc and gallium of the production target measured at the ISOLDE facility [80]. It allows to purify the beam if a cut on the time since proton impact is imposed.
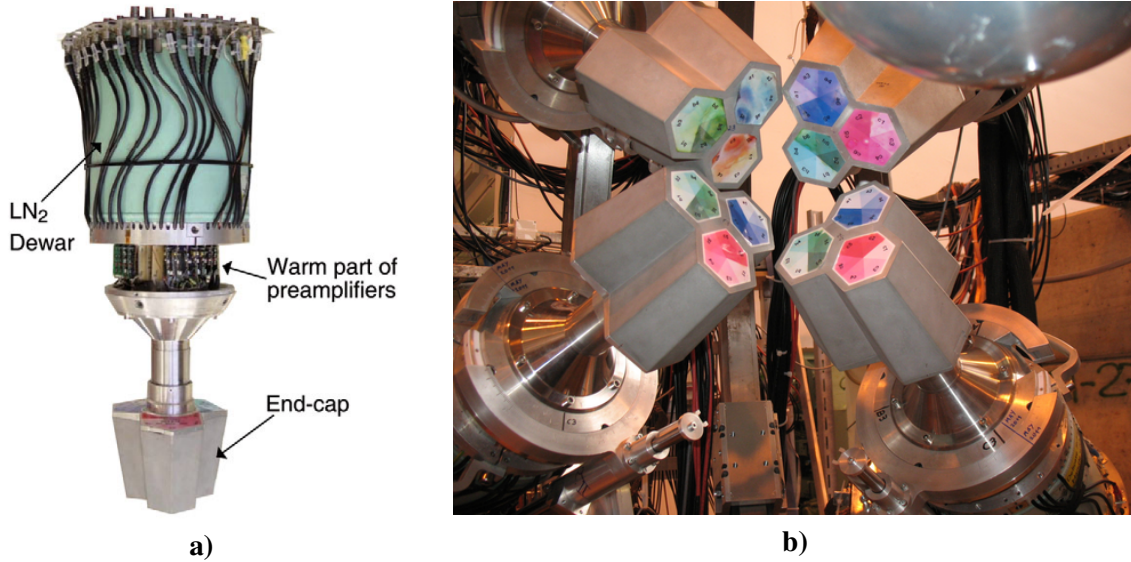
Fig. 3.7: a) A MINIBALL triple cluster housing three hexagonal six-fold segmented HPGe crystals. The picture was taken from [81]. **b)** Four MINIBALL clusters which are mounted on the flexible frame at REX-ISOLDE. The three crystals in one cluster are shown here with the colors red, green and blue and their segmentation is visualized with different degrees of transparencies of the colors. On the top right, a part of the Coulex vacuum chamber is seen. The photograph was taken from [82].

3.2 The MINIBALL Spectrometer

The final states of transfer reactions and of Coulex reactions can be associated to excited states of the outgoing nuclei. Their deexcitation process into the ground state is, in general, performed though the emission of γ-rays which carry important information about the populated final excited states. At REX-ISOLDE these γ-rays are detected with the high efficient γ-ray spectrometer MINIBALL [81]. MINIBALL consists of 24 High Purity Germanium (HPGe) crystals which are grouped in eight triple clusters with a common cryostat each (c.f. fig. 3.7). Each crystal is a coaxial detector with a diameter of $d = 7$ cm and a length of $l = 7.8$ cm. To ensure a good angular coverage, the crystals are tapered. Hence, a hexagonal front is achieved. For easier handling, the HPGe crystals are individually encap-

sulated in a thin aluminum can. Furthermore, they are electrically six-fold segmented into sectors (c.f. fig. 3.7)[8]. The big advantage of the segmentation is a more precise determination of the γ-ray interaction point which plays a crucial role for performing a Doppler correction. The Doppler correction capabilities of MINIBALL are further studied in sec. 4.4. The 168 signals[9] from the MINIBALL array are processed with XIA DGF-4C modules which deliver energy and time information for each channel above the trigger threshold [84]. Apart from that, as MINIBALL is designed as an European multi-purpose germanium array, the MINIBALL clusters are mounted on a flexible frame which allows to optimize their positions for each experiment. At REX-ISOLDE all MINIBALL clusters are arranged in a sphere around the ancillary silicon detectors and the target. The mean distance between the target at the origin of the sphere and a front of a MINIBALL cluster is about 10cm for the traditional Coulex setup (c.f. sec. 3.4). Thus, the complete MINIBALL array has a photopeak efficiency of $\epsilon_{MB} = 7.8\%$ at $E_\gamma = 1.3\,\text{MeV}$ γ-ray energy using the addback procedure. The actual efficiency curves for the ^{72}Zn experiments are given in sec. 4.3.1.

3.3 The Transfer Setup T-REX

The main goal of transfer experiments is to determine the differential cross sections as a function of the scattering angle (c.f. fig. 2.2 a)), as they contain information about the transferred angular momentum, i.e. the spin and parity of the populated state (c.f. sec. 2.2.2). Furthermore, a comparison of the experimental differential cross section with theoretical calculations gives a direct insight into the wave function of the final state (c.f. sec. 2.2.2). Hence, the experimental setup should measure the angular distribution over a large range of scattering angles.

Requirements for the Transfer Setup at REX-ISOLDE
The ^{72}Zn transfer experiments at REX-ISOLDE were performed in inverse kinematics, i.e. the heavy ^{72}Zn beam was impinging on a light target which provides the neutrons for the neutron transfer reactions. For the study of the two-neutron transfer from ^{72}Zn to ^{74}Zn, a radioactive tritium target is used which had an activity of almost $A = 10\,\text{GBq}$ at the time of its production [54, 55]. As carrier material for the tritium serves a thin strip of a $0.5\,\text{mg/cm}^2$ titanium foil. The atomic ratio between tritium and titanium is about $N(^3\text{H})/N(\text{Ti}) = 1.58$, resulting in an effective thickness of $40\,\mu\text{g/cm}^2$ ^{3}H at its production time in 2008. Dependent on how many neutrons are transferred, a proton (2n transfer to ^{74}Zn) or a deuteron (1n transfer to ^{73}Zn) is the resulting recoil of ^{3}H. Furthermore, the one-neutron transfer reaction to ^{73}Zn is studied separately using a $105\,\mu\text{g/cm}^2$ thin deuterated polyethylene (dPE) foil, which can be used as a reference measurement[10]. Besides the transfer reactions, also the strong elastic channel is of importance, resulting in an outgoing triton or a deuteron for the tritium and the dPE target, respectively. Fig. 3.8 visualizes the scattering angle θ_{lab} in the laboratory frame of the reaction products as a function of the center of mass scattering angle θ_{CM} of all relevant reaction mechanisms. It shows that in all cases the beam like particles ^{72,73,74}Zn are strongly forward peaked whereas the light reaction products, i.e. the tritons, deuterons and protons, cover a large range of scattering angles in the laboratory frame. Their detection provides insight into the outgoing beam-like nuclei by exploiting energy, momentum and angular momentum conservation. Thus, the basic features of an ideal experimental setup are a good energy and position resolution, a large angular coverage as well as an efficient particle identification to discriminate between different reaction channels.

---

[8]Note, that in contrast to the AGATA detectors [83], MINIBALL does not have a segmentation in depth.

[9]168 MINIBALL signals = 8 clusters $\times$ 3 detectors in one cluster $\times$ 7 (1 core + 6 segments) signals

[10]As the Q-values of the (t,d) and the (d,p) reaction differs, different states are populated in ^{73}Zn due to the Q-value matching (c.f. sec. 2.2.2).
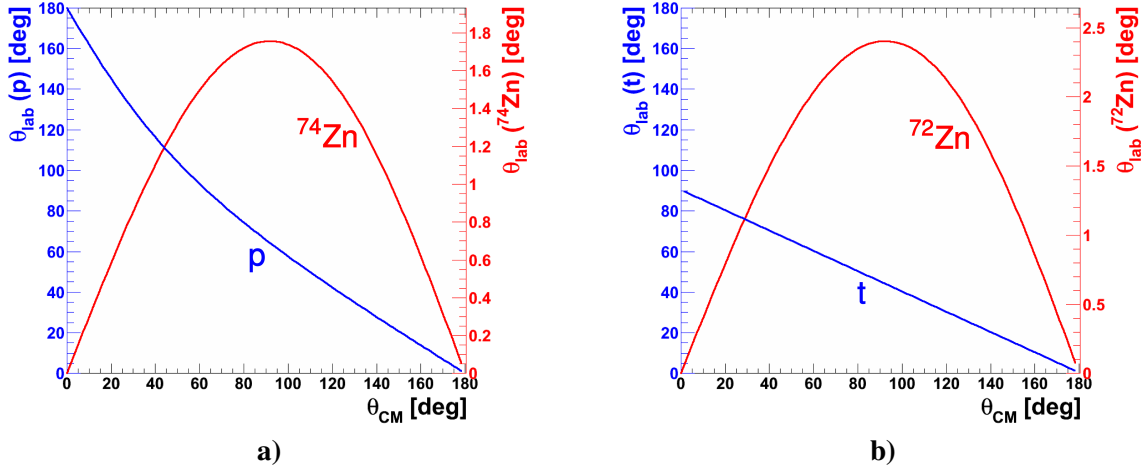
Fig. 3.8: The relations between the scattering angle θ_{CM} in the center-of-mass system and the laboratory angles θ_{lab} of the outgoing particles. Fig. **a)** visualizes the case for the two-neutron transfer reaction $\mathrm{t}(^{72}\mathrm{Zn},\mathrm{p})^{74}\mathrm{Zn}$. The one-neutron transfer reactions $\mathrm{t}(^{72}\mathrm{Zn},\mathrm{d})^{73}\mathrm{Zn}$ and $\mathrm{d}(^{72}\mathrm{Zn},\mathrm{p})^{73}\mathrm{Zn}$ have similar kinematics. **b)** Kinematics for the elastic channel $\mathrm{t}(^{72}\mathrm{Zn},\mathrm{t})^{72}\mathrm{Zn}$. For the calculation of the reaction kinematics a $^{72}\mathrm{Zn}$ beam energy of $E_{beam} = 2.7\,\mathrm{MeV/u}$ has been used. Note, the different scale on the θ_{lab}-axis of both plots.

Overview of the Silicon Array T-REX

A setup, fulfilling all these requirements, is the T-REX[11] silicon array which was designed and built by Vinzenz Bildstein at TUM for transfer experiments at REX-ISOLDE [85]. A schematic drawing and a photograph of T-REX are shown in fig. 3.9. The whole T-REX array consists of 16 position sensitive ΔE-E silicon telescopes which have a total solid angle coverage of about 66% [85]. The ΔE-E stacks do not only provide a precise energy measurement, but also a particle identification capability, as the energy loss depends on the charge and the mass of the particle (c.f. sec. 5.1.1). In principle, T-REX has two types of silicon telescopes: Close to the target are the so called Barrel detectors which are arranged in two boxes. Upstream and downstream of the Barrel detectors, circular CD detectors are installed. Thus, in the complete configuration of T-REX the forward angles $\theta_{lab} \in [8°, 78°]$ are covered by the forward CD ΔE-E telescope (FCD) and the forward Barrel box (FBarrel), while the backward Barrel (BBarrel) and the backward CD ΔE-E stack (BCD) can detect particles with laboratory angles $\theta_{lab} \in [102°, 172°]$. The emphasis in the design phase of the T-REX array was set on achieving a compact setup featuring a minimum amount of material in order to keep the efficiency of the surrounded MINIBALL array. Thus, T-REX only has a length of about 13 cm and a diameter of about 12 cm. The cylindrical T-REX vacuum chamber has an inner diameter of 14 cm and a wall thickness of 2 mm.

T-REX Detectors

In the following, the Barrel and CD detectors, which are used in the T-REX array, are explained in more detail. A short summary of the most important detector parameters is given in tab. 3.2.

One Barrel box consists of four identical ΔE-E Barrel stacks (c.f. fig. 3.10 a)). Each ΔE Barrel detector[12] has a thickness of $140\,\mu\mathrm{m}$ and a quadratic active area of 50×50 mm. Moreover, the ΔE detector is segmented into 16 $\Delta d = 3.125$ mm wide resistive strips which are arranged perpendicular to the beam axis. They are read out at one side of the strip. By comparing their signal to the unsegmented rear side of the Barrel ΔE detector, also the interaction position of a particle along a strip can be determined. Hence, a two dimensional position resolution is achieved. 2.2 mm behind the ΔE Barrel detector an unsegmented E_{rest} detector[13] is installed. It has a thickness of $1000\,\mu\mathrm{m}$ which ensures in

---

[11]Transfer at REX

[12]Resistive Silicon Strip Detectors (RSSD) from Micron Semiconductors (design X1)

[13]Pad detector from Canbera (design RF)
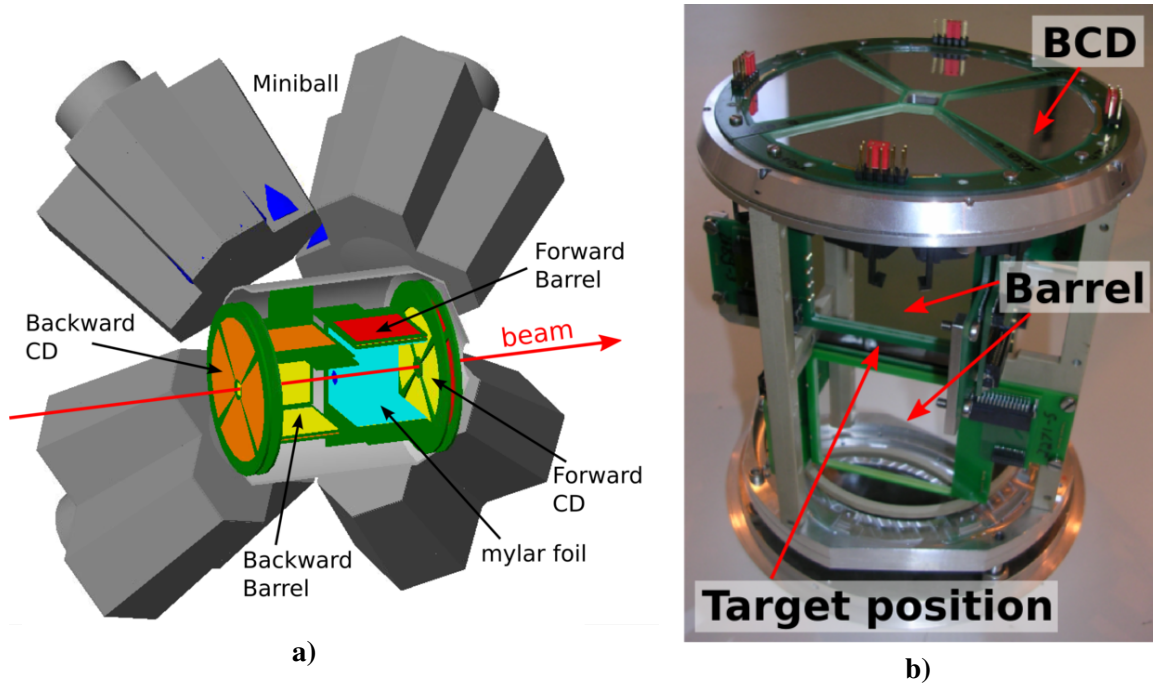
Fig. 3.9: a) Overview of the full T-REX setup which was used in the ^{72}Zn transfer experiment in 2011. This configuration contains two Barrel boxes as well as two CD disks upstream and downstream of the target. The target (small dark blue disk) is placed in the center of T-REX. For a better visualization only three Barrel detectors of each Barrel box are shown. Furthermore, the mylar protection foils in front of the FBarrel are shown in light blue. **b)** A photograph of the T-REX setup. This configuration includes the FBarrel, the BBarrel and the BCD detectors. The photograph was adapted from [86].
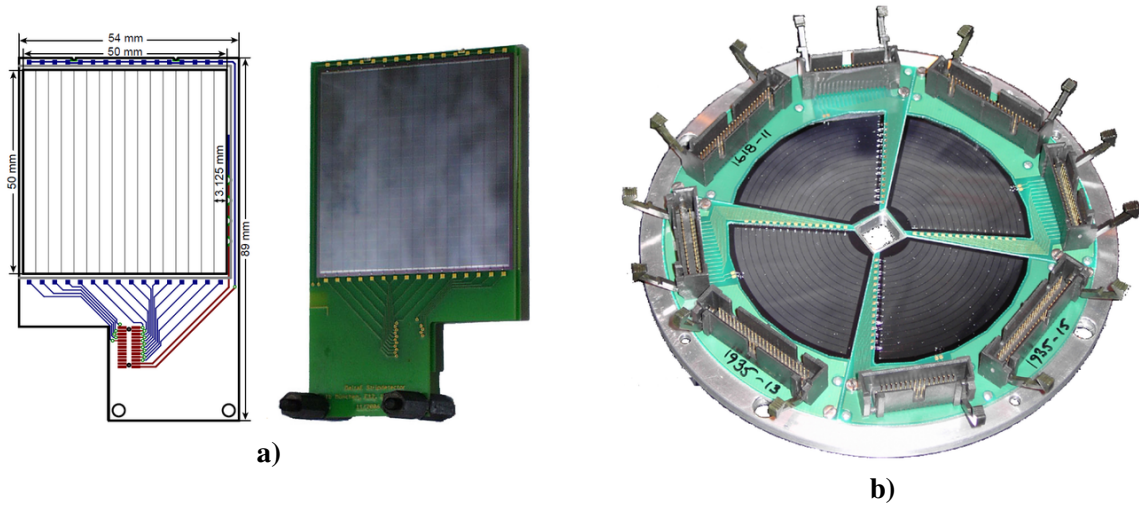
Fig. 3.10: a) A schematic drawing of a Barrel ΔE detector (left) and a photograph of a Barrel ΔE-E stack (right). Both pictures show the segmentation of the Barrel ΔE detector into 16 resistive strips. Behind the ΔE detector in the photograph an unsegmented E_{rest} detector is installed. **b)** A photograph of a CD ΔE detector with four quadrants, each featuring 16 annular rings and 24 radial strips. The front view only shows the segmentation into rings. The strip segmentation is on the back. The pictures were adapted from [86].

Detector	Thickness	Active area	Segmentation	θ_{lab} range
FBarrel ΔE	$140\mu m$	50×50 mm	16 resistive strips with 3.125 mm pitch	27° - 78°
BBarrel ΔE			$\Rightarrow$ 2D position resolution	102° - 153°
FBarrel E_{rest}	$1000\mu m$	50×50 mm	unsegmented	
BBarrel E_{rest}				
FCD ΔE	$500\mu m$	$r \in [9,41]$ mm	16 annular rings (2 mm width),	8° - 27°
BCD ΔE		$\phi \in [0, 81.6°]$	24 radial strips (3.4° width)	153° - 172°
FCD E_{rest}	$1500\mu m$	$r \in [9,50]$ mm	unsegmented	
BCD E_{rest}	$500\mu m$	$\phi \in [0, 82°]$		

Tab. 3.2: Summary of the most important parameters of the Barrel and CD ΔE-E silicon telescopes of the T-REX array. The parameters are given for one quadrant and for the configuration which was used in the ^{72}Zn transfer experiments performed in 2011.

most cases that the outgoing light reaction product is stopped in the E_{rest} detector, allowing to detect the total energy of the particle (c.f. sec. 5.1.1).

Like the Barrel detectors, the circular CD detectors consist of four quadrants, each featuring a DSSSD ΔE detector[14] and an unsegmented E_{rest} detector[15]. A photograph of a CD ΔE detector is shown in fig. 3.10 b). Each ΔE CD quadrant has an annular segmentation into 16 rings at the front and a radial segmentation into 24 strips at the back side. Thus, a two dimensional position resolution is obtained. The rings have a pitch of 2 mm with an active radial width of $\Delta r = 1.9$ mm and each strip has an opening angle of $\Delta\phi = 3.4°$. To reduce the number of electronic channels, the inner 16 strips are electrically combined to eight strips, leading to 16 strip signals per quadrant. The thickness of the ΔE quadrant is typically $500\mu m$, whereas the E_{rest} detector has a thickness of $1500\mu m$ and of $500\mu m$ for the FCD and the BCD, respectively. The asymmetry in detector thickness is due to the fact, that the light reaction products in forward direction have much more energy compared to the backward direction.

Foil System

Besides the transfer reactions and the elastic scattering on the tritium or the deuterium, it is also possible that the beam scatters elastically on the carrier material of the target, i.e. on the titanium of the tritium target or the carbon of the dPE target. According to the elastic reaction cross section, the scattered target particles have their maximum intensity in forward direction close to $\theta_{lab} = 90°$, resulting in high count rates in the FBarrel detectors. Hence, dead-time problems can occur or the detectors can even be damaged. To protect the detectors, a $d = 11.75\mu m$ thick protection foil is permanently installed 2 mm in front of the FBarrel ΔE quadrants[16]. The thickness of the foil is chosen that the light reaction products such as protons, deuterons, tritons and α-particles can pass the foil, while heavy reaction products like elastic scattered beam, ^{12}C and ^{48}Ti from the target are stopped in the foil. As the FCD features no protection foil, it was used to study the Coulomb excitation of the ^{72}Zn beam with the carrier material ^{48}Ti of the tritium target. This served as a test experiment for the Coulomb excitation experiment done in 2012. Furthermore, it is a good reference system, e.g. for estimating the beam energy and for beam tuning.

---

[14]Double Sided Silicon Strip Detector (DSSD) from Micron Semiconductors (design QQQ2)

[15]Pad detector from Micron Semiconductors (design QQQ1)

[16]Additional foils can be also installed in the T-REX setup: A vertical foil with a circular hole directly behind the target can be useful to stop elastic backscattered particles in case of dealing with normal reaction kinematics (c.f. e.g. the ^{32}Mg experiment at REX-ISOLDE [54]). Furthermore, a foil in front of the FCD can be easily installed.
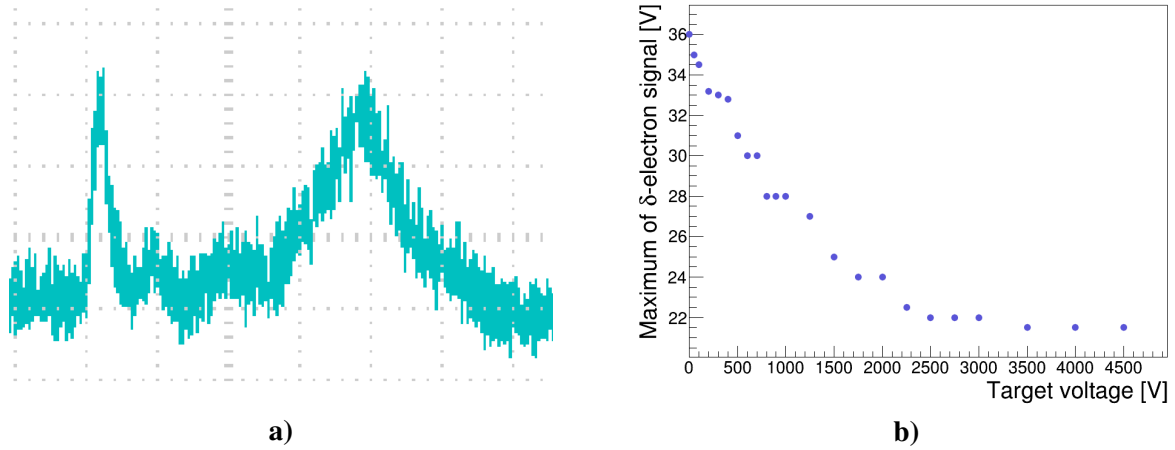
a)   **b)**

Fig. 3.11: a) BBarrel noise signal after the preamplifier and the shaper. The noise is mainly due to δ-electrons which are produced by the interaction of the beam with the target. The structure of the noise is similar to the structure of the beam, i.e. the EBIS release curve (c.f. fig. 3.6 a)). **b)** Increasing the voltage on the target reduces the noise in the BBarrel detectors since the electrons are hindered to reach the detectors by the positive voltage.

Target Voltage

Due to the interaction of the beam with the target, δ-electrons are produced, especially for high Z beams such as the ^{72}Zn beam. These δ-electrons have enough energy to leave the target and to reach the detector where they can represent the main contribution to the noise of the detector. As the intensity of the δ-electrons is directly proportional to the beam intensity, the noise signal has the same structure as the beam (c.f. fig. 3.11 a) and fig. 3.6 a)). This is especially a problem of resistive strip detectors as the energy signal comes from the huge unsegmented rear side of the detectors. Thus, due to the large solid angle of the rear electrode, the δ-electrons can produce a large noise signal. Hence, the δ-electrons force the detection threshold of the Barrel detectors to be increased which is in conflict with the low expected energies of the light transfer products. To solve this problem a bias voltage of $+4000\,$V with respect to the rest of the setup was applied to a newly designed tritium target ladder for the 2011 and the 2012 experimental campaigns. It was made of PEEK[17] to ensure that the high voltage is only applied to the area around the target. The positive effect of the target voltage is visualized in fig. 3.11 b) which shows that the noise level in the Barrel detector drops significantly with increasing voltage. The used value $+4000\,$V for the target was chosen to be in the plateau area of the plot. This ensures that also the BBarrel noise signal does not feature a beam like structure anymore, i.e. the δ-electrons cannot hit the detector. [81]

Beam Diagnostics

Besides the two main detector systems T-REX and MINIBALL, there are several other ancillary detectors for beam diagnostics:

For instance, the position of the beam is monitored with an active collimator which is installed directly before the T-REX vacuum chamber. It consists of four quadratic $10 \times 10\,$mm PiN-diodes which are positioned around a hole with $10\,$mm diameter. A second detector for measuring the beam position is a 10μm thick circular diamond detector which can be mounted on target position. Due to its nine fold segmentation it allows to center the beam on the target and, thus, complements the active collimator for beam tuning.

Apart from that, to measure the beam composition, an ionization chamber is installed about $4\,$m behind T-REX at the beam dump. The two main components of the ionization chamber are a $1\,$cm thick volume filled with CF_4 gas and a $300\,\mu$m thick Si detector [87]. The chamber measures the energy

---

[17]PEEK: PolyEther Ether Ketone, i.e. a non-conducting organic polymer which is suitable for in vacuum use.

loss in the CF_4 gas which is related to the charge Z of the incoming beam, whereas the silicon detector measures the residual energy. The total detected energy depends on the mass A of the particle as all beam particles with the same mass are accelerated to the same kinetic energy. Therefore, a determination of beam contaminants is possible (c.f. sec. 5.1.3 and sec. 6.1.6).

Furthermore, a γ-ray detector, the so called beam dump detector, is positioned close to the beam dump. It allows to measure the γ-rays resulting from the β-decay of the radioactive beam. Hence, conclusions about the beam composition can be made.

T-REX Electronics

The analogue electronics of the T-REX setup is based on standard Mesytec modules. In general, the electronic setup is split into two identical parts, the so called trigger groups. If a single detector is triggering, all detectors of the corresponding trigger group are read out simultaneously. T-REX can cope with only two identical trigger groups, as the expected count rates of transfer reactions with radioactive beams are low enough. The first trigger group "Top-Left" deals with all top and left detectors while the second trigger group "Bottom-Right" compromises all bottom and right detectors with respect to the beam direction. A detailed description and a schematic drawing of the T-REX electronics can be found in appendix A.

3.4 The Coulex Setup C-REX

Complementary to the one- and two-neutron transfer experiment with a ^{72}Zn beam, the multiple Coulomb excitation of ^{72}Zn using a 1.17 mg/cm^2 thick ^{109}Ag target[18] is studied in this work. In the following, the experimental setup is described which has been newly designed and successfully used for the first time in the course of this thesis.

The Standard Coulex Setup

Fig. 3.12 a) shows the standard Coulex setup which has been used in all previous Coulex experiments at REX-ISOLDE [81]. In this setup the scattered beam and target ions are detected with one segmented ΔE CD detector which is also included in the previously described T-REX setup. Hence, it consists of four quadrants having 16 rings and 24 strips each. Similar to T-REX, the two neighboring strips are combined to reduce the number of electronic strip channels to 12. The CD detector is positioned at a fixed distance of about 30 mm from the target ($\theta_{lab} \in [16.8°, 53.7°]$). Furthermore, it features a spherical vacuum chamber which allows to position the MINIBALL detectors as close as possible around the target position. This setup was used very successfully for many years at ISOLDE to study the Coulomb excitation of various nuclei over the whole nuclear chart.

The New C-REX Setup

However, due to the fixed CD-target distance, the standard Coulex setup is limited to experiments with moderate beam intensities, since Rutherford scattering can cause too high count rates in the inner rings of the CD. As ^{72}Zn is close to the valley of stability, the expected mean beam intensity is about $I = 7 \cdot 10^6$ ions/s at the MINIBALL target. In combination with a 1.17 mg/cm^2 thick ^{109}Ag target a mean count rate of 25 kHz is expected, i.e. about 1500 hits per spill in the CD. Thus, the new setup "C-REX" (c.f. fig. 3.12 b)) was designed in the framework of this thesis on the basis of the T-REX silicon array. C-REX features a variable distance of the CD detector to the target. Hence, this distance can be optimized for each experiment separately to optimize the angular coverage and to achieve tolerable count rates of the elastically scattered particles. The distance can be varied between 2.3 cm and 6.4 cm.

---

[18]The target thickness has been determined by Josef Lichtinger with his high precision setup for the determination of the thickness of human brain tissues [88]. The thickness is extracted (position dependent) by a comparison of the measured energy loss to the calculated energy loss of α-particles through the material [89].
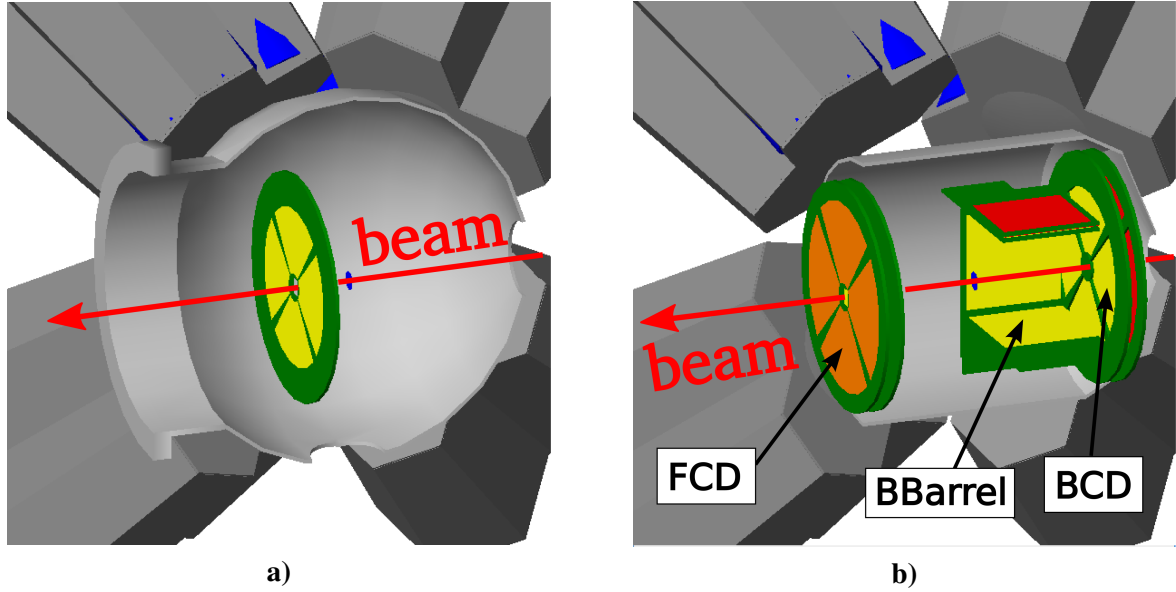
Fig. 3.12: a) The standard Coulex setup at REX-ISOLDE with one single segmented CD detector which is installed about 30 mm away from the target position. It is housed in a spherical vacuum chamber. **b)** The new C-REX setup which features a movable segmented FCD detector as well as detectors in backward direction to reach a high sensitivity for multiple Coulomb excitation. C-REX is surrounded by the cylindrical T-REX vacuum chamber and by the MINIBALL γ-ray spectrometer.
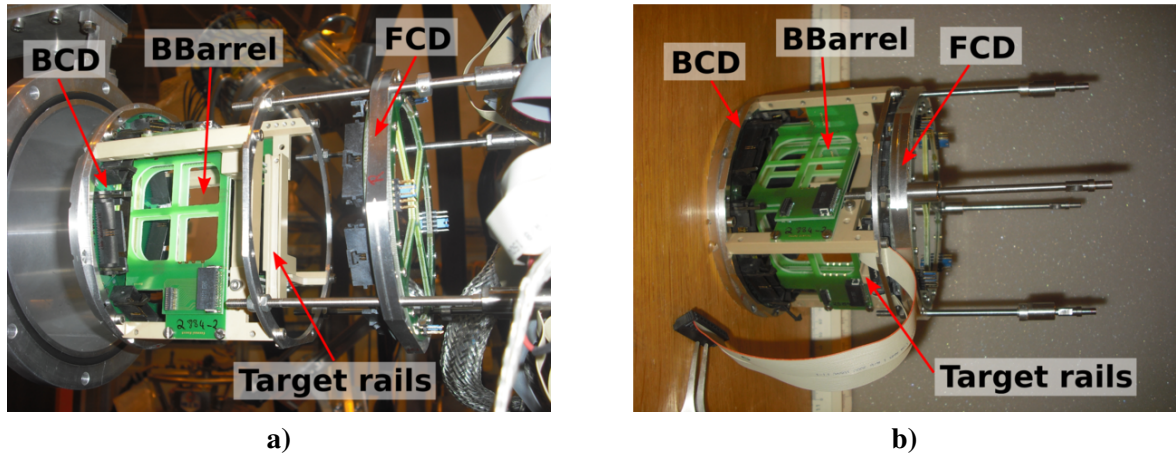
Fig. 3.13: Two photographs of the new C-REX setup. In both pictures the beam is coming from the left. In picture **a)** C-REX is mounted at the MINIBALL target position with the FCD further away. Contrary, the picture **b)** shows the closest possible distance between the FCD and the target which is about 2.3 cm.

This movable FCD is identical to the FCD of the T-REX setup: It is designed as a ΔE-E telescope for calibration measurements of the MINIBALL angles (c.f. sec. 4.4) and features the same segmentation as T-REX into 16 rings and 16 strips which is necessary to perform a Doppler correction. Apart from that, C-REX is equipped with additional detectors in backward direction: a segmented BCD and four segmented BBarrel ΔE detectors. Due to these additional detectors, the multiple Coulomb excitation can be studied more precisely than in the previous Coulex setup (c.f. sec. 2.3.2). Especially the effect of the quadrupole moment is largest at backward angles (c.f. fig. 2.5). In tab. 3.3, the basic features of C-REX are summarized. Fig. 3.13 shows two photographs of the C-REX setup. In fig. 3.13 a) the setup is mounted at the MINIBALL target position with the FCD further away. Contrary, fig. 3.13 b) shows the closest possible distance between the FCD and the target which was used in the ^{72}Zn

Detector	Thickness	Active area	Segmentation	θ_{lab} range
BBarrel ΔE	140μm	50×50 mm	16 resistive strips with 3.125 mm pitch	102° - 153°
FCD ΔE	500μm	$r \in [9, 41]$ mm	16 annular rings (2 mm width),	variable
BCD ΔE		$\phi \in [0, 81.6°]$	24 radial strips (3.4° width)	153° - 172°
FCD E_{rest}	1500μm	$r \in [9, 50]$ mm		
BCD E_{rest}	500μm	$\phi \in [0, 82°]$	unsegmented	

Tab. 3.3: Summary of the most important parameters of the Barrel and CD ΔE-E silicon telescopes of the C-REX array. Here the parameters are shown for one quadrant and for the configuration with was used in the ^{72}Zn Coulex experiment performed in 2012. Note, that the BCD E_{rest} detector was not read out. It was only installed to avoid that scattered beam, which does not originate from the target, does not hit the BCD ΔE detector from behind.

Coulomb excitation experiment. The target rails in the picture indicate the position of the target ladder which is identical to the T-REX setup. Like in the transfer experiment, a high voltage was applied to the ^{109}Ag target to reduce the noise, caused by δ-electrons, in the BBarrel detectors (c.f. sec. 3.3). Apart from that, all ancillary detectors for beam diagnostics which have been introduced in sec. 3.3 were used in the ^{72}Zn Coulex experiment, too.

C-REX Electronics

Due to the higher expected count rates, the T-REX electronics was modified for the C-REX experiments. To gain a factor of two in the readout rate, the two trigger groups Top-Left and Bottom-Right have been replaced by four independent trigger groups, i.e. one trigger for each quadrant: Top, Left, Bottom and Right. Like the T-REX electronics, the readout of C-REX is based on Mesytec modules. A detailed description and a schematic drawing of the C-REX electronics can be found in appendix A.

4

Calibration and Doppler Correction

For the physics analysis of the experiment each individual detector channel has to be calibrated in a first step. The data flow and the calibration procedures are very similar for the T-REX and C-REX experiments. Hence, they are described simultaneously in the following. In case of different methods, both are specified separately. In sec. 4.1, an overview of the data flow of the offline analysis is given, while sec. 4.2 deals with the calibration of the T-REX and C-REX silicon detectors. In sec. 4.3 and sec. 4.4, the calibration of the γ-ray spectrometer MINIBALL is described. It includes the precise determination of the MINIBALL detector angles for Doppler correction. Here a new method of iterative minimization for the angles has been developed in the scope of this thesis. Finally, the alignment of the timestamps of the particle and the γ-ray detectors is outlined in sec. 4.5.

4.1 Data Flow Overview

The data from the ADCs is recorded with the MBS[1] based data acquisition MARaBOU[2] [90] and is saved as binary MED[3] files. They are analyzed using a program package based on the C++ programming language and the ROOT framework [91]. The code for the transfer analysis was originally developed by Vinzenz Bildstein [86] and Kathrin Wimmer [54] and afterwards modified by Anna Katharina Nowak [55]. Within this thesis it was further improved by e.g. introducing better fit functions, by considering the detector dead-layers and by implementing a time-dependent calibration. Furthermore, it was used as a basis for the newly developed code of the ^{72}Zn Coulex analysis[4]. Both analysis codes are organized in four steps:

- **Event building:** In a first step, the list mode (MED) files from the data acquisition are read, unpacked and an event building is performed. An event is defined by all detector hits within a coincidence window of 1μs. This event building groups particle data and γ-ray data according to their timestamps. Hence, one event contains all real coincidences between particles and γ-rays of one reaction, but also random coincidences. These random coincidences allow for a precise background subtraction in a high level analysis.

- **Calibration:** Afterwards, all particle and γ-ray detectors are calibrated to obtain position, energy (in keV) and time information for each hit. This is outlined in the rest of this chapter.

- **Reconstruction:** In the reconstruction step, physical objects, i.e. Lorentz 4-vectors for all particles and γ-rays, are calculated. Considering energy loss and 4-momentum conservation allow to determine excitation energies of the outgoing nuclei in case of transfer reactions (c.f. sec. 5.1) or for a kinematic reconstruction of reaction partner which have not been detected in case of Coulomb excitation experiments[5] (c.f. sec. 6.1).

---

[1]Multi Branch System, developed by GSI
[2]MBS and ROOT based Online/Offline Utility
[3]MBS Event Data
[4]The standard Coulex analysis code for MINIBALL experiments is not used as the incoming data streams differ too much.
[5]As the energies of the outgoing nuclei in Coulex experiments are at least one or two orders of magnitude higher than the excitation energy, the excitation energy is neglected in the kinematic reconstruction.

- **High level analysis:** The last analysis step deals with the high level physics analysis which has to be individually redesigned for each experiment (c.f. chap. 5 and chap. 6 for the transfer and the Coulex experiment, respectively). In this step, e.g. Doppler corrected γ-ray spectra and reaction cross sections are extracted.

4.2   Calibration of the Particle Detectors

This section provides a short summary of the calibration procedures of all T-REX and C-REX silicon detectors. In the scope of this work, the calibration procedures developed for the previous experiments [54, 55, 86] were adjusted to the specific requirements of the experiments discussed in this thesis. The modified calibration procedures are briefly outlined in the following, concentrating on the improvements compared to the previous experiments. A more detailed description can be found in appendix B. Additionally, dedicated user operation manuals for both, the C-REX and the T-REX detector and electronics configurations were created for a standardized calibration procedure in the course of this thesis (c.f. [92] and [93]).

ΔE Barrel Detectors
The calibration of the energy signal and of the position signal along the resistive strip of the ΔE Barrel detectors is done with an standard quadruple α-calibration source[6] which is installed at the target position (for details see appendix B.1). Its main challenge is the fact that the energy signal depends on the hit position along the strip: Due to the resistive layer of the strip, hits occurring close to the readout side feature larger energy signals compared to hits far away from the readout side (c.f. fig. B.1 b)).
Additionally, to calibrate the T-REX FBarrel detectors, the energy loss of the α-particles in the $11.75\,\mu$m thick mylar protection foil has to be considered. As the effective foil thickness depends not only on the strip number (c.f. fig. B.2 b)), but also on the hit position along the strip (c.f. fig. B.2 a)), the energy loss in the foil was modeled, contrary to previous experiments, with a detailed Geant4 simulation.

Barrel Pad Detectors
Dependent on the expected energy depositions in the pad detectors (about 1 MeV in backward direction and about 10 MeV in forward direction) two complementary calibration procedures are used[7] (c.f. appendix B.2):
The low energy calibration is done with a ^{152}Eu source, exploiting its $E_\gamma = 1.4$ MeV γ-rays which Compton scatter in the Barrel pad detector and are subsequently absorbed in MINIBALL. These events show an anti-correlation line in the pad detector energy vs. MINIBALL energy spectrum (c.f. fig. B.3 a)). Thus, with a good MINIBALL calibration, the anti-correlation defines the energy loss in the pad detector. Hence, it can be used to calibrate the energy signal of the pad detector.
The high energy calibration of the Barrel pad detectors is performed with a stable beam experiment. In this thesis, the d(^{22}Ne, p)^{23}Ne reaction ($E_{beam} = 2.7$ MeV/u) was chosen. The known reaction kinematics (i.e. the dependence of the energy of outgoing proton as a function of its scattering angle) as well as the measured energy deposition in the (calibrated) ΔE Barrel detector allow to predict the energy deposition E_{pad} in the pad detector (c.f. fig. B.3 b)). Thus, a comparison of the experimental $\Delta E - E_{pad}$ Barrel spectra with the spectra obtained from a realistic Geant4 simulation of the d(^{22}Ne, p)^{23}Ne reaction allows to calibrate the energy calibration of the Barrel pad detector for $E \sim 10$ MeV.
The Barrel pad detectors are only used in the transfer experiments, as the heavy scattered ions in the Coulex experiment are already stopped in the ΔE Barrel detectors.

---

[6]The four strongest α-lines of the quadruple α-source originate from the isotopes ^{148}Gd (3.18 MeV), ^{239}Pu (5.16 MeV), ^{214}Am (5.49 MeV) and ^{244}Cm (5.81 MeV).
[7]A calibration with an α-source is not possible as the α-source can not be mounted directly in front of the pad detectors.

ΔE CD Detectors

Due to the multiplexing of the ΔE CD detector signals in the T-REX and in the C-REX setup, the calibration is done in two steps (c.f. appendix B.3):

First, the position signal has to be de-multiplexed to decode which ring or strip has been hit. Here, the linear dependence of the position signal on the ring/strip number is used (c.f. fig. B.4). However, this relation was found to be unstable over time. Hence, a time-dependent de-multiplexing was used in the transfer as well as in the Coulex analysis for the first time.

Second, the energy of each ring or strip has to be calibrated. For the transfer experiments, this is done with a standard quadruple α-source. Contrary, due to the higher energy depositions of up to 200 MeV, the ΔE FCD detector in the ^{72}Zn Coulex experiment is not calibrated with an α-source, but with a high intensity stable $A/Q = 4$ EBIS beam impinging on the 1.17 mg/cm^2 thick ^{109}Ag Coulex target. The calibration is based on the known reaction kinematics of the elastic scattering of the $A/Q = 4$ beam ions (^{4}He^{+}, ^{12}C^{3+}, ^{20}Ne^{5+} and ^{40}Ar^{10+}) on the ^{109}Ag target. As an exact energy calibration of the FCD is essential for the Doppler correction (c.f. sec. 4.4.4), the following improvements have been added in the energy calibration: First, to avoid an extrapolation to ^{72}Zn energies, also the elastically scattered ^{72}Zn ions of the Coulex experiment are included in the calibration. Second, also here a time-dependent energy calibration was developed as the calibration shifted about 5% over the whole experiment. Third, the silicon dead layers as well as the aluminum metalization of the detectors has been considered as the energy loss in these layers is about 6-10 MeV for scattered ^{72}Zn ions and about 6-14 MeV for scattered ^{109}Ag particles.

CD Pad Detectors

The calibration of the CD pad detectors is done with a standard quadruple α-source. This is possible as, in contrast to the Barrel pad detectors, the T-REX and the C-REX setup allow to mount the source directly behind the CD pad detector.

4.3 Calibration of the γ-ray Detectors

One key point in the experiments discussed in this thesis is a precise and reliable calibration of the γ-ray spectrometer MINIBALL in terms of energy and photopeak efficiency (c.f. sec. 4.3.1). The capability of MINIBALL to cope with high count rates is studied in sec. 4.3.2. Most important for the energy resolution is an accurate determination of the positions of the MINIBALL detectors to perform a precise Doppler correction, especially for Coulomb excitation experiments (c.f. sec. 4.4).

4.3.1 Energy Calibration and Efficiency Determination

The energy calibration of all γ-ray detectors is done using a ^{152}Eu source, which is mounted at the MINIBALL target position. Due to the rich γ-ray decay spectrum of ^{152}Eu between 122 keV and 1408 keV a precise calibration of all MINIBALL segments and cores is possible. The eight most dominant γ-ray peaks were fitted in all raw spectra and their positions were compared to the literature values. Subsequently, a linear calibration was performed since MINIBALL features a negligible non-linearity of less than 0.025% [81]. No additional calibration points from other sources are necessary as all γ-ray energies, which are discussed in this thesis, are in or close to the ^{152}Eu energy range.

Efficiency Determination

A precise knowledge of the photopeak efficiency of the γ-ray spectrometer MINIBALL allows to calculate absolute γ-ray yields and to compare γ-ray yields at different energies with each other. Hence, the determination of the MINIBALL efficiency is essential to extract transfer and Coulex reaction cross sections from the yield of γ-ray gated events (c.f. sec. 5.1.2 for transfer reactions and 6.2.1 for
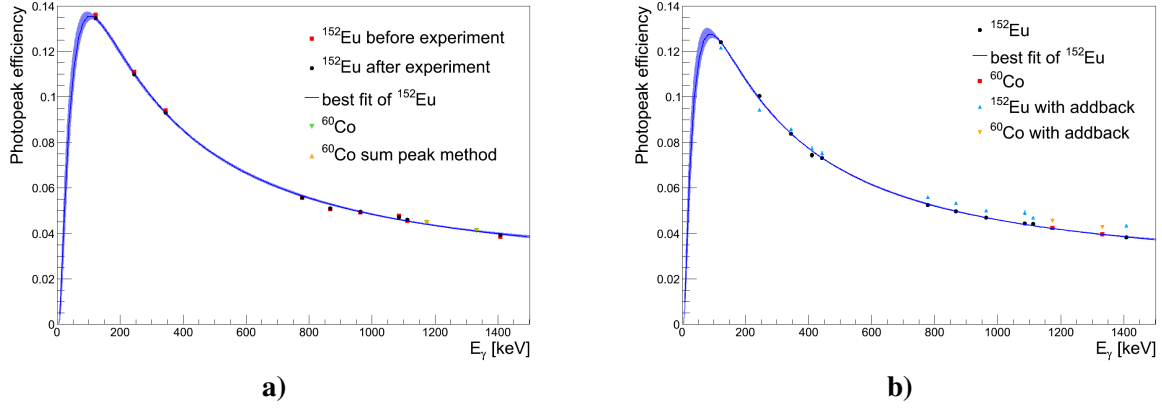
Fig. 4.1: a) The absolute photopeak efficiency of MINIBALL in 2011. It has been determined with two ^{152}Eu measurements, one before and one after the transfer experiment. As both ^{152}Eu efficiency measurements are in good agreement, it can be assumed that MINIBALL was stable over the whole experiment. To evaluate the efficiency at arbitrary γ-ray energies, the data points have been fitted with an empirical function (c.f. eq. (4.2)). The fit is shown as a blue line, while the shaded blue area indicates its 1σ contour. Furthermore, the efficiency has been determined with a ^{60}Co source with two different methods: First using eq. 4.1 and second using the sum peak method [92, 94]. Both are in excellent agreement with the ^{152}Eu data, indicating that the absolute efficiency is correct. **b)** The absolute photopeak efficiency of MINIBALL in 2012. It has been calculated from a ^{152}Eu and a ^{60}Co source measurement, which coincide well. Again a fit to the ^{152}Eu data is shown. Additionally, the efficiency after applying the addback procedure is displayed.

Coulex experiments). The energy dependent photopeak efficiency $\epsilon(E_\gamma)$ is defined as

$$\epsilon(E_\gamma) = \frac{\text{Counts in the photopeak with energy } E_\gamma}{\text{Total number of emitted } \gamma\text{-rays with energy } E_\gamma}. \tag{4.1}$$

The counts in the photopeak were determined via a Gaussian fit to the peak and assuming a superposition of a linear function and a step function as a background model. The total number of emitted γ-rays from the ^{152}Eu source was calculated from the relative γ-ray intensity, the run time of the ^{152}Eu measurement and the source activity. The resulting absolute photopeak efficiencies of MINIBALL are shown in fig. 4.1 a) for the transfer experiment in 2011 and in fig. 4.1 b) for the Coulex experiment in 2012. To obtain an energy dependent efficiency curve $\epsilon(E_\gamma)$, which can be evaluated for arbitrary γ-ray energies, an empirical function is fitted to the ^{152}Eu data points [65]:

$$\epsilon(E) = \exp\left[\sum_{i=0}^{3} a_i \ln\left(\frac{E}{50\,\text{keV}}\right)\right], \tag{4.2}$$

with a_i being the fit parameters. The fit including its 1σ confidence level is indicated in blue in fig. 4.1. Furthermore, to crosscheck the absolute value of the efficiency, an additional measurement with a ^{60}Co source was performed. It fits nicely to the efficiency curve of the ^{152}Eu source. Hence, systematic errors, e.g. resulting from a wrong source activity, can be excluded. As additional crosscheck, the efficiency was determined independently of the source activity by applying the sum peak method on the ^{60}Co data [92, 94]. Again, the resulting absolute photopeak efficiencies coincide well with the other analysis methods[8].

For the sake of completeness the efficiency curve using the addback procedure is shown for the 2012 experiment (c.f. fig. 4.1 b)). At γ-ray energies above $\approx 400\,$keV it features a slightly higher photopeak efficiency summing up all coincident γ-rays in all three detectors of the MINIBALL clusters. However,

---

[8]Note, that the sum peak method could only be applied to the measurement in 2011, as in 2012 a strong background line (resulting from the β-decay of the ^{72}Zn beam) is superimposed with the sum peak of the two ^{60}Co lines.
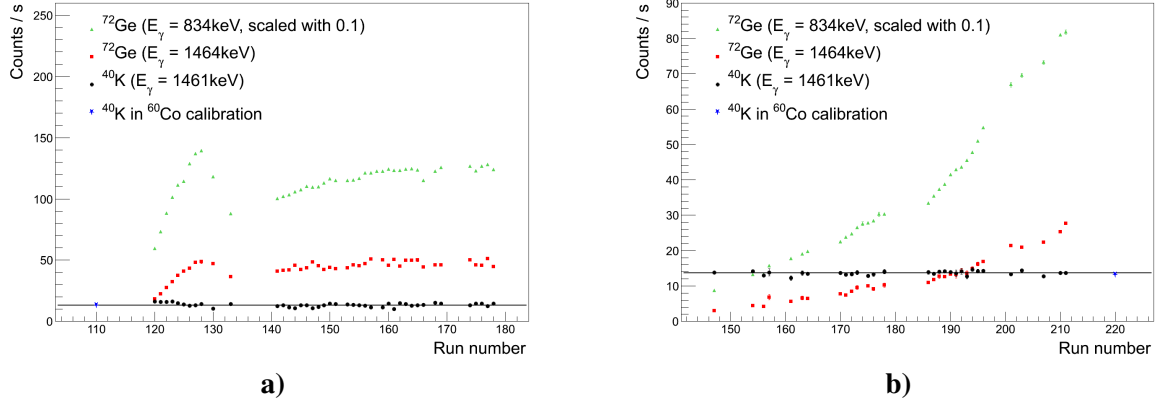
Fig. 4.2: The evolution of the total MINIBALL count rate of two strong ^{72}Ge β-decay lines (originating from the ^{72}Zn beam) and of the ^{40}K natural background line is shown for the transfer experiment (**a**)) and the Coulex experiment (**b**)). For comparison the count rate of ^{40}K is displayed during the ^{60}Co efficiency calibrations. As its rate had not changed over time (see horizontal straight line fit) for all radioactive beam runs and the ^{60}Co calibration runs, the MINIBALL efficiency was constant in time, although the count rate of the MINIBALL detectors had increased gradually due to the accumulating β-decay of the ^{72}Zn beam (^{72}Zn $\rightarrow ^{72}$Ga $\rightarrow ^{72}$Ge). The sudden drop of the β-decay rate in the transfer experiment around run 130 was caused by the installation of a lead shielding around the active collimator (c.f. sec. 3.3). This collimator was positioned close to the T-REX chamber and MINIBALL and stopped a part of the beam due to improper beam tuning. Fortunately, this was not the case in the Coulex experiment. Consequently, due to the perfectly aligned beam in the Coulex campaign, the β-decay rate was much lower compared to the transfer campaign, although the ^{72}Zn beam intensity was much higher (c.f. tab. 3.1). Note, that the mean count rate during the On-Beam window is shown and that the error bars are in most cases smaller than the marker size.

for lower γ-ray energies, it is possible that γ-rays which are in random coincidence are added by mistake which lowers the photopeak efficiency. Therefore, the addback procedure was not used in the further physics analysis to avoid systematic uncertainties.

4.3.2 MINIBALL at High Count Rates

As the calculation of transfer and Coulomb excitation cross sections is generally based on γ-ray gated events, it is essential that the MINIBALL efficiency is constant or at least known over the whole experiment. However, due to the high intensity of the long lived ^{72}Zn beam ($T_{1/2} = 46.5$ h [13]), it is possible that the γ-ray detection efficiency also depends on the total count rate respective time after the start of the experiment. The total count rate increased up to 6 kHz per MINIBALL detector with accumulating β-activity of the stopped radioactive beam. At high count rates the dead time of the γ-ray spectrometer can increase, resulting in a drop of its photopeak efficiency. Consequently, in both ^{72}Zn experiments, the MINIBALL efficiency was permanently monitored by observing the amount of the natural ^{40}K background radiation which should be constant over the experiment[9]. Fig. 4.2 a) and b) show its count rate as a function of the run number in the transfer and the Coulex experiment, respectively. Additionally, the ^{40}K rate was determined in the ^{60}Co MINIBALL efficiency run (c.f. sec. 4.3.1). The horizontal straight line fits in fig. 4.2 demonstrate that the MINIBALL efficiency did not change significantly over the whole experimental campaign, although the background caused by the β-decay of the beam increased about a factor of ten over time: As an example, the evolution of the β-decay rate is indicated in fig. 4.2 with the strong $E_\gamma = 834$ keV γ-ray line of the ^{72}Zn decay product ^{72}Ge. Moreover, the rate of the $E_\gamma = 1464$ keV ^{72}Ge γ-ray line is shown, as is is quite close to the $E_\gamma = 1461$ keV ^{40}K line. Hence, the counts of both lines are determined in a combined fit.

---

[9]The natural background line of ^{40}K is chosen as all other visible natural background lines are superimposed with a β-decay line of the beam.

4.4 Precise Determination of the MINIBALL Angles for Doppler Correction

This section deals with the Doppler correction capabilities of MINIBALL. After a short introduction in the Doppler correction formalism (c.f. sec. 4.4.1), the analysis methods to determine the MINIBALL angles, which are mandatory for applying a Doppler correction, are presented. First, the traditional method using transfer reactions of a ^{22}Ne beam is outlined in sec. 4.4.2. Finally, sec. 4.4.3 details the newly developed optimization of the MINIBALL angles using a Coulomb excitation experiment. As a last point, the obtained performance of the Doppler correction using the different methods is discussed.

4.4.1 Doppler Correction Formalism

The excited outgoing nuclei which can result from a nuclear reaction often de-excite via γ-ray emission. All transfer and Coulex reactions which are discussed in this thesis, feature γ-rays which are emitted in flight. Consequently, they are Doppler shifted in the laboratory frame. Hence, to extract excitation energies of the nuclei, the measured γ-ray energies have to be transformed in the center-of-mass frame by applying a Doppler correction:

$$E_{rest} = E_{lab} \cdot \gamma \cdot [1 - \beta \cdot \cos \alpha] = \frac{E_{lab}}{\sqrt{1 - \beta^2}} \cdot (1 - \beta \cdot \cos \alpha), \tag{4.3}$$

with E_{rest} and E_{lab} being the γ-ray energy in the center-of-mass and in the laboratory frame, respectively. $\beta = v/c$ is the velocity of the emitting nucleus relative to the speed of light c in vacuum. The angle α represents the angle between the moving nucleus and its emitted γ-ray:

$$\cos \alpha = \cos \theta_\gamma \cos \theta_p + \sin \theta_\gamma \sin \theta_p \cos(\phi_\gamma - \phi_p), \tag{4.4}$$

with $\theta_{p,\gamma}$ and $\phi_{p,\gamma}$ being the polar angle and azimuthal angle respectively of the particle and the γ-ray. Thus, to perform a Doppler correction, the directions of the particle and the γ-ray have to be measured with position sensitive detectors. Furthermore, the velocity of the nucleus has to be determined. In general, this is done with two different methods[10]: First, the velocity can be extracted directly from the deposited energy E_{dep} of the nucleus in the silicon array:

$$\beta = \sqrt{\frac{2E_{dep}}{m_0 c^2}}, \tag{4.5}$$

with $m_0 c^2$ being the rest mass of the nucleus. This method requires a precise energy calibration of the particle detectors (c.f. sec. 4.2). Second, β can be calculated from the direction of the detected nucleus in T-REX or C-REX using the reaction kinematics. Hence, a precise knowledge of the position of the particle detectors is needed not only for the calculation of the angle α, but also to determine the velocity β. This is realized with a high segmentation and an exact mechanical mounting of the particle detectors (c.f. sec. 3.3 and sec. 3.4). However, in contrast to the particle detectors, the position of the MINIBALL crystals cannot be extracted with high precision from the mechanical mounting frame[11]. Moreover, the exact position of the HPGe crystals in the cryostats is unknown. For this work, the θ_{MB} and ϕ_{MB} angles of each MINIBALL channel were determined exploiting a physical reaction. In general, this is a two step process: First, start values of the MINIBALL angles are extracted from ^{22}Ne transfer reactions (c.f. sec. 4.4.2). Second, these values are improved using the data of a Coulomb excitation experiment (c.f. sec. 4.4.3). Finally, the performance of the Doppler correction is discussed in sec. 4.4.4.

---

[10]Both methods assume that the nuclei de-excites directly after the target.

[11]During the construction of the MINIBALL frame the focus was not set on precision but on flexibility allowing to position the MINIBALL crystals in many configurations.

4.4.2   Traditional Determination with ^{22}Ne Transfer Reactions

The standard procedure to determine the MINIBALL angles at REX-ISOLDE is based on transfer reactions of a high intensity, stable ^{22}Ne beam which impinges on a thin deuterated PE target. The transfer channels with the highest cross sections and their most dominant γ-rays are the one-neutron transfer reaction d(^{22}Ne, p)^{23}Ne with a 1017 keV γ-ray and the one-proton transfer reaction d(^{22}Ne, n)^{23}Na with a 440 keV γ-ray. In the following the polar angle θ_{MB} and the azimuthal angle ϕ_{MB} of all MINIBALL cores and segments are determined successively with the help of these reactions.

Determination of θ_{MB}

Looking at the reaction kinematics of one-proton or one-neutron transfer reactions, the outgoing ejectile ^{23}Na or ^{22}Ne has only a small scattering angle of less than 5° (c.f. also fig. 3.8). Hence, its direction can be approximated with the beam direction and the Doppler correction formulas eq. (4.3) and eq. (4.4) simplify to

$$\theta_p \approx 0 \quad \Rightarrow \quad \alpha \approx \theta_\gamma = \theta_{MB} \quad \Rightarrow \quad E_{rest} = \frac{E_{lab}}{\sqrt{1-\beta^2}} \cdot (1 - \beta \cos \theta_{MB}). \tag{4.6}$$

The velocity β of the ejectile can also be approximated to be constant and is calculated using the reaction kinematics. According to eq. (4.6) θ_{MB} of each MINIBALL core and each segment is calculated from the known γ-ray energy E_{rest} of the reaction and its corresponding Doppler shifted line E_{lab}. As the detected intensity of the 440 keV γ-ray line of the d(^{22}Ne, n)^{23}Na is stronger than the 1017 keV γ-ray line from the d(^{22}Ne, p)^{23}Ne, the 440 keV line in the MINIBALL spectra[12] was used for the determination of θ_{MB}.

Determination of ϕ_{MB}

In a second step, the azimuthal angles ϕ_{MB} of MINIBALL are determined with the help of the one-neutron transfer reaction to ^{23}Ne. To keep the ϕ-dependence in the Doppler correction formulas eq. (4.3) and eq. (4.4), the direction of the outgoing ^{23}Ne must not be approximated along the beam axis. Instead, the ^{23}Ne direction is kinematically reconstructed from the transfer proton. The transfer proton is detected and identified in the ΔE-E telescope of the FBarrel (T-REX setup) or the FCD (C-REX setup). As an example, a typical identification plot of one FCD ring is shown in fig. 4.3 a). Its lower branch corresponds to the transfer protons, whereas the upper branch belongs to the elastically scattered deuterons[13]. After the reconstruction of the 4-momentum vector of ^{23}Ne and knowing the polar angle θ_{MB} of every MINIBALL channel, all quantities in the Doppler correction formulas eq. (4.3) and eq. (4.4) are determined except the azimuthal angle ϕ_{MB} of MINIBALL. It can be extracted using the strongest γ-ray line of the one-neutron transfer reaction (1017 keV): For each MINIBALL detector the Doppler correction of the 1017 keV γ-ray line can be calculated for various MINIBALL ϕ_{MB} angles ranging between 0 and 360°. The smallest line width and hence the best Doppler correction is obtained at the true MINIBALL ϕ_{MB} angle. The figure of merit FOM to quantify the quality of the Doppler correction is defined using the standard deviation σ of the Gaussian fit of the Doppler corrected peak and the deviation of the mean value E_{mean} of the Gaussian to the true γ-ray energy of $E_{rest} = 1017$ keV:

$$FOM = \sqrt{\sigma^2 + (E_{mean} - E_{rest})^2}. \tag{4.7}$$

Subsequently, the figure of merit is calculated for all possible MINIBALL ϕ_{MB} angles (c.f. fig. 4.3 b)). The minimum of this distribution defines the actual MINIBALL ϕ_{MB} angle. The width of the 1017 keV photopeak in the Doppler corrected sum spectrum of the whole MINIBALL array is about $\Delta E(1017 \text{keV}) \approx 10$ keV (FWHM[14]).

---

[12]Not Doppler corrected MINIBALL spectra of each core and segment without any further cuts have been used for the fit of the Doppler shifted line E_{lab}, to keep the maximum of statistics.

[13]Details about the light particle identification can be found in sec. 5.1.1.
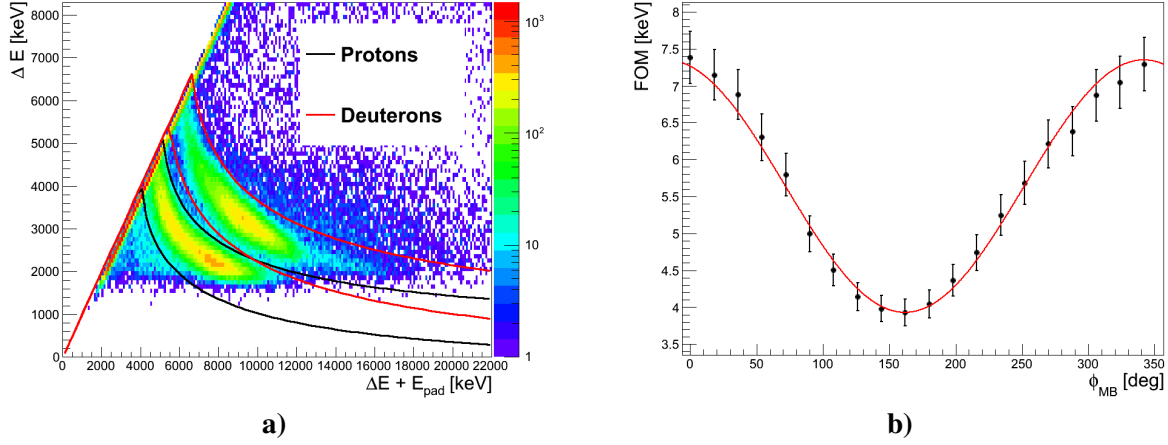
[14]FWHM: Full Width at Half Maximum

Fig. 4.3: a) A particle identification plot of a FCD ring for a ^{22}Ne beam impinging on a 0.105 mg/cm^2 thin deuterated PE target. The upper red lines indicate the elastically scattered deuterons, while the lower black lines show the transfer protons resulting from the one-neutron transfer reaction d(^{22}Ne, p)^{23}Ne. **b)** The figure of merit *FOM* (c.f. eq. (4.7)) which controls the quality of the Doppler correction as a function of all possible ϕ_{MB} angles of a MINIBALL crystal. The true ϕ_{MB} angles corresponds to the minimum of the distribution. The minimum is determined by fitting a sinus curve to account for the periodic behavior: $a_0 + a_1 \sin(\phi_{MB} + a_2)$, with a_0, a_1 and a_2 being the fit parameters.
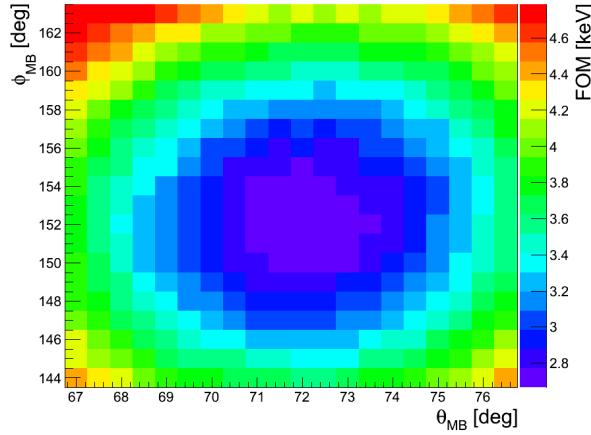

Fig. 4.4: The figure of merit *FOM* (c.f. eq. 4.7) of the Doppler correction of one MINIBALL segment as a function of the MINIBALL angles θ_{MB} and ϕ_{MB}. Its minimum corresponds to the actual position of the MINIBALL segment. In this case the $2^+_1 \rightarrow 0^+_1$ γ-ray transition of ^{72}Zn has been used.

4.4.3 Optimization of the Angles with a Coulomb Excitation Reaction

In the previous sec. 4.4.2, the MINIBALL angles have been determined from ^{22}Ne transfer reactions. However, the disadvantage of one-proton or one-neutron transfer reactions is, that the ejectile nuclei are strongly forward peaked. Thus, the ϕ-dependence is quite weak. Subsequently, it is difficult to extract high precision MINIBALL ϕ-angles. In Coulex reactions, the outgoing nuclei can feature large scattering angles and the Doppler correction is therefore much more sensitive to ϕ. Thus, the Coulomb excitation of a high intense ^{72}Zn beam with a thin ^{109}Ag target is used to finalize the MINIBALL angles. The analysis is based on the 653 keV γ-ray transition of ^{72}Zn from the first excited 2^+ state to the ground state. The quality of the Doppler correction of this transition is monitored using the figure of merit *FOM* from eq. (4.7) while varying the MINIBALL θ_{MB} and ϕ_{MB} angle of each segment around the ^{22}Ne values simultaneously. As an example, the *FOM* as a function of θ_{MB} and ϕ_{MB} for one MINIBALL segment is shown in fig. 4.4. The best MINIBALL angles correspond again

a)

^{22}Ne MINIBALL start angles

Transition	E_γ [keV]	^{72}Zn in FCD	^{109}Ag in FCD
^{72}Zn($2_1^+ \to$ g.s.)	653	10.5	11.7
^{109}Ag($3/2^- \to$ g.s.)	311	4.9	4.6
^{109}Ag($5/2^- \to$ g.s.)	415	5.5	4.7

^{72}Zn MINIBALL, β from FCD θ

Transition	E_γ [keV]	^{72}Zn in FCD	^{109}Ag in FCD
^{72}Zn($2_1^+ \to$ g.s.)	653	6.7	8.0
^{109}Ag($3/2^- \to$ g.s.)	311	3.6	3.5
^{109}Ag($5/2^- \to$ g.s.)	415	4.6	4.2

^{72}Zn MINIBALL angles, β from FCD energy

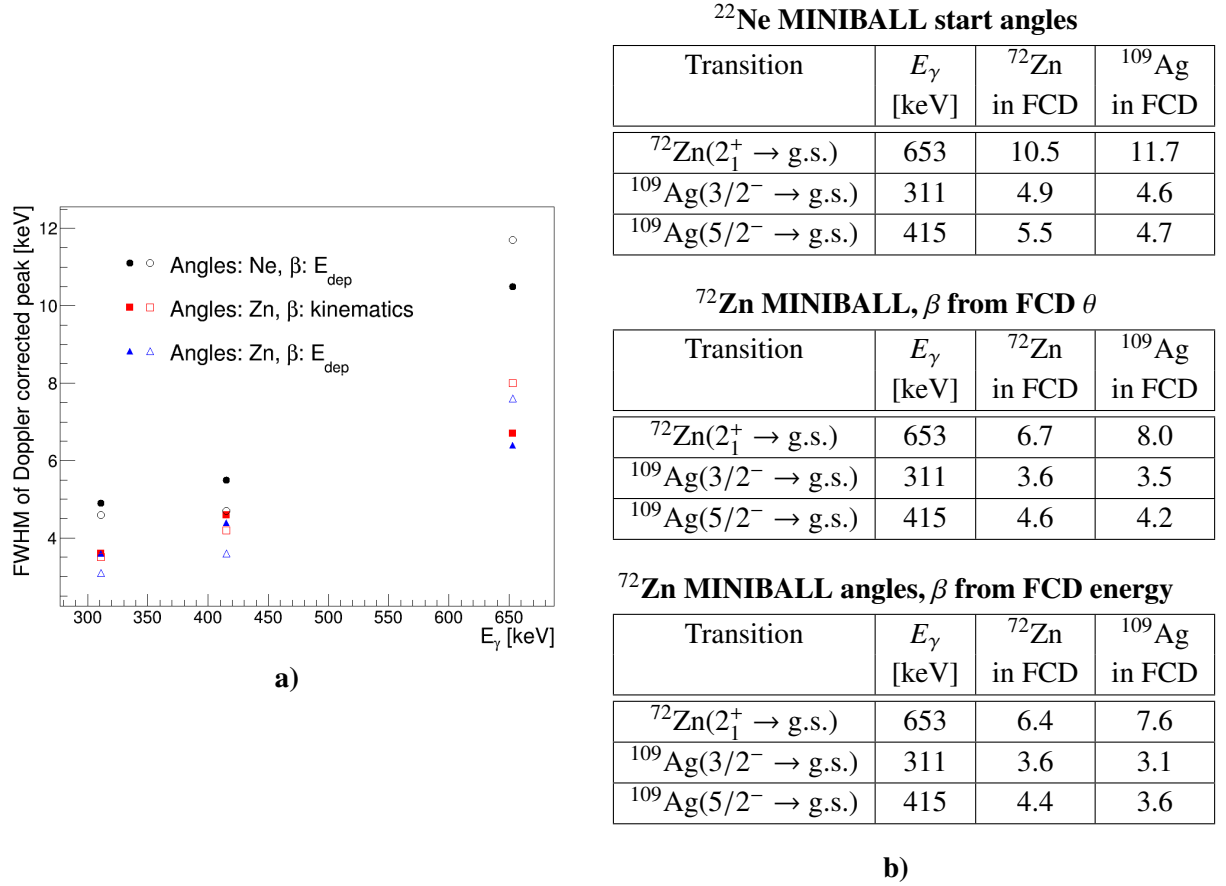| Transition	E_γ [keV]	^{72}Zn in FCD	^{109}Ag in FCD
^{72}Zn($2_1^+ \to$ g.s.)	653	6.4	7.6
^{109}Ag($3/2^- \to$ g.s.)	311	3.6	3.1
^{109}Ag($5/2^- \to$ g.s.)	415	4.4	3.6

b)

Fig. 4.5: The performance of the Doppler correction using different methods for the determination of the MINI-BALL angles and the velocity β of the emitting nucleus. It is investigated with the three strongest Doppler corrected γ-ray lines of the Coulomb excitation experiment with a ^{72}Zn beam and a ^{109}Ag target. The filled symbols in **a)** show the quality of the Doppler correction if the ^{72}Zn is detected in the FCD of C-REX and open symbols correspond to the detection of the ^{109}Ag in the FCD. The obtained line widths (FWHM) in keV are also summarized in table **b)**. For the first time, a significant improvement of the Doppler correction is achieved by tuning the ^{22}Ne MINIBALL angles with a Coulex reaction. A further (smaller) enhancement of the performance is gained by measuring the velocity β of the nucleus directly using the energy deposition of the nucleus in the (well calibrated) silicon detector instead of calculating the velocity from the reaction kinematics using solely the position information of the particle detector. The direct energy measurement has the advantage that the reaction position in the target as well as the exact beam energy is taken into account. Apart from that, the Doppler correction features a better performance if the nucleus which emits the γ-ray is detected, as no kinematic reconstruction of the velocity of the excited particle is required.

to the minimum of the figure of merit. As a result, with these optimized MINIBALL angles, the performance of the Doppler correction improves significantly (c.f. sec. 4.4.4). However, note that tuning the MINIBALL angles with a Coulomb excitation experiment is only possible if the statistics is high enough, i.e. high intensity beams are required as the γ-ray peak must be visible at reasonable statistics in each MINIBALL segment.

4.4.4 Performance of the Doppler Correction

This section presents the performance of the Doppler correction. Fig. 4.5 compares the obtained line widths of the three strongest Doppler corrected γ-ray lines of the Coulomb excitation experiment (c.f. chap. 6) using two steps of position calibration for the MINIBALL detectors and using different methods to calculate the velocity β of the excited nuclei. After all steps, the obtained line width at a
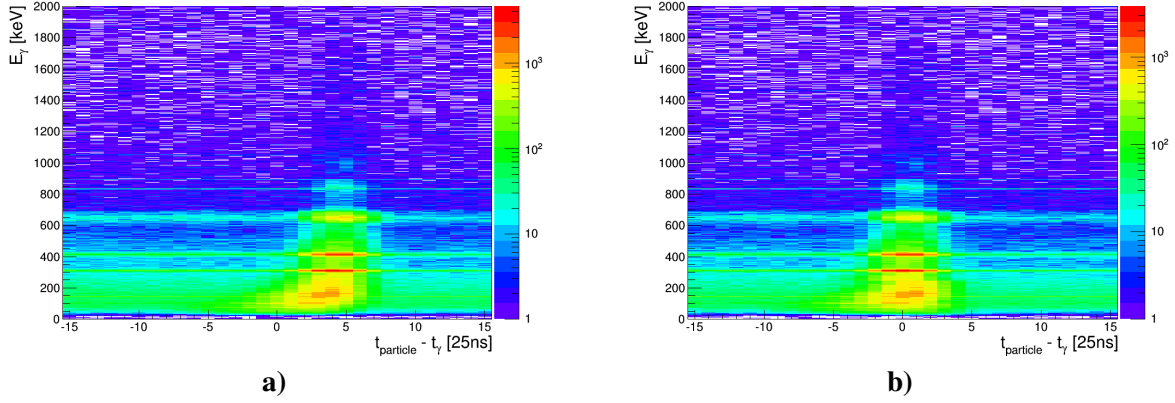
Fig. 4.6: a) The γ-ray energy vs. time difference between particles and γ-rays for the Top trigger group of the ^{72}Zn Coulex experiment in 2012. A walk effect due to the leading-edge discriminators of MINIBALL is visible for low γ-ray energies. The vertical bent line corresponds to real particle-γ-ray coincidences. **b)** The same spectrum, but corrected for the offset and the walk effect.

γ-ray energy of $E_\gamma = 653\,$keV is only $\Delta E = 6.4\,$keV (FWHM). In general, also for the other observed transition the obtained resolution in the Doppler corrected γ-ray spectra of the Coulex experiment is about 1%. This unique performance is achieved dominantly by inventing a two step calibration of the MINIBALL detector angles and by using particle velocities determined from their full energy deposition in the silicon detectors. This excellent Doppler correction allows to discriminate close lying γ-ray transitions, such as the $4_1^+ \rightarrow 2_1^+$ ($E_\gamma = 847\,$keV) and the $0_2^+ \rightarrow 2_1^+$ ($E_\gamma = 858\,$keV) transition in ^{72}Zn which have been discussed in this thesis (c.f. chap. 6).

4.5   Timing Properties

In both, the transfer and the Coulex experiment, coincidence conditions between γ-rays and particles play a crucial role to select a specific reaction channel and to reduce background. Each γ-ray and particle event is assigned a timestamp which allows to gate on the time difference between them. For both, particle and γ-ray detectors, a 40 MHz clock is used which corresponds to a timing resolution of $\sigma_T \approx 25/\sqrt{12} = 7.2\,$ns [81]. Fig. 4.6 a) shows the distribution of the events as a function of the time difference between particle and γ-ray and of the γ-ray energy. Clearly a coincidence pattern is visible above a rather flat background in time. The coincidence pattern is bent in the low γ-ray energy region which is due to the leading-edge discriminators of the MINIBALL electronics: The trigger point in time strongly depends on the signal height. Hence, low γ-ray energies feature slower time signals compared to high γ-ray energy signals. To correct this so called "walk effect", this bending was fitted with an empirical exponential function

$$walk(E_\gamma) = a_0 + a_1 \cdot \exp\left(\frac{a_2}{\sqrt{E_\gamma}}\right), \tag{4.8}$$

with a_0, a_1 and a_2 being the fit parameters. The offset a_0 depends on the trigger group and accounts for the different delays of each trigger group in the analog electronics of the particle detectors. After applying offset and walk correction, fig. 4.6 b) was obtained showing a nearly constant time difference between particles and γ-rays which is not dependent on the γ-ray energy anymore. The achieved time resolution of the coincidence peak is about $\Delta t = 125\,$ns (FWHM). It is dominated by the drifting charge carriers in the large volume MINIBALL germanium detectors.

<div style="text-align: right; font-size: 3em; font-weight: bold;">5</div>

Transfer Experiments with a ^{72}Zn Beam

The analyses and the results of the one- (1n) and two-neutron (2n) transfer experiments, which have been performed in the course of this thesis, are presented in this chapter. The experiments were conducted in 2011 at REX-ISOLDE with a radioactive ^{72}Zn beam impinging on a radioactive tritium target and on a deuterated polyethylene target, respectively. The light transfer products were detected with the T-REX silicon detector array which has been introduced in sec. 3.3. In sec. 5.1, the data analysis procedures of the transfer experiments are detailed. Subsequently, the results of the elastic reaction channels (c.f. sec. 5.2), of the 1n transfer channels t(^{72}Zn, d)^{73}Zn and d(^{72}Zn, p)^{73}Zn (c.f. sec. 5.3) and of the 2n transfer reaction t(^{72}Zn, p)^{74}Zn (c.f. sec. 5.4) are presented.

5.1   Data Analysis

This section briefly describes the main analysis steps, which are common to all reaction channels of the ^{72}Zn transfer experiments. It includes the identification of the reaction mechanism (c.f. sec. 5.1.1), the calculation of reaction cross sections (c.f. sec. 5.1.2) as well as a discussion of the beam purity (c.f. sec. 5.1.3).

5.1.1   Identification of the Reaction Channel

The identification of the reaction mechanism is of particular importance for the analysis of transfer experiments, since various reaction channels have to be disentangled. In the case of the ^{72}Zn 2n transfer experiment using the tritium target, the following reactions with the tritium can occur: The elastic channel t(^{72}Zn, t)^{72}Zn, the 1n transfer t(^{72}Zn, d)^{73}Zn and the 2n transfer t(^{72}Zn, p)^{74}Zn. Thus, the T-REX detectors have to be able to distinguish with high precision between tritons, deuterons and protons. This is especially important for the detectors covering the forward direction in the laboratory frame. Note, that in backward direction all particles are considered to be light transfer products, as, due to the inverse kinematics of the ^{72}Zn transfer experiment, the elastically scattered particles are only detected in forward direction (c.f. fig. 3.8). Despite the reaction kinematics, an explicit particle identification in backward direction is not possible, since the particle energies are too low to apply the ΔE-E technique.

Particle Identification with ΔE-E Telescopes
T-REX is equipped with silicon ΔE-E telescopes which allow a particle identification due to the characteristic energy loss of each particle species. As an example, fig. 5.1 a) shows the energy correlation of the deposited energy in the $140 \mu m$ thick ΔE-detector and the total deposited energy in the silicon telescope for the case of the ^{72}Zn beam impinging on the tritium target. Due to the charge and mass dependence of the energy loss, different particles are located in different regions. The black lines show the used proton identification cut. The protons originate from 2n transfer reactions or correspond to elastically scattered protons which are also contained in the target. The deuterons (red identification cut) result from the 1n transfer reaction t(^{72}Zn, d)^{73}Zn. Furthermore, the events confined by the green lines show elastically scattered tritons from the target. Apart from that, at higher energies α-particles are visible which are e.g. produced by (t,α) reactions (blue region). Particles which are fully stopped in the ΔE detector or geometrically miss the second layer of silicon appear on the diagonal in fig.
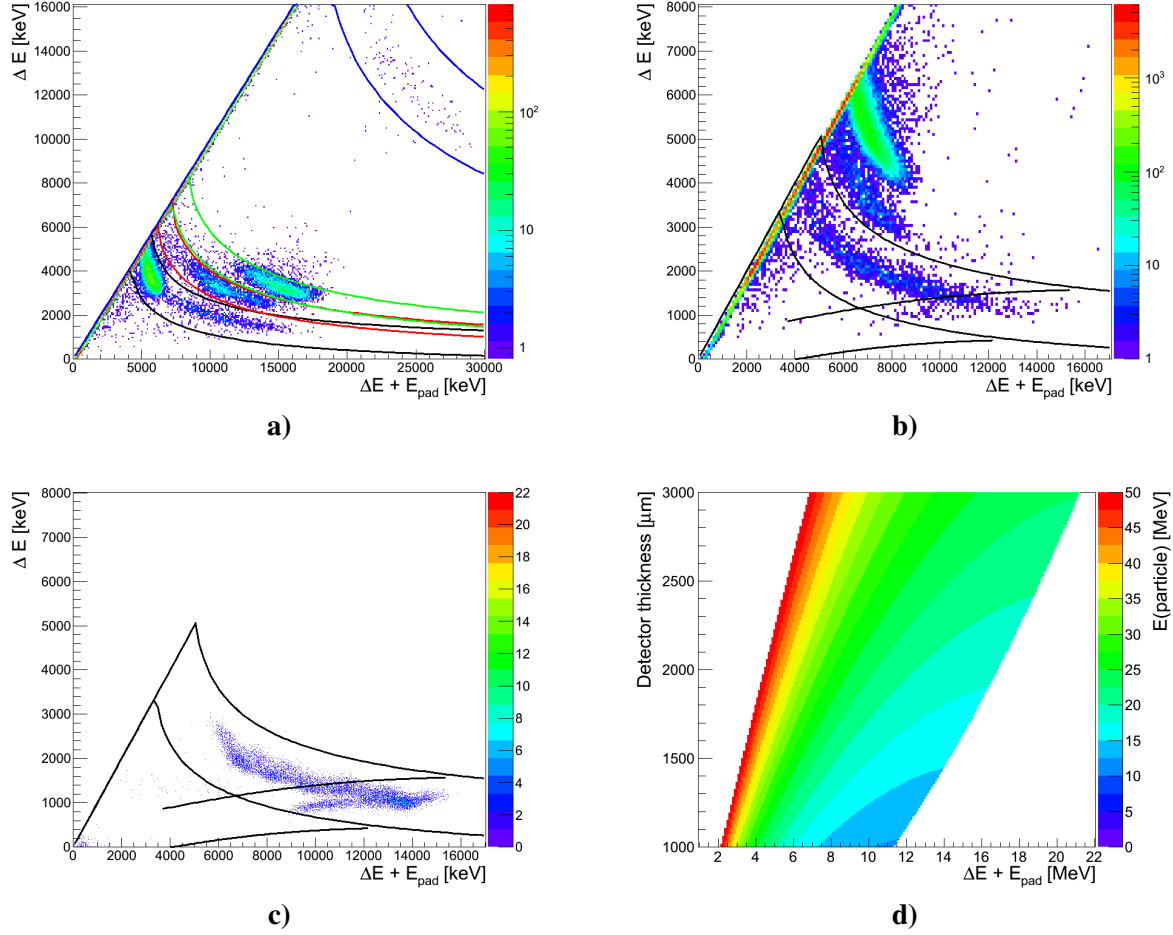
Fig. 5.1: a) The ΔE-E spectrum of strip eight ($\theta_{lab} \approx 40°$) of one Forward Barrel (FBarrel) silicon telescope measured with a ^{72}Zn ISOLDE beam which was impinging on the tritium target. Due to the characteristic energy loss of each particle type, a particle identification is possible. The protons between the black identification cuts originate from the 2n transfer reaction to ^{74}Zn or represents elastically scattered protons from the target ($\Delta E + E_{rest} \approx 5$ MeV). The deuterons (red cuts) results from the t(^{72}Zn, d)^{73}Zn reaction, while the elastically scattered tritons are located between the green curves. Furthermore, α-particles are identified which originate from (t,α) reactions (blue curves). **b)** The ΔE-E plot of FBarrel strip two ($\theta_{lab} \approx 80°$). Due to the reaction kinematics some of the transfer protons punch through the ΔE-E telescope indicated by the backbending of the correlation band at small $\Delta E < 1.2$ MeV signals. **c)** The transfer proton ΔE-E spectrum of strip two of the FBarrel detector resulting from a Geant4 simulation of the t(^{72}Zn, p)^{74}Zn reaction for comparison. **d)** Calculated proton energy as a function of the effective detector thickness and the total deposited energy in the silicon telescope from which the full energy of punch through protons was evaluated.

5.1 a). To conclude, the T-REX silicon ΔE-E telescopes allow to some extent to identify the reaction channel. However, a prerequisite of this method is that the particles punch through the ΔE-detector and are subsequently stopped in the 1 mm thick E_{rest}-detectors.

However, not all protons are stopped in the E_{rest}-detector. According to the reaction kinematics of the 2n transfer reaction from ^{72}Zn to ^{74}Zn, it is possible that the transfer protons have enough energy to punch through the E_{rest}-detector as well. This is seen in the experimental data (c.f. fig. 5.1 b)) as well as in a detailed Geant4 simulation (c.f. fig. 5.1 c)) of the experiment. These protons are located at the reversing branch in the ΔE-E plot. Thus, the total deposited energy in the silicon telescope does not correspond to the energy of the protons. Their energy can be reconstructed using the two energy depositions in the ΔE-E telescope and the effective thickness of the detector[1]: Fig. 5.1 d) relates

---

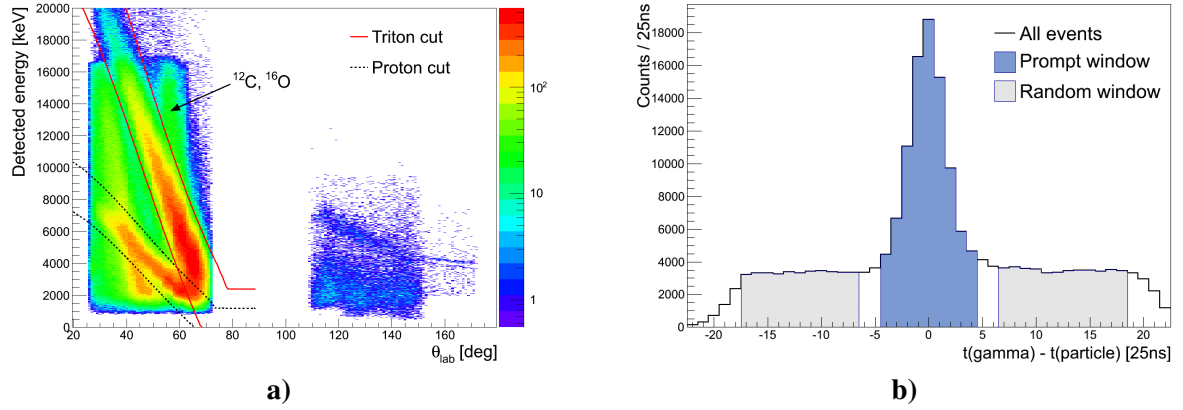[1]The effective thickness is the length of the traveled path of the particle through the detector.

Fig. 5.2: a) The detected particle energy in the T-REX ΔE-E telescopes as a function of the scattering angle θ_{lab} in the laboratory frame for ^{72}Zn beam ($E_{beam} = 2.7$MeV/u) impinging on the tritium target. In forward direction ($\theta_{lab} \in [26°, 72°]$) the data of the FBarrel is shown. In backward direction between $\theta_{lab} = 110°$ and $\theta_{lab} = 152°$ the BBarrel data is presented, while the data points beyond $\theta_{lab} = 152°$ belong to the BCD. Note, that the intensities of the different detector types cannot be compared with each other, as not all quadrants of all detectors had been fully operational during the experiment. Additionally, in forward direction, the identification cuts for the elastics protons and tritons which are obtained from the reaction kinematics are visualized. They are used if a particle identification with the ΔE-E telescope is not possible which is the case if the particles are stopped in the ΔE-detector. In backward direction all particles are assigned to transfer protons (for details c.f. sec. 5.4.1). **b)** Another possibility to select a specific reaction channel is to look at coincidences between particles and characteristic γ-rays of the reaction. The plots shows the distribution of the time difference between a particle and a γ-ray being detected in the same event. The peaks corresponds to the coincidence events between particles and γ-rays which originate from the same reaction. The background corresponds to random coincidences. The colored areas define the prompt and random windows which are used for the background subtraction in the analysis.

the energy deposition and the effective detector thickness unambiguously to the original proton energy.

Particle Identification using the Reaction Kinematics

For the case that the particles already deposit their total energy in the ΔE-detector, a different identification method than the ΔE-E telescope is required as these stopped particles are all located on the diagonal line in the ΔE-E plot (c.f. fig. 5.1 a)). The only remaining method to identify the stopped particles is to look at their characteristic reaction kinematics: Fig. 5.2 a) shows the total detected particle energy as a function of its scattering angle θ_{lab} in the laboratory frame. The displayed identification cuts for the elastically scattered protons and tritons from the target are calculated using 4-momentum conservation. In the calculation, the energy resolution of the detectors and the energy loss in the target as well as in the mylar protection foil are considered. As a result, elastic protons and tritons can be discriminated over a wide range of scattering angles.

Energy Reconstruction and Calculation of Excitation Energies

After the particle identification, the kinetic energy of the ejectile at the reaction vertex has to be reconstructed. The reconstructed energy is obtained from the detected energy in the T-REX detectors which is corrected for the energy loss in the target and for the energy loss in the mylar protection foil which is installed in front of the FBarrel detectors. Subsequently, the energy of the light reaction product (transfer proton, elastically scattered triton, ...) at the reaction position allows to reconstruct the Lorentz 4-vector of the outgoing heavy beam-like nucleus, although it is not detected in T-REX due to its small scattering angle (c.f. fig. 3.8). To get the best possible reconstruction, the in 2005 measured ISOLTRAP masses for ^{72,73,74}Zn are used in the 4-momentum calculation [95, 96].

From the reconstructed ejectile energy, the excitation energy of the zinc nucleus can be extracted from

the measured light reaction product. Furthermore, knowing the velocity and the direction of the heavy nucleus results in a more precise Doppler-correction compared to the Doppler correction which is obtained with the assumption that the outgoing nucleus coincides with the beam axis (c.f. sec. 4.4).

Particle-γ-ray Coincidences

Besides the capability of T-REX, another method to identify unambiguously the reaction channel is to search for a characteristic γ-ray in MINIBALL of the reaction which is in coincidence to the identified particle. Fig. 5.2 b) shows the time difference between all detected particles in T-REX and all detected γ-rays in MINIBALL. The peak around zero corresponds to the real physics coincidences, while the flat background left and right of the peak originates from random coincidences between particles and γ-rays of different reactions[2]. These random coincidences are used to subtract the random background in the prompt peak area of the real coincidences. The energy spectrum of these coincident γ-rays has also been used to define the purity of the different methods of particle identification. A detailed description of the background subtraction in particle-γ-ray events can be found in sec. 6.1.4.

5.1.2 Determination of Differential Cross Sections

In transfer experiments the differential cross sections contain important information about the transferred angular momentum i.e. the orbitals in which the neutron(s) is/are transferred (c.f. sec. 2.2). The main steps in the determination of differential cross sections $d\sigma/d\Omega$ from experimental data are summarized in the following: The number of counts N which have been detected in a detector segment with a sufficiently small solid angle $\Delta\Omega$ is given by

$$N = \mathcal{L} \cdot \frac{d\sigma}{d\Omega} \cdot \Delta\Omega \cdot \epsilon_{T-REX}, \qquad (5.1)$$

with $\mathcal{L}$ being the time-integrated luminosity of the experiment and ϵ_{T-REX} the particle detection efficiency of T-REX. Hence, the differential cross section reads

$$\frac{d\sigma}{d\Omega} = \frac{N}{\mathcal{L} \cdot \Delta\Omega \cdot \epsilon_{T-REX}}. \qquad (5.2)$$

The integrated luminosity $\mathcal{L}$ is determined with the elastic scattering data (c.f. sec. 5.2.2).

Solid Angle

To obtain the differential cross section as a function of the scattering angle, the detector is divided into small solid angle segments $\Delta\Omega$ according to its segmentation: Each of the 16 resistive Barrel strips is divided into 16 quadratic pixels and each CD ring is considered as a separate solid angle segment. In case of low statistics the Barrel pixels and CD rings with similar scattering angles are grouped together. Furthermore, it has to be considered that the outermost CD rings are partly covered by the Barrel detectors. After the division of the data into solid angle bins, their solid angles and their scattering angles are transformed from the laboratory frame to the center-of-mass frame[3]. This transformation has the advantage that the experimental cross section can be compared directly to theoretical calculations.

Particle Detection Efficiency

Another important quantity for the determination of experimental cross sections is the efficiency ϵ_{T-REX} of the T-REX detectors. It includes the efficiency of the identification cuts (c.f. sec. 5.1.1), the energy thresholds of the detectors, broken detector channels and the influence of the extend beam profile in x and y-direction. Additionally, the efficiency considers the case that a particle can geometrically miss the E_{rest}-detector, although it has been detected in the ΔE-detector of the silicon telescope[4].

---

[2]The main background originates from β-decay γ-rays of the radioactive ^{72}Zn beam.

[3]The formulas for the transformation can be found in [97].

[4]This is likely at the edges of the silicon telescope as both detectors have the same size, but the E_{rest}-detector is installed 2.4 mm behind the ΔE-detector [86].

All these effects can be quantified using a realistic Geant4 simulation which includes the complete reaction kinematics as well as the exact geometrical setup of all T-REX detectors. These simulated events are subsequently analyzed with the same analysis code as the experimental data to ensure that the same detection thresholds and identification cuts are applied to both data sets. If an isotropic angular distribution in the center-of-mass frame is used in the simulation and assuming a 100% efficient detector setup, the predicted number of counts N_{pred} in a solid angle $\Delta\Omega_{CM}$ is given by

$$N_{pred} = N_{sim} \cdot 4 \cdot \frac{\Delta\Omega_{CM}}{4\pi}. \tag{5.3}$$

N_{sim} is the number of simulated events and $\Delta\Omega_{CM}/(4\pi)$ the fraction of the solid angle of the detector segment in the center-of-mass-frame from the total solid angle 4π. The factor 4 results from the four symmetric quadrants of T-REX, since only one quadrant is simulated to save time. Hence, the detection efficiency reads

$$\epsilon_{T-REX} = \frac{N_{det}}{N_{pred}}, \tag{5.4}$$

with N_{det} being the detected events (of all simulated events) in the solid angle $\Delta\Omega$ which pass all analysis steps. However, the Geant4 simulation is not able to reproduce all aspects of the experiment, since not all quantities (e.g. beam profile, energy resolution of the detectors, exact detector thicknesses, ...) are known with high precision. Hence, an additional systematic error $\Delta\epsilon_{T-REX}/\epsilon_{T-REX} \approx 5\%$ of the particle detection efficiency has been included.

5.1.3 Beam Purity

In the determination of the differential cross section, the luminosity $\mathcal{L}$ plays a crucial role (c.f. eq. 5.2). The luminosity itself depends strongly on the beam intensity, the local target thickness, the beam position and the local target enrichment with tritium. As these parameters are not known with high precision, the luminosity is measured using the elastic scattering data. However, the elastic scattered tritons originate not only from reactions with the ^{72}Zn beam, but also from isobaric beam contaminants which typically cannot be avoided completely at REX-ISOLDE despite its incredible selectivity. Contrary, the contaminants do not contribute to the 1n and 2n transfer cross section of ^{72}Zn. Hence, a dedicated analysis of the beam composition is essential.

In this experiment, the beam content was monitored with an ionization chamber (c.f. sec. 3.3). Fig. 5.3 a) shows the silicon signal vs. the gas signal of the ionization chamber of the $A/Q = 3.6$ ^{72}Zn^{20+} beam. Its analysis reveals that the beam cocktail[5] consists of ^{72}Zn, the isobaric contaminant ^{72}Ga which has been surface ionized in the hot cavities of the transfer line and of the laser ion source, as well as the gases ^{18}O^{5+} and ^{36}Ar^{10+} originating from the buffer gas of the charge-breeding system REXTRAP and REXEBIS. Due to the similar atomic number Z and mass number A, it is challenging to discriminate between ^{72}Zn and ^{72}Ga. Hence, to obtain reliable results for the number of counts in the ^{72}Zn and in the ^{72}Ga peak, the deviation of the silicon signal from the expected signal of ^{72}Zn has been histogrammed (c.f. fig. 5.3 b)). Note, that only the events close to the ^{72}Zn and ^{72}Ga peaks, i.e. events featuring a gas signal between 220 a.u. and 520 a.u. are used. Subsequently, the obtained 1D spectrum is fitted using a Gaussian convoluted with an exponential decay for the peaks as well as for the background model. The background corresponds to pile-up events which occur due to the high beam intensity of about $I \approx 5 \cdot 10^6$ pps (c.f. sec. 5.2.2). The results of the fit as well as the contribution of the gaseous contaminants ^{18}O and ^{36}Ar are summarized in tab. 5.1.

---

[5]A detailed discussion of the beam content can be found in appendix D.1.

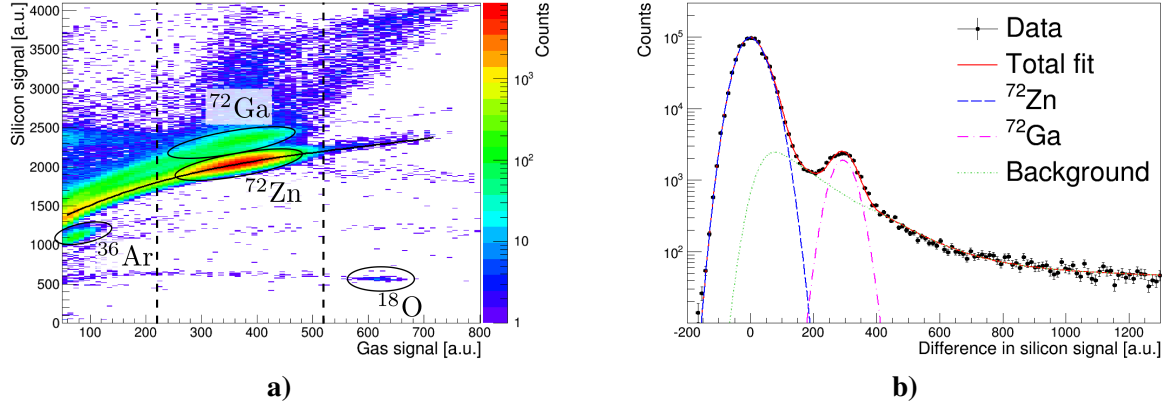a)   b)

Fig. 5.3: a) The ionization chamber spectrum of the transfer experiments. Four beam components are identified: the beam ^{72}Zn, the surface ionized isobaric contaminant ^{72}Ga and the gases ^{36}Ar and ^{18}O originating from the charge-breeding system REXTRAP and REXEBIS. For details about the ionization chamber see sec. 3.3. **b)** The difference of the silicon signal and the black line in fig. a) is shown for events featuring a gas signal between 220 a.u. and 520 a.u. The fit allows to determine the count rates in the ^{72}Zn and ^{72}Ga peaks as well as of the background.

I_{Ga}/I_{Zn} [%]	I_{Ar}/I_{Zn} [%]	I_{O}/I_{Zn} [%]	I_{Zn}/I_{tot} [%]	I_{Ga}/I_{tot} [%]	I_{Ar}/I_{tot} [%]	I_{O}/I_{tot} [%]
1.71(2)	0.012(1)	0.537(8)	97.8(2)	1.68(2)	0.526(8)	0.012(1)

Tab. 5.1: The beam composition of the ^{72}Zn transfer experiments. The beam contaminant ^{72}Ga is produced in the primary ISOLDE target, while the ^{36}Ar and the ^{18}O contaminants originate from the buffer gas of the charge-breeding system of the REX-ISOLDE accelerator.

5.2 Elastic Channels

First, the analysis of the elastic data is presented, as it gives important input for the transfer cross sections: The elastic data mainly provides the luminosity of the experiment. Additionally, optical model parameters can be determined which can be used for the theoretical calculation of transfer cross sections in the modeling of the in- and out-going channels as well as of the core-core interaction (c.f. sec. 2.2.1). The focus in this section is set on the elastically scattered tritons, as they cover a larger scattering angle range which allows for a more precise determination of the luminosity and the optical model parameters. For the sake of completeness, the elastically scattered protons, which feature a limited scattering range, are discussed in appendix C.1.

5.2.1 Kinematics and Excitation Energies

The kinematics of the identified, elastically scattered tritons from the tritium target is shown in fig. 5.4 a). To obtain a clean data set, the identification of the tritons was done with the ΔE-E telescope of the FBarrel detector as described in sec. 5.1.1. The selected events nicely follow the kinematic expectation.

After the particle identification, excitation energies of the elastic tritons were calculated using the approach described in sec. 5.1.1. Its distribution is visualized in fig. 5.4 b). As expected for elastic scattering data, the mean value coincidences with zero. A resolution of $\Delta E = (653 \pm 1)$ keV (FWHM) ha been achieved which is dominated by the energy straggling in the target and by the position resolution of the T-REX array in this experiment.
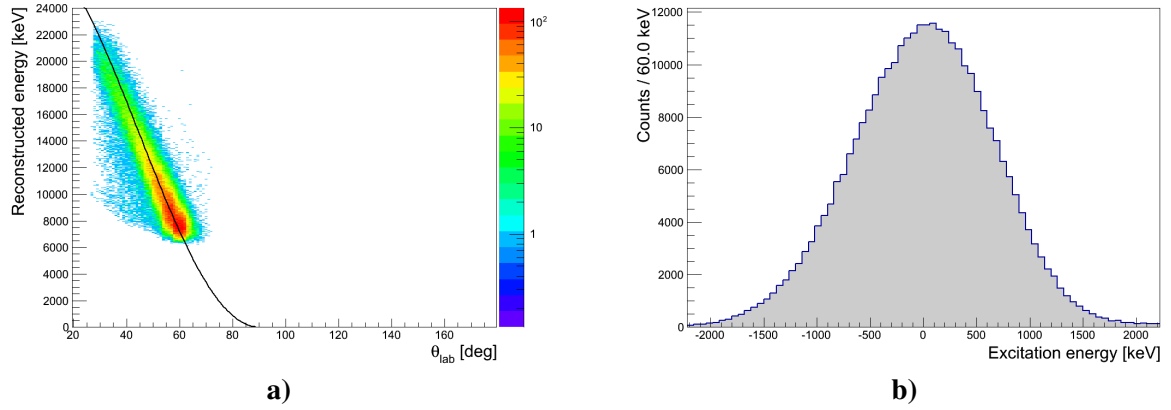
a)

b)

Fig. 5.4: a) Reconstructed energy vs. θ_{lab} spectrum of all tritons which were identified with the $\Delta E\text{-}E$ telescope of the FBarrel detector. **b)** The excitation energy of the identified tritons shown in fig. a). Due to the selection of the elastic scattering channel, the excitation energy is distributed around zero.
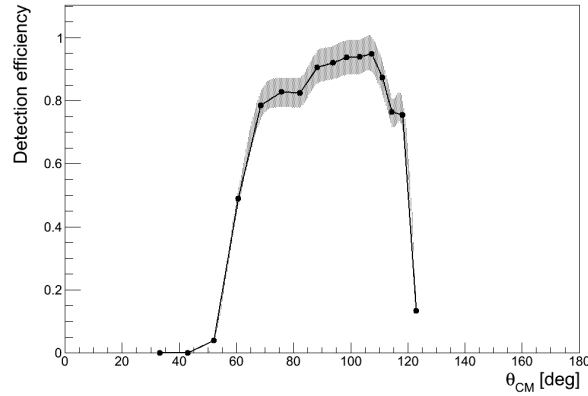

Fig. 5.5: Detection efficiency of the FBarrel detector for identified elastic tritons, determined following sec. 5.1.2. The particle identification was done with the $\Delta E\text{-}E$ telescope of the Barrel detector and not with the kinematic splines shown in fig. 5.2 a).

5.2.2 Differential Cross Sections and Luminosity Determination

The differential cross section of the elastically scattered tritons was calculated by binning the tritons, identified with the $\Delta E\text{-}E$ technique, into small scattering angle bins. According to eq. 5.2, the counts in the bins were subsequently divided by the corresponding solid angle $\Delta\Omega_{CM}$ in the center-of-mass frame and the particle detection efficiency $\epsilon_{T-REX}(\theta_{CM})$. The latter is shown in fig. 5.5. The detection efficiency drops going to small θ_{CM} angles. This is due to the fact that small θ_{CM} angles correspond to large θ_{lab} angles which feature small energies of the elastic particles. Hence, at small θ_{CM} the particles are already stopped in the ΔE-detector of the silicon telescope. Therefore, a particle identification with the $\Delta E\text{-}E$ method is not possible which reduces the efficiency. The decrease of ϵ_{T-REX} at $\theta_{CM} \approx 110°$ originates from the shape of the FBarrel in the $\theta - \phi$ plane. In the calculation of the differential cross section only the scattering angles which do not feature a large variation in their particle detection efficiency were considered. Thus, the influence of systematic errors was reduced.

Luminosity and Optical Model Parameters

The absolute scale of the cross sections, i.e. the time-integrated luminosity $\mathcal{L}$ of the experiment was fitted using SFRESCO [100] which is a MINUIT [101] based fit program on top of FRESCO [102, 103, 104]. FRESCO is a Fortran based coupled reaction channels calculation code which allows to predict elastic differential cross sections using the optical model (c.f. sec. 2.1). Fig. 5.6 a) shows
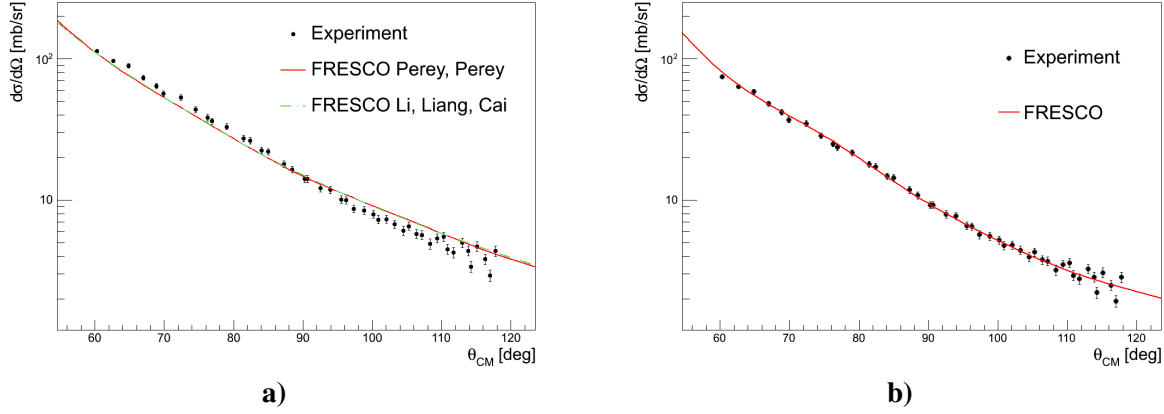
a)   b)

Fig. 5.6: Differential cross section of the elastically scattered tritons. The experimental data points are compared to two FRESCO calculations using two global optical model parameterizations [98, 99] (**a**)) and using optical model parameters which were fitted to the triton data (**b**)). The parameters are summarized in tab. 5.2 and tab. 5.3.

Parameterization	r_c [fm]	V [MeV]	r_0 [fm]	a_0 [fm]	W [MeV]	r_W [fm]	a_W [fm]
Perey, Perey	1.30	162.56	1.20	0.72	24.99	1.40	0.84
Li, Liang, Cai	1.42	164.28	1.08	0.76	10.82	1.28	1.20
fitted	1.30 (fixed)	140(22)	1.18(1)	0.83(1)	15(10)	1.50(19)	0.78(7)

Tab. 5.2: The global optical parameters for the t(^{72}Zn, t)^{72}Zn reaction at 2.7 MeV/u ^{72}Zn beam energy (i.e. $E_t = 8.1$ MeV triton energy in normal kinematics) from Perey, Perey [98] and from Li, Liang and Cai [99]. The parameterization of the optical potential U corresponds to eq. 2.2. The parameterization of Li, Liang and Cai also includes a complex surface potential with the parameters $W = 20.60$ MeV, $r_s = 1.14$ fm and $a_s = 0.86$ fm. Additionally, the fitted optical parameters are given. In the fit only the real and the complex volume terms of the optical potential U were taken into account.

Parameterization	$\mathcal{L}$ [mbarn^{-1}]	χ^2/NDF
Perey, Perey	$(1.18 \pm 0.01) \cdot 10^4$	3.83
Li, Liang, Cai	$(1.18 \pm 0.02) \cdot 10^4$	3.78
fitted	$(1.80 \pm 0.11) \cdot 10^4$	0.37

Tab. 5.3: The integrated luminosities and χ^2/NDF values obtained from the fits of the elastically scattered tritons in fig. 5.6. Their corresponding optical model parameters are given in tab. 5.2.

a comparison between the experimental triton data and two FRESCO calculations with two different global parameter sets for the optical model: the Perey, Perey parametrization [98] and the Li, Liang and Cai parameterization [99]. Hence, the integrated luminosity $\mathcal{L}$ is the only fit parameter. In addition to the luminosity, the optical model parameters can also be released in the fit. The best fitted theoretical cross sections are shown in fig. 5.6. The fitted luminosities as well as the global optical model parameters are given in tab. 5.2 and tab. 5.3. Comparing the fitted optical model parameters to the global models, only small deviations are present which underlines that the experimental triton data can be well described using physically reasonable parameters of the depth, the radius and the diffuseness of the real and complex optical potentials. The small differences between the fitted and the global parameters can be due to the fact that the global optical model parameters are only valid for higher triton beam energies $E_t = 15 - 20$ MeV [98], but the triton energy in normal kinematics is only $E_t = 8.1$ MeV. Furthermore, the global optical model parameters have been determined for stable targets, however, the proton-neutron asymmetry of radioactive neutron-rich isotopes may have
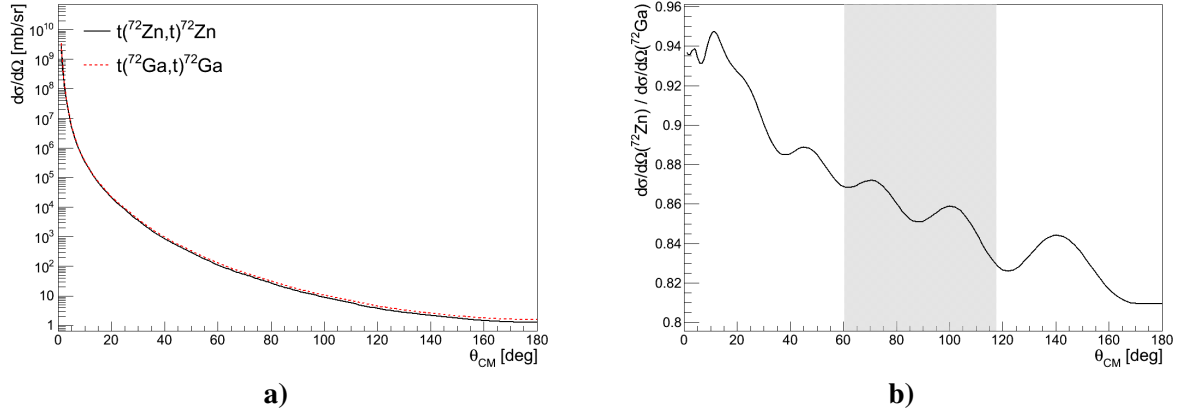
Fig. 5.7: a) The cross sections for the elastic scattering of the ^{72}Zn beam and its contaminant ^{72}Ga on the tritons of the tritium target. The cross sections have been calculated with FRESCO using the optical model parameters from Perey, Perey [98]. **b)** The ratio of cross sections shown in fig. a). The shaded area indicates the scattering angle region which is covered by the experimental data (c.f. fig. 5.6). For the luminosity determination of the ^{72}Zn beam with eq. (5.6), the mean value of the ratio in the shaded area is used.

a significant influence on the optical model parameters.

Influence of the Isobaric Beam Contaminant ^{72}Ga on the Luminosity of ^{72}Zn

In the analysis of the transfer reaction channels, the obtained triton integrated luminosity is used to convert the number of efficiency corrected counts per solid angle into a differential cross section. However, the evaluation of the transfer channels is only sensitive to reactions with the ^{72}Zn beam, while the elastic scattering data also includes a small contribution from the isobaric beam contaminant[6] ^{72}Ga. Hence, the ^{72}Ga content in the luminosity has to be subtracted. The total number N_{tot} of elastically scattered tritons reads

$$N_{tot} = N_{Zn} + N_{Ga} = \mathcal{L}_{Zn}\sigma_{Zn} + \mathcal{L}_{Ga}\sigma_{Ga} = \mathcal{L}_{Zn}\sigma_{Zn}\left(1 + \frac{I_{Ga}}{I_{Zn}}\frac{\sigma_{Ga}}{\sigma_{Zn}}\right), \tag{5.5}$$

with $I_{Ga}/I_{Zn} = (1.71 \pm 0.02)\%$ (c.f. tab. 5.1) and σ_{Ga}/σ_{Zn} being the ratio of the beam intensities and the cross sections of ^{72}Ga and ^{72}Zn. The cross sections σ_{Zn} and σ_{Ga} as well as their ratio ($\sigma_{Ga}/\sigma_{Zn} = 0.86 \pm 0.02$) are shown in fig. 5.7. Thus, the ^{72}Zn integrated luminosity is given by

$$\mathcal{L}_{Zn} = \frac{\mathcal{L}}{1 + \frac{I_{Ga}}{I_{Zn}}\frac{\sigma_{Ga}}{\sigma_{Zn}}}, \tag{5.6}$$

with $\mathcal{L}$ being the total integrated luminosity determined with the SFRESCO fit to the triton data (c.f. tab. 5.3).

Beam Intensity

The obtained ^{72}Zn integrated luminosity can be used to approximate the beam intensity I_{Zn}. The luminosity is given by

$$\mathcal{L}_{Zn} = \frac{\rho d N_A}{A} \cdot I_{Zn} \cdot t, \tag{5.7}$$

with $\rho d = 34 \pm 3\,\mu$g/cm^2 being the tritium target thickness during the ^{72}Zn transfer experiment [54, 55], N_A the Avogadro constant, A the molar mass of the target and t the measurement time of the

---

[6]The other beam contaminants ^{36}Ar and ^{18}O from the REXEBIS can be neglected in the calculation, as their beam intensities are much smaller compared to ^{72}Ga. Furthermore, their atomic number Z is much smaller than the atomic number of ^{72}Zn and ^{72}Ga, which reduces the cross section (Rutherford cross section $\propto Z^2$) and, thus, their influence on the elastic scattering data of the tritons.
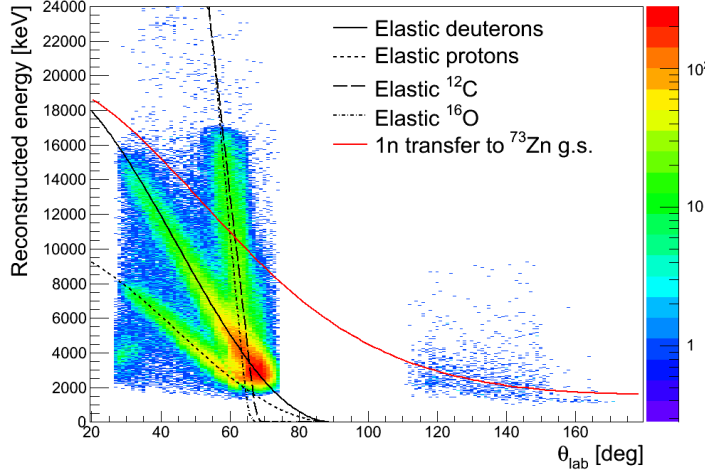
Fig. 5.8: The reconstructed particle energy in the T-REX ΔE-E telescopes as a function of the scattering angle θ_{lab} in the laboratory frame for a ^{72}Zn beam (E_{beam} = 2.7 MeV/u) impinging on the deuterated polyethylene target. In forward direction (θ_{lab} = 26° − 72°) the data of the FBarrel is shown. In backward direction between θ_{lab} = 110° and θ_{lab} = 152° the BBarrel data is presented, while the data points beyond θ_{lab} = 152° belong to the BCD. Note, that the intensities of the different detector types cannot be compared with each other as not all quadrants of all detectors were operational during the experiment. The lines represent kinematic calculations of all reactions. All elastically scattered particles correspond to components of the target.

experiment. Hence, the mean beam intensities are I_{Zn} = $(5.4 \pm 0.7) \cdot 10^6$ pps for the Perey, Perey parameters and for the Li, Liang and Cai parameters and $I_{Zn} = (8.3 \pm 0.9) \cdot 10^6$ pps for the fitted optical model parameters. The large difference between the values for the beam intensities is dominated by the optical model and cancels later almost completely in the calculation of the transfer reaction cross sections which uses the same optical model parameters as input (c.f. sec. 5.3.4).

5.3   One-Neutron Transfer Channels to ^{73}Zn

The 1n transfer from ^{72}Zn to ^{73}Zn is studied with the t(^{72}Zn, d)^{73}Zn reaction using the tritium target and with the d(^{72}Zn, p)^{73}Zn reaction using a 0.105 mg/cm^2 thick deuterated polyethylene target. Both experiments were performed with the same radioactive ^{72}Zn REX-ISOLDE beam (E_{beam} = 2.7 MeV/u) in 2011. The results of the 1n transfer channels can deal as additional input for the sequential transfer of two neutrons from ^{72}Zn to ^{74}Zn which is discussed in sec. 5.4.

5.3.1   Kinematics and Excitation Energies

In fig. 5.8 the reconstructed energy of all particles as a function of the scattering angle θ_{lab} in the laboratory frame is shown for the case that the ^{72}Zn beam impinges on the deuterated polyethylene target. The particle identification and the reconstruction of the energy at the reaction vertex is performed by applying the methods of sec. 5.1.1. As the beam is heavier than all components of the target (inverse kinematics), all elastically scattered target particles are detected in the FBarrel. In backward direction all particles are assigned as transfer protons. Small contributions from the light beam contaminants which can undergo fusion reactions are neglected in this consideration.

Fig. 5.9 a) and b) shows the reconstructed energy vs. θ_{lab} for all particles which are selecting the 1n transfer channels to ^{73}Zn, i.e. the identified deuterons from the t(^{72}Zn, d)^{73}Zn reaction and the identified transfer protons from the d(^{72}Zn, p)^{73}Zn reaction, respectively. The main difference between both spectra is that the kinematics of the (t,d) reaction is much steeper than of the (d,p) reaction. Hence, no transfer deuterons could be detected in backward direction, as their energy is well below the energy
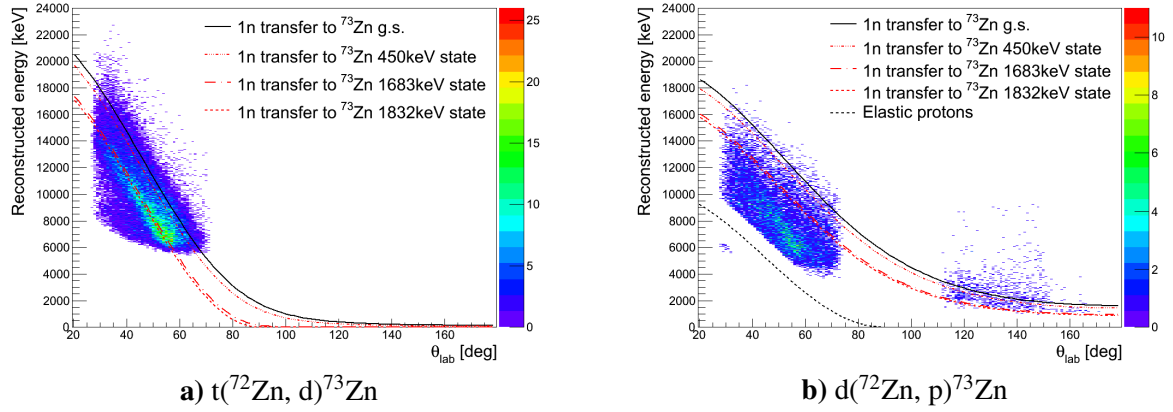
a) t(^{72}Zn, d)^{73}Zn   **b)** d(^{72}Zn, p)^{73}Zn

Fig. 5.9: The reconstructed particle energy of the transfer deuterons (**a**)) and transfer protons (**b**)) as a function of the scattering angle θ_{lab} in the laboratory frame for a ^{72}Zn beam (E_{beam} = 2.7MeV/u) impinging on the tritium target **a)** and a deuterated polyethylene (**b**)) target, respectively. In forward direction ($\theta_{lab} = 26° - 72°$), the data of the FBarrel is shown. In case of the (d,p) reaction in fig. b) the BBarrel data is presented between $\theta_{lab} = 110°$ and $\theta_{lab} = 152°$, while the data points beyond $\theta_{lab} = 152°$ belong to the BCD. Note that, the intensities of the different detector types cannot be compared to each other, as not all quadrants of all detectors were operational during the experiment. Furthermore, note the high thresholds close to 2 MeV of the BBarrel and the BCD. Additionally, the lines represent kinematic calculations for the most important reactions.
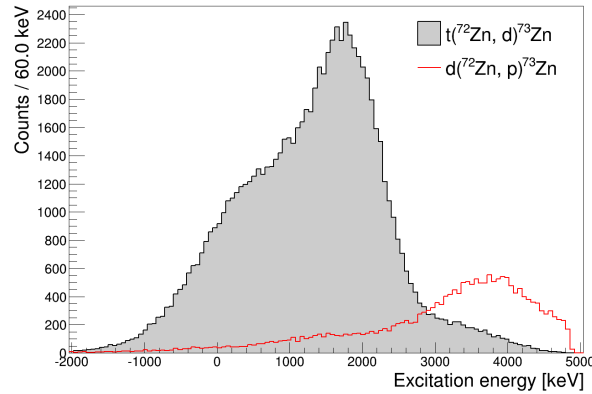

Fig. 5.10: The total excitation energy spectra of the t(^{72}Zn, d)^{73}Zn ($Q = -0.74$ MeV) and the d(^{72}Zn, p)^{73}Zn reaction ($Q = 3.3$ MeV). Due to the Q-value matching of transfer reactions, different levels in ^{73}Zn have been populated. The different statistics results from the different measurement time of the experiments.

threshold of the detectors. Contrary, the transfer protons from the (d,p) reaction are detected by the BBarrel and the BCD. Moreover, a comparison of the data to the kinematic predictions reveals that the (d,p) reaction populates higher levels in ^{73}Zn than the (t,d) reaction. This results from the Q-value matching (c.f. sec. 2.2.2): The Q-value of the (t,d) reaction is $Q = -0.74$ MeV, while the Q-value for the (d,p) reaction is much higher ($Q = 3.3$ MeV) leading to a population of higher excited states in ^{73}Zn.

The different population of the ^{73}Zn states by the two different 1n transfer reactions can best be seen in their excitation energy spectra (c.f. fig. 5.10). However, due to the insufficient energy resolution of the T-REX setup, a discrimination between single states is not possible.

5.3.2 Particle-γ-ray Coincidences

The excellent energy resolution of MINIBALL allows to select specific levels in ^{73}Zn by applying a cut on a characteristic γ-ray in addition to the identification of the reaction channel with the particle
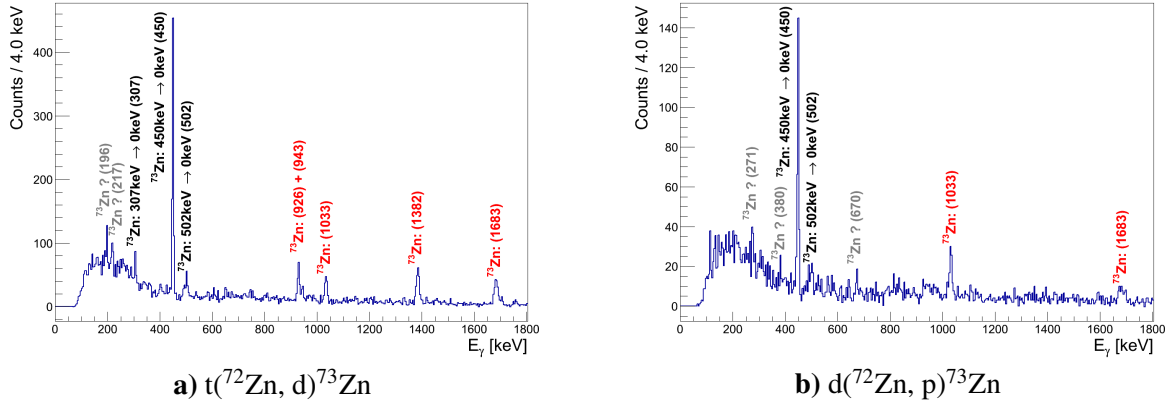
a) t(^{72}Zn, d)^{73}Zn   **b)** d(^{72}Zn, p)^{73}Zn

Fig. 5.11: The Doppler corrected and background subtracted (c.f. sec. 5.1.1) γ-ray spectra of all γ-rays which were emitted in coincidence with a transfer deuteron in the t(^{72}Zn, d)^{73}Zn reaction (**a**)) or in coincidence with a transfer proton in the d(^{72}Zn, p)^{73}Zn reaction (**b**)), respectively. The observed γ-ray lines, especially the new ^{73}Zn γ-rays in red, are discussed in sec. 5.3.3. In black the previously known γ-ray lines are marked. The gray γ-ray transitions could not be assigned explicitly to ^{73}Zn due to their low intensities. In brackets the γ-ray energy of the corresponding transition is given.

identification of T-REX. Hence, using the γ-ray information allows to determine excitation energy spectra showing only the levels from which the selected γ-rays originate. Fig. 5.11 a) and b) display the Doppler corrected γ-ray spectra of all γ-rays which are detected in coincidence with a transfer deuteron from the t(^{72}Zn, d)^{73}Zn reaction and with a transfer proton from the d(^{72}Zn, p)^{73}Zn reaction, respectively[7]. Both γ-ray spectra feature at least two peaks which can be assigned to the today's known level scheme of ^{73}Zn (c.f. fig. 5.14 a) from [13, 105, 106]). Furthermore, a large number of currently unknown γ-ray peaks are observed in both spectra at high intensities. Note, that these unknown γ-rays cannot be assigned to other possible reactions, such as (t,dn) or (d,pn) reactions, of the ^{72}Zn beam or of beam contaminants. Thus, they are good candidates for being produced in the 1n transfer reactions to ^{73}Zn. A comparison of their relative γ-ray intensities between the two reaction channels reveals again the different level population which is caused by the Q-value matching.

5.3.3   Level Scheme of ^{73}Zn

In a next step, the new γ-rays should be placed in the level scheme of ^{73}Zn. To separate feeding transitions from direct level population, the level from which the γ-rays originate can be determined in a plot of the γ-ray energy vs. the excitation energy: see fig. 5.12 a) for the (t,d) reaction and fig. 5.12 b) for the (d,p) reaction, respectively. Events which are positioned on the red bisecting line in the spectra correspond to transitions to the ^{73}Zn ground state, while events which are centered around the dotted line (the bisecting line which is shifted by 450 keV to higher excitation energies) show transitions to the 450 keV level of ^{73}Zn. For an additional visual evaluation, fig. 5.13 shows the distribution of the excitation energy after applying cuts on the most dominant γ-rays in fig. 5.11. Note, that these spectra are corrected for random coincidences. In the following, each spectrum is discussed in order to build the level scheme of ^{73}Zn. For comparison fig. 5.14 a) shows the currently known level scheme from NNDC [13] which is based on [105, 106], fig. C.3 in appendix C.2 shows the resulting levels from a detailed β-decay study of ^{73}Cu to ^{73}Zn at ISOLDE [107] and finally fig. 5.14 b) displays the level scheme of ^{73}Zn developed in this thesis:

- **Cut on $E_\gamma = 450$ keV**: The previously known $(3/2)^- \rightarrow (1/2)^-$ ground state transition with $E_\gamma = 450$ keV is the strongest transition in the γ-ray spectra of fig. 5.11. The excitation energy

---

[7]Of course, the spectra shown in fig. 5.11 are background subtracted, i.e. the random coincidences have been taken into account using the method described in sec. 5.1.1.
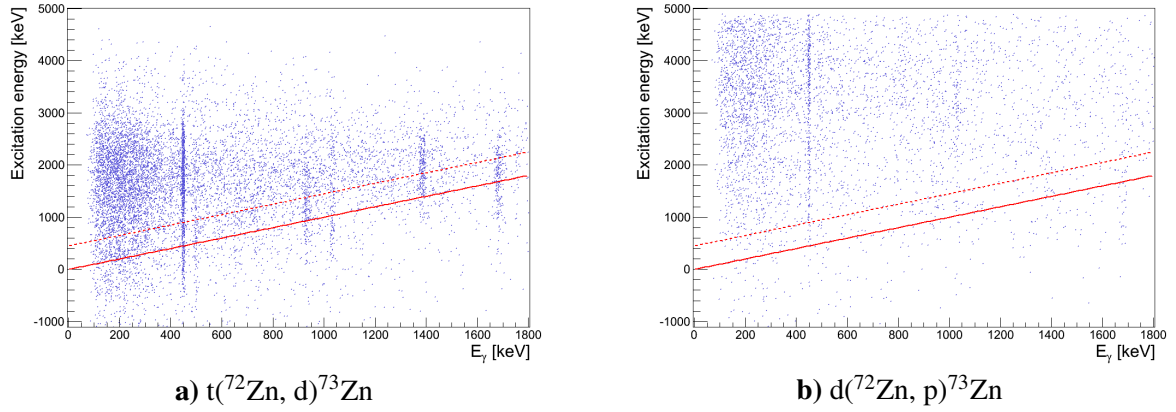
a) t(^{72}Zn, d)^{73}Zn   **b)** d(^{72}Zn, p)^{73}Zn

Fig. 5.12: The ^{73}Zn excitation energy vs. the Doppler corrected γ-ray energy of all events which feature a coincidence between a γ-ray and an identified transfer deuteron from the t(^{72}Zn, d)^{73}Zn reaction (**a**)) or an identified transfer proton from the d(^{72}Zn, p)^{73}Zn reaction (**b**)), respectively. As the Q-value of the (d,p) reaction is much higher, this reaction channel populates dominantly states at high excitation energies compared to the (t,d) reaction channel. Events on the solid red lines indicate ground state transitions, while events on the dotted red lines correspond to transitions to the 450 keV state of ^{73}Zn.

spectrum with the cut on the $E_\gamma = 450$ keV γ-ray line (c.f. fig. 5.13 a)) reveals that the t(^{72}Zn, d)^{73}Zn reaction populates directly the $(3/2)^-$ level at 450 keV only to a small extend. Most of the population of this state occurs via feeding of higher lying states. In the excitation energy spectrum of the d(^{72}Zn, p)^{73}Zn reaction only feeding to the $(3/2)^-$ level, instead of a direct population, is visible due to the higher Q-value.

- **Cut on $E_\gamma = 926$ keV**: According to the level scheme of the β-decay experiment [107], the $E_\gamma = 926$ keV γ-ray originate from the 1377 keV level (c.f. fig. C.3). Hence, the $E_\gamma = 450$ keV γ-ray should be emitted in coincidence with the $E_\gamma = 926$ keV γ-ray. However, this coincidence has not been observed in the 1n transfer experiments, although 8.4 counts would be expected in the (t,d) experiment (c.f. fig. C.4 b)). Furthermore, the level scheme of [107] would additionally require that the $E_\gamma = 874$ keV γ-ray, which also depopulates the 1377 keV level, should be visible, too. The $E_\gamma = 874$ keV γ-ray is proposed to have about half of the intensity of the clearly visible $E_\gamma = 926$ keV γ-ray and thus, should be observed in this experiment. Nevertheless, it is not seen in the transfer data set. In summary, the transfer experiments which are discussed in this thesis do not support the 1377 keV level. Looking at the excitation energy spectrum with a γ-ray gate on $E_\gamma = 926$ keV (c.f. fig. 5.13 b)), another possibility is that the $E_\gamma = 926$ keV γ-ray decays into an isomeric state around 200 keV. A candidate would be the 196 keV state which has a half life of 13 ms, i.e. the $E_\gamma = 929$ keV γ-ray would be emitted from the 1125 keV state. But, according to [107] the 1125 keV level features much stronger transitions such as the $E_\gamma = 675$ keV and the $E_\gamma = 622$ keV γ-ray which both have not been observed in the 1n transfer experiments. To sum up, an exact placement of the $E_\gamma = 929$ keV γ-ray is not possible, especially as no coincidences to other γ-rays have been observed.

- **Cut on $E_\gamma = 943$ keV**: The $E_\gamma = 943$ keV γ-ray is only visible in the t(^{72}Zn, d)^{73}Zn reaction and not in the d(^{72}Zn, p)^{73}Zn reaction. This indicates that it originates from a relative low lying level in ^{73}Zn. The distribution of the excitation energy with a cut on the $E_\gamma = 943$ keV line (c.f. fig. 5.13 c)) confirms the placement of the $E_\gamma = 943$ keV γ-ray on top of the isomer at 196 keV, i.e. it is emitted from the 1138 keV level. However, the proposed ground state transition in [107] featuring a similar intensity than the $E_\gamma = 943$ keV γ-ray has not been observed in the transfer experiments.

- **Cut on $E_\gamma = 1033$ keV**: Fig. 5.13 d) supports the proposal of [107] that the $E_\gamma = 1033$ keV
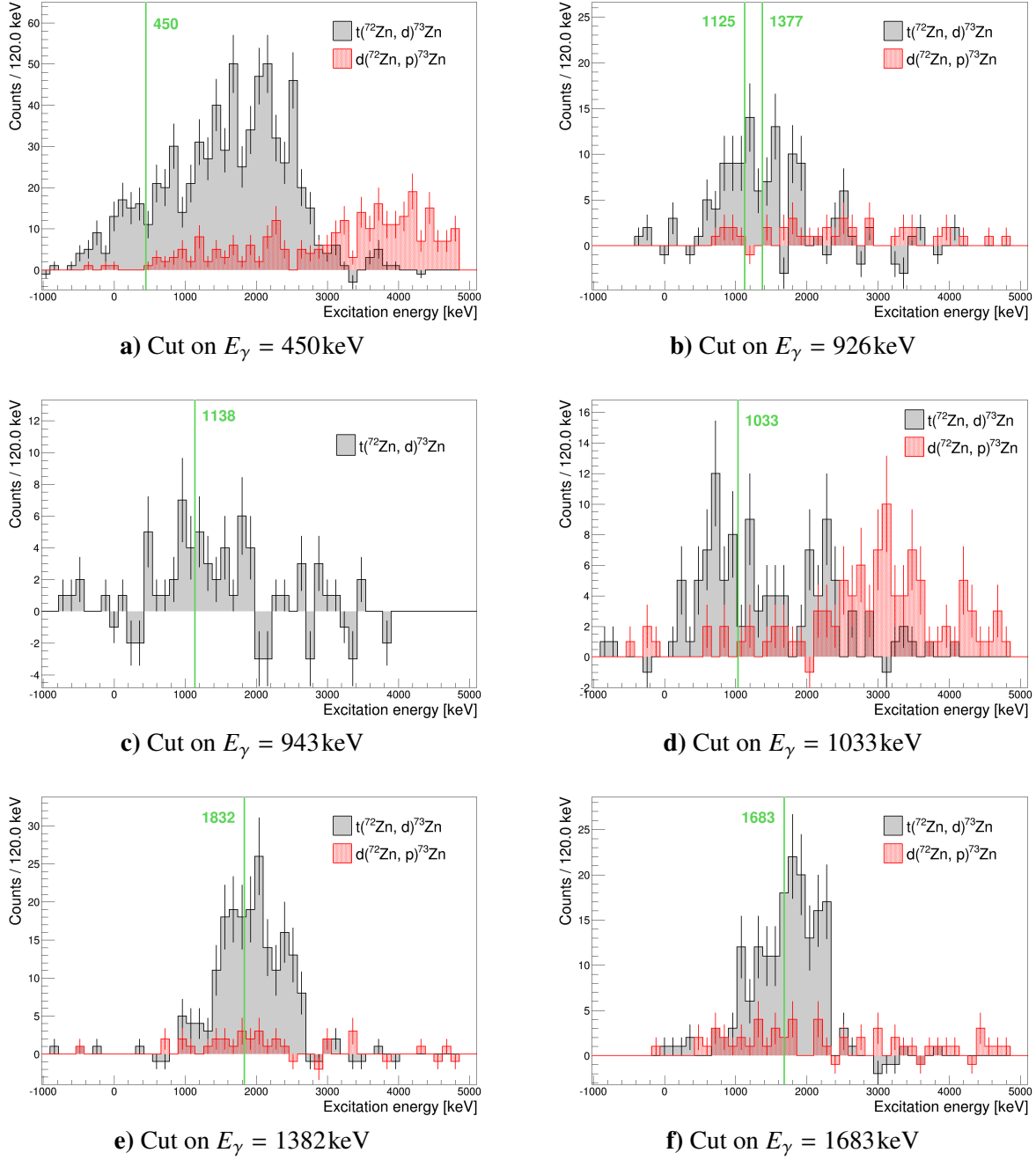
Fig. 5.13: The excitation energy spectra of the t(^{72}Zn, d)^{73}Zn ($Q = -0.74$ MeV) and the d(^{72}Zn, p)^{73}Zn reaction ($Q = 3.3$ MeV) using different cuts on the most dominant γ-rays. Due to the Q-value matching of transfer reactions, different levels in ^{73}Zn have been populated. The different statistics result from the different measurement times of the experiments. The vertical green lines correspond to possible populated levels in ^{73}Zn from which the corresponding γ-ray can originate. The negative counts results from a background subtraction which accounts for the fact that the photopeak of the respective γ-ray transition is superimposed with a background (e.g. originating from Compton scattered γ-rays from higher lying transitions) in the γ-ray spectrum.

Fig. 5.14: a) Level scheme of ^{73}Zn measured with a ^{73}Cu β-decay experiment which was performed using t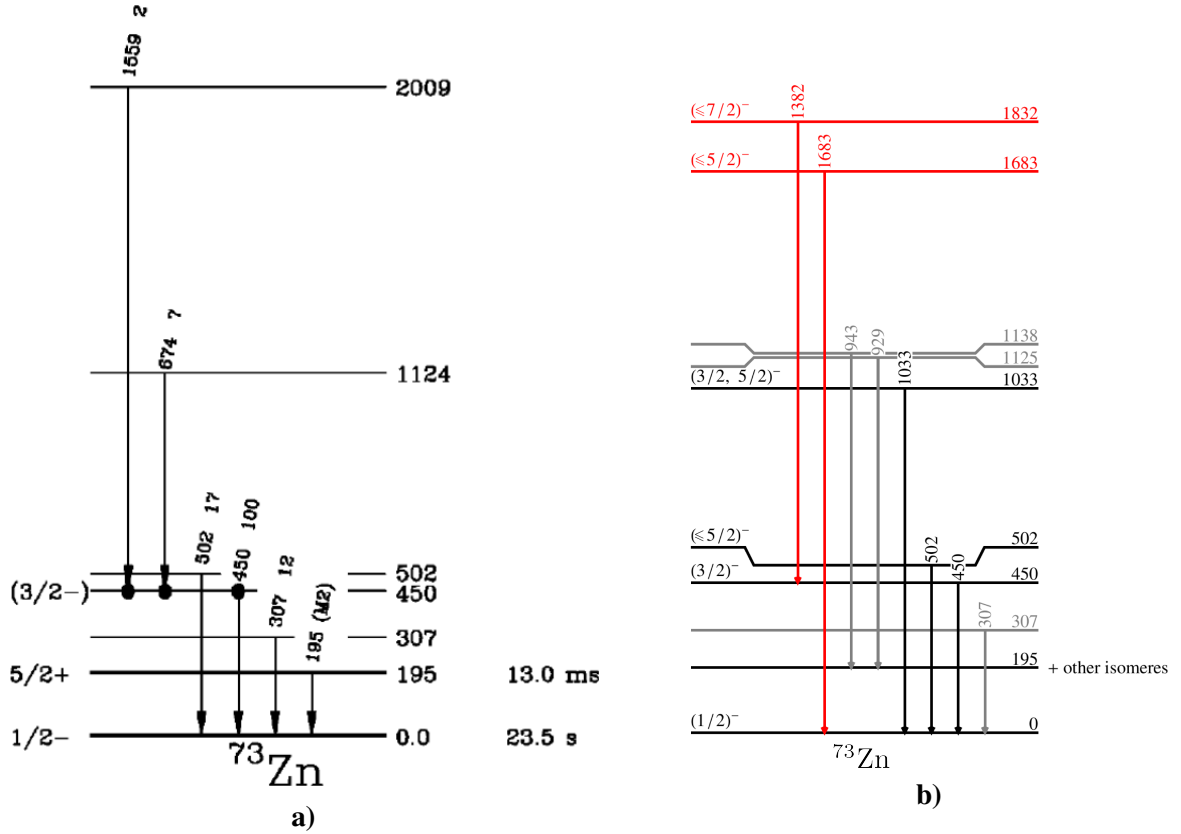he K1200 Cyclotron and the A1200 fragment separator at the National Superconducting Cyclotron Laboratory at Michigan State University. Adapted from [105]. The ground state as well as the levels at 307 keV, 502 keV and 1124 keV were also observed in [106]. **b)** The level scheme which has been obtained from the 1n transfer reactions t(^{72}Zn, d)^{73}Zn and d(^{72}Zn, p)^{73}Zn, which are discussed in this thesis. The confirmed levels and γ-rays are shown in black, the levels and γ-rays with ambivalent positions are visualized in gray and the newly discovered levels and γ-rays are displayed in red.

γ-ray is a ground state transition. However, a feeding contribution from higher lying states is present in both excitation energy spectra.

- **Cut on E_γ = 1382 keV**: The $E_\gamma = (1382 \pm 2)$ keV γ-ray is observed for the first time in a ^{73}Zn γ-ray spectrum. Nevertheless, it can be unambiguously placed in the level scheme, as it features a clear coincidence to the $E_\gamma = 450$ keV γ-ray (c.f. fig. C.4 a) and e)). Furthermore, its excitation energy spectrum (c.f. fig. 5.13 e)) is centered around 1832 keV = 1382 keV + 450 keV. Hence, a new level at (1832 ± 2) keV in ^{73}Zn has been discovered.

- **Cut on E_γ = 1683 keV**: A second new γ-ray with $E_\gamma = (1683 \pm 2)$ keV has been observed in ^{73}Zn. As its excitation energy (c.f. fig. 5.13 f)) has a mean value which corresponds to the same energy, it can be concluded that the γ-ray corresponds to a ground state transition. Therefore, a new ^{73}Zn level at (1683 ± 2) keV can be placed in the level scheme.

The 307 keV and the 502 keV levels and their γ-rays from ^{73}Zn were previously known[8]. Their excitation energy spectra are dominated by feeding from higher lying states. Moreover, the γ-ray lines which are marked in light gray in fig. 5.11 could not be discussed further in this thesis as their intensity is too low to built a reasonable excitation energy spectrum, especially as they are positioned on a large

---

[8]The 307 keV γ-ray is placed differently in previous β-decay measurements. [105] suggest a ground state transition from a 307 keV level, while [107] (c.f. fig. C.3) proposed to assign the $E_\gamma = 307$ keV γ-ray to the 502 keV level.

background in the γ-ray spectrum.

In summary, the resulting level scheme, which is obtained with the 1n transfer reactions, is shown in fig. 5.14 b). The existence of the $E_\gamma = 307$ keV, $E_\gamma = 450$ keV and $E_\gamma = 502$ keV γ-rays , already observed in [105, 107], has been confirmed. However, the claim from [107], stating that the decay corresponding to the $E_\gamma = 929$ keV γ-ray originates from the 1377 keV level in ^{73}Zn, could not be verified. Furthermore, the transfer data does not fully support the association of the $E_\gamma = 943$ keV γ-ray to the 1138 keV ^{73}Zn level as proposed in [107]. Instead, their γ-ray gated excitation energy spectra (c.f. fig. 5.13 b) and c)) indicate that the $E_\gamma = 929$ keV and the $E_\gamma = 943$ keV γ-ray decay into an additional isomeric state around 200 keV. This assumption is also supported by [105], where a $9/2^+$ state is proposed close to the $5/2^+$ isomer. Moreover, the 1033 keV level, proposed in [107], has been confirmed. Apart from that, in the analysis of the 1n transfer data two new levels in ^{73}Zn at (1683 ± 2) keV and at (1832 ± 2) keV have been discovered.

5.3.4 Differential Cross Sections

As the energy resolution of T-REX is not sufficient to discriminate between single states close in energy (c.f. fig. 5.10), differential cross section can only be calculated using the γ-ray gated excitation energy spectra (c.f. fig. 5.13). However, a cut on a characteristic γ-ray does not ensure that only the desired state is selected. It is also possible that higher lying states which feed into the desired state are still contained in the data set. This is e.g. the case in the excitation energy spectrum with a γ-ray cut on $E_\gamma = 450$ keV (c.f. fig. 5.13 a)). Hence, due the dominating feeding component, a clean separation between different states and therefore, the determination of the differential cross section of the 450 keV state is impossible. Additionally, only the (t,d) data set allows to extract reasonable cross sections, as the (d,p) reaction is dominated by feeding and as it suffers from low statistics. Apart from that, due to the MINIBALL efficiency ($\epsilon_{MB} \approx 6\%$), the limited statistics only allow to determine the cross sections of the new ^{73}Zn states[9] at 1683 keV and at 1832 keV which have been populated in the t(^{72}Zn, d)^{73}Zn reaction. Fig. 5.15 shows their differential cross sections which have been extracted using the method described in sec. 5.1.2. As the spins of the 1683 keV and of the 1832 keV level are unknown, the experimental data is compared to several FRESCO calculations assuming possible spins which are motivated by the selection rules for γ-ray transitions (c.f. eq. 2.24). However, due to the similar angular dependence of the theoretical cross sections in the covered range of the experimental data points, a spin assignment for the new ^{73}Zn states is not possible. This is especially a problem of the low beam energy available at ISOLDE. With the higher beam energies available at HIE-ISOLDE (c.f. sec. 7.3), the dependence of the angular distributions on the momentum transfer is more pronounced. To account for the influence of the optical model parameters, the FRESCO calculations were done with the Perey, Perey optical model parameterization [98] as well as with the fitted optical model parameters (c.f. tab. 5.2). The shape and the magnitude of the experimental and theoretical cross sections for different optical parameters differ only slightly. Hence, only the angular distribution of the Perey, Perey parametrization is shown in fig. 5.15.

As described in sec. 2.2.2, the scaling factor between the FRESCO calculation (assuming a pure single-particle configuration) and the experimental data contains information about the nuclear structure. This scaling factor is often called "spectroscopic factor" (c.f. eq. (2.11)). It describes the overlap between the initial state in ^{72}Zn and the final state in ^{73}Zn. However, in theoretical calculations the spectroscopic factor deals with the overlap of the total wave functions, while transfer reactions, as direct reactions, only probe the wave functions at the nuclear surface. Hence, the scaling factor between the experimental and the FRESCO cross section does not strictly correspond to the spectroscopic fac-

---

[9]The differential cross section of the ground state has not been evaluated. Without a γ-ray coincidence it is not possible to disentangle the ground state from energetically close lying excited states, especially as there are known isomeric states (with partially unknown spin assignments) around 200 MeV. Furthermore, the ground state is superimposed by the 450 keV state.
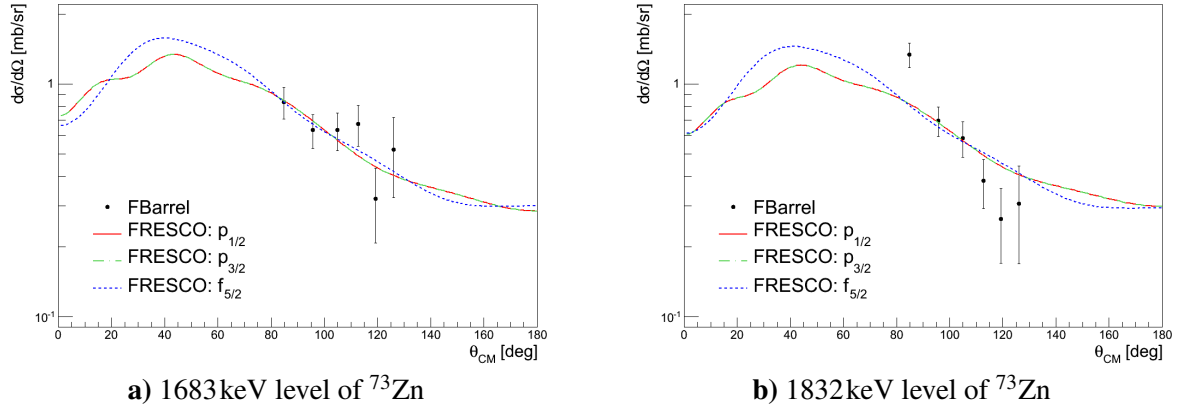
a) 1683 keV level of ^{73}Zn   **b)** 1832 keV level of ^{73}Zn

Fig. 5.15: The differential cross section of the ^{73}Zn states at 1683 keV (**a**)) and at 1832 keV (**b**) measured in the t(^{72}Zn, d)^{73}Zn reaction. The experimental cross section is obtained from the γ-ray gated excitation energy spectra of fig. 5.13 f) and e), respectively. Additionally, FRESCO calculations assuming different populated shells for the transferred neutron are shown (Perey, Perey parametrization [98] of the optical model). The calculations, which assume single-particle character, are scaled to fit best to the experimental data. Their scaling factors, which are related to the spectroscopic factors, are summarized in tab. 5.4. However, the data does not allow to determine in which orbital the neutron has been transferred.

Level [keV]	Proposed J	Neutron orbit	Perey, Perey parameterization	Fitted optical model
	1/2	$p_{1/2}$	0.57 ± 0.05	0.49 ± 0.04
1683	3/2	$p_{3/2}$	0.29 ± 0.02	0.24 ± 0.02
	5/2	$f_{5/2}$	0.67 ± 0.06	0.55 ± 0.05
	1/2	$p_{1/2}$	0.59 ± 0.05	0.51 ± 0.04
1832	3/2	$p_{3/2}$	0.30 ± 0.02	0.25 ± 0.02
	5/2	$f_{5/2}$	0.67 ± 0.05	0.55 ± 0.04

Tab. 5.4: The obtained scaling factors of the 1683 keV and the 1832 keV state of ^{73}Zn. They were obtained by fitting the theoretical single-particle differential cross sections to the experimental cross section (c.f. fig. 5.15). In the calculation of the theoretical cross section with FRESCO, all possible spin assignments (according to the γ-ray selection rules) and all possible orbitals for the transferred neutron were considered. Furthermore, two different parameters sets of the triton optical model and their respective luminosities were used: the Perey, Perey parametrization [98] as well as the fitted parameters from tab. 5.2 and tab. 5.3. Both states have been populated in the t(^{72}Zn, d)^{73}Zn reaction.

tor [58]. This issue has to be taken into account in the interpretation of the scaling factor. The fitted values for the 1683 keV and the 1832 keV state of ^{73}Zn are given in tab. 5.4. Both optical model parameterizations feature similar scaling factors, which substantiates the reliability of the obtained results. In a simple model, assuming pure particle configurations, the spectroscopic factors of states in odd nuclei, which are populated via 1n transfer reactions, can be estimated with [59]

$$S = 1 - \frac{N-1}{2j+1}, \qquad (5.8)$$

with N being the number of nucleons in the valence orbit of spin j. Hence, in the single-particle model, if the neutron is transferred to the last free magnetic substate of the nl_j orbit (i.e. the orbit is fully occupied after the transfer), the $2p_{1/2}$, $2p_{3/2}$ or $1f_{5/2}$ orbits result in spectroscopic factors of 0.5, 0.25 and 0.17, respectively. A lower occupancy in the shells increase the spectroscopic factors. Thus, a comparison of this single-particle expectation with the obtained scaling factors of the experiment indicates that the p-shells are nearly fully occupied. Moreover, the large scaling factor for a proposed
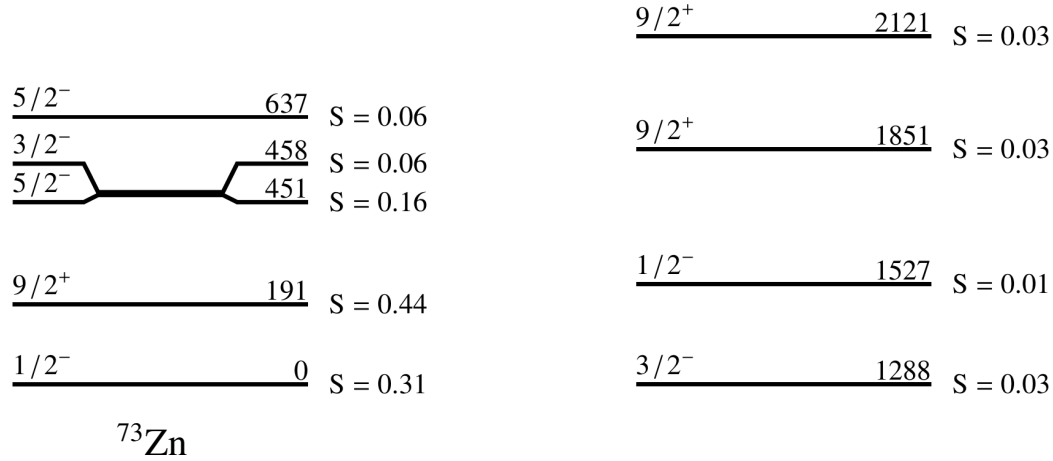
$9/2^+$ ——————————— 2121 S = 0.03

$5/2^-$ ——————— 637 S = 0.06

$9/2^+$ ——————————— 1851 S = 0.03

$3/2^-$ ——————— 458 S = 0.06
$5/2^-$ ——————— 451 S = 0.16

$1/2^-$ ——————————— 1527 S = 0.01

$9/2^+$ ——————— 191 S = 0.44

$1/2^-$ ——————— 0 S = 0.31

$3/2^-$ ——————————— 1288 S = 0.03

^{73}Zn

Fig. 5.16: The level scheme of ^{73}Zn which results from a shell model calculation using the jj44 model space and the jj44bpn interaction [108, 110]. Especially, the ground state spin, the low lying isomeric states and the strong $(3/2)^-$ state at 450 keV are well reproduced. Note, that only the states which feature a significant spectroscopic factor S are shown. Further note, that between 637 keV and 1288 keV are only levels with negligible spectroscopic factors placed.

5/2 spin would suggest a roughly half filled $1f_{5/2}$ orbit. This behavior is not expected, as shell model calculations already favor at least four neutrons in the ^{72}Zn ground state (c.f. tab. D.11). Thus, a 5/2 spin for the 1683 keV and the 1832 keV state of ^{73}Zn is considered to be more unlikely than a 1/2 or 3/2 spin. The large scaling factor for the $1f_{5/2}$ shell compared to the p-shell can be explained as the scaling factor has to compensate the larger angular momentum mismatch of $\Delta l = 3$ instead of $\Delta l = 1$ (c.f. sec. 2.2.2). However, note that the presented cautious interpretation of the scaling factors is only a qualitative estimate, as single-particle configurations are unlikely. Instead configuration mixing is expected in the neutron-rich zinc isotopes.

5.3.5 Discussion

To get a deeper insight into the nuclear structure of ^{73}Zn, the experimental results can be compared to a detailed shell model calculation. The shell model calculation which has been used in this thesis was performed by Kathrin Wimmer [108] using the NuShellX@MSU code [109] and using the jj44 model space. It includes the $1f_{5/2}$, $2p_{3/2}$, $2p_{1/2}$ and $1g_{9/2}$ orbitals for protons as well as for neutrons. Hence, a ^{56}Ni core ($N = Z = 28$) is chosen. The calculation is based on the jj44bpn interaction[10] [110]. A first check for a shell model calculation is the comparison to the experimental level scheme: Fig. 5.16 shows the calculated ^{73}Zn level scheme which includes all levels featuring a significant spectroscopic factor[11]. A comparison to the experimentally obtained level scheme in fig. 5.14 reveals that the ground state spin and parity is correctly reproduced. Furthermore, an isomeric states at 191 keV is predicted. This is in good agreement with the experimental data, as in the 1n transfer experiments a lot of γ-ray transitions to isomeric states with level energies around 200 keV are observed (c.f. sec. 5.3.3). Additionally, the $9/2^+$ state is favored by [105]. Furthermore, the strongly populated $(3/2)^-$ level at 450 keV is nicely reproduced by the shell model calculation at 458 keV. Its small predicted spectroscopic factor by the shell model calculation qualitatively agrees with the fact that the population of the 450 keV state is dominated by feeding from higher lying states. However, due to the unknown spin and parity and due to the high level density, the higher lying experimentally observed

---

[10]For more information about the shell model calculation see sec. 6.4.3.

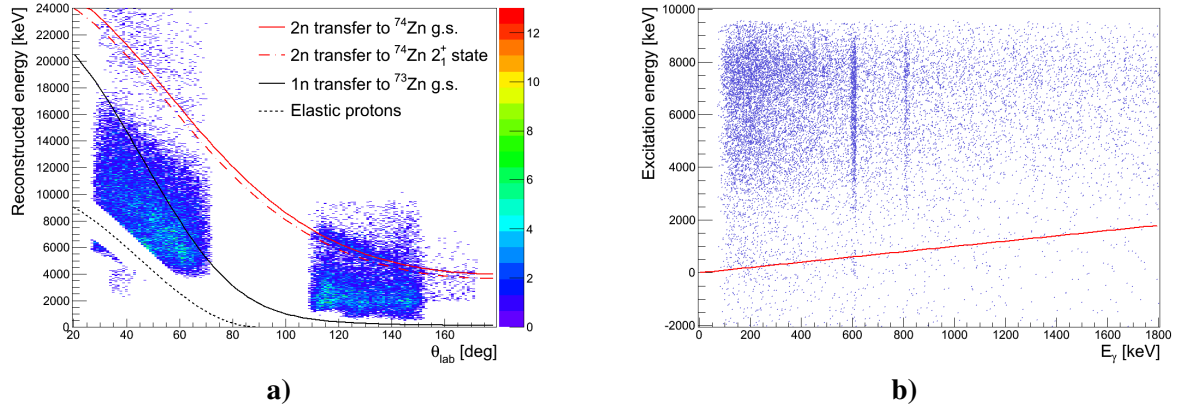[11]The level scheme of ^{72}Zn is shown in fig. 6.32.

Fig. 5.17: a) The reconstructed particle energy of the identified transfer protons in the T-REX ΔE-E telescopes as a function of the scattering angle θ_{lab} in the laboratory frame for a ^{72}Zn beam (E_{beam} = 2.7 MeV/u) impinging on the tritium target. In forward direction (θ_{lab} = 26° − 72°) the data of the FBarrel is shown. In backward direction between θ_{lab} = 110° and θ_{lab} = 152°, the BBarrel data is presented, while the data points beyond θ_{lab} = 152° belong to the BCD. Note that, the intensities of the different detector types cannot be compared to each other, as not all detectors quadrants were fully operational during the experiment. Additionally, the lines represent predictions from kinematic calculations for the most important reactions. Note that the elastic scattered protons are excluded. **b)** The ^{74}Zn excitation energy plotted vs. the Doppler corrected γ-ray energy of all events which feature a coincidence between a γ-ray and an identified transfer proton. The data of all detectors has been considered. Events on the solid red line indicate ground state transitions. Due to the high Q-value (Q = 5.24 MeV) the 2n transfer reaction populates dominantly levels around 5 MeV which deexcite over the 4_1^+ state at 1419 keV ($E_\gamma(4_1^+ \rightarrow 2_1^+)$ = 813 keV) and the 2_1^+ state at 606 keV of ^{74}Zn.

states cannot be unambiguously assigned to states in the shell model calculation. Nevertheless, the most important features of the ^{73}Zn level scheme coincide in the experiment and in the shell model calculation. Hence, it can be used as input for the theoretical prediction of the sequential 2n transfer from ^{72}Zn to ^{74}Zn using ^{73}Zn as intermediate state.

5.4 Two-Neutron Transfer Channel to ^{74}Zn

The 2n transfer channel to ^{74}Zn is studied with a ^{72}Zn beam (E_{beam} = 2.7 MeV/u) impinging on a 0.5 mg/cm^2 thick radioactive tritium target that provides two neutrons for the transfer to ^{74}Zn. In sec. 5.4.1, the kinematics of the transfer protons are discussed along with the resulting excitation energy spectrum of ^{74}Zn. Combing the excitation energy spectrum with the γ-ray spectrum the populated excited states in ^{74}Zn can be determined (c.f. sec. 5.4.2). Based on these results, in sec. 5.4.3, the differential cross sections are extracted and compared to FRESCO calculations using shell model input. This section also includes the determination of an upper limit of the currently unknown 0_2^+ state in ^{74}Zn. Sec. 5.4.4 concludes with a discussion of the results, especially in the contest of previous transfer experiments.

5.4.1 Kinematics and Excitation Energies

The reconstructed energy of the transfer protons as a function of the scattering angle θ_{lab} in the laboratory frame is shown in fig. 5.17 a). Additionally, predictions from kinematic calculations of the 2n transfer reaction to the ^{74}Zn ground state and the 2_1^+ state are displayed. Their comparison to the experimental data reveals that these two states can be well discriminated in the BCD. However, the resolution of the T-REX Barrel detectors is not sufficient to easily disentangle the 0_1^+ and the 2_1^+ state in ^{74}Zn. This is due to the wider segmentation of the Barrel detector compared to the BCD (c.f. tab. 3.2). Additionally, the excitation energy resolution deteriorates towards θ_{lab} = 90° as the solid angle

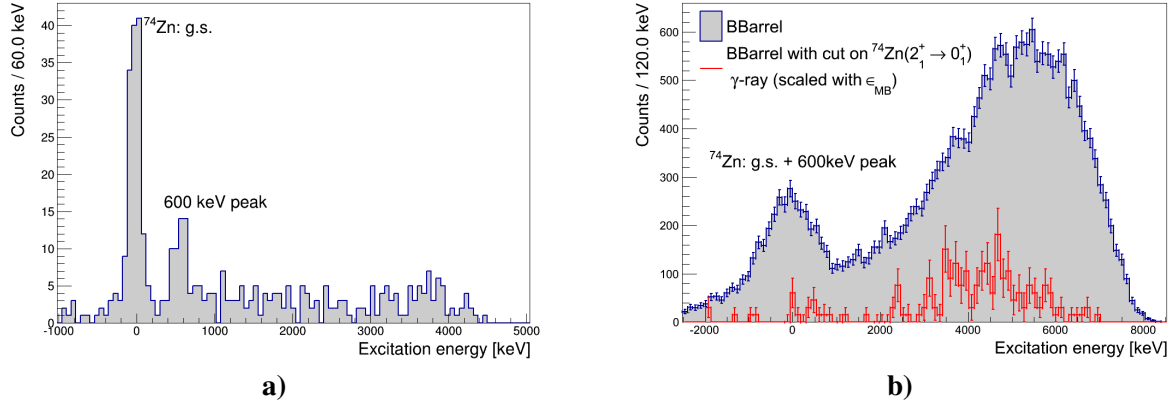a)   b)

Fig. 5.18: a) The excitation energy spectra of all transfer protons detected in the BCD Left and Bottom quadrant. The BCD Top and Right quadrant were not fully operational in the experiment and are excluded in the analysis. **b)** The excitation energy spectra of all transfer protons detected in the BBarrel. Additionally, the BBarrel spectrum with a γ-ray gate on the $2^+_1 \rightarrow 0^+_1$ transition of ^{74}Zn is shown. For a better comparison the γ-ray gated spectrum is scaled with the MINIBALL efficiency. The difference between both BBarrel spectra is due to a huge δ-electron background (for details, see text). The soft cut off around 7 MeV excitation energy is due to the different energy thresholds of the Barrel detector quadrants (c.f. fig. 5.17 a)). The events at negative excitation energy are due to pile-up events with high energy depositions in the detector (c.f. fig. 5.17 a)).

of the Barrel strips close to the target is larger compared to the strips close to the BCD. Apart from that, the energy straggling in the target close to $\theta_{lab} = 90°$ is increased due to the increased effective target thickness for the transfer protons. Hence, the band in fig. 5.17 a) representing the ground state and the 2^+_1 state of ^{74}Zn broadens going from $\theta_{lab} = 172°$ towards $\theta_{lab} = 90°$.

In backward direction, the transfer protons from the 2n transfer reaction feature very low energies. Hence, the majority of the protons are already stopped in the ΔE-detector of the ΔE-E telescope which makes a particle identification in backward direction impossible. But, as the kinematic prediction for the 1n transfer reaction t(^{72}Zn, d)^{73}Zn is positioned energetically below the energy threshold of the backward T-REX detectors (c.f. black solid line in fig. 5.17 a)), all particles in backward direction can be safely tagged as transfer protons.

Excitation Energies

The kinematic curves in fig. 5.17 a) already indicate that the 2n transfer channel seems to dominantly populate high lying states around 5 MeV in ^{74}Zn (c.f. also fig. 5.17 b)). This results from the high Q-value ($Q = 5.24$ MeV) of the t(^{72}Zn, p)^{74}Zn reaction (c.f. sec. 2.2.2). A deeper insight into the population of the ^{74}Zn states is given by the excitation energy spectra. They have been extracted for each T-REX detector type separately, since their energy resolutions differ.

Fig. 5.18 a) shows the excitation energy spectrum of the BCD. Two distinct peaks a visible: A peak at $E_{ex} = 0$ keV which corresponds to the ^{74}Zn ground state and a peak around $E_{ex} \approx 600$ keV. The latter peak is a candidate for the 2^+_1 state in ^{74}Zn. Furthermore, several unresolved states at higher energies are populated.

Fig. 5.18 b) shows the excitation energy spectrum which is extracted from the transfer protons detected in the BBarrel. Compared to the BCD it features a different shape: First, the energy resolution is not sufficient to resolve the ^{74}Zn ground state and the peak at $E_{ex} \approx 600$ keV. Second, a dominant peak at higher lying excitation energies is visible. To analyze the origin of this peak, the excitation energy spectrum for events requiring additionally a detected $2^+_1 \rightarrow 0^+_1$ γ-ray of ^{74}Zn in MINIBALL is displayed. This γ-ray gated spectrum is scaled with the MINIBALL efficiency to allow for a comparison with the unrestricted excitation energy spectrum. Using the good assumption, that the majority of higher lying states in ^{74}Zn (even-even nucleus) deexcite via the 2^+_1 state, it is expected that the two

spectra are nearly coincident at high excitation energies. However, this is not observed in the data at all. Hence, it can be concluded that the majority of the events in the huge peak around $E_{ex} \approx 5\,\text{MeV}$ do not originate from the 2n transfer reaction to ^{74}Zn. Contrary, as explained in the following, they are likely to be attributed to δ-electrons which are produced by the interaction of the heavy ^{72}Zn beam with the tritium target. A large fraction of these δ-electrons is already suppressed by applying high voltage to the target (c.f. fig. 3.6 and fig. D.1). However, the remaining δ-electrons, which still reach the detector, produce a noise signal which is in the same order of magnitude as the signal of the transfer protons. This is especially a problem for resistive strip detectors, like the Barrel detectors, as the energy is determined from the signal of the huge, unsegmented rear side of the detectors. Thus, the combined effect of many δ-electrons can produce a large signal due to the large solid angle of the rear electrode. This is also consistent with the fact that these events feature strip signals which are much lower than the rear signal, since the solid angle of a strip is significantly smaller compared to the solid angle of the rear side[12]. Additionally, these noise events scale with the beam intensity[13] and the atomic number Z of the beam. Hence, this noise is much more relevant in the current ^{72}Zn experiment than in the previous experiments featuring much lower beam intensities and much lighter beams, such as ^{44}Ar [55], ^{30}Mg [54, 86] or ^{22}Ne.

In summary, the δ-electrons are likely to be responsible for the excess of the ungated excitation energy spectrum of the BBarrel compared to the γ-ray gated spectrum. However, the effect of the δ-electrons on the other T-REX detectors is smaller: In the FBarrel detector the δ-electron noise is suppressed, as the FBarrel is shielded by the mylar foil (c.f.sec. 3.3). Only the first strip, which is closest to the target, features δ-electrons as it is not completely covered by the foil. Hence, the innermost strip was excluded in the analysis[14]. Furthermore, the δ-electrons are not visible in the CD spectra, as the CD detectors are segmented in rings and strips which feature a much smaller solid angle each compared to the rear side of the Barrel detectors. Thus, the number of the δ-electrons hitting the CD segments is low enough to be below the detection threshold of the ring or of the strip.

5.4.2 Particle-γ-ray Coincidences

The excitation energy spectrum of BCD and the γ-ray gated excitation energy spectrum of the BBarrel already indicate that not only the ground state and the 2_1^+ state are populated in the 2n transfer reaction, but also a significant amount of higher lying states. As the energy resolution of the T-REX is not sufficient to disentangle single states, the excellent energy resolution of MINIBALL is exploited. The characteristic γ-rays detected in MINIBALL allow to identify the populated states. Fig. 5.19 a) and b) show the background corrected spectrum of all γ-rays which are emitted in coincidence with a transfer proton. For comparison, the state of the art level scheme of ^{74}Zn is visualized in fig. 5.20 a) [13]. The identified γ-ray transitions of this 2n transfer experiment are highlighted with blue solid arrows. The strongest γ-ray lines belong to the $2_1^+ \rightarrow 0_1^+$ and the $4_1^+ \rightarrow 2_1^+$ transitions. Additionally, two transitions from the (2_2^+) state have been observed. Moreover, the cascade $2675\,\text{keV} \rightarrow 2099\,\text{keV} \rightarrow 2_1^+$ is identified[15]. Furthermore, there is a third state at $2354\,\text{keV}$ with an unknown J^π assignment which decays through the 2_1^+ state. In addition, there are two unassigned γ-ray lines at $E_\gamma = 493\,\text{keV}$ and $E_\gamma = 539\,\text{keV}$. Due to their low intensity it is not clear if they are emitted in coincidence with the strongest $2_1^+ \rightarrow 0_1^+$ transition in ^{74}Zn. Hence, they cannot be related unambiguously to the level scheme of ^{74}Zn, although an assignment to other background reactions such as the 1n transfer to ^{73}Zn

---

[12]Introducing a threshold for the strip signal to eliminate the δ-electrons is not possible, as the strip signal is used to extract the position of a hit on the strip (c.f. sec. 3.3).

[13]The dependence of the δ-electron noise as a function of the beam intensity can be seen by plotting the excitation energy as a function of the release curve of the beam, i.e. the time difference between the detector signal and the last proton pulse on the primary ISOLDE target (c.f. sec. 3.1.1).

[14]Additionally, the innermost strip of the BBarrel has also been excluded in the analysis as the δ-electron noise dominates the transfer proton signal.

[15]Note, that the spin and parity of the $2675\,\text{keV}$ and $2099\,\text{keV}$ states are not known yet.
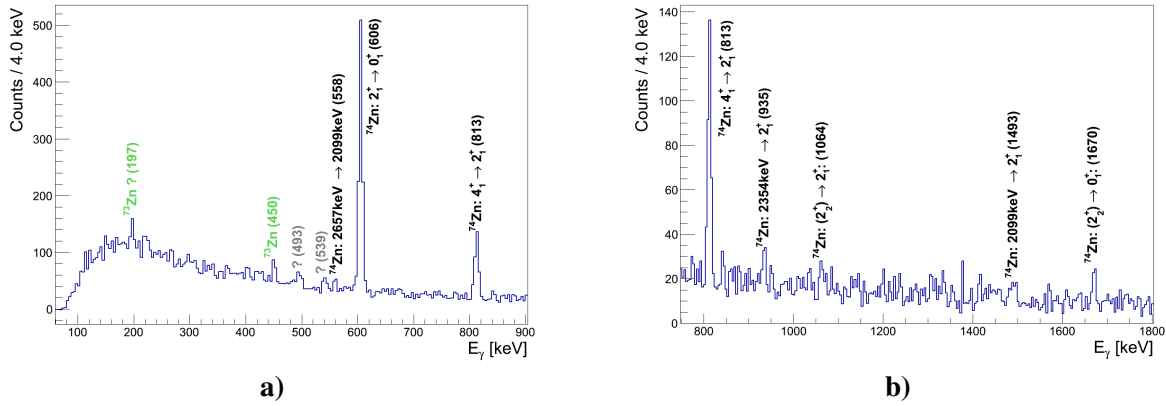
Fig. 5.19: a) and **b)** The Doppler corrected and background subtracted (c.f. sec. 5.1.1) γ-ray spectrum of all γ-rays which were emitted in coincidence with a transfer proton. Spectrum b) shows a zoomed view of spectrum a) on γ-ray energies above $E_\gamma = 750$ keV. In brackets the γ-ray energy of the corresponding transition is given. The black γ-ray transition can be clearly assigned to ^{74}Zn, while the green γ-ray transitions belong to ^{73}Zn. In gray the transitions which cannot be assigned are marked.
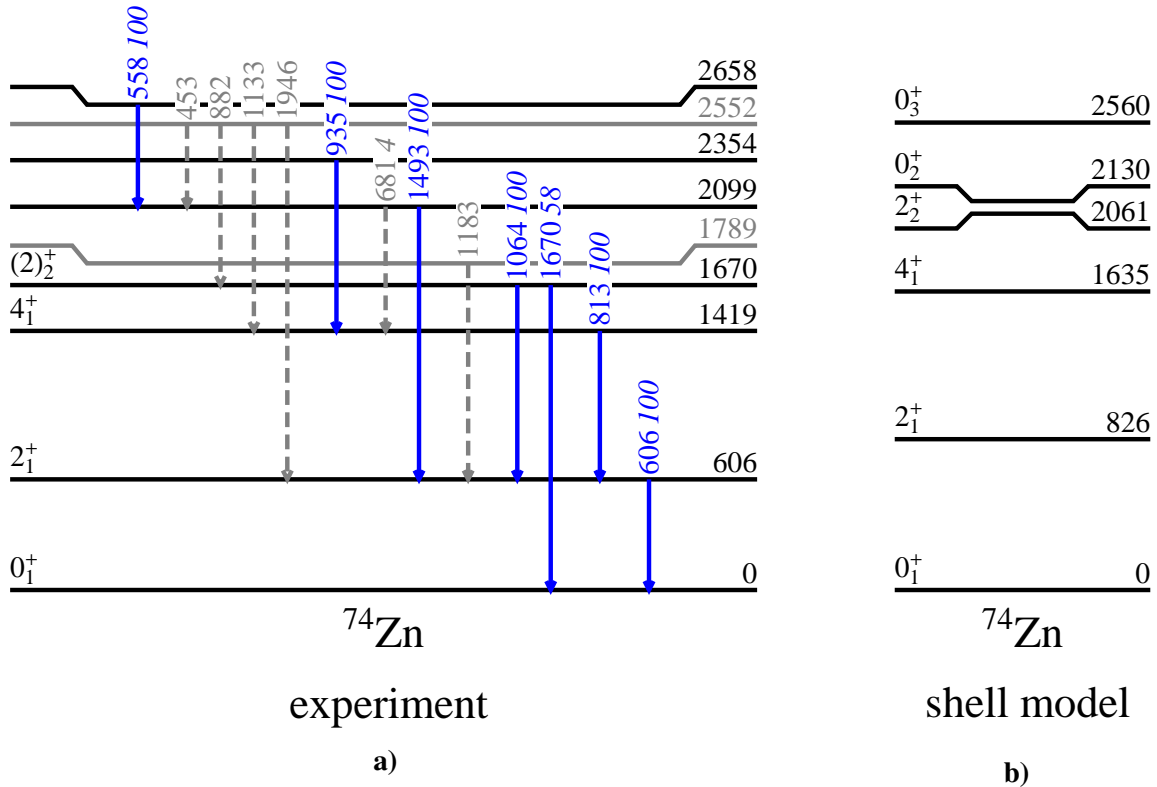

Fig. 5.20: a) An excerpt of the level scheme of ^{74}Zn measured with ^{74}Cu β-decay experiments [111, 112]. In a Coulomb excitation experiment at ISOLDE, the level at 1419 keV was assigned to be the 4_1^+ state [41]. The levels and transitions which have been observed in the 2n transfer experiment are marked in black and blue, respectively. The gray levels and the dashed gray transitions have not been identified in this experiment. Data taken from [13]. **b)** The level scheme which is obtained from a shell model calculation using the jj44 model space ($1f_{5/2}$, $2p_{3/2}$, $2p_{1/2}$ and $1g_{9/2}$ orbitals for protons and neutrons) and the jj44bpn interaction [110].

or to reactions with the beam contaminant (e.g. ^{72}Ga) is unlikely, too (c.f. sec. 5.4.3). Apart from that, a small contamination of ^{73}Zn is present, since its strongest γ-ray transition with $E_\gamma = 450$ keV is visible. This indicates that some deuterons are misidentified as protons.

From which states the identified γ-rays originate can be estimated by correlating the γ-ray energy with the calculated excitation energy of the transfer protons (c.f. fig. 5.17 b)): Fig. 5.18 b) and 5.17 b) reveal that the 2_1^+ state at $E_{ex} = 606$ keV is only to a small amount populated directly. Instead, feeding from higher lying states around $E_{ex} \approx 5$ MeV into the 2_1^+ state is preferred due the high Q-value ($Q = 5.24$ MeV) of the 2n transfer reaction. Furthermore, all counts in the $4_1^+ \rightarrow 2_1^+$ transition of fig. 5.19 result from feeding, whereas the direct population of the 4_1^+ state is not observed (c.f. fig. 5.17 b)). The direct population is kinematically suppressed, as for a 4_1^+ state an angular momentum transfer of the two neutrons with $\Delta l = 4$ from the ^{72}Zn ground state is required (c.f. sec. 2.2.2). Apart from that, all other states, which have been identified in the γ-ray spectra in fig. 5.19, feature a dominating feeding contribution from states around the reaction Q-value ($Q = 5.24$ MeV). In summary, only the ground state and the 2_1^+ state of ^{74}Zn are populated directly with sufficient statistics. Hence, their differential cross sections are determined and discussed in sec. 5.4.3.

5.4.3 Differential Cross Sections

From the obtained data the differential cross sections of the ground state and the 2_1^+ state of ^{74}Zn were calculated. Furthermore, an upper limit for the cross section of the unknown 0_2^+ state was determined. All cross sections were extracted using the method which has been described in sec. 5.1.2. Only the backward detectors have been considered, as the FBarrel hits do not show a significant contribution to the direct population of these states.

Peak at $E_{ex} \approx 600$ keV Excitation Energy
In the BCD excitation energy spectrum the $E_{ex} \approx 600$ keV peak is well separated from the ^{74}Zn ground state at $E_{ex} \approx 0$. The $E_{ex} \approx 600$ keV peak is a candidate for the 2_1^+ state at 606 keV level energy of ^{74}Zn. Its differential cross section, obtained solely from the counts in the excitation energy spectrum of the BCD, is shown with blue upper triangles in fig. 5.22. However, the shape of the cross section is not typical for transfer reactions to the 2_1^+ state, since it peaks around zero, while a maximum between $\theta_{CM} = 20°$ and $\theta_{CM} = 40°$ is expected (c.f. fig. 2.2 a)). Hence, the hypothesis that the $E_{ex} \approx 600$ keV can be assigned to the 2_1^+ state of ^{74}Zn was carefully tested, especially since the missing particle identification capability in the backward detectors of T-REX does not allow to exclusively select a reaction channel. Therefore, the mean energy of the peak at $E_{ex} \approx 600$ keV in the excitation energy spectrum, which is calculated assuming a 2n transfer reaction to ^{74}Zn, is the only indication for the 2_1^+ state in ^{74}Zn. To unambiguously identify the reaction channel, the characteristic γ-ray decay of the 2_1^+ state to the ground state with $E_\gamma = 606$ keV has been studied. In the following, the γ-ray gated excitation energy spectra of the BCD and the BBarrel are discussed:
Gating on an additional γ-ray with $E_\gamma(2_1^+ \rightarrow 0_1^+) = 606$ keV,

$$N_{pred} = N_{600\,\text{keV peak}} \cdot \epsilon_{MB} = (43.5 \pm 11.06) \cdot \epsilon_{MB} = 2.88 \pm 0.73 \tag{5.9}$$

counts in the BCD excitation energy spectrum are expected. $N_{600\,\text{keV peak}}$ is the number of counts in the $E_{ex} \approx 600$ keV peak of the BCD spectrum shown in fig. 5.18a) and ϵ_{MB} corresponds to the MINIBALL efficiency at $E_\gamma = 606$ keV. Fig. 5.23 a) displays the γ-ray gated excitation energy spectrum of the BCD. Using the signal and background regions[16] as defined in fig. 5.23 a), zero counts are observed

---

[16]Note that the same signal and background regions have also been used to determine the cross section of the $E_{ex} \approx 600$ keV peak.
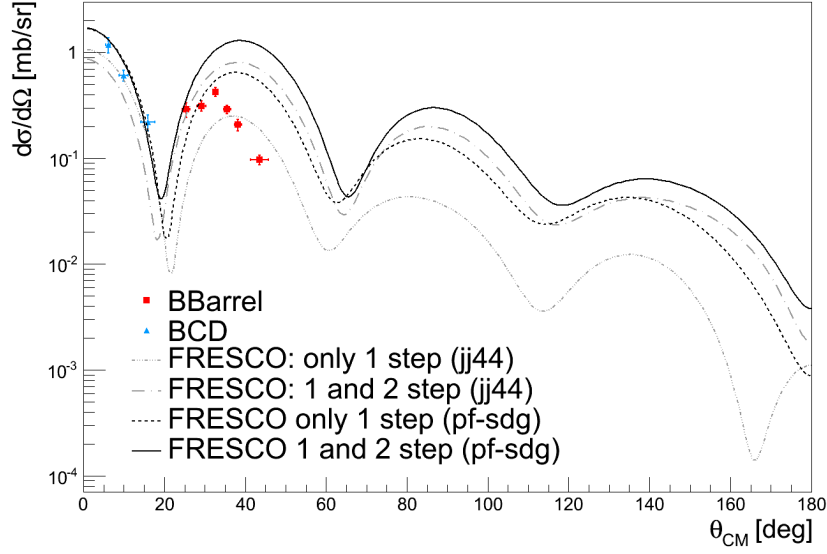
Fig. 5.21: The experimental differential cross section of the ^{74}Zn ground state as a function of the scattering angle θ_{CM} in the center-of-mass frame. Additionally, theoretical calculations which were performed with FRESCO using shell model input are presented. Two shell model calculations are shown: First, a calculation was performed in the jj44 model space ($1f_{5/2}$, $2p_{3/2}$, $2p_{1/2}$ and $1g_{9/2}$ orbitals for protons and neutrons) and using the jj44bpn interaction. Second, a calculation using an extended model space ($fp-sdg$) done by B.A. Brown is shown. In both calculations two cases have been considered: first, the simultaneous transfer of the two neutrons (1 step) and second, the sequential 2 step process is considered in addition. For a detailed discussion, see text.

Fig. 5.22: The experimental differential cross section of the $E_{ex} \approx 600$ keV peak and the 2_1^+ state of ^{74}Zn (at 606 keV) as a function of the scattering angle θ_{CM} in the center-of-mass frame. Additionally, theoretical calculations which were performed with FRESCO using shell model input are presented. Two shell model calculations are shown: First, a calculation was performed in the jj44 model space ($1f_{5/2}$, $2p_{3/2}$, $2p_{1/2}$ and $1g_{9/2}$ orbitals for protons and neutrons) and using the jj44bpn interaction. Second, a calculation using an extended model space ($fp-sdg$) done by B.A. Brown is shown. In both calculations two cases have been considered: first, the simultaneous transfer of the two neutrons (1 step) and second, the sequential 2 step process is considered in addition. For a detailed discussion, see text.
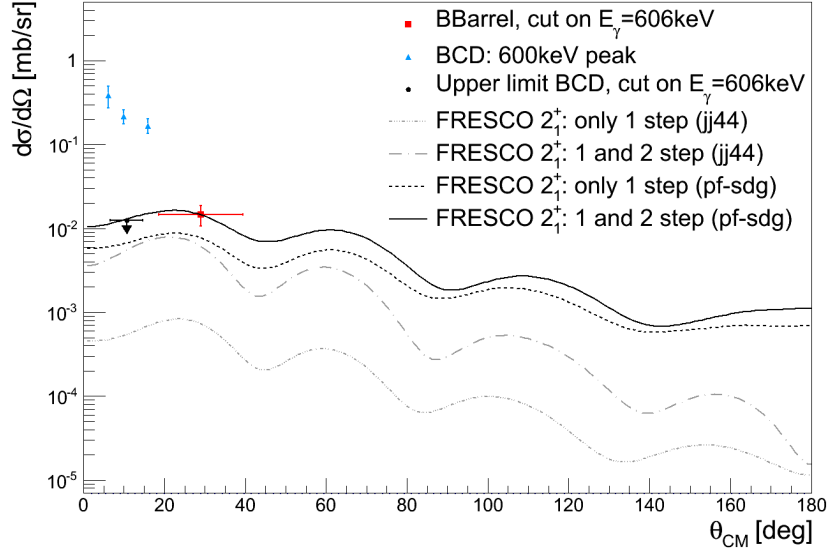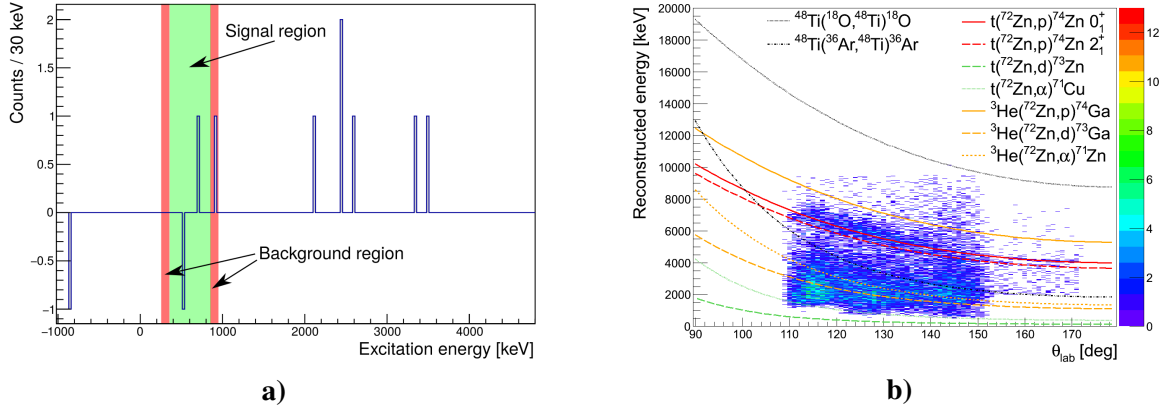
a)

b)

Fig. 5.23: a) The excitation energy spectrum of the BCD quadrants Left and Bottom with an additional cut on the γ-ray energy $E_\gamma = 606\,\text{keV}$ in MINIBALL. Note, that the BCD Top and Right quadrant were not fully operational in the experiment and are therefore excluded in the analysis. The negative counts results from a background subtraction which accounts for the fact that the photopeak of the $2_1^+ \rightarrow 0_1^+$ γ-ray transition is superimposed with a background (e.g. originating from Compton scattered γ-rays from higher lying transitions) in the γ-ray spectrum. The green area visualizes the signal region of the $E_{ex} \approx 600\,\text{keV}$ peak in the ungated BCD spectrum, whereas the neighboring red regions show the background regions. The obtained zero counts in the signal region indicate that the peak at $E_{ex} \approx 600$keV does not fully correspond to the 2_1^+ state in ^{74}Zn, since 2.88 ± 0.73 counts are expected. The counts at higher excitation energies result from higher lying states which deexcites through the 2_1^+ state. **b)** The detected particle energy in the T-REX ΔE-E telescopes as a function of the scattering angle θ_{lab} in the laboratory frame. Additionally, the predicted kinematics of dominant reaction channels of the experiment which feature a light charged particle in the exit channel are shown. As they disagree with the $E_{ex} \approx 600\,\text{keV}$ peak, i.e. with the kinematic line of the 2n transfer to the 2_1^+ state in ^{74}Zn, they cannot explain the excess of the counts in the $E_{ex} \approx 600\,\text{keV}$ peak.

in the $E_{ex} \approx 600\,\text{keV}$ peak of the γ-ray gated BCD spectrum. The probability $P(N_{obs})$ of observing N_{obs} counts is given by the Poisson statistics [113]

$$P(N_{obs}) = \frac{N_{pred}^{N_{obs}}}{N_{obs}!} \exp(-N_{pred}). \qquad (5.10)$$

The probability of observing $N_{obs} = 0$ counts, while $N_{pred} = 2.88 \pm 0.73$ are predicted, is $P(0) = (5.6 \pm 4.1)\%$. Therefore, the γ-ray gated excitation energy spectrum of the BCD does not support the interpretation that the $E_{ex} \approx 600\,\text{keV}$ peak corresponds fully to the 2_1^+ state. Although zero counts have been observed the γ-ray gated excitation energy spectrum of the BCD, they can be used to calculate an upper limit for the cross section of the 2_1^+ state using Feldman-Cousins approach [114]:

$$\left(\frac{d\sigma}{d\Omega}\right)_{\text{upper limit}}^{1\sigma\,\text{CL}} (2_1^+) = 0.013 \,\frac{\text{mb}}{\text{sr}} \quad \text{for a } 1\sigma \text{ confidence level and}$$

$$\left(\frac{d\sigma}{d\Omega}\right)_{\text{upper limit}}^{2\sigma\,\text{CL}} (2_1^+) = 0.11 \,\frac{\text{mb}}{\text{sr}} \quad \text{for a } 2\sigma \text{ confidence level.} \qquad (5.11)$$

Both upper limits are in agreement with the calculated cross section of the 2_1^+ state of ^{74}Zn (c.f. fig. 5.22).

Apart from that, the BBarrel excitation energy spectrum with an additional γ-ray cut on $E_\gamma = 606\,\text{keV}$ was used to determine the cross section of the 2_1^+ state of ^{74}Zn. It is visualized in fig. 5.18 b). With a total of only 13 observed events, only a mean differential cross section for the whole BBarrel could be calculated (c.f. fig. 5.22). It is consistent with the upper limit of eq. (5.11), determined with the γ-ray gated BCD spectrum. But, it is more than one magnitude below the cross section of the $E_{ex} \approx 600\,\text{keV}$

peak, obtained from the ungated BCD excitation energy spectrum.

In summary, combining the conclusions drawn with the γ-ray gated excitation energy spectra from the BCD and the BBarrel, there are strong indications that the majority of the counts in the $E_{ex} \approx 600$ keV peak cannot be attributed to the 2_1^+ state of ^{74}Zn. In the following, possible origins of the $E_{ex} \approx 600$ keV peak are discussed: Due to the associated events being detected in the BCD, only reactions which feature a charged particle in its exit channel have to be taken into account. Possible reaction channels with charged reaction products are:

- t(^{72}Zn, α)^{71}Cu: α-particles are indeed identified in the ΔE-E telescope of the FBarrel (c.f. fig. 5.1 a)), but their kinetic energy is below the detection threshold of the BBarrel and the BCD (c.f. fig. 5.23 b)). Thus, this reaction channel cannot explain the $E_{ex} \approx 600$ keV peak.

- t(^{72}Zn, d)^{73}Zn: Analogously to the (t,α) channel, the transfer deuterons are below the energy thresholds of the T-REX detectors in backward direction (c.f. fig. 5.17 a).

- ^{3}He(^{72}Zn, α)^{71}Zn, ^{3}He(^{72}Zn, p)^{74}Ga and ^{3}He(^{72}Zn, d)^{73}Ga: The kinematics of these reaction channels do not produce a peak corresponding to $E_{ex} \approx 600$ keV in the BCD (c.f. fig. 5.23 b)). ^{3}He can originate from the β-decay of the tritium in the target ($T_{1/2} = 12.3$ y [13]).

- Elastic scattering of the ^{72}Zn beam and its contaminants in inverse kinematics do not contribute to the $E_{ex} \approx 600$ keV peak, as due to the inverse kinematics all particles are scattered in forward direction in the laboratory frame.

- Elastic scattering of beam contaminants in normal kinematics: ^{48}Ti(^{18}O, ^{48}Ti)^{18}O and ^{48}Ti(^{36}Ar, ^{48}Ti)^{36}Ar feature different kinematics compared to the kinematics of the transfer protons after the 2n transfer to the 2_1^+ state of ^{74}Zn (c.f. fig. 5.23 b)).

- Reactions with the beam contaminants ^{72}Ga, ^{36}Ar and ^{18}O are unlikely to produce reaction cross sections in the order of 1 mb/sr, since they are suppressed by at least a factor of 50 due to their low beam intensity (c.f. tab. 5.1).

To sum up, the listed reactions cannot explain the $E_{ex} \approx 600$ keV peak in the BCD excitation energy spectrum. Furthermore, fusion and break-up reactions (e.g. t(^{72}Zn, pn)^{73}Zn) with the target carrier material ^{48}Ti or with ^{3}H featuring more than two particles in the exit channel are negligible, since they would not result in a sharp peak in the BCD excitation energy spectrum. Furthermore, unexpected detector effects cannot be fully excluded, although the $E_{ex} \approx 600$ keV peak is visible in the ring and the strip signal of all operational detectors. Apart from that, a similar not fully understood peak is present in the t(^{66}Ni, p)^{68}Ni experiment [27] (c.f. also sec. 5.4.4), which was conducted directly before the ^{72}Zn transfer experiment. In conclusion, the origin of the $E_{ex} \approx 600$ keV peak in the BCD is still unclear, but it cannot be fully assigned to the 2_1^+ state in ^{74}Zn.

Ground State of ^{74}Zn

The ground state is clearly visible in the BBarrel and in the BCD excitation energy spectrum (c.f. fig. 5.18). However, due to the different energy resolution of both detectors, it can only be separated from the energetically close lying $E_{ex} \approx 600$ keV peak in the BCD. The peak around zero in the BBarrel excitation energy spectrum corresponds to the ^{74}Zn ground state as well as to the $E_{ex} \approx 600$ keV peak. The 2_1^+ component of the $E_{ex} \approx 600$ keV peak is negligible, since the 2_1^+ state is populated only weakly compared to the ground state (c.f. fig. 5.18 b)). Additionally, the influence of the background component of the $E_{ex} \approx 600$ keV peak seems to decrease with decreasing θ_{lab} angles: For all angular bins, expect the angular bin close to the BCD, the peak maximum is at $E_{ex} \approx 0$ keV and its shape can be well described with a single, symmetric Gaussian distribution. Only the angular bin close to the BCD features a shift of the peak position to positive excitation energies. Hence, the $E_{ex} \approx 600$ keV peak has been neglected in the low θ_{lab} ranges. The angular region of the BBarrel which is close to
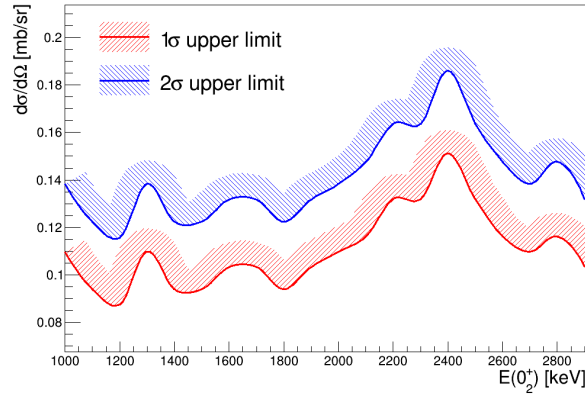
Fig. 5.24: The upper limit for the cross section of the 0_2^+ state of ^{74}Zn obtained with the Feldman Cousins method [114]. As the 0_2^+ state has not been identified in ^{74}Zn yet, the upper limit for cross section is shown as a function of the assumed 0_2^+ level energy $E(0_2^+)$. In the calculation, only the BCD region $\theta_{CM} \in [6°, 16°]$ is used. Hence, the upper limit of the mean differential cross section for this angular range is shown.

the BCD is ignored in the calculation of the differential cross section, as in this θ_{lab} region, the counts in the ground state and the counts in the $E_{ex} \approx 600$ keV peak state cannot be determined with the required precision, especially as these two states are superimposed by the δ-electron background[17]. As background model for the δ-electrons an exponential function is used. The obtained differential cross section of the ground state is shown in fig. 5.21 as a function of the scattering angle θ_{CM} in the center-of-mass frame. As expected for angular momentum transfers of $\Delta l = 0$, it features its first maximum at $\theta_{CM} = 0$. However, note that only the cross section determined with the counts in the BCD does not feature a contamination from the $E_{ex} \approx 600$ keV peak, while the cross section in the BBarrel region may be overestimated due to the $E_{ex} \approx 600$ keV peak. The theoretical prediction of the ^{74}Zn ground state cross section using shell model input and FRESCO are discussed in sec. 5.4.4.

Upper Limit for Unobserved 0_2^+ State of ^{74}Zn
The 0_2^+ state in ^{74}Zn has been observed neither in previous measurements [13] nor in the 2n transfer experiment which is discussed in this thesis. Nevertheless, according to the 0_2^+ systematics (c.f. fig. 1.7) and the shell model prediction (c.f. fig. 5.20 b)), it can be concluded that the 0_2^+ state should have an energy above 1 MeV. The clean excitation energy spectrum of the BCD can be used to extract an upper limit for the 0_2^+ cross section in ^{74}Zn as a function of the 0_2^+ energy $E(0_2^+)$. Note, that the BBarrel spectrum is not suited for this analysis as it is dominated by the strong δ-electron background. Fig. 5.24 shows the upper limit of the mean 0_2^+ state cross section using the data of the whole BCD as a function of the assumed 0_2^+ energy. It is determined for two confidence levels (1σ and 2σ) following the method of Feldman Cousins [114]. Assuming a 1σ confidence level, the upper limit of the 0_2^+ cross section is always smaller than $d\sigma/d\Omega = 0.15$ mb/sr for $\theta_{CM} \in [6°, 16°]$. Note, that this estimation is very conservative as it is likely that the 0_2^+ state is superimposed with other highly excited ^{74}Zn states which have not been considered here.

5.4.4 Discussion

A comparison of the experimental cross sections to FRESCO DWBA[18] calculations using shell model input allows to extract nuclear structure information. In FRESCO all possible channels to transfer the

---

[17]A combined fit of two Gaussian functions for the ground state and for the 2_1^+ state including a background model for the δ-electrons does not give reasonable results. The fit performance cannot even be improved if the mean values of the Gaussian distributions are fixed, or if the relative distance between the two peaks are fixed or if additionally the standard deviations of the Gaussian distribution are set to the same value for the ground state and the 2_1^+ state.

[18]DWBA: Distorted Wave Born Approximation, for details c.f. sec. 2.2.

State of ^{74}Zn	$(2p_{3/2})^2$	$(1f_{5/2})^2$	$(2p_{1/2})^2$	$(1g_{9/2})^2$
0_1^+	-0.39	-0.63	-0.45	1.01
0_2^+	-0.03	0.02	-0.10	0.01
0_3^+	-0.01	-0.25	0.01	0.05

Tab. 5.5: The two-neutron-amplitudes (TNAs) for the 2n transfer reaction t(^{72}Zn, p)^{74}Zn obtained from a shell model calculation using the jj44 model space ($1f_{5/2}$, $2p_{3/2}$, $2p_{1/2}$ and $1g_{9/2}$ orbitals for protons and neutrons) and the jj44bpn interaction [108].

two neutrons have to be considered (c.f. sec. 2.2.3). Hence, the total cross section for the 2n transfer reads

$$\frac{d\sigma}{d\Omega} = \left| \underbrace{\sum_i TNA_i \, f_{i,1step}^{DWBA}(\theta_{CM})}_{\text{Direct transfer}} + \underbrace{\sum_{i,j} SA_i \, f_{i,2step}^{DWBA}(\theta_{CM}) \cdot SA_j \, f_{j,2step}^{DWBA}(\theta_{CM})}_{\text{Sequential transfer}} \right|^2 . \qquad (5.12)$$

The first sum runs over all possible configurations i of the direct 2n transfer and the second sum runs over all paths of the sequential neutron transfer. f_i^{DWBA} denotes the scattering amplitude of the pure configuration i. Note that, all reaction channels can interfere with each other. In case of the 1 step transfer the scattering amplitude is weighted with the two-neutron amplitude TNA and in case of the 2 step process the scattering amplitudes are weighted with their corresponding spectroscopic amplitude SA of each step. Since no experimental data for the TNAs and the SAs is available, they have been calculated with a shell model calculation (c.f. tab. 5.5). In the sequential path, only the most dominant channels have been taken into account. Like in the case of ^{73}Zn (c.f. sec. 5.3.5), the shell model calculation was performed by Kathrin Wimmer [108] using the NuShellX@MSU code [109] with the jj44 model space ($1f_{5/2}$, $2p_{3/2}$, $2p_{1/2}$ and $1g_{9/2}$ orbitals for protons and neutrons) and the jj44bpn interaction [110]. The level scheme of ^{74}Zn predicted by the shell model calculation is displayed in fig. 5.20 b). Compared to the experimental data (shown in fig. 5.20 a)) the ordering of the states concerning their spins is identical. This is a prerequisite of a reliable shell model calculation. In the following, the theoretical cross sections are compared to the experimental data of the present 2n transfer experiment.

In addition to the discussion of the agreement between experimental cross sections and the theoretical DWBA cross sections using shell model input, the obtained experimental cross sections are compared to previous 2n transfer experiments which were performed on the neutron-rich zinc isotopes [52] (c.f. fig. 1.9 b)). However, a direct comparison is not possible, as the triton beam energy of these experiments was $E_t = 12$ MeV, while the 2n transfer experiment which is discussed in this thesis features a lower triton energy of $E_t = 8.1$ MeV in normal kinematics. Hence, due to the lower beam energy, a FRESCO calculation estimates that the cross sections in this thesis are roughly a factor of 1.8 lower.

Ground State of ^{74}Zn

In fig. 5.21, the cross section of the ^{74}Zn ground state is compared to two FRESCO calculations using a shell model calculation in the jj44 model space ($1f_{5/2}$, $2p_{3/2}$, $2p_{1/2}$ and $1g_{9/2}$ orbitals for protons and neutrons) and the jj44bpn interaction [110] as input: First, to the theoretical cross section which is obtained if only the simultaneous transfer of the two neutrons (1 step process) is considered and second, to the cross section which results if additionally the sequential path via intermediate ^{73}Zn (2 step process) is included.

Fig. 5.21 indicates that the 1 step process describes the experimental data for the transfer to the ground state well. According to the TNAs (c.f. tab. 5.5) and the difference in occupation number of the ^{74}Zn and the ^{72}Zn ground state (c.f. fig. 5.25 a)), the two neutrons are both transferred in about 60% of the
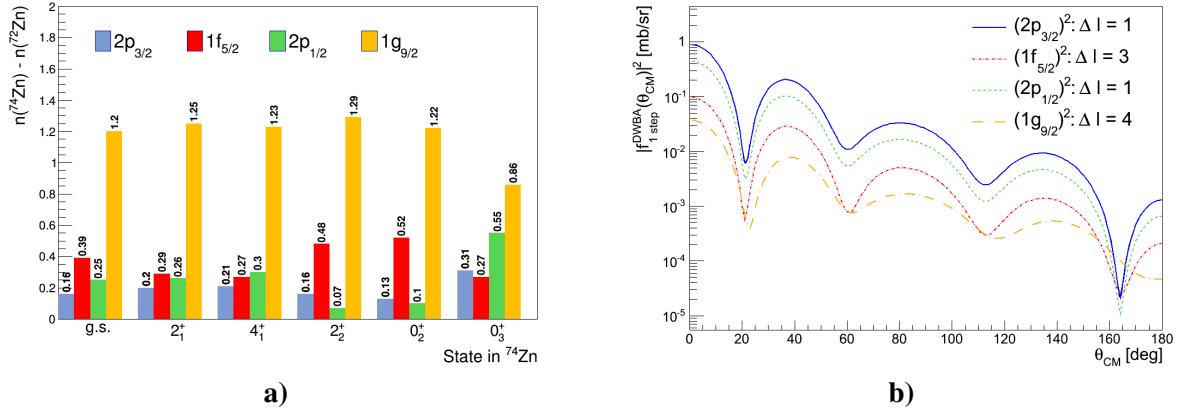
Fig. 5.25: a) The difference in occupation numbers of the low lying ^{74}Zn states and the ^{72}Zn ground state. Hence, the bar chart shows in which orbitals the two neutrons from the 2n transfer reaction t(^{72}Zn, p)^{74}Zn are transferred. Here the same assumption as in the FRESCO DWBA calculation is made: The proton configuration is the same in ^{72}Zn and in ^{74}Zn. This assumption may not be fully fulfilled in the zinc isotopes due to their two protons outside the magic $Z = 28$ shell. The occupation numbers have been obtained from a shell model calculation using the jj44 model space ($1f_{5/2}$, $2p_{3/2}$, $2p_{1/2}$ and $1g_{9/2}$ orbitals for protons and neutrons) and the jj44bpn interaction [110]. **b)** The 1 step 2n transfer cross sections / scattering amplitudes $d\sigma/d\Omega = |f_{1step}^{DWBA}|^2$ to the ^{74}Zn ground state assuming only a single pure configurations each. Comparing the cross sections of the different two neutron configurations reveals that with increasing momentum transfer Δl of the single neutrons the cross section decreases. Hence, taking only the angular momentum matching into account, the two neutrons are dominantly transferred to the p-shell.

cases to the $1g_{9/2}$ orbital. The huge $TNA((1g_{9/2})^2)$ dominates the cross section, although the $(1g_{9/2})^2$ configuration kinematically suppresses the cross section due to the large transferred momentum $\Delta l = 4$ for each neutron (c.f. sec. 2.2.2). The influence of the angular momentum transfer Δl of the neutrons is visualized in fig. 5.25 b) which shows the 2n transfer cross section from the ^{72}Zn ground state to the ^{74}Zn ground state for all possible pure configurations (i.e. assuming all $TNA = 1$) in the considered model space.

However, including also the 2 step process the agreement between the experimental data and the shell model prediction slightly deteriorates using the shell model calculation in the jj44 model space (c.f. fig. 5.21). One possible reason for this discrepancy can be that the sequential transfer is not perfectly modeled due to the large number of possible intermediate states in ^{73}Zn which feature experimentally unknown spectroscopic factors. Moreover, if additionally all other orbits of the pf- and of the sdg-shell are included in the calculation using a perturbation approximation [115], the measured cross section can be reproduced. However, note that these orbitals are not mandatory to describe the experimental ground state data.

Adapting the ground state cross section of this experiment to the higher beam energies, used in previous 2n transfer experiments with stable zinc isotopes (c.f. fig. 1.9 b)), yields a cross section which is in the same order of magnitude than the results from previous measurements [52].

Excited 0^+ States of ^{74}Zn

Although the 0_2^+ state of ^{74}Zn was not observed in the 2n transfer experiment t(^{72}Zn, p)^{74}Zn an upper limit for the cross section was determined. It can be compared to the prediction of the shell model calculation. According to the level scheme resulting from the shell model in the jj44 model space (c.f. fig. 5.20 b)), two excited 0^+ states have to be considered, since they are relatively close in energy at 1560 keV and at 2130 keV and since their cross sections are predicted to be in the same order of magnitude (at least if only the direct transfer is considered). Their absolute TNAs, which are also given in tab. 5.5, are much smaller than the TNAs of the ground state. This indicates that the excited 0^+ states are only weakly populated compared to the ground state, which is consistent with the experimental

data[19].

Apart from that, in $^{66-70}$Zn the ratio of the 2n transfer cross sections for the 0_2^+ state and the ground state is below $\sigma_{max}(0_2^+)/\sigma_{max}(0_1^+) = 0.04$. However, it increases to $\sigma_{max}(0_2^+)/\sigma_{max}(0_1^+) = 0.11$ for ^{72}Zn. In the current experiment the ratio $\sigma_{max}(0_2^+)/\sigma_{max}(0_1^+)$ is estimated to be less than $\sigma_{max}(0_2^+)/\sigma_{max}(0_1^+) = 0.2$ for 0_2^+ state energies between 1 and 2 MeV and less than $\sigma_{max}(0_2^+)/\sigma_{max}(0_1^+) = 0.3$ for 0_2^+ state energies between 2 and 3 MeV using the 1σ confidence level of the upper limit, which is consistent with data of ^{72}Zn. Thus, the statistics and the sensitivity of the 2n transfer experiment is not sufficient to describe the evolution of the 0_2^+ cross sections in the neutron-rich Zn isotopes. Nevertheless, the small 0_2^+ 2n transfer cross section compared to the ground state cross section indicates that both states seem to have a different structure, while the structure of the ^{72}Zn ground state and the ^{74}Zn ground state is similar. The nature of the 0_2^+ state in ^{72}Zn is further discussed in the Coulomb excitation experiment in sec. 6.4.

Note, that the interpretation of the cross sections and the occupation numbers is only a qualitative discussion, as interference terms between the different configurations can play a crucial role. Furthermore, the sequential transfer can be important. However, it is challenging to model the 2 step process, as the populated states of the intermediate ^{73}Zn nucleus with the corresponding spectroscopic factors have not been measured yet. Hence, the results can be very model dependent.

2_1^+ State of ^{74}Zn

After discussing the 0^+ states, the cross section of the 2_1^+ state is reflected. Fig. 5.22 shows its experimental cross section compared to FRESCO calculations which are based on the shell model input. However, the calculated DWBA cross section of the 2_1^+ state using the jj44 model space and the jj44bpn interaction shows a discrepancy of almost one order of magnitude. The same phenomenon has also been observed in the 2_1^+ state of ^{68}Ni which has been populated via the 2n transfer reaction t(^{66}Ni, p)^{68}Ni [27]. In both nuclei, the agreement between the theoretical calculation and the experimental data is improved, if additionally all other orbits of the pf- and of the sdg-shell are included in the calculation using a perturbation approximation [115] (c.f. fig. 5.22). Especially, the $2d_{5/2}$-neutron-orbit, which is above the $1g_{9/2}$ orbit, should play a significant role. A scattering of the two neutrons across the magic $N = 50$ shell gap into the $2d_{5/2}$ orbital would indicate that the $N = 50$ shell gap it not very pronounced in ^{68}Ni and ^{74}Zn compared to nuclei featuring nearly 50 neutrons. This is in agreement with a shell model calculation done by K. Sieja and F. Nowacki using a large model space (pf for protons, $fpgd$ for neutrons) [116]. However, it has to be noted that the theoretical DWBA calculation is based on many parameters which have not been experimentally confirmed. Hence, it is not excluded that the theoretical calculation can also reproduce the experimental 2_1^+ cross section without including neutron orbitals above $N = 50$.

Furthermore, the 2_1^+ cross section of ^{74}Zn is compared to previous 2n transfer experiments with stable zinc isotopes [52]. For $^{66-72}$Zn the previous measurements feature a ratio between the maximum of the 2_1^+ cross section and the 0_1^+ cross section of about $\sigma_{max}(2_1^+)/\sigma_{max}(0_1^+) \approx 0.03$ which is consistent with the current experiment $\sigma_{max}(2_1^+)/\sigma_{max}(0_1^+) \approx 0.025 \pm 0.008$.

---

[19]An explicit calculation of the 0_2^+ (as well as of the 0_3^+) cross section was not performed, as the sequential transfer can play a crucial role. Its influence cannot be estimated in a reliable way since the spectroscopic amplitudes as well as the levels of the intermediate ^{73}Zn nucleus cannot be calculated with sufficient precision. Even for the 2_1^+ state the 2 step processes seems to be modeled incorrectly (c.f. fig. 5.22)). Apart from that, in the Coulex experiment of this thesis, it has been shown that the 0_2^+ state of ^{72}Zn is not described correctly by the shell model calculation using the jj44bpn interaction. Thus, it is likely that the same deviation is present in ^{74}Zn.

6

Multiple Coulomb Excitation of ^{72}Zn

This chapter deals with the results of the multiple Coulomb excitation experiment of ^{72}Zn studying the structure of the yrast band as well as of the 0_2^+ and the 2_2^+ state in ^{72}Zn. In sec. 6.1, the data analysis is detailed: Here the particle identification is described, the experimental setup is characterized and coincidences between scattered ions and γ-rays are evaluated. The main results are Doppler corrected γ-ray spectra for all detectors. Their excellent statistics allows to determine the yields of a large number of γ-ray transitions even from higher lying states of the projectile ^{72}Zn and the target ^{109}Ag. These γ-ray yields are subsequently used to extract large sets of electromagnetic matrix elements for ^{72}Zn and ^{109}Ag by comparing them to γ-ray yields predicted by theory (c.f. sec. 6.2). Finally, in sec. 6.3, the obtained ^{72}Zn matrix elements are discussed. They are compared to other experimental results for ^{72}Zn and interpreted in the context of modern mean field and shell model calculations.

6.1 Data Analysis

The precision of the resulting matrix elements of the nucleus studied via Coulomb excitation depends strongly on the quality of the Doppler corrected γ-ray spectra (c.f. sec. 6.1.5). The Doppler correction itself is influenced by many factors: the precise knowledge of the experimental setup (c.f. sec. 4.4, 6.1.1, 6.1.2 and 6.1.3) including its calibration (c.f. chap. 4), the choice of the target which defines the reaction kinematics (c.f. sec. 6.1.1) and the background subtraction (c.f. sec. 6.1.4).

6.1.1 Reaction Kinematics and Particle Identification

The ^{72}Zn Coulex experiment was performed at the ISOLDE facility using the C-REX silicon array which is coupled to the MINIBALL γ-ray spectrometer (c.f. sec. 3.4 and 3.2). The angular coverage of C-REX restricts the choice of the target material which is used to excite the ^{72}Zn beam. To obtain a good Doppler correction (c.f. sec. 4.4.1), it is essential that C-REX is capable to identify the particle type (ejectile $\hat{=}$ beam-like particle or recoil $\hat{=}$ target-like particle) over its whole covered angular range. Hence, according to the reaction kinematics it is important that the beam and the target do not feature a similar mass. Furthermore, it is crucial to disentangle the γ-rays of the beam and the target in the Doppler-corrected spectra: The γ-ray lines of interest of ^{72}Zn should not be close in energy to the γ-ray lines of the target material. Moreover, as emphasized in sec. 6.2, the electromagnetic matrix elements of the target should be known, since this allows to use the γ-ray yields of the target excitation to normalize the γ-ray yields of the beam excitation (c.f. sec. 6.2.1). The advantage of this normalization is that a lot of systematic errors, such as the imprecise knowledge of the beam intensity, are canceled. Furthermore, the target material has to be a stable element and has to be suitable to produce a thin target foil with high purity out of it. As a result of these considerations, a 1.17 mg/cm^2 thick ^{109}Ag target[1] was chosen for the ^{72}Zn Coulex experiment which fulfills all the mentioned requirements.

Reaction Kinematics
The reaction kinematics, i.e. the energy of the ejectile and the recoil as a function of the scattering

---

[1] The target thickness has been determined by Josef Lichtinger with his high precision setup for the determination of the thickness of human brain tissues [88]. The thickness is extracted (position dependent) by a comparison of the measured energy loss to the calculated energy loss of α-particles through the material [89].
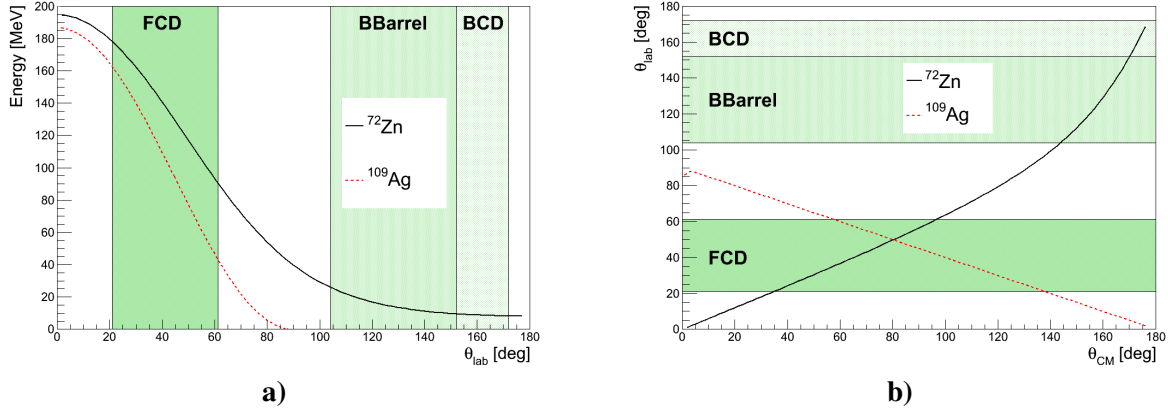
Fig. 6.1: a) The reaction kinematics, i.e. the kinetic energy of the nucleus as a function of its scattering angle of a 2.85 MeV/u ^{72}Zn beam which impinges on a 1.17 mg/cm^2 thick ^{109}Ag target. For the calculation, it is assumed that the reaction occurs in the middle of the target, i.e. the energy loss of the nuclei in the target is considered. Due to the normal kinematics, the ^{72}Zn ions can be scattered into every direction while the recoiling ^{109}Ag is only scattered in forward direction. **b)** The relation between the center-of-mass scattering angle θ_{CM} (of ^{72}Zn) and the scattering angles of the ^{72}Zn and the ^{109}Ag ions in the laboratory frame. In both figures the green shaded areas show the angular coverage of the C-REX detectors.

angle θ_{lab} in the laboratory frame, of a ^{72}Zn beam (E_{beam}=2.85 MeV/u) impinging on a 1.17 mg/cm^2 thick ^{109}Ag target is shown in fig. 6.1. Due to the normal kinematics[2], the ^{72}Zn beam is scattered into all angles θ_{lab}, while the ^{109}Ag particles are restricted to the forward direction ($\theta_{lab} < 90°$). Hence, the Forward CD (FCD) detects both particle species, whereas the Backward Barrel (BBarrel) and the Backward CD (BCD) only detect the scattered ^{72}Zn ions. Fig. 6.2 a) shows the two dimensional distribution of the detected energy of the C-REX detectors and the scattering angle θ_{lab} in the laboratory frame. To guide the eye kinematic lines for the beam and the target as well as for the beam contaminants are included in fig. 6.2 a). They are obtained assuming that the reaction happens in the middle of the target. In addition to the energy loss in the target, the energy loss in the dead layers of the silicon detectors is considered (c.f. sec. 4.2). The effect of the target thickness is shown in fig. 6.2 b) which visualizes the reaction kinematics for the cases that the reaction happens at the beginning, in the middle or at the end of the target. As these kinematic lines are not overlapping, it is in principle possible to discriminate between ^{72}Zn and ^{109}Ag in the whole angular region covered by the detectors.

Particle Identification
For a good Doppler correction, the velocity of the nucleus which emits the γ-ray has to determined properly. Thus, it is important that the detected particle is correctly identified. Nevertheless, the ^{72}Zn and the ^{109}Ag region are not clearly separated in fig. 6.2 a). However, the separation is improved if only events which feature a γ-ray in coincidence[3] within $1\,\mu s$ are considered (c.f. fig. 6.2 c)). The improved visual separation results mainly from the fact that the dominating Rutherford scattering is suppressed by an additional γ-ray cut. Using this coincidence dataset, the identification cuts (shown in fig. 6.2 c)) can be easily defined for each particle type. The events in the innermost ring of the FCD are not considered in the analysis as the peaks of the scattered particles feature significant tails to the lower energetic side. This is caused by the design of the FCD silicon detectors: As the first ring is close to the edge of the detector, the applied electric field is not strong enough to collect all the created charge from the energy deposition during the shaping time. Therefore, a part of the signal is

---

[2]The situation that the target is heavier than the beam corresponds to the normal kinematics case while the reverse situation is called inverse kinematics.

[3]The chosen coincidence window of $1\,\mu s$ in this analysis step corresponds to the time window which is used to define events in the event builder (c.f. sec. 4.1).
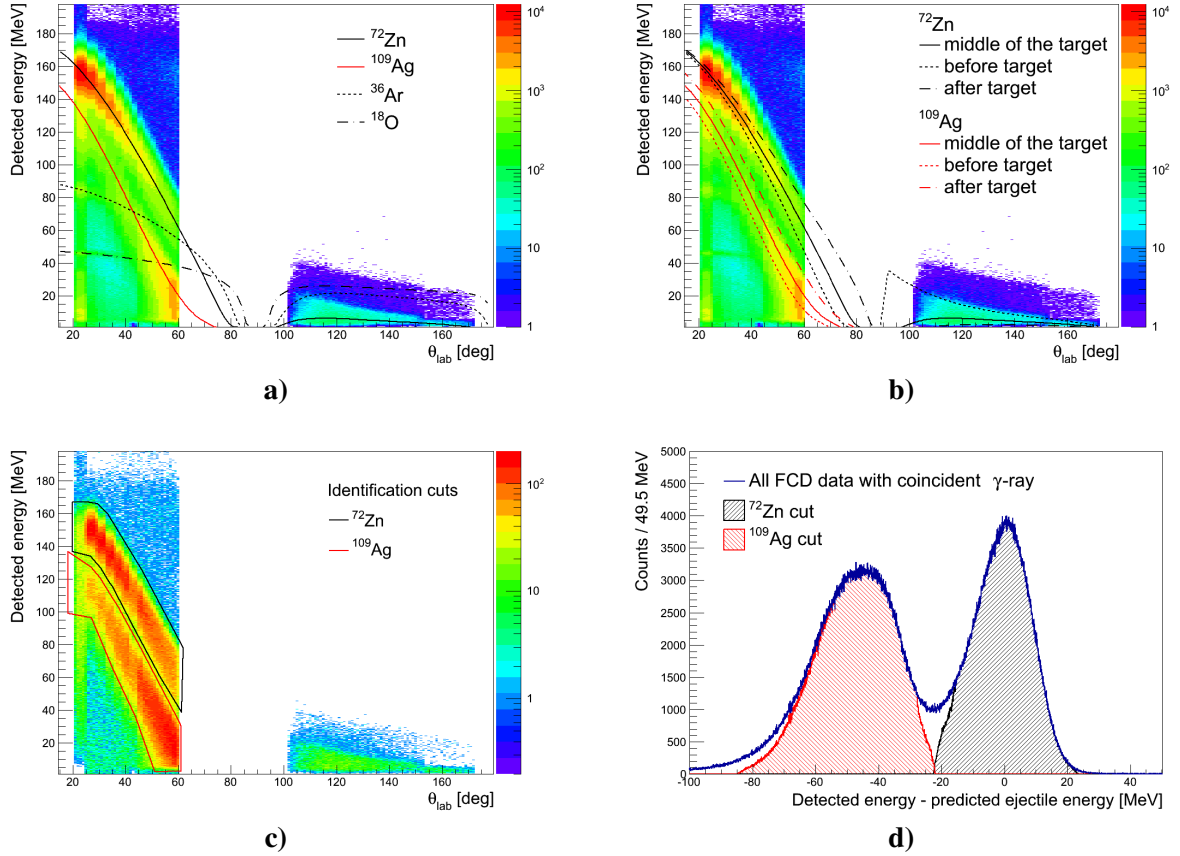
Fig. 6.2: a) The detected particle energy in the C-REX detectors as a function of the scattering angle θ_{lab} in the laboratory frame of all events. The vertical steps visualize the rings of the FCD detector. In the analysis it is assumed that the hits are uniformly distributed on each ring. Additionally, the kinematic predictions for the ^{72}Zn beam and the ^{109}Ag target are displayed. Furthermore, the beam contaminants ^{36}Ar and ^{18}O originating from the EBIS buffer gas are shown. A detailed study of the beam composition is given in sec. 6.1.6 and appendix D.1. **b)** The same plot as a), but the kinematic lines show the influence of the reaction position in the target. The different kinematics result from the dependence of the energy loss on the interaction position in the target. **c)** The detected energy vs. θ_{lab} for events which feature an additional γ-ray in coincidence (within $1\,\mu$s) to the detected particle. Compared to fig. a) and b) the visual separation between the ^{72}Zn and the ^{109}Ag band is significantly improved. The boxes indicate the identification cuts which are used in the analysis. **d)** The distribution of the difference between the detected energy and the calculated mean energy of ^{72}Zn. The peak at zero corresponds to the ^{72}Zn ions while the peak around -50 MeV is attributed to the scattered ^{109}Ag. The clear separation between the peaks shows that both particle types can be well identified. The shaded areas show the particles which are selected by the identification cuts from fig. c). In fig. a), b) and c) all particles in backward direction are assigned as ^{72}Zn.

lost which results in a lower detected energy. Finally, fig. 6.2 d) qualitatively shows the performance of the particle identification in the FCD. The two distinct peaks indicate that the ^{72}Zn and the ^{109}Ag ions are well separated. In backward direction all detected particles are assigned to ^{72}Zn ions as ^{109}Ag ions cannot be scattered in backward direction due to the normal reaction kinematics.

Simultaneous Detection of the Ejectile and the Recoil

Kinematically, it is possible that the ^{72}Zn and the ^{109}Ag nuclei are detected simultaneously in the FCD. These events provide additional information in the Coulex analysis and thus can be used to determine several geometrical properties of the setup with high precision. According to fig. 6.1 b), a simultaneous detection of both scattered reaction partners is possible if the ^{72}Zn scattering angle θ_{CM} in the center-of-mass frame is in the range of $\theta_{CM} \in [57.3°, 96.8°]$. This corresponds to a detection of the

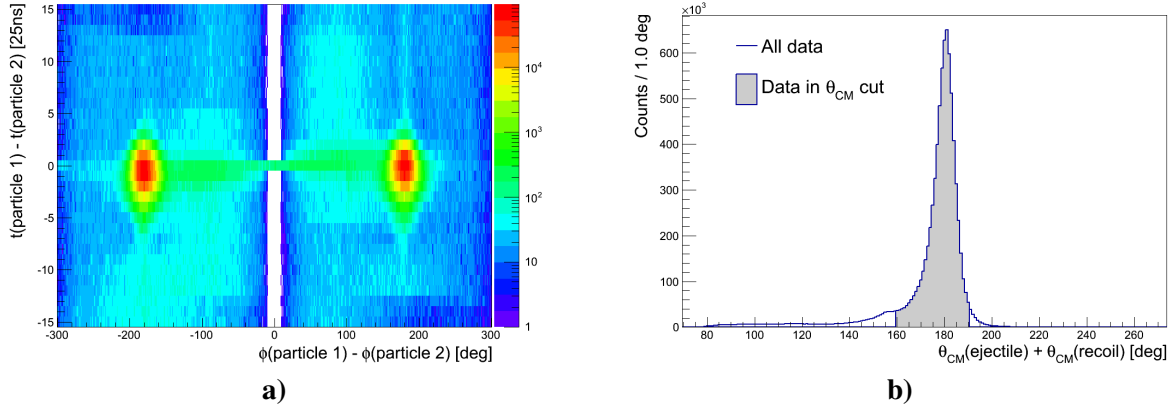a)   b)

Fig. 6.3: a) The time difference between two particles being detected in the same event, i.e. within $1\,\mu s$ versus their difference in the azimuthal angle ϕ. The peaks corresponds to the coincidence events representing scattered ^{72}Zn and ^{109}Ag ions which originate from the same reaction. The background corresponds to random coincidences. **b)** The sum of the center-of-mass scattering angles of the two particles in the same event. The peak contains the ^{72}Zn and ^{109}Ag ions coming from the same reaction. The used coincidence window is shown by the shaded gray area.

^{72}Zn ions in the rings[4] [4, 15] with $\theta_{lab}(^{72}$Zn$) \in [35.9°, 60.2°]$ and of the recoiling ^{109}Ag in the last rings [6, 15] with $\theta_{lab}(^{109}$Ag$) \in [41.8°, 60.2°]$. To disentangle these events from random coincidences, three additional cuts are imposed: First, the ejectile ^{72}Zn and the recoil ^{109}Ag must have similar time-stamps (c.f. fig. 6.3 a)) to ensure that they originate from the same reaction, i.e. they must fulfill the condition $|t(^{72}$Zn$) - t(^{109}$Ag$)| \leq 3 \cdot 25\,$ns. Second, due to momentum conservation both particles are scattered back-to-back, i.e. they must satisfy the condition $|\phi(^{72}$Zn$) - \phi(^{109}$Ag$) - 180°| < 20°$ (c.f. fig. 6.3 a). Furthermore, the kinematics ensure that the sum of the scattering angles in the center-of-mass frame is $180°$. Hence, the third condition $160° < \theta_{CM}(^{72}$Zn$) + \theta_{CM}(^{109}$Ag$) < 190°$ has to be fulfilled (c.f. fig. 6.3 b) and fig. 6.4 a).

This selection results in a rich dataset of about $6.7 \cdot 10^6$ events which allows to extract the exact distance between the FCD and the target (c.f. sec. 6.1.2) and to determine the beam position (c.f. sec. 6.1.3). Furthermore, the dead time of the system can be evaluated (c.f. sec. D.1.1) by analyzing the ratio of the expected and detected two particle events.

6.1.2 Determination of the Target - Forward Detector Distance

The Doppler correction requires the angle between the detected γ-ray and the direction of the nucleus which emits the γ-ray as input parameter (c.f. sec. 4.4.1). In case of forward scattering, the reconstructed particle direction depends on the distance between the FCD and the target. In the used C-REX setup, this distance is variable (c.f. sec. 3.4). Due to the mechanical design of C-REX and the target ladder a precise adjustment is challenging. Hence, it has to be determined experimentally[5]. The best approach to extract the FCD position is to exploit the reaction kinematics of events in which

---

[4]The innermost ring has the ring number 0.

[5]The simplest approach for its determination is based on the energy-θ_{lab} relation (c.f. fig. 6.1 a)) of the scattered ^{72}Zn and ^{109}Ag nuclei which is fully defined by the reaction kinematics and the energy loss in the target. However, as the energy calibration is done with an $A/Q = 4$ beam, the energy calibration exploits the kinematics of the elastic scattered $A/Q = 4$ beam and thus depends on the distance between the FCD and the target (c.f. sec. 4.2). Consequently, this approach is not applicable here. A different approach is to fit the $1/\sin^4(\theta_{CM}/2)$ dependence of the Rutherford cross section to the ^{72}Zn distribution of the counts in the FCD. However, this method does not give a precise result for the target-FCD distance as it crucially depends on the identification cut efficiency of the scattered ^{72}Zn ions which is unknown. Furthermore, the Doppler correction cannot be used to extract the target-FCD distance as the MINIBALL angles are determined with the help of the direction of the scattered particles which depends on the location of the FCD (c.f. sec. 4.4). Therefore, this method results in a circular argument as it would only give the distance which was used to determine the MINIBALL angles.
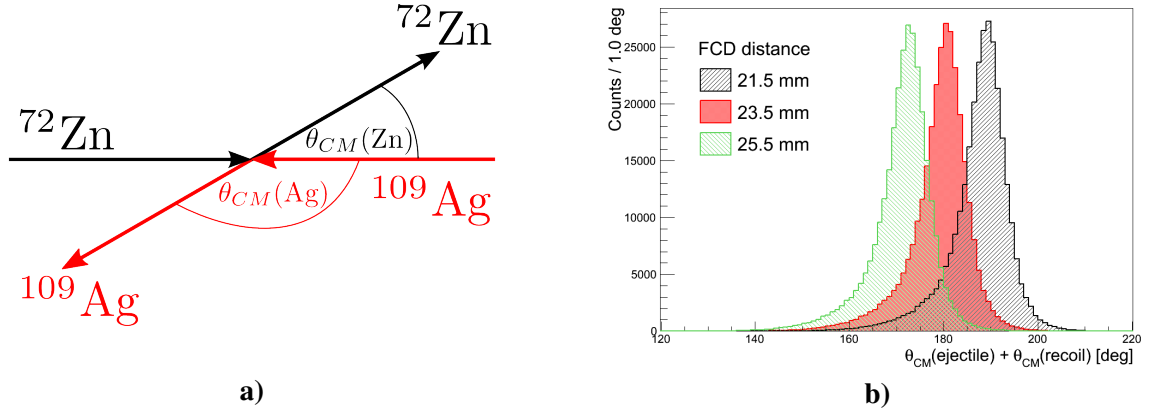
Fig. 6.4: a) Definition of the center-of-mass scattering angles of the ejectile ^{72}Zn and the recoil ^{109}Ag. **b)** The influence of the target-FCD distance on the sum of the scattering angles of the ejectile (^{72}Zn) and the recoil (^{109}Ag). According to energy and momentum-conservation this sum should be around 180°. This is the case for the distance $z_{FCD} = 23.5$ mm.

both the ^{72}Zn and the ^{109}Ag nuclei are detected in the FCD (c.f. sec. 6.1.1). Energy and momentum conservation ensures that the sum of the ejectile and the recoil scattering angle in the center-of-mass frame has to be 180°. The definition of the center-of-mass angles is given in fig. 6.4. In the case of elastic scattering the scattering angle in the center-of-mass frame θ_{CM} reads [97]

$$\cos(\theta_{CM}) = \cos(\theta_{lab})\left[x\cos(\theta_{lab}) + \sqrt{1 - x^2\sin^2(\theta_{lab})}\right] - x \quad \text{and} \quad \theta_{lab} = \arctan\left(\frac{r_{ring}}{z_{FCD}}\right), \quad (6.1)$$

with $x = m(^{72}\text{Zn})/m(^{109}\text{Ag})$ being the ratio of the ^{72}Zn and the ^{109}Ag mass for the case that the ejectile ^{72}Zn is detected and $x = 1$ for the case that the recoil ^{109}Ag is detected. r_{ring} is the radius of the hit FCD ring and z_{FCD} corresponds to the distance between the target and the FCD. Hence, the sum θ_{CM}(ejectile) + θ_{CM}(recoil) is strongly related to the target-FCD distance z_{FCD}. In fig. 6.4 this quantity is histogrammed for three different z_{FCD}. The distribution for $z_{FCD} = 23.5$ mm has its peak around 180° and thus corresponds to the real distance between the target and the FCD. In this analysis it is assumed that the symmetry axis of the FCD coincides with the beam axis. However, due to the mechanical design of C-REX this condition is not perfectly fulfilled. Hence, the obtain distance z_{FCD} is only a mean distance which has been determined qualitatively. Subsequently, no error for z_{FCD} is given. Compared to the other methods (differential Rutherford cross section, energy-θ_{lab} dependence from reaction kinematics, Doppler correction, ...) to extract z_{FCD}, this approach has the advantage that it is completely independent on the energy calibration, the efficiency of the particle identification and the Doppler correction. Thus, a circular argument is avoided.

6.1.3 Determination of the Beam Spot Position

Besides the geometry of the setup, another important parameter for the Doppler correction is the position of the beam spot on the target. It defines the reaction position in the $x - y$ plane and thus has an influence on the determination of the scattering angles of the particles and the γ-rays. In REX-ISOLDE experiments the beam is aligned using the information which is provided by the active collimator before the target and the segmented diamond detector which can be placed directly at the target position (c.f. sec. 3.3). Additionally, in the ^{72}Zn experiment, the high beam intensity allowed a beam alignment with the FCD detector exploiting the fact that the counts in the four FCD quadrants should be symmetric (c.f. fig. 6.5 a)). However, the symmetry of the counts in the FCD cannot be used to determine the beam position precisely, e.g. due to different trigger thresholds of the four FCD quadrants. A more precise method is based on the coincidence detection of the ejectile and the recoil
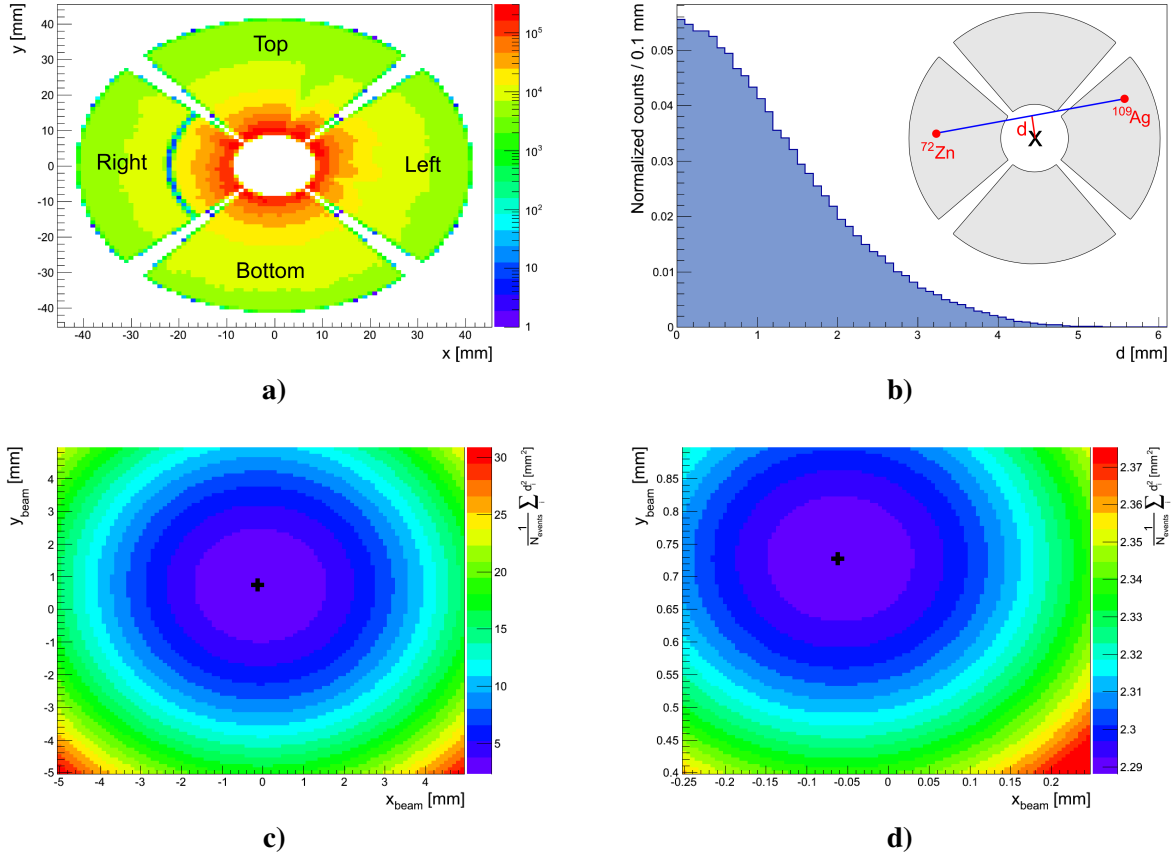
Fig. 6.5: a) All detected particles in the FCD are shown. The symmetric distribution indicates that the beam is aligned close to the center of the coordinate system. The huge intensity loss in the right quadrant is due to the fact that its 6th ring was broken during the experiment. **b)** The inset shows the definition of quantity d which corresponds to the shortest distance between the beam axis and the connection line between the scattered ^{72}Zn and ^{109}Ag nuclei originating from the same reaction. The histogram shows the distribution of d assuming that the beam is aligned at $(x_{beam}, y_{beam}) = (-0.06\,\text{mm}, 0.73\,\text{mm}.)$ **c)** The mean distance d as a function of the beam spot position (x_{beam}, y_{beam}). Its minimum corresponds to the true beam spot position (black cross). **d)** A zoomed view of figure c) with a finer binning. The fitted beam spot is marked with a black cross and is positioned at $x_{beam} = (-0.06 \pm 0.01)\,\text{mm}$ and $y_{beam} = (0.73 \pm 0.01)\,\text{mm}$.

particle (c.f. sec. 6.1.1). If both nuclei originate from one reaction, the position of the reaction vertex (i.e. the beam position) should be close to the connection line between the detected ejectile ^{72}Zn and the detected recoil ^{109}Ag (c.f. inset of fig. 6.5 b)). In most cases the distance d between the center of the beam spot and the connection line is not exactly zero due to the finite position resolution of the FCD and the extended beam spot (c.f. fig. 6.5 b)). However, the distance distribution should be narrowest for the true beam center. Hence, the beam position (x_{beam}, y_{beam}) is defined by the minimization of the mean squared distance d^2 of all events featuring a coincidence between a ^{72}Zn and a ^{109}Ag ion:

$$d^2 = \frac{1}{N_{events}} \sum_{i=1}^{N_{events}} d_i^2, \tag{6.2}$$

with N_{events} being the number of events. The minimization procedure was performed using the MI-NUIT package [101] which is included in the ROOT framework [91]. The fitted beam position is

$$x_{beam} = (-0.06 \pm 0.01)\,\text{mm}, \quad y_{beam} = (0.73 \pm 0.01)\,\text{mm}. \tag{6.3}$$

The uncertainty has been determined using the T-REX Geant4 simulation where the exact beam position is known. For a better visualization fig. 6.5 c) and d) show the mean squared distance d^2 as
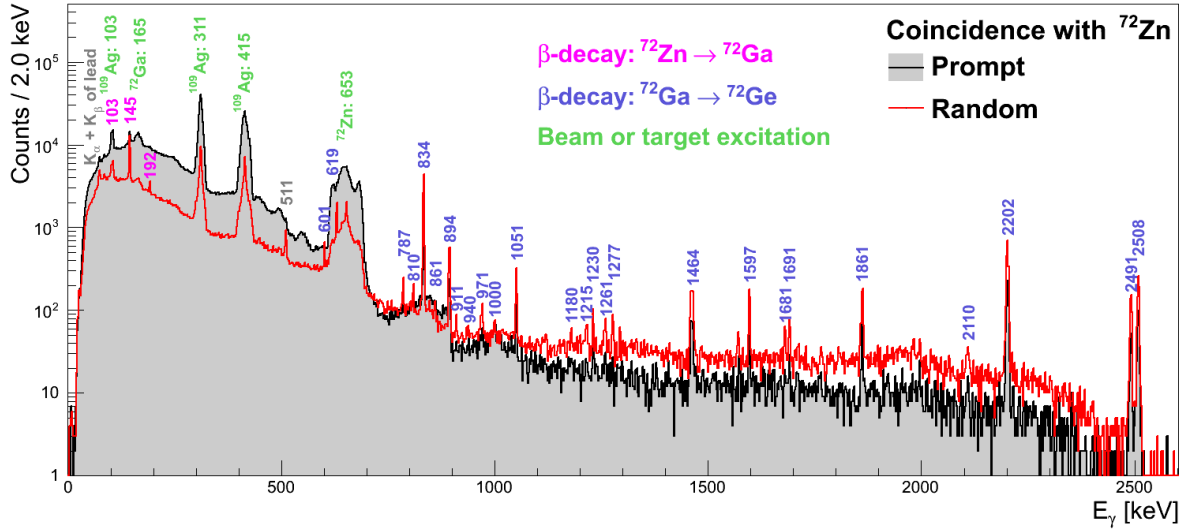
Fig. 6.6: γ-ray spectra which are obtained if a prompt or random gate on an identified ^{72}Zn ion is set (c.f. fig. 6.7 a)). Both spectra feature γ-ray peaks from the Coulomb excitation of the beam and the target as well as a huge amount of β-decay lines of the beam. But, only the prompt spectrum contains true particle-γ-ray coincidences. Thus, in order to obtain a clean spectrum for the Coulomb excitation without β-decay lines, the random spectrum has to be subtracted properly from the prompt spectrum. Note, that the shown spectra are not scaled, i.e. the time window of the random spectrum is almost three times bigger than the prompt spectrum (c.f. fig. 6.7). Furthermore, the Coulex peaks in the random spectrum originate from accidental coincidences between γ-rays and particles from different reactions.

a function of the beam position (x_{beam}, y_{beam}). The beam spot is marked with a black cross. As the deviation of the beam center from $x = y = 0$ is small compared to the size of the smallest segments in MINIBALL and C-REX, it is neglected in the following analysis.

6.1.4 Background Subtraction

The γ-ray spectra are dominated by the β-decays of the stopped radioactive REX-ISOLDE beam, even if they are already gated on a particle which is detected in the silicon array C-REX (c.f. fig. 6.6). Hence, to obtain reliable and precise values for the counts in the Doppler corrected γ-ray peaks from the beam or target excitation, it is crucial to subtract the huge β-decay background properly. A correct subtraction is especially important if γ-ray lines from the Coulex reaction are close to β-decay lines. This is e.g. the case for the strong $E_\gamma = 103$ keV ^{103}Ag line which is superimposed by the ^{72}Zn $\rightarrow^{72}$Ga β-decay line at the same energy. Furthermore, the broad peak at $E_\gamma = 653$ keV which corresponds to the $2_1^+ \rightarrow 0_1^+$ transition of ^{72}Zn is overlain by the $E_\gamma = 601$ keV and $E_\gamma = 619$ keV ^{72}Ga $\rightarrow^{72}$Ge β-decay lines. Apart from that, there is an additional background component caused by accidental coincidences between particles and γ-rays of different Coulex reactions. Consequently, the γ-ray spectra have to be cleaned from these backgrounds. To be able to statistically subtract the background correctly, its contribution to the signal has to be known. The main difference between Coulex events and background events is the time correlation between the γ-ray detected in MINIBALL and the particle detected in C-REX. Fig. 6.7 a) shows the distribution of the time difference between the γ-rays and the particles. Its peak around zero represents true coincidences, while the flat background corresponds to random coincidences which are uniformly distributed in time. Hence, to obtain a clean background sample a "random" coincidence window is defined (c.f. fig. 6.7 a)). Additionally, a "prompt" signal window is chosen around the coincidence peak to optimize the signal to background ratio. The resulting prompt and random spectra are shown in fig. 6.6. As the random window is chosen as big as possible to maximize statistics, the resulting background spectrum has to be weighted before
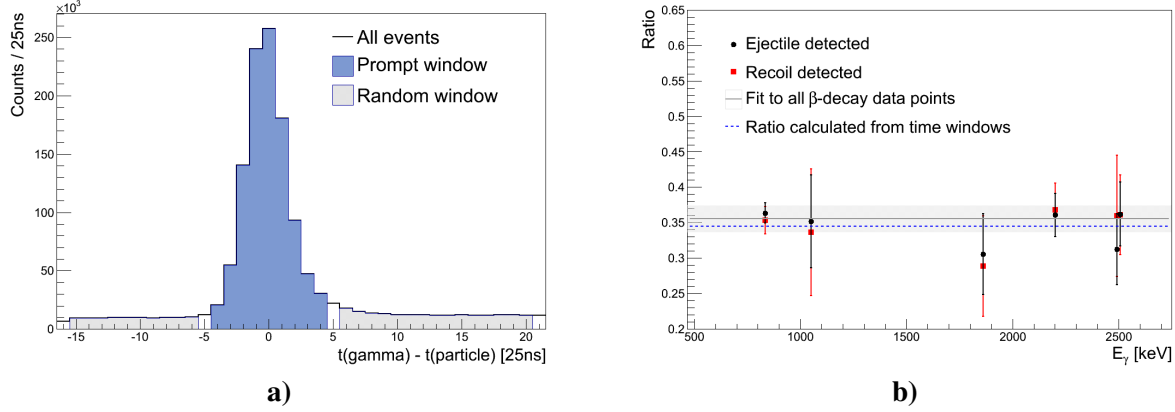
a)   b)

Fig. 6.7: a) The time difference of a γ-ray and a particle in the Top quadrant of the FCD which were both detected in one event, i.e. within $1\,\mu$s. The blue area shows the prompt coincidences, while the shaded gray areas corresponds to the background region which is used to subtract the random coincidences from the prompt peak. The time window for the prompt gate has a width of $9 \cdot 25$ ns which is $2 \cdot 25$ ns wider than for the particle-particle coincidence, described in sec. 6.1.1. This results from the fact that due to the slow γ-ray signals their time resolution is worse compared to the time resolution of the fast particle signals (c.f. also fig. 4.6). **b)** The ratio between the count rates in the prompt and the random time window (c.f. fig. a)) of the most intense β−decay lines of the ^{72}Zn beam. The data set is divided into the cases that an ejectile ^{72}Zn or a recoil ^{109}Ag is detected in coincidence with the γ-ray. Moreover, the gray line results from a fit with a constant to all data points. The shaded gray area visualizes its 1σ-contour. For comparison the ratio $w_{time} = 0.345$ calculated from the length of the prompt and the random time window is shown (blue dotted line). It is in good agreement with the scaling factor $w_\beta = 0.355 \pm 0.019$, obtained by the β-decay ratios.

subtracting it from prompt spectrum containing the real Coulex events. The required weighting factor $w_{time} = 0.345$ for the background subtraction is calculated from the length of the random and the prompt time windows, exploiting that the background rate is the same in both windows[6]. For an additional cross-check, the weighting factor of the random coincidences can also be determined from the counts in the β-decay lines in the prompt and in the random γ-ray spectrum. Their ratio for the most dominant γ-ray peaks is shown in fig. 6.7 b). The weighting factor $w_\beta = 0.355 \pm 0.019$ was obtained by a fit with a constant function. Within the uncertainties, it is consistent with the time weighting factor $w_{time} = 0.345$ showing the reliability of the background treatment.

This background subtraction is applied to every γ-ray spectrum in the following analysis.

6.1.5   Doppler Corrected γ-ray Spectra

After the detector calibration (c.f. chap. 4), the characterization of the setup (c.f. sec. 6.1.2 and 6.1.3), the particle identification (c.f. sec. 6.1.1) as well as the background subtraction (c.f. sec. 6.1.4), Doppler corrected γ-ray spectra can be obtained by looking at coincidences between γ-rays in MINIBALL and identified ejectiles or recoils in the C-REX detectors. The resulting spectra are divided into different groups, depending on which particle is detected and for which particle the Doppler correction is performed. Furthermore, the spectra differ in the C-REX detector detecting the scattered particle. Each group is discussed separately in the following.

Doppler Correction with Respect to ^{72}Zn, ^{72}Zn is Detected in C-REX

Fig. 6.8 shows the γ-ray spectra Doppler corrected with respect to ^{72}Zn for the case that the scattered ^{72}Zn ion is detected in the FCD (top), in the BBarrel (middle) and in the BCD (bottom). Due to the excellent statistics, transitions from the energetic lowest ^{72}Zn states are visible: $E_\gamma(2_1^+ \rightarrow 0_1^+) =$

---

[6]The weighting factor corresponds to all quadrants. Thus, is cannot be calculated only from fig. 6.7 a) as this figure considers only the Top trigger group. For the other trigger groups the background windows differ.

a) Forward CD

b) Backward Barrel

c) Backward CD

Fig. 6.8: Doppler corrected γ-ray spectra for the case that the ejectile ^{72}Zn is detected in the FCD (top), in the BBarrel (middle) or in the BCD (bottom). The Doppler correction has been done with respect to ^{72}Zn. Besides the ^{72}Zn projectile as well as the ^{109}Ag target excitation, also a γ-ray line which corresponds to the beam contaminant ^{72}Ga is visible at $E_\gamma = 165\,\text{keV}$.

a)   b)
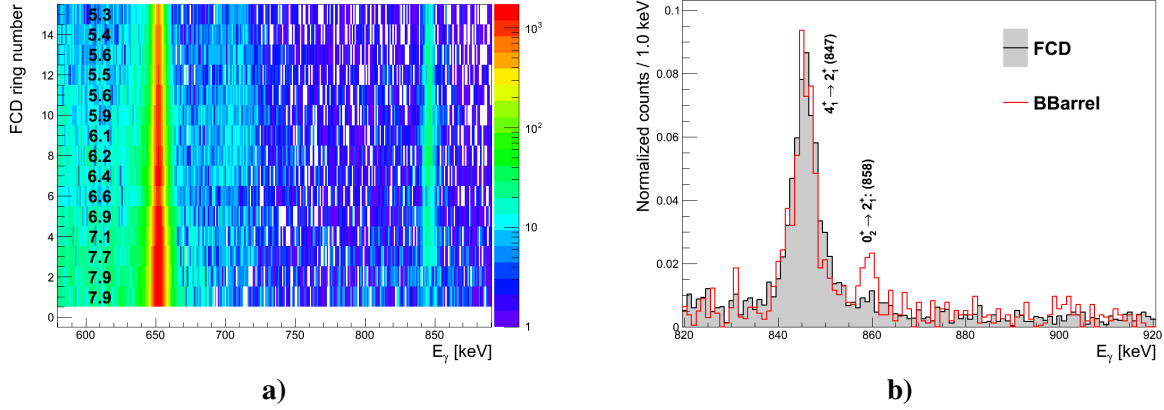
Fig. 6.9: a) The γ-ray spectrum after Doppler correction with respect to ^{72}Zn as a function of the FCD ring number. The two strong lines at $E_\gamma = 653$ keV and at $E_\gamma = 847$ keV represent the $2_1^+ \rightarrow 0_1^+$ and $4_1^+ \rightarrow 2_1^+$ transition in ^{72}Zn, respectively. The numbers next to the $E_\gamma = 653$ keV peak correspond to the widths of the peaks in keV (FWHM). Their decrease with increasing ring number indicates that the Doppler correction improves when going to higher ring numbers of the FCD. This results from the fact that the θ_{lab}-resolution, and subsequently the Doppler correction, improves with higher ringer numbers due to the larger distance to the target. Note, that the first ring was excluded in the analysis as it features an incomplete charge collection (c.f. fig. 6.2). **b)** A comparison between the Doppler corrected γ-ray spectra obtained in coincidence with particles detected in the FCD and the BBarrel. Due to the excellent Doppler correction, the transitions of the 4_1^+ state and the 0_2^+ state to the 2_1^+ state can be well discriminated, although they only have an energy difference of about $\Delta E = 11.5$ keV. Note, that the $0_2^+ \rightarrow 2_1^+$ transition is only visible in the BBarrel. A further discussion of this observation can be found in sec. 6.3.

652.7 keV, $E_\gamma(4_1^+ \rightarrow 2_1^+) = 846.8$ keV, $E_\gamma(2_2^+ \rightarrow 2_1^+) = 1004.7$ keV and $E_\gamma(2_2^+ \rightarrow 0_1^+) = 1657.6$ keV. The excellent statistics allow to extract a large set of ^{72}Zn matrix elements which is unique in the zinc isotopes, although ^{72}Zn is radioactive. Furthermore, the most dominant peak of the beam contamination ^{72}Ga at $E_\gamma = 165$ keV is present. Additionally, three broad (Doppler corrected with respect to the wrong particle) γ-ray peaks from the ^{109}Ag target excitation at $E_\gamma = 103$ keV, $E_\gamma = 311$ keV and $E_\gamma = 415$ keV are visible. Comparing the FCD, the BBarrel and the BCD spectra, the Doppler correction improves if the ^{72}Zn scattering angle increases. This results from the decreasing ^{72}Zn velocity (c.f. fig. 6.1 a)) which corresponds to a smaller Doppler shift (c.f. (4.3)). Furthermore, the solid angle of the detector segments decrease with increasing $\theta_{lab}(^{72}$Zn): The BCD has an approximately three times larger distance to the target compared to the FCD. The improvement of the Doppler correction with the distance of the silicon detector segment to the target can also be seen if the Doppler corrected spectrum of fig. 6.8 a) is plotted as a function of the FCD ring number (c.f. fig. 6.9 a)). With increasing ring number, the width of the $2_1^+ \rightarrow 0_1^+$ transition in ^{72}Zn constantly decreases whereas the mean value is constant at its literature value $E_\gamma = 653$ keV.

A closer look at the FCD and the BBarrel spectra reveals that an additional transition of the 0_2^+ state to the 2_1^+ state at $E_\gamma = 858.3$ keV in the BBarrel is present (c.f. fig. 6.9 b)). It is missing in the FCD spectrum. Although this line is quite close ($\Delta E = 11.5$ keV) to the $E_\gamma = 846.8$ keV transition from the 4_1^+ state, it can be well discriminated. Hence, the effort to obtain a high quality of the Doppler correction (c.f. sec. 4.4, 6.1) has payed off in the analysis of these two peaks. A further discussion of the behavior of the 0_2^+ state can be found in the following sections.

Doppler Correction with Respect to ^{109}Ag, ^{72}Zn is Detected in C-REX

Fig. 6.10 shows the γ-ray spectra if the Doppler correction is done with respect to the ^{109}Ag target. Like in fig. 6.8 the scattered ^{72}Zn ions were detected in C-REX. Hence, the direction and the velocity of the ^{109}Ag ion is reconstructed from the energy and the direction of the detected ^{72}Zn using the reaction kinematics. The broad peaks at $E_\gamma = 653$ keV and $E_\gamma = 165$ keV represent the strongest γ-ray

a) Forward CD

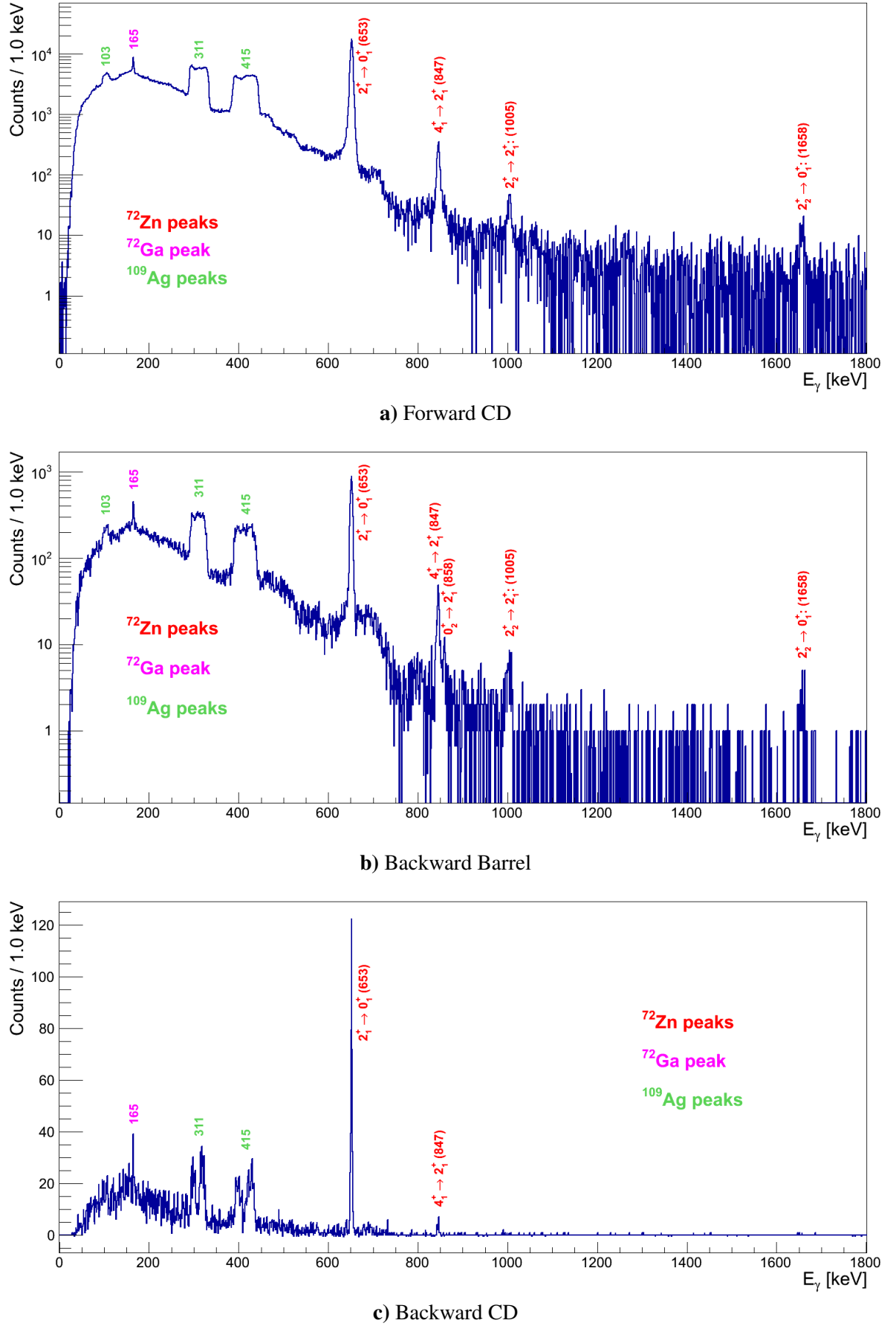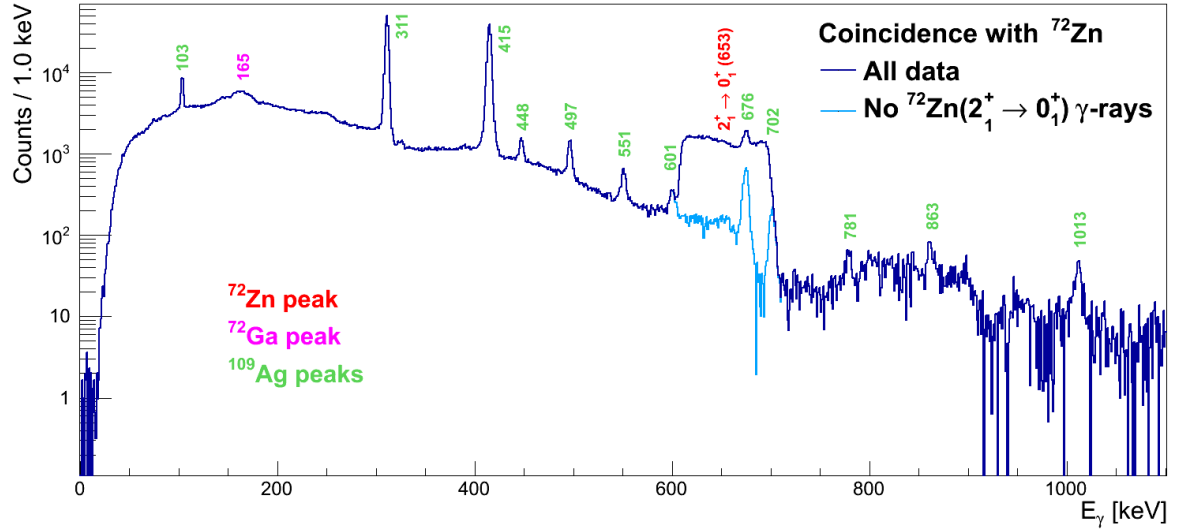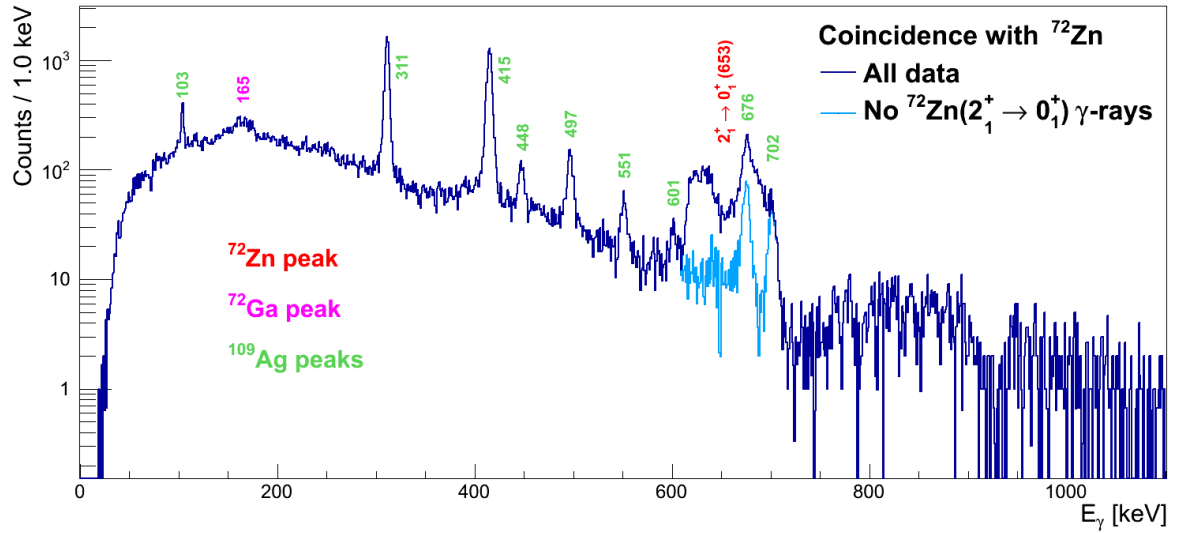**b)** Backward Barrel
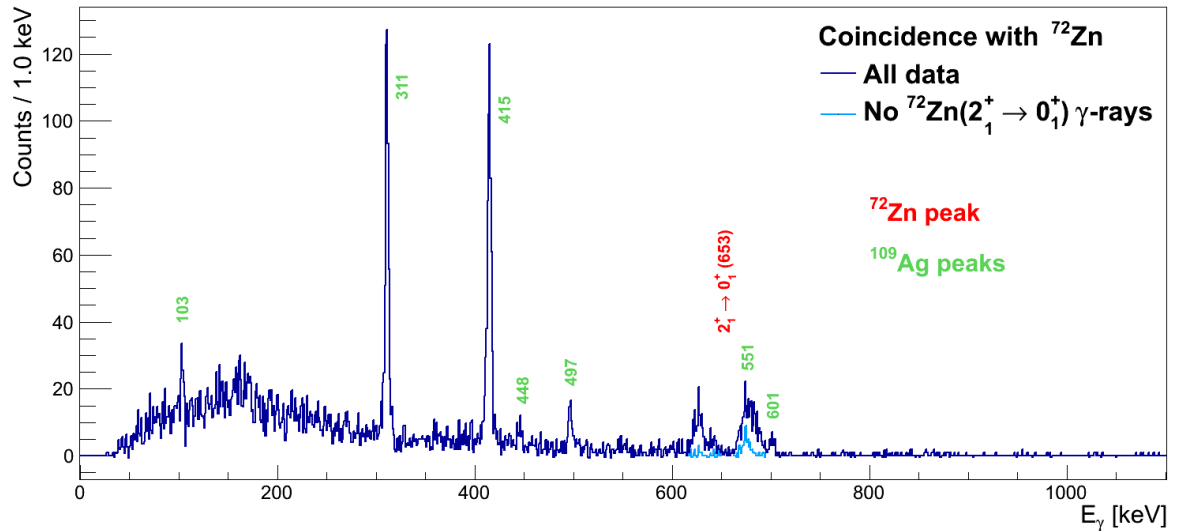
c) Backward CD

Fig. 6.10: a) Doppler corrected γ-ray spectra for the case that the ejectile ^{72}Zn is detected in the FCD (top), in the BBarrel (middle) or in the BCD (bottom). The Doppler correction has been done with respect to ^{109}Ag. Besides the ^{72}Zn projectile as well as the ^{109}Ag target excitation, also a γ-ray line which corresponds to the beam contaminant ^{72}Ga is visible at $E_\gamma = 165$ keV.

Data set	I_{Ga}/I_{Zn} [%]	I_{Ar}/I_{Zn} [%]	I_{O}/I_{Zn} [%]	I_{Zn}/I_{tot} [%]	I_{Ga}/I_{tot} [%]	I_{Ar}/I_{tot} [%]	I_{O}/I_{tot} [%]
Laser On,Off	8.42(7)	1.13(4)	0.31(2)	91.02(6)	7.67(6)	1.03(3)	0.28(2)
All runs	7.51(61)	1.01(9)	0.28(3)	91.92(52)	6.90(56)	0.93(8)	0.26(3)

Tab. 6.1: The beam composition of the ^{72}Zn Coulex experiment. The first row corresponds to the beam content in the laser On runs which are close in time to the laser Off measurements, while the second row represents the over all beam content in the experiment. The beam contaminant ^{72}Ga is produced in the primary ISOLDE target, while the ^{36}Ar and the ^{18}O contaminants originate from the buffer gas of the charge-breeding system of the REX-ISOLDE accelerator.

lines from the ^{72}Zn beam and its contaminant ^{72}Ga. The huge number of sharp peaks correspond to the multiple Coulomb excitation of the ^{109}Ag target. They allow a precise extraction of the ^{109}Ag electromagnetic matrix elements which is unique (c.f. sec. 6.3.4). To visualize also the ^{109}Ag γ-ray lines which are close to the $E_\gamma = 653$ keV ^{72}Zn excitation an additional spectrum is shown in fig. 6.10. To obtain this spectrum, the Doppler correction was done twice: with respect to ^{72}Zn and with respect to ^{109}Ag. If the Doppler corrected energy with respect to ^{72}Zn is close to $E_\gamma = 653$ keV, the event is not filled into the spectrum. As a result, the new spectrum is identical to the total spectrum, but the broad $2_1^+ \rightarrow 0_1^+$ transition of ^{72}Zn is excluded. Thus, it is possible to also identify the $E_\gamma = 602$ keV, the $E_\gamma = 676$ keV and the $E_\gamma = 702$ keV transition of the ^{109}Ag target.

Doppler Corrected Spectra if ^{109}Ag is Detected in C-REX
Due to the reaction kinematics the scattered ^{109}Ag can only be detected in the FCD. Fig. D.3 in appendix D.4 show the resulting Doppler corrected γ-ray spectra with respect to ^{72}Zn (top) and with respect to ^{109}Ag (bottom). Both spectra feature the same peaks as in fig. 6.8 a) and fig. 6.10 a). However, in fig. D.3 a), the ^{72}Zn peaks are sitting on a broad plateau which corresponds to events where the γ-ray is emitted at rest, as without applying a Doppler correction these events results in a peak in the spectrum. This effect occurs if the ^{109}Ag is detected in the innermost rings of the FCD. In this case the scattered ^{72}Zn ions feature a scattering angle close to $\theta_{lab} = 90°$ (c.f. fig. 6.1 b)), i.e. it is likely that they are stopped in the target.

6.1.6   Beam Purity

Due to the production mechanism of the ^{72}Zn REX-ISOLDE beam (c.f. sec. 3.1), it is expected that the beam is not 100% pure, i.e. it does not contain only ^{72}Zn but also other isotopes. The investigation of the beam composition is of extreme importance for the analysis, as the beam contaminants also contribute to the ^{109}Ag target excitation which is used as normalization for the ^{72}Zn beam excitation. In the transfer experiment, the beam content was determined from the signal of the ionization chamber (c.f. sec. 3.3 and sec. 5.1.3). However, due to the high ^{72}Zn beam intensity, it could not be used in this experiment to avoid damage to the ionization chamber. Instead, the beam composition was determined from the comparison of laser On and laser Off runs. In this experiment two additional challenges occurred during the analysis of the beam content: First, the traditional laser On/Off method had to be further improved to take the large variation of the beam purity with time into account[7]. Second, due to the high beam intensity, the dead time of the silicon detectors has to be taken into account carefully. A dedicated study showed that a correct dead time handling is crucial (c.f. appendix D.1.1). Details about the exact determination of the beam composition can be found in appendix D.1. The results for the intensities of the beam components (^{72}Zn, ^{72}Ga, ^{36}Ar and ^{18}O) are summarized in tab. 6.1. They are in excellent agreement with the previous neutron-rich zinc experiments ([49] and this transfer

---

[7]The large variation of the beam purity was caused by an unstable RILIS laser system.

experiment in sec. 5.1.3), which show that the gallium contamination decreases with decreasing mass number.

6.2 Determination of Electromagnetic Matrix Elements

6.2.1 Concept

The counts in the peaks of the Doppler corrected γ-ray spectra are related to the differential cross section $d\sigma/d\Omega$ of the Coulomb excitation. The cross section itself depends on the electromagnetic matrix elements connecting the initial and the final nuclear state. Hence, from the counts in the γ-ray transitions nuclear structure information can be obtained. The concept is detailed in the following. The number N_{ex} of excited nuclei in a given state which are detected in a solid angle $\Delta\Omega$ of a silicon detector segment reads

$$N_{ex} = \mathcal{L} \cdot \frac{d\sigma}{d\Omega} \cdot \Delta\Omega \cdot \epsilon_{Si}. \tag{6.4}$$

$\mathcal{L}$ is the time-integrated luminosity of the experiment, $d\sigma/d\Omega$ the differential Coulex cross section and ϵ_{Si} is the detection efficiency of the silicon detector. The deexcitation of this state usually proceeds via the emission of γ-rays. The number of detected γ-rays in a germanium detector is given by

$$N_{\gamma,det} = N_{ex} \cdot f_{IC} \cdot BR \cdot W \cdot f_{feeding} \cdot \epsilon_{Ge} = \underbrace{\frac{d\sigma}{d\Omega} \cdot \Delta\Omega \cdot f_{IC} \cdot BR \cdot W \cdot f_{feeding}}_{N_{\gamma,emit}} \cdot \mathcal{L} \cdot \epsilon_{Si} \cdot \epsilon_{Ge}. \tag{6.5}$$

The factor f_{IC} takes the probability of internal conversion which competes with γ-ray emission into account. BR is the branching ratio of the transition, W the angular distribution which depends on the electromagnetic multipole character of the transition, $f_{feeding}$ a factor which corrects for feeding contributions of higher lying states and ϵ_{Ge} is the detection efficiency of the germanium detector. The first factors in eq. (6.5) can be merged to $N_{\gamma,emit}$ which is the number of emitted γ-rays (per unit luminosity) for the case that the nucleus (which emits the γ-ray) is scattered in the solid angle element $\Delta\Omega$. $N_{\gamma,emit}$ can be calculated with a Coulex code, such as CLX/DCY or GOSIA (c.f. sec. 6.2.2). However, the number of predicted counts in the γ-ray peaks cannot be calculated with high precision, as the luminosity $\mathcal{L}$ (beam intensity, target thickness) and the detection efficiency ϵ_{Si} of the silicon detector cannot be determined with accuracy. Especially the determination of the efficiency of the used particle identification cuts (c.f. fig. 6.2 c) and d)) which contributes to the quantity ϵ_{Si} is challenging. Furthermore, the dead time of the system has to be known. Therefore, instead of an absolute measurement a relative measurement is performed: The counts in the γ-ray peaks are normalized to a well known γ-ray transition with known matrix element(s): The number of emitted γ-rays, if the nucleus is scattered in the solid angle $\Delta\Omega$, can be written as

$$N_{\gamma,emit} = \underbrace{N_{\gamma,emit,norm}}_{\text{Coulex code}} \cdot \underbrace{\frac{N_{\gamma,det}/\epsilon_{Ge}}{N_{\gamma,det,norm}/\epsilon_{Ge,norm}}}_{\text{experiment}}. \tag{6.6}$$

The superscript "*norm*" indicates the quantities of the normalization transition. This normalization has the advantage that the luminosity as well as the efficiency of the particle detector cancel out. Additionally, the uncertainty of the target thickness is minimized by normalizing to the target excitation. As normalization transition a γ-ray line of the beam or the target can be used. The uncertainty of the quantity $N_{\gamma,emit}$ is calculated via Gaussian error propagation including the statistical error of the counts in the γ-ray peaks (c.f. sec. 6.1.5 and appendix D.5), the error of the germanium detector efficiency (c.f. sec. 4.3.1) and the error of the counts in the normalization transition.

Normalization of Beam Yields to Target Yields

If the normalization is done with respect to a target transition, its γ-ray counts $N^{tot}_{\gamma,det,norm}$ have to be corrected as it is possible that not only the desired beam nuclei ^{72}Zn excite the target, but also the beam contaminants ^{72}Ga, ^{36}Ar and ^{18}O. The experimental γ-ray intensity of the target excitation $N^{Zn}_{\gamma,det,norm}$ originating only from ^{72}Zn can be written as[8] [66]

$$N^{Zn}_{\gamma,det,norm} = \frac{N^{tot}_{\gamma,det,norm}}{1 + \sum_X \frac{I_X}{I_{Zn}} \frac{N^X_{\gamma,emit,norm}}{N^{Zn}_{\gamma,emit,norm}}}, \tag{6.7}$$

with $N^{Zn,X}_{\gamma,emit,norm}$ being the emitted target γ-rays per unit luminosity induced by the ^{72}Zn beam and its contaminants. Their ratios $N^X_{\gamma,emit,norm}/N^{Zn}_{\gamma,emit,norm}$ account for the different target excitation cross sections of the beam components. As they are defined per unit luminosity, they have to be additionally scaled with the fractions I_X/I_{Zn} of the beam intensities (sec. 6.1.6). Thus, the precise determination of the beam content is important, as it influences directly the counts in the target normalization transition which is the basis to extract the nuclear matrix elements of the beam. The uncertainty of $N^{Zn}_{\gamma,det,norm}$ includes the uncertainty of the counts in the γ-ray peak of the normalization transition (c.f. sec. 6.1.5 and appendix D.5) and the error of the beam contamination (c.f. sec. 6.1.6).

6.2.2   Tools for the Calculation of Coulex Cross Sections

Coulomb excitation codes aim to extract nuclear matrix elements from measured γ-ray yields or to predict γ-ray yields which is useful for the preparation of future experiments. The calculation is based on the semi-classical theory which has been already introduced in sec. 2.3.1. Furthermore, the Coulomb excitation and deexcitation are seen, due to their different time scales, as independent processes: First, the Coulex code calculates the population of each considered nuclear state based on a given set of electromagnetic matrix elements. In a second step, the same matrix elements are used to predict the γ-ray emission. The Coulex codes which have been used in this thesis are the CLX/DCY code [69] and the GOSIA code [65]. Both are based on the Winther and de Boer code [70, 65].

CLX/DCY

The CLX code calculates Coulomb excitation cross sections as a function of the scattering angle θ_{CM} in the center-of-mass frame. The main input parameters are the charge Z and mass A of the projectile and the target, the beam energy in the middle of the target, the level scheme and all relevant matrix elements. Subsequently, the output of CLX is used as input for the DCY program. DCY calculates the yields of the γ-rays integrated over the angular coverage of the particle and γ-ray detector. Hence, as input the θ_{CM} and ϕ angles of all particle detectors, as well as θ and ϕ angles of the germanium detectors are given. In the calculation, the γ-ray angular distribution is taken into account including the influence of the finite size of the γ-ray detectors as well as the deorientation effect. The deorientation effect can flatten the γ-ray angular distribution due to the hyperfine interaction of the excited nuclear state with the high magnetic field produced by the atomic electron shell [61]. Furthermore, feeding from higher lying states and the possibility of a deexcitation by internal conversion is considered.

GOSIA

GOSIA is a semi-classical coupled-channel multiple Coulex least-square fitting code which aims to analyze rich Coulex datasets involving many γ-ray yields which are described by a large set of electromagnetic matrix elements. In addition to the CLX/DCY input, the following parameters have to be given: First, the stopping powers dE/dx for the calculation of the energy loss in the target. Second, additional available spectroscopic data such as lifetimes, branching ratios, multipole mixing ratios and

---

[8]Note, that only the contaminants which are inside the identification cuts of fig. 6.2 c) and d) are considered.
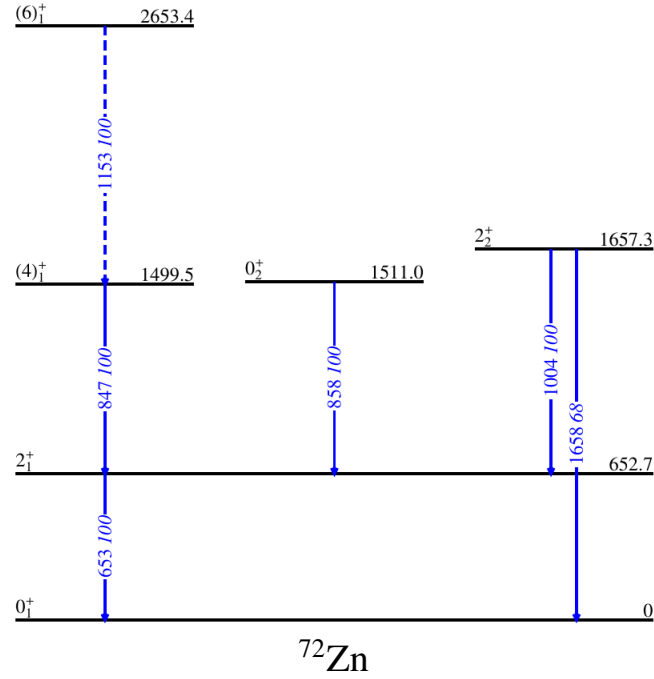
Fig. 6.11: Level scheme of ^{72}Zn. The solid blue transitions have been seen in the Coulomb excitation experiment (c.f. fig. 6.8 and fig. D.3). The dashed transitions have not been observed.

known matrix elements. Third, the photo peak efficiency curve of the γ-ray detectors. No direct parameters for the deorientation effects are given, as they are calculated internally using an appropriate model. Forth, integration and minimization parameters. The least-square statistic which is used by GOSIA in the minimization procedure can be written as [65]

$$S(\{\mathcal{M}\}) = \frac{1}{N}(S_{yields} + S_{upl} + S_{sd}), \qquad (6.8)$$

with N being the total number of data points (experimental γ-ray yields, lifetimes, branching ratios, multiple mixing ratios, known matrix elements) which have to be fitted. The summand S_{yields} corresponds to the least-square statistic of the experimental and predicted GOSIA yields. The second term S_{upl} of eq. (6.8) takes care of the observation limit of the experiment. Unphysical matrix elements which produce unobserved yields which exceed a given upper limit, result in an additional contribution to the least-square statistic. The last term S_{sd} of eq. (6.8) deals with the known spectroscopic data which can be included as additional data points in the fit. After the minimization algorithm has found the best set of matrix elements $\{\mathcal{M}\}$, their errors can be calculated including all correlations between the matrix elements.

6.2.3   Relevant Matrix Elements of ^{72}Zn and ^{109}Ag

Before determining the matrix elements of the projectile ^{72}Zn and the target ^{109}Ag with the Coulex codes CLX/DCY and GOSIA, all relevant nuclear levels, transitional matrix elements and their diagonal matrix elements have to be identified.

^{72}Zn Levels, Relevant Matrix Elements and Spectroscopic Data

The ^{72}Zn level scheme, determined mainly by a β-decay experiment of ^{72}Cu [117], including all observed transition in the γ-ray spectra of fig. 6.8, 6.9 and D.3 a) is shown in fig. 6.11. Additionally, to include the feeding probability from higher lying states, the 6^+_1 state of ^{72}Zn is included in the fit of the matrix elements. Furthermore, an additional low lying level at 1612.6 keV with unknown spin

Method	State	τ [ps]	$B(E2) \downarrow [e^2\text{fm}^4]$	Reference
RDDS in Legnaro with AGATA	2_1^+	17.6 ± 1.4	392^{+34}_{-29}	[38]
	4_1^+	$5.2^{+0.8}_{-0.7}$	361^{+57}_{-47}	[38]
	6_1^+	3.0 ± 0.9	134^{+57}_{-31}	[38]
RDDS at GANIL (Niikura et al.)	2_1^+	17.9 ± 1.8	385 ± 39	[39]
RDDS at GANIL (Celikovic et al.)	2_1^+	19.4 ± 5.5	354 ± 100	[40]
	4_1^+	6.4 ± 2.4	292 ± 110	[40]
	6_1^+	3.0 ± 1.2	133 ± 51	[40]
Intermediate Coulex at GANIL	2_1^+	-	348 ± 42	[118]

Tab. 6.2: Previously measured lifetimes and reduced transition probabilities of ^{72}Zn determined with the Recoil Distance Doppler Shift (RDDS) method and intermediate Coulomb excitation at INFN-LNL Legnaro and GANIL. More information about the measurements can be found in sec. 1.2.

and parity exits. As its dominant transition ($E_\gamma = 960\,$keV) to the 2_1^+ state has not been observed in the Doppler corrected γ-ray spectra, it is neglected in the analysis. Fig. 6.13 a) visualizes all matrix elements which are included in the fit. Six $E2$ and one $M1$ transitional matrix elements are considered as well as the quadrupole moments (i.e. the diagonal matrix elements) of the 2_1^+, the 4_1^+ and the 2_2^+ state of ^{72}Zn. Furthermore, the previous measured lifetimes of the 2_1^+, the 4_1^+ and the 6_1^+ state can be used as additional parameters in the fit of the matrix elements. They are summarized in tab. 6.2. Apart from that, the measured branching ratio[9] $BR = P(2_2^+ \to 0_1^+)/P(2_2^+ \to 2_1^+) = 0.68 \pm 0.05$ from the β-decay experiment of ^{72}Cu [117] can be included.

^{109}Ag Levels, Relevant Matrix Elements and Spectroscopic Data

The considered level scheme in the ^{109}Ag Coulex analysis including all observed transitions in the Doppler corrected γ-ray spectra (c.f. fig. 6.10 and D.3 b)) is shown in fig. 6.12 a). It can be concluded that the excitation of negative parity states is preferred as also the $1/2^-$ ground state features a negative parity. Fig. 6.12 b) visualizes a second excerpt of the ^{109}Ag levels containing mainly positive parity states. Although the $5/2_1^+ \to 7/2_1^+$ transition with $E_\gamma = 781\,$keV has been observed in the experiment, all positive parity states have been neglected in the analysis as they feature long lifetimes which are at least on the nanosecond scale and which are not connected to the negative parity states in fig. 6.12 a). Furthermore, the decay of the $5/2_1^+$ state is strongly fragmented. Nevertheless, its dominant transition $E_\gamma = 781\,$keV is quite weak as its intensity is only about 0.1% of the intensity of the $E_\gamma = 415\,$keV transition. Fig. 6.13 b) indicates all matrix elements which are considered in the Coulex analysis. They are additionally constrained by a large set of available spectroscopic data from previous experiments. The formerly measured $E2$ and $M1$ matrix elements, lifetimes, multipole mixing ratios and branching ratios are summarized in appendix D.2. The data set of ^{109}Ag in appendix D.2 is quite rich as it has been studied extensively due to the fact that it is a stable isotope and an often used Coulex target. However, due to the excellent statistics and the broad range of scattering angles covered by the present experiment, it can complement the previous measurements.

6.3 Results

After the brief introduction of the relevant states, matrix elements and available spectroscopic data of ^{72}Zn and ^{109}Ag (c.f. sec. 6.2.3), their γ-ray yields (c.f. sec. 6.1.5) are used as input for the Coulex codes CLX/DCY and GOSIA. The procedure to extract the final matrix elements is presented in this section. Afterwards the obtained matrix elements from both Coulex codes are compared.

---

[9]The definition of the branching ratio is given in eq. 2.30.
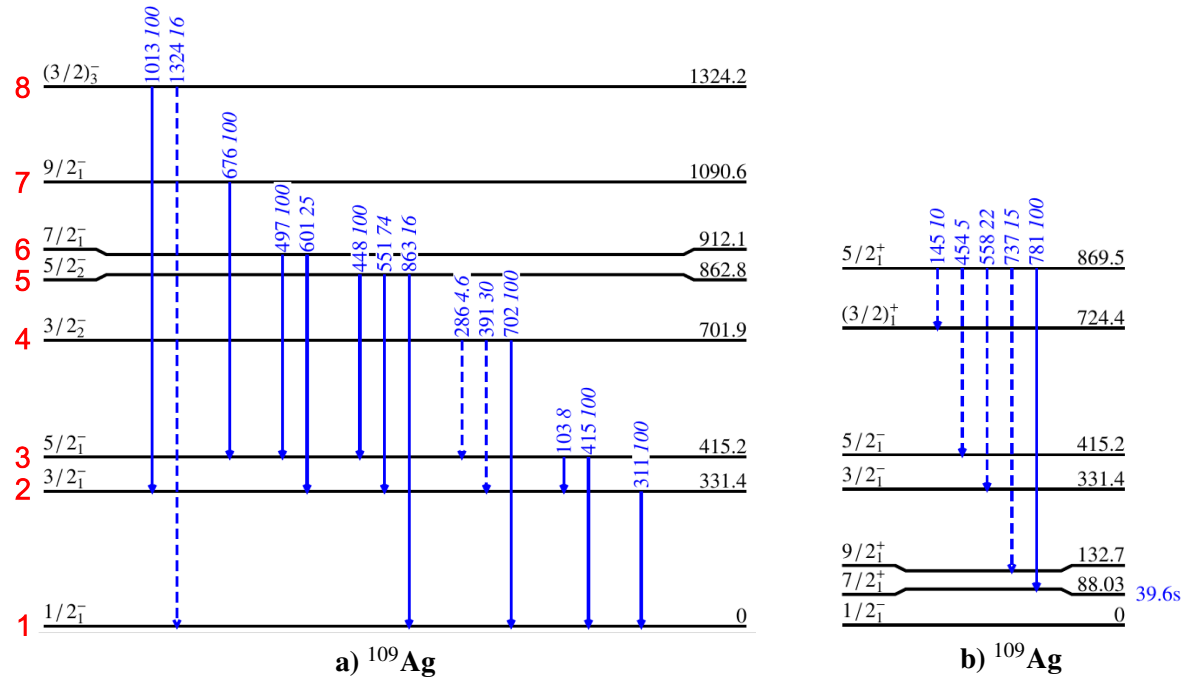
Fig. 6.12: a) Level scheme of ^{109}Ag. The solid blue transitions were detected in the Coulomb excitation experiment (c.f. fig. 6.10 and fig. D.3). The dashed transitions were not observed. All observed transitions are between negative parity states. **b)** The 869.5 keV state including all associated transitions. Although, the $E_\gamma = 781$ keV γ-ray was observed, it has been neglected in the analysis as it originates from a positive parity state and decays into an isomer with a positive parity.
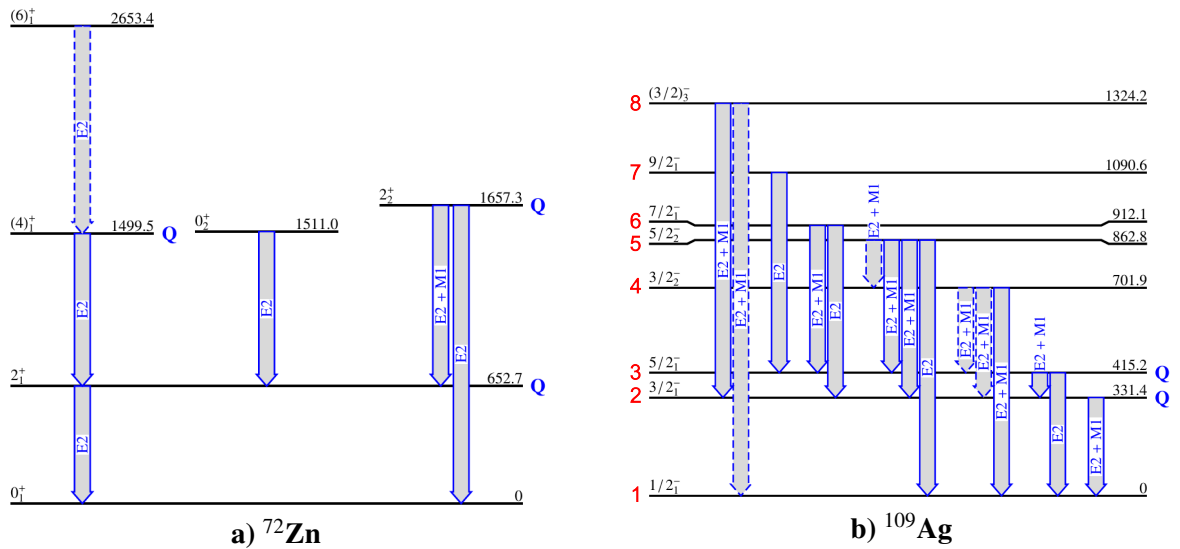
Fig. 6.13: a) The transitional $E2$ and $M1$ matrix elements as well as the quadrupole moments Q which are included in the Coulex analysis. The dashed transitions were not observed.

6.3.1 ^{72}Zn CLX/DCY Analysis

As the CLX/DCY analysis requires less input parameters than GOSIA, it is an ideal tool to get a first idea of the magnitude of the matrix elements and the correlations between them. Subsequently, the obtained values can be used as good start parameters for the more sophisticated GOSIA code. Without a good set of start matrix elements for GOSIA, it is difficult to extract reliable matrix elements, as it has to be ensured that the GOSIA fit algorithm, which fits all matrix elements simultaneously, converges into the global χ^2 minimum. Contrary, in the CLX/DCY analysis only small subsets of the matrix elements are fitted simultaneously and the influence of the other remaining fixed matrix elements is discussed afterwards. The matrix elements are extracted using a maximum likelihood fit which is described in the following. As input data for the fit the experimental counts in the ^{72}Zn γ-ray transitions (c.f. appendix D.3) are used. To compare them to the expected counts from the CLX/DCY code, they are converted into the number of emitted γ-rays per unit luminosity using eq. (6.6) and using the $5/2_1^- \rightarrow 1/2_1^-$ ($E_\gamma = 415\,\mathrm{keV}$) ^{109}Ag transition as normalization[10]. The strong $E_\gamma = 415\,\mathrm{keV}$ γ-ray transition is suited for the normalization as it is a pure $E2$ transition, while the second strong $3/2_1^- \rightarrow 1/2_1^-$ ($E_\gamma = 311$ keV) transition is a mixed $E2/M1$ transition. Two sets of ^{109}Ag matrix elements have been used in the ^{72}Zn CLX/DCY analysis: First, the literature values of ^{109}Ag which are summarized in appendix D.2. Second, the fitted ^{109}Ag matrix elements obtained with GOSIA from the Coulex experiment of this thesis (c.f. sec. 6.3.4 and tab. 6.5). Furthermore, to be more sensitive to the ^{72}Zn transitional and diagonal matrix elements, the Coulex data set is divided into different particle scattering ranges (c.f. fig. 6.14 a)): Fist, the γ-ray yields of three neighboring FCD rings are combined. Furthermore, the BBarrel and the BCD is treated as a single dataset each. A detailed description of the subdivision of the whole Coulex data set into angular bins can be found in appendix D.3.

Determination of the $\mathcal{M}(0_1^+ \rightarrow 2_1^+)$ and $\mathcal{M}(2_1^+ \rightarrow 2_1^+)$ Matrix Elements in ^{72}Zn
In a first step of the ^{72}Zn CLX/DCY analysis, the counts in the ^{72}Zn $2_1^+ \rightarrow 0_1^+$ transition are used to extract its transitional matrix element $\mathcal{M}(0_1^+ \rightarrow 2_1^+)$ and its diagonal matrix element $\mathcal{M}(2_1^+ \rightarrow 2_1^+)$. An increase of $\mathcal{M}(0_1^+ \rightarrow 2_1^+)$ or of $\mathcal{M}(2_1^+ \rightarrow 2_1^+)$ results in a higher count rate of the $2_1^+ \rightarrow 0_1^+$ γ-ray peak[11]. However, according to fig. 2.5 the impact of both matrix elements on the 2_1^+ state differ: At small particle θ_{CM} angles the transitional matrix elements dominates, while for larger θ_{CM} the quadrupole moment (diagonal matrix element) gets, as a second order effect, more and more important. Hence, if the count rate of the $2_1^+ \rightarrow 0_1^+$ γ-ray peak is divided into different θ_{CM} bins, the experiment is sensitive to both matrix elements. The simultaneous fit of $\mathcal{M}(0_1^+ \rightarrow 2_1^+) = \mathcal{M}_{02}$ and $\mathcal{M}(2_1^+ \rightarrow 2_1^+) = \mathcal{M}_{22}$ to the experimental data is done with the maximum likelihood method [119, 120]: If all experimental data points $\{N_{\gamma,emit,i}^{exp}\}$ are considered to be independent of each other, the likelihood function L is defined as

$$L = L(\mathcal{M}_{02}, \mathcal{M}_{22}) = P(\{N_{\gamma,emit,i}^{exp}\} \mid \mathcal{M}_{02}, \mathcal{M}_{22}) = \prod_i P(N_{\gamma,emit,i}^{exp} \mid \mathcal{M}_{02}, \mathcal{M}_{22}). \qquad (6.9)$$

The product runs over all experimental yields of the $2_1^+ \rightarrow 0_1^+$ transition corresponding to different θ_{CM} silicon detector angles. Assuming Gaussian errors, the probability density function $P(N_{\gamma,emit,i}^{exp} \mid \mathcal{M}_{02}, \mathcal{M}_{22})$ for one experimental yield $N_{\gamma,emit,i}^{exp}$ with its uncertainty $\Delta N_{\gamma,emit,i}^{exp}$ reads

$$P(N_{\gamma,emit,i}^{exp} \mid \mathcal{M}_{02}, \mathcal{M}_{22}) = \frac{1}{\sqrt{2\pi}\Delta N_{\gamma,emit,i}^{exp}} \exp\left[-\frac{\left(N_{\gamma,emit,i}^{exp} - N_{\gamma,emit,i}^{cal}(\mathcal{M}_{02}, \mathcal{M}_{22})\right)^2}{2(\Delta N_{\gamma,emit,i}^{exp})^2} \right], \qquad (6.10)$$

with $N_{\gamma,emit,i}^{cal}$ being the calculated yield for data set i obtained by CLX/DCY. The best fitted matrix elements $\mathcal{M}_{02}$ and $\mathcal{M}_{22}$ corresponds to the maximum of the likelihood L with respect to $\mathcal{M}_{02}$ and

---

[10]Of course also the other ^{109}Ag matrix elements play a crucial role in the normalization procedure, especially since there are many transitions which feed into the $5/2_1^-$ state.

[11]The influence of matrix elements from higher lying states which can feed the 2_1^+ state is discussed below.

$\mathcal{M}_{22}$. It is equivalent to the minimum of the negative logarithmic likelihood $\mathcal{L}$

$$\mathcal{L}(\mathcal{M}_{02}, \mathcal{M}_{22}) = -\ln(L) = C + \sum_i \frac{\left(N_{\gamma,emit,i}^{exp} - N_{\gamma,emit,i}^{cal}(\mathcal{M}_{02}, \mathcal{M}_{22})\right)^2}{2(\Delta N_{\gamma,emit,i}^{exp})^2}, \qquad (6.11)$$

with C being a constant. The 1σ contour defining the errors of the matrix elements is given by [120]

$$\mathcal{L} < \mathcal{L}_{min} + \frac{1}{2}. \qquad (6.12)$$

Fig. 6.14 a) visualizes the obtained 1σ contours for the transition $2_1^+ \rightarrow 0_1^+$ in ^{72}Zn as a function of the matrix elements $\mathcal{M}(0_1^+ \rightarrow 2_1^+)$ and $\mathcal{M}(2_1^+ \rightarrow 2_1^+)$. The data sets represent examples of different scattering angle ranges. The different inclination of the 1σ contours indicate the varying dependence of the γ-ray yields corresponding to a certain particle scattering angle on the transitional and diagonal matrix element. The total negative logarithmic likelihood is shown in fig. 6.14 b). Its minimum corresponds to the matrix elements reproducing the experimental data best. The resulting 1σ contour is shown in fig. 6.14 c). The uncertainties of the matrix elements, which are due to the fit, are given by the projection of the 1σ contour on the coordinate axes. Hence, the maximum likelihood method yields

$$\mathcal{M}(0_1^+ \rightarrow 2_1^+) = 0.411^{+0.002}_{-0.002}\text{eb} \quad \text{and} \quad \mathcal{M}(2_1^+ \rightarrow 2_1^+) = -0.33^{+0.03}_{-0.02}\text{eb} \quad \text{for literature }^{109}\text{Ag } \mathcal{M},$$

$$\mathcal{M}(0_1^+ \rightarrow 2_1^+) = 0.420^{+0.002}_{-0.002}\text{eb} \quad \text{and} \quad \mathcal{M}(2_1^+ \rightarrow 2_1^+) = -0.31^{+0.03}_{-0.02}\text{eb} \quad \text{for fitted }^{109}\text{Ag } \mathcal{M}. \quad (6.13)$$

The first matrix elements are obtained if the literature values of the ^{109}Ag matrix elements are used for normalization (c.f. D.2), while the second ^{72}Zn matrix elements results if the fitted ^{109}Ag matrix elements determined in sec. 6.3.4 (c.f. tab. 6.5) are used for normalization. The slightly differing resulting ^{72}Zn matrix elements for the two ^{109}Ag matrix element data sets underline the importance of a good nuclear structure knowledge of the normalization nucleus. Note, that the given uncertainty is only a diagonal error, as it does not include correlations to other matrix elements. Furthermore, the approximations used in the CLX/DCY code result in an additional systematic error[12]. Apart from that, the uncertainties of the ^{109}Ag matrix elements have to be included in the total uncertainty of the ^{72}Zn matrix elements. A quantitative evaluation of the systematical uncertainties has not been performed in the course of the CLX/DCY analysis. But, this is done in the following GOSIA analysis, as GOSIA allows to include the uncertainty of the normalization transition and as GOSIA considers correlation between matrix elements.

As a cross-check for the obtained matrix elements, the expected emitted γ-ray yields are calculated with these matrix elements using DCX/DCY and are finally compared to the experimental values calculated with eq. (6.5). As an example, fig. 6.14 d) shows an excellent agreement between the experimental and the calculated yield for the case that the fitted ^{109}Ag matrix element set is used.

The matrix elements $\mathcal{M}(0_1^+ \rightarrow 2_1^+)$ and $\mathcal{M}(2_1^+ \rightarrow 2_1^+)$ have been determined using fixed, appropriate values for all other matrix elements of the higher lying states[13] (c.f. fig. 6.13 a)). The largest influence on $\mathcal{M}(0_1^+ \rightarrow 2_1^+)$ and $\mathcal{M}(2_1^+ \rightarrow 2_1^+)$ has the $\mathcal{M}(2_1^+ \rightarrow 4_1^+)$ matrix element, as the $4_1^+ \rightarrow 2_1^+$ transition is the second strongest transition in the ^{72}Zn Coulex experiment and as the 4_1^+ states feeds to 100% into the 2_1^+ state. Hence, a wrong $\mathcal{M}(2_1^+ \rightarrow 4_1^+)$ value can spoil the obtained $\mathcal{M}(0_1^+ \rightarrow 2_1^+)$ and $\mathcal{M}(2_1^+ \rightarrow 2_1^+)$ matrix elements. To evaluate the influence of $\mathcal{M}(2_1^+ \rightarrow 4_1^+)$, the number of emitted γ-rays of the $2_1^+ \rightarrow 0_1^+$ transition is calculated while varying $\mathcal{M}(2_1^+ \rightarrow 4_1^+)$ by $\pm 20\%$ around its actual value. From fig. 6.15 it can be concluded that the variation obviously has a strong impact on the $4_1^+ \rightarrow 2_1^+$ yield, but only a small influence on the expected counts in the $2_1^+ \rightarrow 0_1^+$ peak. A second

---

[12]The uncertainty of the Coulex code arises from the approximations of the semi-classical treatment, from the model for the deorientation effect, . . .

[13]In a first step, all matrix elements have been chosen by hand to reproduce the experimental counts in the γ-ray peaks. Subsequently, an iterative procedure has been performed to tune these start values: One or two matrix elements are fitted while the others are kept fixed at their current best values.
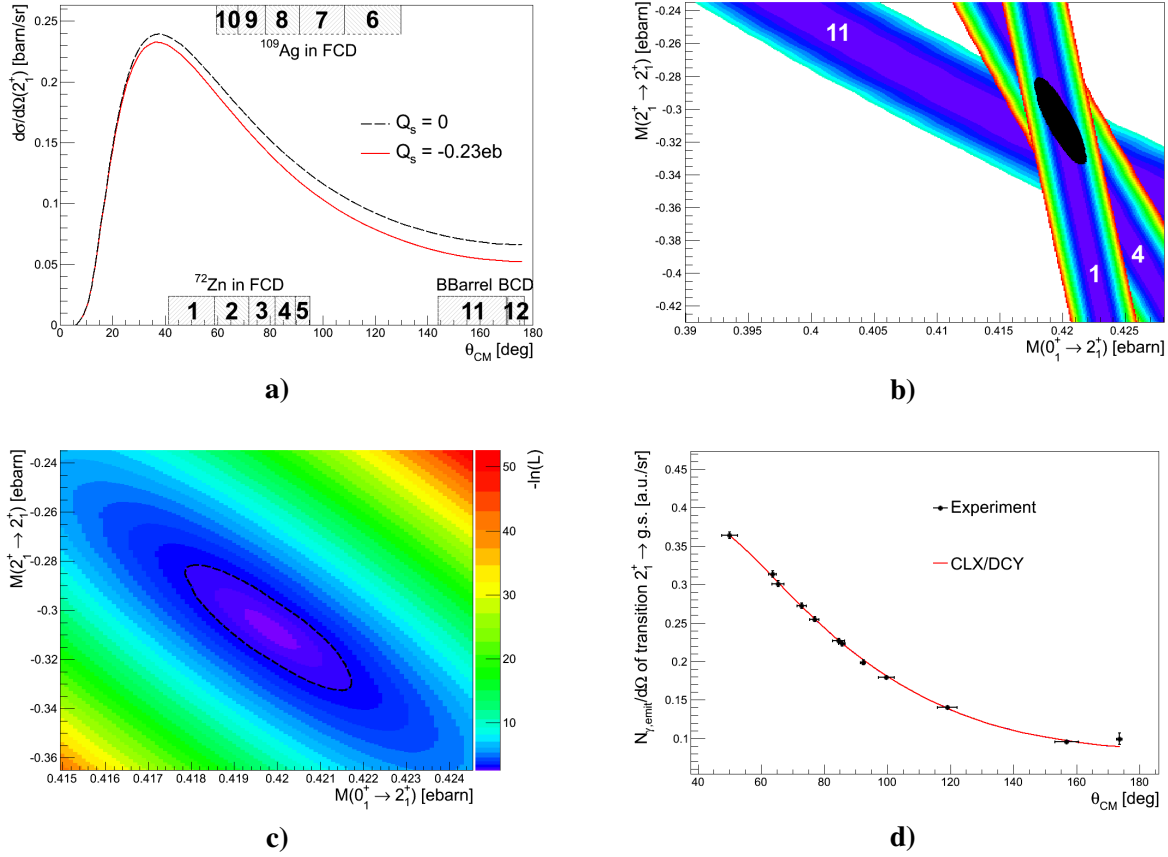
Fig. 6.14: a) The influence of the quadrupole moment $Q_s(2_1^+)$ (diagonal matrix element) on the Coulex cross section of the 2_1^+ state (for details c.f. sec. 2.3.2). The transitional and the diagonal matrix element can be disentangled by dividing the total angular coverage of C-REX into small bins of particle scattering angles. They are indicated with the numbers. The first $10 = 5 \cdot 2$ subdivisions correspond to the data of the 15 FCD rings where always three rings are combined for the detection of the scattered ^{72}Zn (range 1-5) or ^{109}Ag (range 6-10) ions (c.f. appendix D.3). Additionally, the last ranges 11 and 12 correspond to the BBarrel and the BCD detector, respectively. **b)** The 1σ contours for the subdivisions 1, 4, and 11. Their different slopes demonstrate the angular dependence of the Coulex cross section on the transitional matrix element $\mathcal{M}(0_1^+ \to 2_1^+)$ and on the diagonal matrix element $\mathcal{M}(2_1^+ \to 2_1^+)$. The black ellipse represents the obtained 1σ contour if all single 1σ contours of the subdivisions are superimposed. The most horizontal band results from the BBarrel data showing that the backward detectors of C-REX are extremely sensitive to $\mathcal{M}(2_1^+ \to 2_1^+)$. **c)** The negative logarithmic likelihood (c.f. eq. (6.11)) which results from the combination of all datasets. Its clear minimum corresponds to the best fitted $\mathcal{M}(0_1^+ \to 2_1^+)$ and $\mathcal{M}(2_1^+ \to 2_1^+)$ values of ^{72}Zn. The dashed ellipse indicates the 1σ contour of the negative logarithmic likelihood. Its boarders define the 1σ errors of the matrix elements $\mathcal{M}(0_1^+ \to 2_1^+)$ and $\mathcal{M}(2_1^+ \to 2_1^+)$. **d)** The number of emitted γ-rays $N_{\gamma,emit}$ from the 2_1^+ state to the ground state in ^{72}Zn. To obtain a smooth curve, $N_{\gamma,emit}$ is divided by the solid angle $\Delta\Omega$ of the particle detector segment. In black the experimental values calculated with eq. (6.6) are shown. Each data point corresponds to a angular range, defined in fig. a). Note, that the horizontal error bars correspond to the angular range of the detector segments multiplied with the standard deviation of a uniform distribution ($= 1/\sqrt{12}$), i.e. it is assumed that the counts are uniformly distributed in one detector segment. In red the result of the CLX/DCY calculation with the best fitted $\mathcal{M}(0_1^+ \to 2_1^+)$ and $\mathcal{M}(2_1^+ \to 2_1^+)$ are shown. It coincides well with the experimental data. The shown plots are created with the fitted ^{109}Ag matrix elements obtained in sec. 6.3.4 (c.f. tab. 6.5).
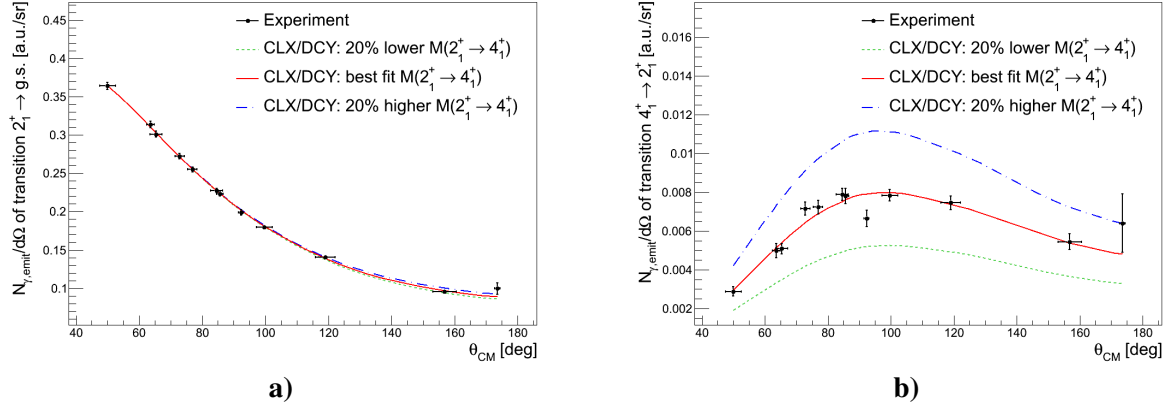
Fig. 6.15: a) The influence of the $\mathcal{M}(2_1^+ \to 4_1^+) = (0.69 \pm 0.01)\,$eb matrix elements on the number of emitted γ-rays of the $2_1^+ \to 0_1^+$ transition. Even a variation of $\pm 20\%$ of the actual value has only a small impact on the $2_1^+ \to 0_1^+$ transition. **b)** In contrast, the obtained yields for the $2_1^+ \to 4_1^+$ transition differ a lot for the three different $\mathcal{M}(2_1^+ \to 4_1^+)$ values. Especially the modifications by $\pm 20\%$ are unrealistic high, as these calculations do not describe the data at all.

maximum likelihood fit of the $\mathcal{M}(0_1^+ \to 2_1^+)$ and $\mathcal{M}(2_1^+ \to 2_1^+)$ matrix elements using the obtained $\mathcal{M}(2_1^+ \to 4_1^+)$ of the next paragraph (c.f. eq. (6.14)), yields results which are within the statistical error bars of $\mathcal{M}(0_1^+ \to 2_1^+)$ and $\mathcal{M}(2_1^+ \to 2_1^+)$ in eq. (6.13).

Determination of the $\mathcal{M}(2_1^+ \to 4_1^+)$ and $\mathcal{M}(4_1^+ \to 4_1^+)$ Matrix Elements in ^{72}Zn

In an analogue way, the transitional matrix element $\mathcal{M}(2_1^+ \to 4_1^+)$ and the diagonal matrix element $\mathcal{M}(4_1^+ \to 4_1^+)$ can be determined with the maximum likelihood method using the counts of the $4_1^+ \to 2_1^+$ transition as input. The negative logarithmic likelihood has been calculated as a function of $\mathcal{M}(2_1^+ \to 4_1^+)$ and $\mathcal{M}(4_1^+ \to 4_1^+)$, while keeping all other matrix elements fixed. The used values for $\mathcal{M}(0_1^+ \to 2_1^+)$ and $\mathcal{M}(2_1^+ \to 2_1^+)$ correspond to the result of the fit of the $2_1^+ \to 0_1^+$ transition (c.f. eq. (6.13)). Furthermore, the matrix elements $\mathcal{M}(4_1^+ \to 6_1^+)$ of the 6_1^+ state which directly feeds into the 4_1^+ state, has been set to the previously measured 6_1^+ lifetime (c.f. tab. 6.2). The fitted matrix elements of the 4_1^+ state yield

$$\mathcal{M}(2_1^+ \to 4_1^+) = 0.69^{+0.01}_{-0.01}\,\text{eb} \quad \text{and} \quad \mathcal{M}(4_1^+ \to 4_1^+) = -0.34^{+0.15}_{-0.14}\,\text{eb} \quad \text{for literature } ^{109}\text{Ag } \mathcal{M},$$

$$\mathcal{M}(2_1^+ \to 4_1^+) = 0.70^{+0.01}_{-0.01}\,\text{eb} \quad \text{and} \quad \mathcal{M}(4_1^+ \to 4_1^+) = -0.35^{+0.14}_{-0.14}\,\text{eb} \quad \text{for fitted } ^{109}\text{Ag } \mathcal{M}. \quad (6.14)$$

Their 1σ contour using the fitted ^{109}Ag matrix elements (c.f. tab. 6.5 in sec. 6.3.4) is shown in fig. 6.16 a). Like in the case of the $\mathcal{M}(0_1^+ \to 2_1^+)$ and the $\mathcal{M}(2_1^+ \to 2_1^+)$ matrix elements the given uncertainties only include the uncertainties of the γ-ray yields, the beam composition and of the MINIBALL efficiency. The uncertainties of the ^{109}Ag matrix elements, the CLX/DCY code and correlations to other matrix elements are not considered. Fig. 6.16 b) visualizes the good agreement between the experimental and the calculated number of emitted $4_1^+ \to 2_1^+$ γ-rays using the obtained matrix elements of eq. (6.13) and (6.14). Additionally, the impact of the 6_1^+ state is displayed. Three different scenarios for $\mathcal{M}(4_1^+ \to 6_1^+)$ are considered: First, the 6_1^+ is neglected by setting its matrix element to zero. Second, the matrix element is defined by the previously measured lifetime, i.e. $\mathcal{M}(4_1^+ \to 6_1^+) = 0.40 \pm 0.07\,$eb (c.f. tab. 6.2). Third, an upper limit for the matrix element $\mathcal{M}(4_1^+ \to 6_1^+) = 0.41\,$eb has been determined with the upper limit of the counts in the unobserved $6_1^+ \to 4_1^+$ γ-ray transition (c.f. sec. D.5 and tab. D.10). According to fig. 6.16 b) all assumptions for the 6_1^+ state coincide well. Hence, its influence can be neglected. As the upper limit does not exclude the lifetime measurement, the latter one has been used in the final result of eq. (6.14).
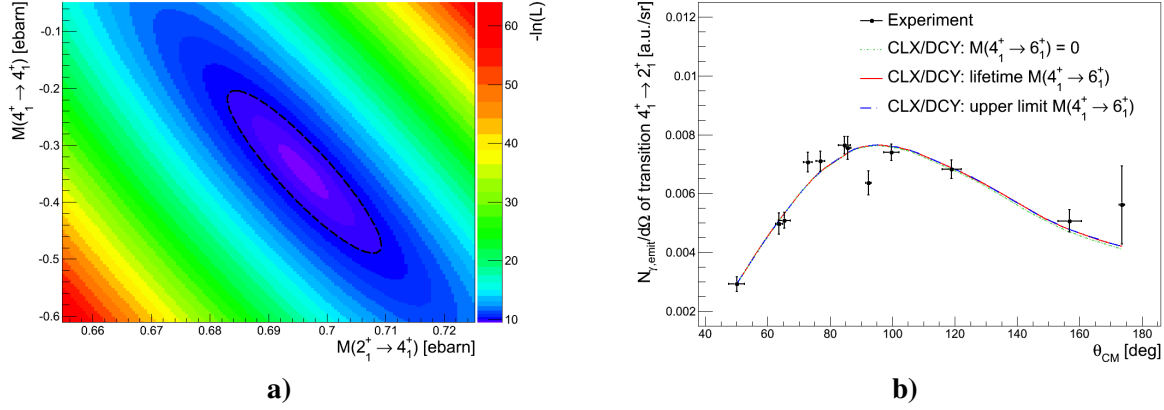
a)   **b)**

Fig. 6.16: a) The negative logarithmic likelihood of the fit of the $2_1^+ \rightarrow 4_1^+$ transition in ^{72}Zn. The 1σ contour is indicated with the dashed ellipse. Its borders define the 1σ errors of the matrix elements $\mathcal{M}(2_1^+ \rightarrow 4_1^+)$ and $\mathcal{M}(4_1^+ \rightarrow 4_1^+)$. **b)** The number of emitted γ-rays $N_{\gamma,emit}$ from the 4_1^+ state to the 2_1^+ state in ^{72}Zn. To obtain a smooth curve, $N_{\gamma,emit}$ is divided by the solid angle $\Delta\Omega$ of the particle detector segment. In black the experimental values calculated with eq. (6.6) are shown. The first $10 = 5 \cdot 2$ points corresponds to the data of the 15 FCD rings where always three rings are combined for the detection of the scattered ^{72}Zn or ^{109}Ag ions (c.f. appendix D.3). Additionally, the last two data points originate from the BBarrel and the BCD detector, respectively. Note, that the horizontal error bars correspond to the angular range of the detector segment multiplied with the standard deviation of a uniform distribution ($= 1/\sqrt{12}$). In red (solid line) the result of the CLX/DCY calculation with the best fitted $\mathcal{M}(2_1^+ \rightarrow 4_1^+)$ and $\mathcal{M}(4_1^+ \rightarrow 4_1^+)$ are shown using the lifetime measurement information for the 6_1^+ state. Apart from that, $N_{\gamma,emit}^{cal}$ for the most extreme cases for $\mathcal{M}(4_1^+ \rightarrow 6_1^+)$ is shown. All scenarios coincide well with the experimental data, indicating that the impact of the 6_1^+ state is negligible. In both figures **a)** and **b)** the normalization has been done with respect to the fitted ^{109}Ag matrix elements (c.f. tab. 6.5 sec. 6.3.4).

Determination of the $\mathcal{M}(2_1^+ \rightarrow 0_2^+)$ Matrix Element in ^{72}Zn

The $\mathcal{M}(2_1^+ \rightarrow 0_2^+)$ matrix element[14] can be determined with a one dimensional maximal likelihood fit using the yield of the $0_2^+ \rightarrow 2_1^+$ peak in the BBarrel. Note, that in the FCD and the BCD this transition was not observed and subsequently only an upper limit can be calculated following the method described in appendix D.3. Fig. 6.17 a) shows the resulting negative logarithmic likelihood[15] including the 1σ contour of $\mathcal{M}(2_1^+ \rightarrow 0_2^+)$. Its minimum corresponds to the final transitional matrix element[16]

$$\mathcal{M}(2_1^+ \rightarrow 0_2^+) = 0.14_{-0.02}^{+0.02}\,\text{eb}\quad \text{for literature } ^{109}\text{Ag } \mathcal{M},$$
$$\mathcal{M}(2_1^+ \rightarrow 0_2^+) = 0.15_{-0.02}^{+0.02}\,\text{eb}\quad \text{for fitted } ^{109}\text{Ag } \mathcal{M}. \tag{6.15}$$

As a cross-check, in fig. 6.17 b) the calculated number of emitted γ-rays of the 0_2^+ to the 2_1^+ state of ^{72}Zn is compared to the experimental values. The fit coincides well with the BBarrel yield and is well below the upper limits.

Determination of the $\mathcal{M}(0_1^+ \rightarrow 2_2^+)$, $\mathcal{M}(E2; 2_1^+ \rightarrow 2_2^+)$ and $\mathcal{M}(2_2^+ \rightarrow 2_2^+)$ Matrix Elements in ^{72}Zn

In a final step of the CLX/DCY analysis, the yields of the $2_2^+ \rightarrow 0_1^+$ transition and of the $2_2^+ \rightarrow 2_1^+$ transition can be used to extract the $E2$ matrix elements elements $\{\mathcal{M}(2_2^+)\} = \{\mathcal{M}(0_1^+ \rightarrow 2_2^+), \mathcal{M}(E2; 2_1^+ \rightarrow 2_2^+), \mathcal{M}(2_2^+ \rightarrow 2_2^+)\}$. Their total likelihood is defined as a product of the single likelihoods of the two γ-ray branches. The final solution for the matrix elements $\{\mathcal{M}(2_2^+)\}$ corresponds to the minimum of its negative logarithmic likelihood $\mathcal{L}(\{\mathcal{M}(2_2^+)\})$. However, as the γ-ray yields depends on three matrix elements, a graphical visualization of the global minimum is not possible. Hence, a profile likelihood

---

[14]The 0_2^+ state does not feature a diagonal matrix element as it only has one magnetic substate ($m = 0$).

[15]In the fit all other matrix elements are fixed to their best values.

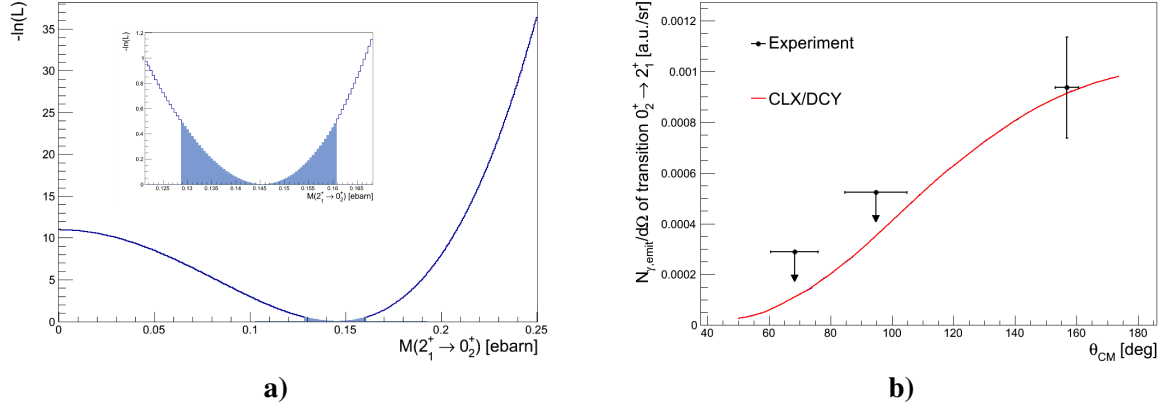[16]Again, the given uncertainty does not include all systematic errors.

Fig. 6.17: a) The negative logarithmic likelihood and its 1σ contour (indicated with the blue shaded area) of the fit of the $0_2^+ \to 2_1^+$ transition in ^{72}Zn. The inlay displays a zoomed view on the obtained $\mathcal{M}(2_1^+ \to 0_2^+)$ matrix element. **b)** The number of emitted γ-rays $N_{\gamma,emit}$ from the 0_2^+ state to the 2_1^+ state in ^{72}Zn. To obtain a smooth curve, $N_{\gamma,emit}$ is divided by the solid angle $\Delta\Omega$ of the particle detector segment. In black the experimental values calculated with eq. (6.6) are shown. The last data point with the error bar corresponds to the data of the BBarrel, whereas the first two arrows indicate the upper limits which are obtained from the unobserved $0_2^+ \to 2_1^+$ transitions in the FCD for the detection of the scattered ^{72}Zn or ^{109}Ag ion. Note, that the horizontal errors corresponds to the angular range of the detector segment multiplied with the standard deviation of a uniform distribution ($= 1/\sqrt{12}$). In red the result of the CLX/DCY calculation with the best fitted $\mathcal{M}(2_1^+ \to 0_2^+)$ is shown.
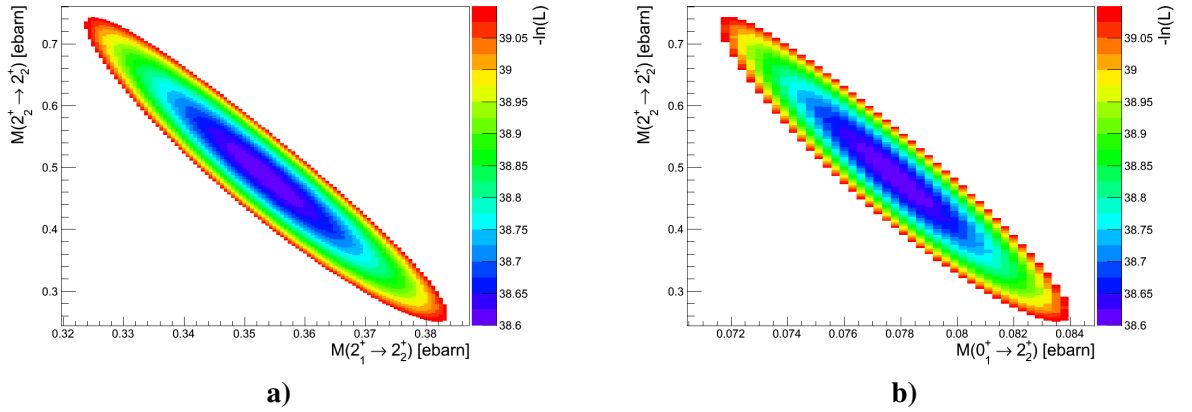

Fig. 6.18: The 1σ contour of the profiled negative logarithmic likelihoods of the matrix elements related to the population of the 2_2^+ state. It can be excited in one step directly from the ground state or in two steps via the 2_1^+ state. The minimum of the 1σ contour correspond to the best fitted $E2$ matrix elements $\mathcal{M}(0_1^+ \to 2_2^+)$, $\mathcal{M}(E2; 2_1^+ \to 2_2^+)$ and $\mathcal{M}(2_2^+ \to 2_2^+)$.

analysis is performed: In fig. 6.18 a) the profiled $\mathcal{L}$ is plotted as a function of the matrix elements $\mathcal{M}(E2; 2_1^+ \to 2_2^+)$ and $\mathcal{M}(2_2^+ \to 2_2^+)$, i.e. the minimum value of $\mathcal{L}$ with respect to $\mathcal{M}(0_2^+ \to 2_2^+)$ is displayed on the z-axis for fixed values of $\mathcal{M}(E2; 2_1^+ \to 2_2^+)$ and $\mathcal{M}(2_2^+ \to 2_2^+)$. Hence, the minimization is done with respect to all three matrix elements. Fig. 6.18 b) shows another profile of $\mathcal{L}$ for a different permutation of the matrix elements. The position of the minimum in fig. 6.18 a) and b) corresponds to the best fitted matrix elements. The following final sets of matrix elements have been obtained for the normalization using the literature ^{109}Ag matrix elements and using the fitted ^{109}Ag matrix elements[17],

---

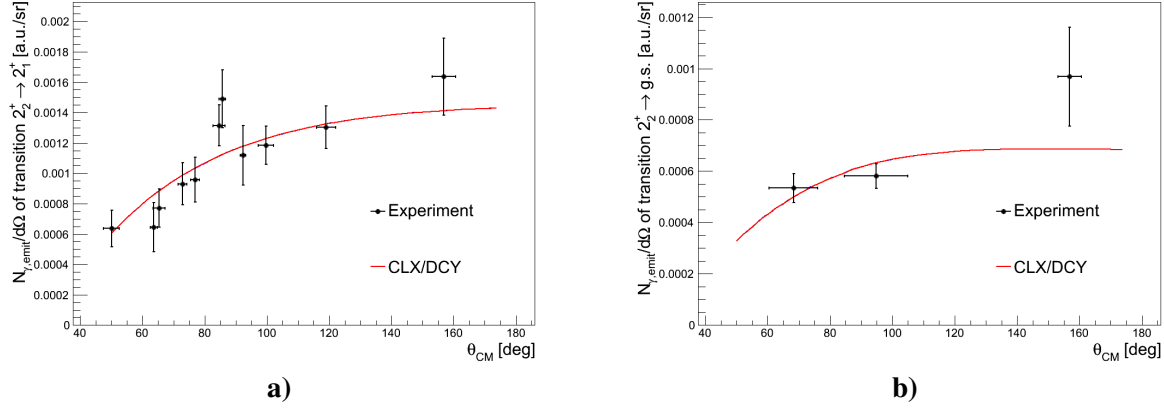[17]Again, the given uncertainty does not included all systematic errors.

Fig. 6.19: The number of emitted γ-rays $N_{\gamma,emit}$ from the 2_2^+ state to the 2_1^+ state (**a**)) and to the ground state (**b**)) in ^{72}Zn. To obtain a smooth curve, $N_{\gamma,emit}$ is divided by the solid angle $\Delta\Omega$ of the particle detector segment. In black the experimental values calculated with eq. (6.6) are shown. For the transition to the 2_1^+ state in fig. a), the first $10 = 5 \cdot 2$ points corresponds to the data of the 15 FCD rings where always three rings are combined for the detection of the scattered ^{72}Zn or ^{109}Ag ions (c.f. appendix D.3). The last data point originates from the BBarrel. The γ-ray yield of the much weaker $2_2^+ \rightarrow 0_1^+$ transition, shown in fig. **b**), can only be divided into three data sets: The first two data points correspond to the case that the scattered ^{72}Zn and ^{109}Ag ion is detected in the FCD, respectively. The last data point represents the BBarrel. Note, that the horizontal error bars correspond to the angular range of the detector segment multiplied with the standard deviation of a uniform distribution ($= 1/\sqrt{12}$). In both figures **a**) and **b**) the normalization has been done with respect to the fitted ^{109}Ag matrix elements (c.f. tab. 6.5 sec. 6.3.4). In red the result of the CLX/DCY calculation with the best fitted $\mathcal{M}(E2; 2_1^+ \rightarrow 2_2^+)$, $\mathcal{M}(0_1^+ \rightarrow 2_2^+)$ and $\mathcal{M}(2_2^+ \rightarrow 2_2^+)$ are shown. It is in good agreement with the experimental data.

respectively:

Literature ^{109}Ag $\mathcal{M}$:

$$\mathcal{M}(E2; 2_1^+ \rightarrow 2_2^+) = 0.35^{+0.03}_{-0.03}\,\text{eb}, \quad \mathcal{M}(0_1^+ \rightarrow 2_2^+) = 0.077^{+0.006}_{-0.006}\,\text{eb}, \quad \mathcal{M}(2_2^+ \rightarrow 2_2^+) = 0.45^{+0.26}_{-0.26}\,\text{eb},$$

Fitted ^{109}Ag $\mathcal{M}$:

$$\mathcal{M}(E2; 2_1^+ \rightarrow 2_2^+) = 0.36^{+0.03}_{-0.03}\,\text{eb}, \quad \mathcal{M}(0_1^+ \rightarrow 2_2^+) = 0.078^{+0.006}_{-0.006}\,\text{eb}, \quad \mathcal{M}(2_2^+ \rightarrow 2_2^+) = 0.48^{+0.27}_{-0.22}\,\text{eb}.$$

$$(6.16)$$

According to [120], the uncertainties of the matrix elements are defined by the 1σ coutures ($\mathcal{L} = \mathcal{L}_{min} + 0.5$) in the profiled negative logarithmic likelihoods. As a consistency check, the experimental γ-ray yields of the $2_2^+ \rightarrow 2_1^+$ and of the $2_2^+ \rightarrow 0_1^+$ transitions are displayed in fig. 6.19 a) and b) for the fitted ^{109}Ag matrix elements, respectively. Their good agreement indicates that the correct set of matrix elements has been found.

Apart from that, the obtained transitional matrix elements are used to calculate the branching ratio of the 2_2^+ state using eq. (2.30):

$$BR = P(2_2^+ \rightarrow 0_1^+)/P(2_2^+ \rightarrow 2_1^+) = \begin{cases} 0.59 \pm 0.14, & \text{for literature } ^{109}\text{Ag } \mathcal{M} \\ 0.58 \pm 0.13, & \text{for fitted } ^{109}\text{Ag } \mathcal{M}. \end{cases} \quad (6.17)$$

These values coincide with the branching ratio $BR = 0.68 \pm 0.05$ resulting from a previous β-decay study of ^{72}Cu [117].

Moreover, note that a possible $M1$ transition of the 2_2^+ state to the 2_1^+ state has been neglected in this CLX/DCY analysis in order to reduce the number of matrix elements in the profiled likelihood fit. Nevertheless, the more sophisticated GOSIA analysis in sec. 6.3.2 shows that $\mathcal{M}(M1; 2_2^+ \rightarrow 2_1^+)$ coincides well with zero within its error (c.f. tab. 6.3).

6.3.2 ^{72}Zn GOSIA Analysis

In sec. 6.3.1 the matrix elements of the low lying ^{72}Zn states have been determined step by step using the CLX/DCY Coulex code. The disadvantage of this procedure is that is is difficult to include correlations between the matrix elements in the error analysis. Thus, this section deals with the determination of the ^{72}Zn matrix elements using the GOSIA code. As GOSIA was developed to analyze large Coulex data sets involving many transitions and matrix elements, it provides a tool for a global minimization of all matrix elements together and it includes a sophisticated error analysis which considers the uncertainties of all matrix elements simultaneously (c.f. sec. 6.2.2).

Subdivision of the Data into Angular Ranges
Like in the CLX/DCY analysis the γ-ray yields are divided into different particle scattering angles to increase the sensitivity of the matrix elements on the shape of the differential Coulex cross section. In both Coulex codes the same subdivisions of the data is used: The large statistics in the FCD detector is divided into five angular bins each for the detection of the ejectile ^{72}Zn (data set 1-5) and the recoil ^{109}Ag (data set 6 - 10), respectively. Each of the FCD bins corresponds to three combined neighboring rings. Thus, the FCD yields 10 different angular bins. Furthermore, the BBarrel (data set 13) and the BCD (data set 14) is treated as one angular range each. Additionally, in the GOSIA analysis two more angular ranges have been considered: One data set containing the events with ^{72}Zn being detected in the FCD (data set 11) and one for the detection of ^{109}Ag in the FCD (data set 12). Data set 11 and 12 are essential for γ-ray transitions with low statistics, e.g. the $2_2^+ \rightarrow 0_1^+$ transition in ^{72}Zn. Furthermore, they are used to take upper limits of unobserved transitions into account. In summary, the GOSIA analysis considers 14 data sets in its minimization procedure. A detailed descriptions of the data subdivision including scattering angles can be found in appendix D.3.

γ-ray Yield Correction
For the 14 data sets, 45 experimental ^{72}Zn γ-ray yields from the Doppler corrected γ-ray spectra (c.f. sec. 6.1.5 and appendix D.5) have been determined which are listed in tab. D.8 in appendix D.6. However, the yields obtained from the γ-ray peaks have to be corrected before they can be used as input data for the GOSIA fit: The uncertainty of the MINIBALL photo peak efficiency curve ϵ_{Ge} (c.f. fig. 4.1 b)) has to be added to the uncertainty of the γ-ray yields, as GOSIA does not provide a different possibility to take the MINIBALL efficiency error in the minimization into account [121].

Upper Limits
However, some transitions are so weak that they cannot be seen even in the large combined data sets 11 and 12 of the FCD. Nevertheless, it can be necessary to include them in the GOSIA minimization to consider their influence on the population of the observed transitions. In ^{72}Zn, this is the case for the $0_2^+ \rightarrow 2_1^+$ transition, which is not observed in any FCD data set[18]. Including this unobserved γ-ray transition as upper limits in the fit of the combined FCD data sets 11 and 12, GOSIA ensures that they are considered in the minimization procedure, as the given upper limits impose an upper limit for their matrix elements. The used upper limits in the GOSIA fit, which have been obtained with eq. (D.13), are summarized in tab. D.10. Additionally, the 4_2^+ state with the corresponding $4_2^+ \rightarrow 2_2^+$ transition has been included in the GOSIA calculation to avoid an artificial population of the 2_2^+ state and to be able to extract the quadrupole moment of 2_2^+ state.

Minimization and Determination of Uncertainties
In the minimization eight transitional and three diagonal matrix elements of ^{72}Zn were fitted (c.f. fig. 6.13 a)) to 45 γ-ray yields which have been obtained from all Doppler corrected γ-ray spectra with respect to ^{72}Zn (c.f. sec. 6.1.5, tab. D.8). Furthermore, the fit considers the upper limits of the data sets

---

[18]However, it shows at least a weak but significant peak in the BBarrel data set.

Multipolarity	Transition	E_γ [keV]	$\mathcal{M}$
$E2$	$0_1^+ \rightarrow 2_1^+$	653	$0.44\,^{+0.01}_{-0.01}$(stat) ± 0.02(sys) ebarn
$E2$	$0_1^+ \rightarrow 2_2^+$	1658	$0.077\,^{+0.003}_{-0.003}$(stat) ± 0.004(sys) ebarn
$E2$	$2_1^+ \rightarrow 2_1^+$	-	$-0.28\,^{+0.05}_{-0.03}$(stat) ± 0.01(sys) ebarn
$E2$	$2_1^+ \rightarrow 4_1^+$	847	$0.68\,^{+0.01}_{-0.01}$(stat) ± 0.03(sys) ebarn
$E2$	$2_1^+ \rightarrow 0_2^+$	858	$0.14\,^{+0.01}_{-0.02}$(stat) ± 0.01(sys) ebarn
$E2$	$2_1^+ \rightarrow 2_2^+$	1004	$0.34\,^{+0.01}_{-0.01}$(stat) ± 0.02(sys) ebarn
$E2$	$4_1^+ \rightarrow 4_1^+$	-	$-0.31\,^{+0.07}_{-0.19}$(stat) ± 0.02(sys) ebarn
$E2$	$2_2^+ \rightarrow 2_2^+$	-	$0.50\,^{+0.04}_{-0.04}$(stat) ± 0.03(sys) ebarn
$M1$	$2_1^+ \rightarrow 2_2^+$	1004	$-0.03\,^{+0.08}_{-0.04}$(stat) ± 0.001(sys) μ_N

Tab. 6.3: The best set of ^{72}Zn matrix elements $\mathcal{M}$ obtained by the ^{72}Zn GOSIA analysis. The normalization was done with respect to the lifetime of the 2_1^+ state. Hence, the $\mathcal{M}(0_1^+ \rightarrow 2_1^+)$ matrix element has not really been fitted. However, it is given in the table to show that it is in agreement with the measured lifetime data (c.f. tab. 6.2). Furthermore, the matrix elements, where only upper limits are given, are not listed due to their low accuracy. The systematic uncertainties result from the approximations used in the GOSIA code [65, 66].

11 and 12. Moreover, as an additional data point the branching ratio $BR = P(2_2^+ \rightarrow 0_1^+)/P(2_2^+ \rightarrow 2_1^+) = 0.68 \pm 0.05$ from the β-decay experiment of ^{72}Cu [117] is included. The matrix elements obtained with the CLX/DCY analysis are used as start values for the fit. A good set of start values is mandatory to ensure that the high dimensional GOSIA fit will not be trapped in a local, wrong minimum. As absolute normalization of the experimental data to the calculated GOSIA yields a normalization transition is mandatory which features a known matrix element or lifetime. In the GOSIA analysis of ^{72}Zn, the $2_1^+ \rightarrow 0_1^+$ transition is chosen where the lifetime was measured in previous experiments (c.f. tab. 6.2). As soon as the GOSIA fit algorithm has reached its minimum, the overall uncertainties including all correlations between the matrix elements are extracted from the multidimensional least-square surface of the fit. The best set of matrix elements describing the ^{72}Zn Coulex data and their uncertainties are summarized in tab. 6.3. The given systematic uncertainties result from the fact that GOSIA uses several approximations in the calculation of the γ-ray yields. The main source of the systematic error is the semi-classical treatment in the calculation of the Coulex cross sections [66]. Furthermore, the used model for the deorientation effect results in a further systematic error[19]. In summary, the total systematic uncertainty of GOSIA was evaluated to be less than 5% [65, 66]. This conservative value has been chosen to determine the systematic uncertainties of the matrix elements.

Finally, the fit can be checked by calculating the predicted γ-ray yields using the fitted set of matrix elements. A comparison of the calculated and the experimental γ-ray yields is shown in fig. 6.20. Its excellent agreement is a first confirmation the result of the minimization procedure. Note, that in contrast to CLX/DCY, GOSIA directly computes and fits the detected γ-ray counts which are observed in the germanium detector array, instead of dealing with the number of emitted γ-rays.

Validation of the Obtained Matrix Elements

As the 11 matrix elements of ^{72}Zn are extracted in a multidimensional fit, it is important to test if really the true global minimum is reached instead of being trapped in a local minimum. Thus, the stability of fit and of the obtained best matrix elements were validated under the following scenarios using e.g. different spectroscopic data measured by previous experiments:

- In a first test, the previously measured branching ratio $BR = P(2_2^+ \rightarrow 0_1^+)/P(2_2^+ \rightarrow 2_1^+) = 0.68 \pm 0.05$ has been excluded from the fit. Without BR, the precision of the final matrix elements decreases, i.e. the obtained error bar of the matrix elements are larger, but the literature value of

---

[19]Of course there are a lot more sources of systematic uncertainties in GOSIA. They are all listed and discussed in [65, 66].
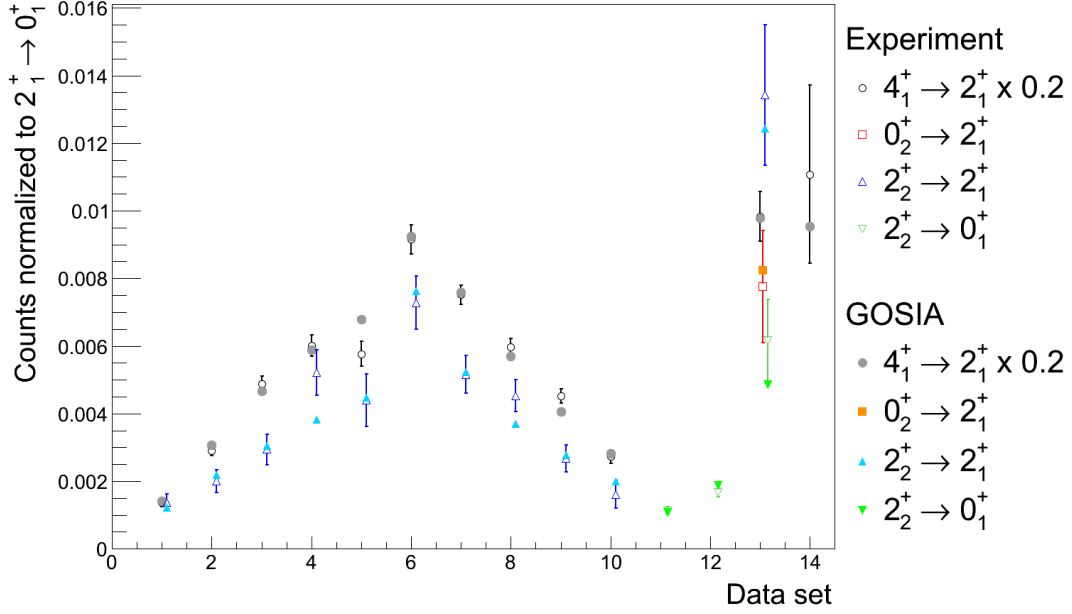
Fig. 6.20: A comparison of the experimental ^{72}Zn γ-ray yields and the yields calculated with GOSIA using the fitted matrix elements of tab. 6.3. The counts are normalized to the ^{72}Zn transition $2_1^+ \rightarrow 0_1^+$. The first 10 data sets represent subdivisions of the FCD data, while the data set 11 and 12 are the overall FCD data for the ^{72}Zn and the ^{109}Ag detection, respectively. Data set 13 and 14 corresponds to the BBarrel and BCD events.

the branching ratio could be confirmed. Hence, it was decided to include the *BR* in the final fit.

- The γ-ray yields are not only sensitive to the magnitude of the matrix elements, but also to their relative signs if more than one excitation path of a state is possible. In the case of ^{72}Zn, the 2_2^+ state can be excited in one step directly from the ground state and in two steps via the 2_1^+ state. The total excitation probability $P(2_2^+)$ of the 2_2^+ state reads[20]

$$P(2_2^+) \propto \left| \mathcal{M}(0_1^+ \rightarrow 2_2^+) \; + \; \mathcal{M}(0_1^+ \rightarrow 2_1^+) \cdot \mathcal{M}(E2; 2_1^+ \rightarrow 2_2^+) \right|^2. \qquad (6.18)$$

The relative sign of the $(E2)$ matrix elements defines the sign of the interference term $\mathcal{M}(0_1^+ \rightarrow 2_2^+) \cdot \mathcal{M}(0_1^+ \rightarrow 2_1^+) \cdot \mathcal{M}(2_1^+ \rightarrow 2_2^+)$ and thus, the value of the total excitation probability. In the GOSIA analysis, a positive and a negative sign of the matrix element $\mathcal{M}(E2; 2_1^+ \rightarrow 2_2^+)$ was evaluated. A negative sign increases the obtained χ^2/NDF value significantly (more than 10%). Hence, all signs in the loop $0_1^+ \rightarrow 2_1^+ \rightarrow 2_2^+ \rightarrow 0_1^+$ are considered to be positive.

- The variation of the matrix elements using different normalizations have been tested in GOSIA. For the $2_1^+ \rightarrow 0_1^+$ normalization transition in ^{72}Zn two lifetimes $\tau(2_1^+)$ were measured using the plunger technique with high precision[21]: $\tau(2_1^+)(\text{GANIL}) = 17.6 \pm 1.4$ ps [38] and $\tau(2_1^+)(\text{Legnaro}) = 17.9 \pm 1.8$ ps. [39]. Four GOSIA fits have been performed: First using the Legnaro lifetime [38], second the GANIL lifetime [39], third their weighted average and forth both lifetimes separately. As all lifetimes agree well within their uncertainties, the obtained set of matrix elements with the GOSIA code coincide well, too. The final minimization was done with the weighted average. Note that the measured ^{72}Zn lifetimes $\tau(4_1^+)$ and $\tau(6_1^+)$ by [38, 40] have not been included in the fit, since in ^{70,74}Zn the measured lifetimes of the 4_1^+ state feature a large deviation to previous Coulex experiments [41, 49] (c.f. sec. 1.2). A detailed discussion of this discrepancy can be found in sec. 6.4.1.

---

[20]The magnetic $\mathcal{M}(M1; 2_1^+ \rightarrow 2_2^+)$ matrix element is negligible (c.f. tab. 6.4).

[21]The third measured lifetime $\tau(2_1^+)(\text{GANIL}) = 19.4 \pm 5.5$ ps [40] has not been considered in the GOSIA analysis as it features a significant larger error than the measurements of [38] and [39].

- The matrix elements involving the 2_2^+ state have been evaluated with special care as the 2_2^+ state features the maximum number of matrix elements while the number of γ-ray yields is minimal compared to the other transitions. Therefore, a large set of start values for the $\mathcal{M}(0_1^+ \rightarrow 2_2^+)$, $\mathcal{M}(E2; 2_1^+ \rightarrow 2_2^+)$ and $\mathcal{M}(2_2^+ \rightarrow 2_2^+)$ has been tested. All configurations converge to the same minimum which confirms that the present Coulex data set is indeed sensitive to these matrix elements.

- Emphasis has been set on a possible $M1$ transition from the 2_2^+ state to the 2_1^+ state. Even with a large start value of $\mathcal{M}(M1; 2_1^+ \rightarrow 2_2^+)$ the fit approaches a value for $\mathcal{M}(M1; 2_1^+ \rightarrow 2_2^+)$ which is consistent with zero, independent of the start values of the other matrix elements involving the 2_2^+ state. However, the fit must be repeated recursively, as the minimum is reached only very slowly. The data features a sensitivity to $M1$ transition, as the backward scattering angles are sensitive to the $E2/M1$ mixing ratio: To explain the observed intensity of the $2_2^+ \rightarrow 2_1^+$ transition in the BBarrel data, a strong $E2; 2_1^+ \rightarrow 2_1^+$ transition is necessary, as the 2_2^+ state has to be populated in two steps, since the two step population is negligible at smaller scattering angles.

In summary, it can be concluded that the obtained matrix elements corresponds to the global minimum of the χ^2 surface and are robust under the in- and exclusion of previously measured spectroscopic data.

6.3.3 ^{72}Zn GOSIA2 Analysis

In sec. 6.3.2, the ^{72}Zn matrix elements have been determined with GOSIA using the measured lifetimes of the ^{72}Zn 2_1^+ state from Legnaro [38] and GANIL [39, 40] as normalization. To confirm the lifetime experiments, in this section the transitional matrix element $\mathcal{M}(0_1^+ \rightarrow 2_1^+)$ of the 2_1^+ state is extracted from the Coulex data by normalizing to the ^{109}Ag target excitation instead. Note that in sec. 6.3.1, $\mathcal{M}(0_1^+ \rightarrow 2_1^+)$ was already determined with the CLX/DCY code using the literature and the fitted ^{109}Ag matrix elements as normalization. However, the CLX/DCY analysis does not take the uncertainties of the ^{109}Ag matrix elements into account, which is crucial as the obtained $\mathcal{M}(0_1^+ \rightarrow 2_1^+)$ matrix element depends strongly on the normalization (c.f. sec. 6.3.1). In contrast, the analysis presented in this section propagates the uncertainties of the target matrix elements to the $\mathcal{M}(0_1^+ \rightarrow 2_1^+)$ matrix element.

The standard GOSIA code only handles the normalization to a transition of the same nucleus, e.g. to a known lifetime (c.f. sec. 6.3.2). Therefore, the GOSIA2 code [65, 66] was developed, which allows to determine the projectile matrix elements while normalizing to a target transition. GOSIA2 performs a simultaneous fit of the projectile and target matrix elements using the same normalization factors between the experimental and predicted GOSIA yields for both nuclei. The normalization factors are defined by the yields of the target γ-ray transitions and their known target matrix elements including their uncertainties which are given as additional data points in the fit. The final set of matrix elements corresponds to a global minimum in χ^2 which is defined by the sum of the individual χ^2 values of the projectile and the target [66]. The huge number of free fit parameters (normalization constants, projectile matrix elements and target matrix elements) in GOSIA2 leads to a complicated, high dimensional structure of the χ^2 function. Thus, a verification of the minimum as well as a reliable error analysis is generally impossible [66]. Hence, an iterative procedure following [66] is chosen instead, which is based on a combined GOSIA and GOSIA2 analysis.

In a first step, the transitional $\mathcal{M}(0_1^+ \rightarrow 2_1^+)$ and the diagonal $\mathcal{M}(2_1^+ \rightarrow 2_1^+)$ $E2$ matrix element of the 2_1^+ state in ^{72}Zn are approximated: A two dimensional total χ^2 surface with respect to $\mathcal{M}(0_1^+ \rightarrow 2_1^+)$ and $\mathcal{M}(2_1^+ \rightarrow 2_1^+)$ is constructed while fixing the higher lying matrix elements of ^{72}Zn to the obtained values of the standard GOSIA analysis (c.f. tab. 6.3). Its global minimum χ^2_{min} corresponds to the best fitted matrix elements. Like in the CLX/DCY maximum likelihood analysis, the 1σ contour can be extracted from the condition $\chi^2 = \chi^2_{min} + 1$. Its projection to the $\mathcal{M}(0_1^+ \rightarrow 2_1^+)$-axis defines the

Multipolarity	Transition	E_γ [keV]	$\mathcal{M}$
E2	$0_1^+ \to 2_1^+$	653	$0.424\,^{+0.002}_{-0.002}$(stat) ± 0.021(sys) ebarn
E2	$0_1^+ \to 2_2^+$	1658	$0.074\,^{+0.005}_{-0.004}$(stat) ± 0.004(sys) ebarn
E2	$2_1^+ \to 2_1^+$	-	$-0.31\,^{+0.04}_{-0.04}$(stat) ± 0.01(sys) ebarn
E2	$2_1^+ \to 4_1^+$	847	$0.68\,^{+0.01}_{-0.01}$(stat) ± 0.03(sys) ebarn
E2	$2_1^+ \to 0_2^+$	858	$0.14\,^{+0.01}_{-0.03}$(stat) ± 0.01(sys) ebarn
E2	$2_1^+ \to 2_2^+$	1004	$0.32\,^{+0.01}_{-0.01}$(stat) ± 0.02(sys) ebarn
E2	$4_1^+ \to 4_1^+$	-	$-0.36\,^{+0.06}_{-0.10}$(stat) ± 0.02(sys) ebarn
E2	$2_2^+ \to 2_2^+$	-	$0.52\,^{+0.05}_{-0.03}$(stat) ± 0.03(sys) ebarn
M1	$2_1^+ \to 2_2^+$	1004	$-0.06\,^{+0.07}_{-0.03}$(stat) ± 0.001(sys) μ_N

Tab. 6.4: The best set of ^{72}Zn matrix elements $\mathcal{M}$ obtained by the combined ^{72}Zn GOSIA-GOSIA2 analysis. The $\mathcal{M}(0_1^+ \to 2_1^+)$ matrix element results from the GOSIA2 analysis. All other matrix elements are obtained from a standard GOSIA analysis using the $\mathcal{M}(0_1^+ \to 2_1^+)$ matrix element resulting from the present GOSIA2 analysis as normalization instead of the previously measured lifetimes [38, 40] of the 2_1^+ state. The systematic uncertainties result from the approximations used in the GOSIA code [65, 66].

uncertainty of the $\mathcal{M}(0_1^+ \to 2_1^+)$ matrix element. It includes the uncertainty of the $2_1^+ \to 0_1^+$ projectile yield, of the fitted ^{109}Ag yields, of the fitted quadrupole moment of the 2_1^+ state of ^{72}Zn and of the known ^{109}Ag matrix elements, but not the uncertainty of higher lying ^{72}Zn states. Note that the influence of the higher lying states on the $\mathcal{M}(0_1^+ \to 2_1^+)$ matrix element is negligible (c.f. fig. 6.15). Thus, this approximation is well justified. Additionally, note that the resulting uncertainty of $\mathcal{M}(0_1^+ \to 2_1^+)$ is dominated by the 5% systematic error due to the GOSIA's semi-classical treatment. As the goal of this analysis step is to extract the transitional matrix element, only the data of the FCD with 10 subdivisions is included in the fit to minimize the influence of the quadrupole moment[22] (c.f. sec. 2.5). Furthermore, the fitted ^{109}Ag matrix elements from sec. 6.3.4 (tab. 6.5) are used as additional data points in the fit for the normalization, since they represent a complete set and feature the lowest uncertainties compared to the literature ^{109}Ag values.

In a second step of the combined GOSIA-GOSIA2 analysis, the $\mathcal{M}(0_1^+ \to 2_1^+)$ matrix element obtained from GOSIA2 is used along with its uncertainty as normalization in a standard GOSIA analysis instead of the 2_1^+ lifetime of ^{72}Zn taken from [38, 39]. The standard GOSIA fit has been performed analogously to sec. 6.3.2 using the data of all detectors. As a result, a complete set of ^{72}Zn matrix elements including correlated errors has been extracted.

According to [66], the first and the second step of the combined GOSIA-GOSIA2 analysis should be repeated iteratively until the matrix elements from both steps converge. However, as in the first GOSIA2 step the higher lying matrix elements are set to the values obtained from the standard GOSIA analysis in sec. 6.3.2, a second iteration is not necessary, since the matrix elements from the standard GOSIA analysis are already in excellent agreement with the matrix elements obtained in the second analysis step. Hence, a further iteration has lead to the same result. The final ^{72}Zn matrix elements are summarized in tab. 6.4. A discussion on the obtained results can be found in sec. 6.3.5 and in sec. 6.4.

6.3.4 ^{109}Ag GOSIA Analysis

Due to the excellent beam quality, not only multiple Coulomb excitation in the ^{72}Zn beam nucleus was observed (c.f. fig. 6.8), but also in the target nucleus ^{109}Ag (c.f. fig. 6.10). Although this is not the ideal case for a Coulomb excitation experiment which aims at the normalization to a known target transition, the rich ^{109}Ag Coulex data set opens the possibility to extract also the ^{109}Ag matrix elements with high

---

[22]As a cross-check the fit has also been performed with the complete Coulex data set, i.e. including the BBarrel and the BCD, which results in a consistent value for the transitional matrix element.

precision. However, due to observed multiple Coulomb excitation populating eight different states and due to the large set of 26 matrix elements which are connecting the states (14 transitional $E2$, 10 transitional $M1$ and two diagonal matrix elements as shown in fig. 6.13 b)), the structure of the odd-even nucleus ^{109}Ag is much more complicated compared to the even-even nucleus ^{72}Zn. Especially, due to the odd proton number $Z = 47$, the $M1$ transitions are of the same importance than the $E2$ transitions in ^{109}Ag. As a result, a CLX/DCY analysis is not suitable for ^{109}Ag, since its matrix elements are strongly correlated. Instead a full GOSIA analysis with a high dimensional fit has to be performed.

Subdivision of the Data into Angular Ranges and Included Known Spectroscopic Information
To be sensitive to the different (de-)excitation paths, the different multipolarities ($E2$ or $M1$) and the involved quadrupole moments, the complete ^{109}Ag Coulex data set has been divided in the same angular ranges like the ^{72}Zn data set (c.f. sec. 6.3.2 and appendix D.3). The 26 matrix elements are fitted to 110 experimental yields (c.f. tab. D.9), two upper limits for the $(3/2)_3^- \rightarrow 1/2_1^-$ transition in the combined FCD data sets 11 and 12 (c.f. tab. D.10), all 13 available branching ratios (c.f. tab. D.2), all eight available multipole mixing ratios (c.f. tab. D.3), four previously measured lifetimes of the states $3/2_1^-, 5/2_1^-, (3/2)_3^-$ and the two known matrix elements $3/2_1^- \rightarrow 1/2_1^-$ and $5/2_1^- \rightarrow 1/2_1^-$ obtained from the Plunger lifetime experiment [122]. Like in the ^{72}Zn GOSIA analysis the errors of the ^{109}Ag γ-ray yields have been propagated with the error of the MINIBALL photopeak efficiency. Furthermore, the ^{109}Ag yields have been corrected for the beam contaminants ^{72}Ga, ^{36}Ar and ^{18}O (c.f. sec. 6.1.6 and sec. 6.2.1) which can also excite the target nuclei ^{109}Ag.

Minimization and Determination of Uncertainties
The minimization was done with respect to the known lifetimes of the $5/2_1^- \rightarrow 1/2_1^-$ transition with $E_\gamma = 415$ keV. As start values for the fit, the previously measured matrix elements, mainly from the Coulex experiment [123] and a plunger experiment [122], are chosen (c.f. appendix D.2). However, the fit procedure for ^{109}Ag was extended compared to the ^{72}Zn GOSIA analysis. Due to the large number of experimental γ-ray yields, the strong γ-ray transitions which can be resolved in each angular bin are dominating the least-square statistic in the fit. Thus, the fit of all data sets together is only little sensitive to matrix elements of weak transitions such as the $5/2_2^- \rightarrow 1/2_1^-$, $(3/2)_3^- \rightarrow 1/2_1^-$ and $(3/2)_3^- \rightarrow 3/2_1^-$ transitions. Hence, to increase their influence in the fit, a recursive algorithm has been chosen to find the best set of ^{109}Ag matrix elements: First, all 14 data sets have been fitted and their resulting set of matrix elements are used as input of a subsequent fit using only the data sets 11-14 (without the subdivisions of the FCD). The result of this reduced data set is finally used as start values for the complete fit with 14 angular ranges. After a few iterations, the global minimum of the GOSIA fit is reached. Like, in the ^{72}Zn analysis, different signs and different start values for the matrix elements were tested to ensure that the fit is not being trapped in a local minimum. Afterwards, the correlated uncertainties of the final set of matrix elements have been calculated and again a systematic uncertainty of GOSIA of 5% has been considered [65, 66].

Final Set of ^{109}Ag Matrix Elements and Comparison to the Experimental Yields
The best set of ^{109}Ag matrix elements, extracted from the data of the present experiment, is summarized in tab. 6.5 and visualized in fig. 6.21. 18 from 26 matrix elements are in good agreement with the previous measurements. Furthermore, the signs of the quadrupole moments of the $3/2_1^-$ (state 2) and the $5/2_1^-$ (state 3) state could be confirmed, however, the present experiment proposes in both cases a smaller absolute value compared to previous measurements. For the three matrix elements $\mathcal{M}(E2; 3/2_1^- \rightarrow 7/2_1^-)$, $\mathcal{M}(E2; 5/2_1^- \rightarrow 3/2_2^-)$ and $\mathcal{M}(E2; 5/2_1^- \rightarrow 9/2_1^-)$ a large discrepancy compared to the literature was found. Moreover, the matrix elements $\mathcal{M}(E2, M1; 5/2_1^- \rightarrow 7/2_1^-)$ could be determined for the fist time. For many other matrix elements the error bars are significantly reduced compared to the previous experiments.
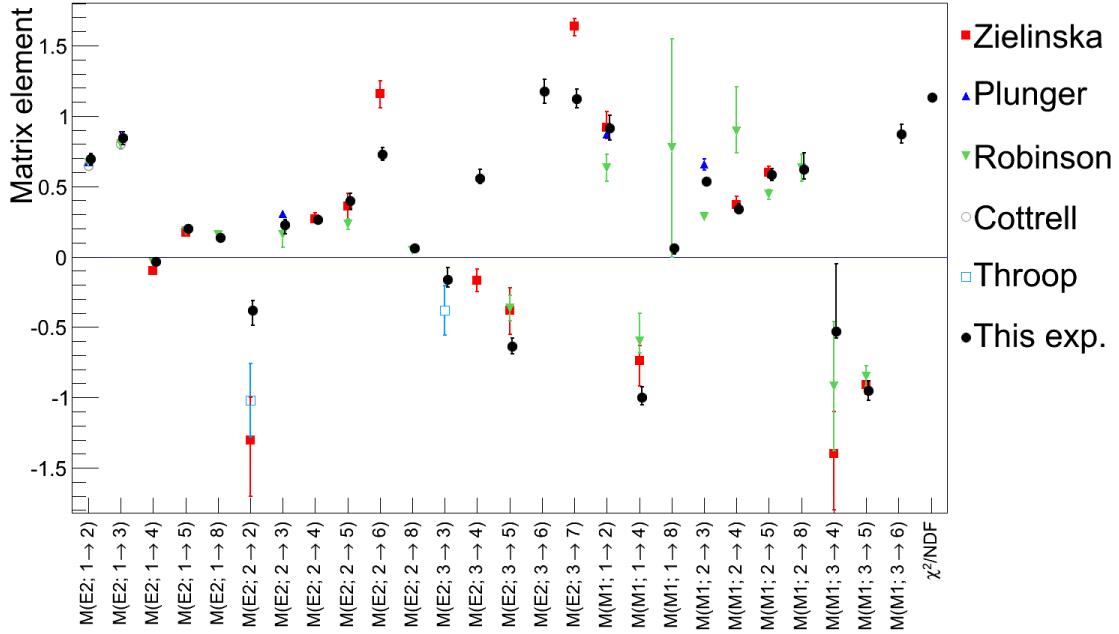A good cross-check, if the best fitting matrix elements describe the experimental data of all γ-ray

Fig. 6.21: A comparison of the obtained ^{109}Ag matrix elements from the current Coulex experiment (black dots and tab. 6.5) with previous measurements. The red squares, the green lower triangles, the open gray dots and the open light blue squares correspond to the Coulex experiments [123], [124], [125] and [126], respectively. The dark blue upper triangles are lifetime measurements using the Cologne plunger [122]. The $E2$ and $M1$ matrix elements are given in ebarn and in μ_N, respectively. The transitions are labeled following the convention introduced in fig. 6.12 a) and tab. 6.5.

transitions well, is to compare the experimental yields with the calculated yields using these matrix elements. Indeed, fig. 6.22 shows a generally good agreement between experiment and the predicted yield of GOSIA for all observed γ-ray transitions. As an additional check, not only the detected γ-ray yields are compared, but also the number $N_{\gamma,emit}$ of emitted γ-rays divided by the solid angle of the particle detector as done in the CLX/DCY analysis in eq. (6.6) and in sec. 6.3.1. This has the advantage that the angular dependence of the cross sections can be seen. Hence, it is also possible to identify erroneous data points. The obtained experimental $N_{\gamma,emit}$ curves are compared in fig. 6.23 with the results of a CLX/DCY calculation using the resulting set of ^{109}Ag matrix elements from the GOSIA analysis. The CLX/DCY calculation with the fitted set of matrix elements describes the experimental data of all transitions in ^{109}Ag very well. Additionally, the dotted blue curves visualize the number of emitted γ-rays calculated with the literature values of ^{109}Ag. Although the deviation of the fitted matrix elements to their literature values is small, a large effect in the γ-ray yield is visible. This underlines the high precision of the data thanks to the excellent statistics of the present experiment. The count rates resulting from the literature ^{109}Ag matrix elements are predicted to be too high as well as too low, depending on the transition. Furthermore, fig. 6.23 h) features a totally different shape in the experimental data and in the predicted counts from the matrix elements of the literature. Hence, a systematic error in the present experiment to explain the deviation is unlikely.

In conclusion, the derived set of ^{109}Ag matrix elements is suited to serve as a precise normalization for future Coulex experiments thanks to the excellent statistics which was achieved by a high intense ISOLDE beam, the newly developed C-REX setup with its large angular coverage and the high efficient MINIBALL spectrometer.

Multipolarity	Transition ID	Transition	E_γ [keV]	$\mathcal{M}$
$E2$	$1 \to 2$	$1/2_1^- \to 3/2_1^-$	311	$0.695\ ^{+0.005}_{-0.004}$(stat) ± 0.035(sys) ebarn
$E2$	$1 \to 3$	$1/2_1^- \to 5/2_1^-$	415	$0.843\ ^{+0.004}_{-0.006}$(stat) ± 0.042(sys) ebarn
$E2$	$1 \to 4$	$1/2_1^- \to 3/2_2^-$	702	$-0.035\ ^{+0.004}_{-0.003}$(stat) ± 0.002(sys) ebarn
$E2$	$1 \to 5$	$1/2_1^- \to 5/2_2^-$	863	$0.200\ ^{+0.003}_{-0.003}$(stat) ± 0.004(sys) ebarn
$E2$	$1 \to 8$	$1/2_1^- \to (3/2)_3^-$	(1324)	$0.13\ ^{+0.01}_{-0.01}$(stat) ± 0.01(sys) ebarn
$E2$	$2 \to 2$	$3/2_1^- \to 3/2_1^-$	-	$-0.38\ ^{+0.05}_{-0.08}$(stat) ± 0.02(sys) ebarn
$E2$	$2 \to 3$	$3/2_1^- \to 5/2_1^-$	103	$0.23\ ^{+0.02}_{-0.05}$(stat) ± 0.01(sys) ebarn
$E2$	$2 \to 4$	$3/2_1^- \to 3/2_2^-$	(391)	$0.27\ ^{+0.01}_{-0.01}$(stat) ± 0.01(sys) ebarn
$E2$	$2 \to 5$	$3/2_1^- \to 5/2_2^-$	551	$0.40\ ^{+0.03}_{-0.04}$(stat) ± 0.02(sys) ebarn
$E2$	$2 \to 6$	$3/2_1^- \to 7/2_1^-$	601	$0.73\ ^{+0.01}_{-0.01}$(stat) ± 0.04(sys) ebarn
$E2$	$2 \to 8$	$3/2_1^- \to (3/2)_3^-$	1013	$0.063\ ^{+0.024}_{-0.025}$(stat) ± 0.003(sys) ebarn
$E2$	$3 \to 3$	$5/2_1^- \to 5/2_1^-$	-	$-0.16\ ^{+0.08}_{-0.04}$(stat) ± 0.01(sys) ebarn
$E2$	$3 \to 4$	$5/2_1^- \to 3/2_2^-$	(286)	$0.56\ ^{+0.03}_{-0.01}$(stat) ± 0.03(sys) ebarn
$E2$	$3 \to 5$	$5/2_1^- \to 5/2_2^-$	448	$-0.64\ ^{+0.03}_{-0.02}$(stat) ± 0.03(sys) ebarn
$E2$	$3 \to 6$	$5/2_1^- \to 7/2_1^-$	497	$1.17\ ^{+0.02}_{-0.03}$(stat) ± 0.06(sys) ebarn
$E2$	$3 \to 7$	$5/2_1^- \to 9/2_1^-$	676	$1.13\ ^{+0.01}_{-0.01}$(stat) ± 0.06(sys) ebarn
$M1$	$1 \to 2$	$1/2_1^- \to 3/2_1^-$	311	$0.92\ ^{+0.04}_{-0.04}$(stat) ± 0.05(sys) μ_N
$M1$	$1 \to 4$	$1/2_1^- \to 3/2_2^-$	702	$-0.10\ ^{+0.03}_{-0.01}$(stat) ± 0.05(sys) μ_N
$M1$	$1 \to 8$	$1/2_1^- \to (3/2)_3^-$	(1324)	$0.062\ ^{+0.026}_{-0.043}$(stat) ± 0.003(sys) μ_N
$M1$	$2 \to 3$	$3/2_1^- \to 5/2_1^-$	103	$0.536\ ^{+0.004}_{-0.003}$(stat) ± 0.027(sys) μ_N
$M1$	$2 \to 4$	$3/2_1^- \to 3/2_2^-$	(391)	$0.34\ ^{+0.02}_{-0.02}$(stat) ± 0.02(sys) μ_N
$M1$	$2 \to 5$	$3/2_1^- \to 5/2_2^-$	551	$0.59\ ^{+0.01}_{-0.01}$(stat) ± 0.03(sys) μ_N
$M1$	$2 \to 8$	$3/2_1^- \to (3/2)_3^-$	1013	$0.62\ ^{+0.08}_{-0.04}$(stat) ± 0.03(sys) μ_N
$M1$	$3 \to 4$	$5/2_1^- \to 3/2_2^-$	(286)	$-0.53\ ^{+0.45}_{-0.02}$(stat) ± 0.03(sys) μ_N
$M1$	$3 \to 5$	$5/2_1^- \to 5/2_2^-$	448	$-0.95\ ^{+0.02}_{-0.023}$(stat) ± 0.05(sys) μ_N
$M1$	$3 \to 6$	$5/2_1^- \to 7/2_1^-$	497	$0.87\ ^{+0.03}_{-0.02}$(stat) ± 0.04(sys) μ_N

Tab. 6.5: The best set of ^{109}Ag matrix elements obtained by the ^{109}Ag GOSIA analysis. The normalization was done with respect to the lifetime of the $5/2_1^-$ state. Hence, the $\mathcal{M}(E2; 3/2_1^+ \to 5/1_1^+)$ has not really been fitted. However, it is given in the table to show that it is in agreement with the measured lifetime data given in tab. D.1. A comparison of all matrix elements between this experiment and the previously measured values is shown in fig. 6.21. The γ-rays which are given in brackets have not been observed in the experiment. The systematic uncertainties result from the approximations used in the GOSIA code [65, 66].

6.3.5 Comparison of the CLX/DCY and GOSIA Results

In the last sections, the CLX/DCY Coulex code (c.f. sec. 6.3.1) as well as the GOSIA Coulex code (c.f. sec. 6.3.2, 6.3.3 and 6.3.4) have been used to determine the most important matrix elements of the ^{72}Zn projectile nucleus and of the ^{109}Ag target nucleus. Finally, this section deals with the comparison of the obtained results. However, before the extracted matrix elements themselves are compared, the calculated yields of CLX/DCY and GOSIA are examined.

Comparison of the Calculated Yields of CLX/DCY and GOSIA Code
One prerequisite to obtain reliable results from both Coulex codes is that their calculated experimental
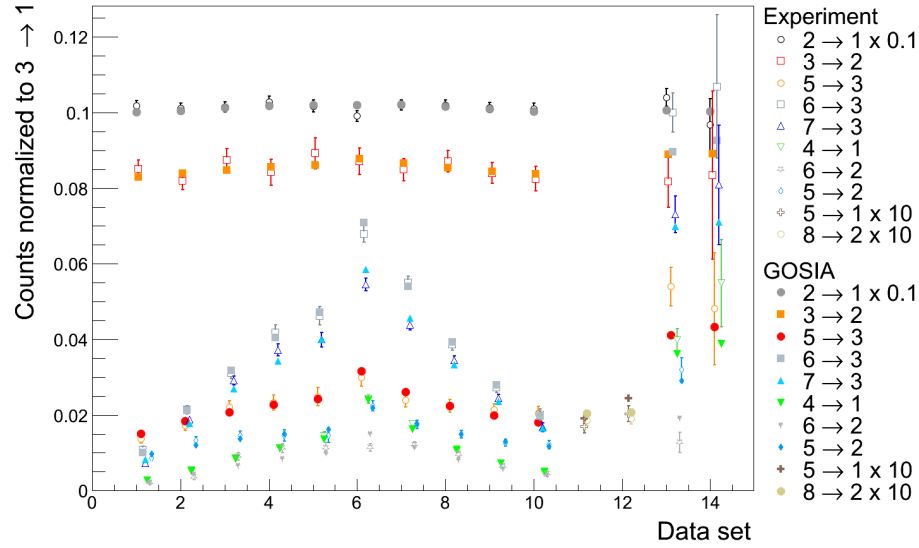
Fig. 6.22: A comparison of the experimental ^{109}Ag γ-ray yields and the yields calculated with GOSIA using the fitted matrix elements of tab. 6.3. The normalization was done with respect to the lifetime of the $5/2_1^-$ state.

yields assuming the same given set of matrix elements coincide[23]. Furthermore, the influence of small differences in the internal calculation of the γ-ray yields can be studied. Fig. 6.24 shows the excellent agreement between the CLX/DCY and GOSIA ^{72}Zn yields for the obtained ^{72}Zn matrix elements in this thesis. Additionally, fig. 6.25 displays the comparison of the reproduced γ-ray yields of the ^{109}Ag target. As the level scheme of ^{109}Ag with its huge number of transitional $E2$ and $M1$ matrix elements as well as quadrupole moments is more complicated compared to ^{72}Zn, the discrepancies between the ^{109}Ag γ-ray yields are slightly bigger compared to ^{72}Zn.

One reason for the deviation is the different treatment of the energy loss of the beam in the target. The CLX/DCY code assumes that all Coulex reactions happen exactly in the middle of the target, while GOSIA considers the whole target and integrates over the given stopping powers. This can results in different reaction energies which can have a influence on the calculated yields, especially in multi-step Coulomb excitation which dominates at large scattering angles.

Besides the beam stopping in the target, a part of the deviation between the Coulex codes is attributed to the deorientation effect [65]. The deorientation effect attenuated the particle-γ-ray angular distribution as the strong fluctuating hyperfine fields of the highly-ionized recoiling ^{72}Zn or ^{109}Ag ions can depolarize the nuclear state alignment as the nuclear spin can couple to the total spin of the electron shell. The strong gradient in the atomic hyperfine field is caused by the deexcitation of the highly-excited and highly-ionized atoms to the atomic ground state. However, an appropriate description of this mechanism is challenging and up to now only simplified models exits. The CLX/DCY code uses the Abragam and Pound theory [127]. It is based on the assumption that the projectile and the target ions recoil in high pressure gas. However, in Coulex experiments the ions recoil in vacuum. As significant deviations between these two scenarios have been found [65], GOSIA does not use the Abragam and Pound model. Instead, GOSIA uses the more sophisticated Brenn and Spehl two state model [128, 129]. It describes the data well, although it still represents a significant simplification of the deorientation effect [65]. Fig. D.5 and fig. D.6 show the influence of the deorientation effect in GOSIA for the ^{72}Zn and the ^{109}Ag yields. Comparing both figures, it can be concluded that the deorientation effects plays a bigger role in ^{109}Ag than in ^{72}Zn. This can be explained by the strong $M1$ components in ^{109}Ag. The magnetic interaction between the atomic hyperfine magnetic fields and the magnetic moments of the nuclear states are responsible for the dominant component of the deori-

---

[23]Such a comparison is also helpful to track errors in the input files of the codes. This is especially important for the complicated GOSIA input file.
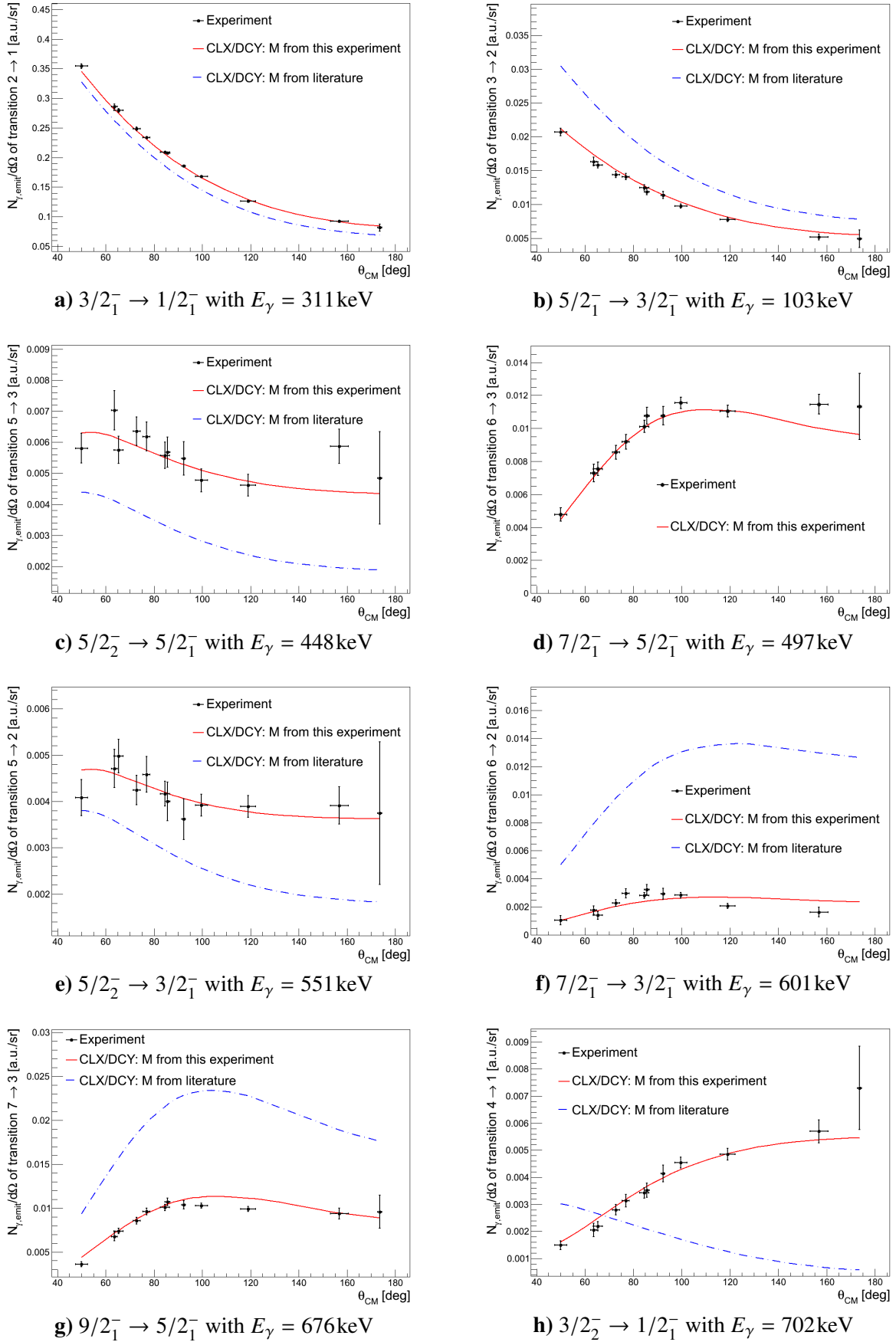
a) $3/2_1^- \rightarrow 1/2_1^-$ with $E_\gamma = 311\,\mathrm{keV}$

b) $5/2_1^- \rightarrow 3/2_1^-$ with $E_\gamma = 103\,\mathrm{keV}$

c) $5/2_2^- \rightarrow 5/2_1^-$ with $E_\gamma = 448\,\mathrm{keV}$

d) $7/2_1^- \rightarrow 5/2_1^-$ with $E_\gamma = 497\,\mathrm{keV}$

e) $5/2_2^- \rightarrow 3/2_1^-$ with $E_\gamma = 551\,\mathrm{keV}$

f) $7/2_1^- \rightarrow 3/2_1^-$ with $E_\gamma = 601\,\mathrm{keV}$

g) $9/2_1^- \rightarrow 5/2_1^-$ with $E_\gamma = 676\,\mathrm{keV}$

h) $3/2_2^- \rightarrow 1/2_1^-$ with $E_\gamma = 702\,\mathrm{keV}$

Fig. 6.23: The experimental γ-ray yields of ^{109}Ag are compared to two calculations using the CLX/DCY code. The calculation shown with the solid red lines results from the fitted matrix elements (c.f. tab. 6.5), whereas the dotted blue lines show the γ-ray yields which are obtained if the literature values (c.f. appendix D.2) of the ^{109}Ag matrix elements are used. Note, that in fig. d) the literature prediction is missing as the relevant matrix elements have not been measured previously.
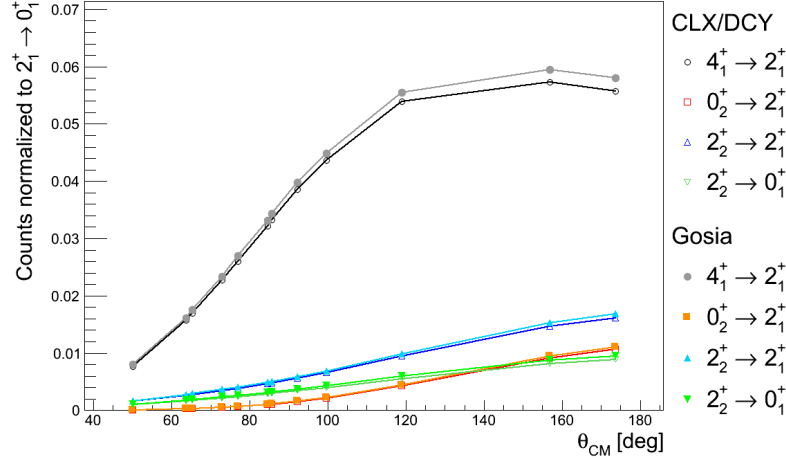
Fig. 6.24: A comparison of the calculated ^{72}Zn yields using the CLX/DCY code and the GOSIA code as a function of the scattering angle θ_{CM} in the center-of-mass frame. In both calculations the same set of matrix elements resulting from sec. 6.3.2 are used. Generally, the agreement between both Coulex codes is quite good for all states. The lines are only shown to guide the eye.
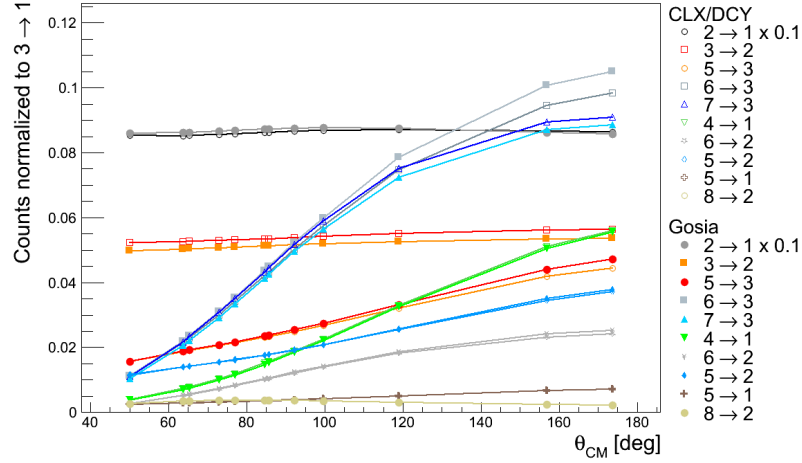

Fig. 6.25: A comparison of the calculated ^{109}Ag yields using the CLX/DCY code and the GOSIA code as a function of the scattering angle θ_{CM} in the center-of-mass frame. In both calculations the same set of matrix elements resulting from sec. 6.3.4 are used. Although a large number of levels and matrix elements are involved in the Coulex calculation, the agreement is generally good. The largest deviations, especially in the $3 \rightarrow 2$ transition, are due to the different models for the deorientation effect which dominates if a significant $M1$ strength is present. The lines are only shown to guide the eye.

entation effect [65]. Furthermore, the lifetimes of the states play a crucial role for the attenuation of the particle-γ-ray angular distribution due to the deorientation effect, as a longer nuclear state lifetime results in a larger interaction time with the hyperfine field [65]. Apart from that, the deorientation effect strongly depends on the ion velocity [65].

Comparison of the ^{72}Zn Matrix Elements Obtained with the CLX/DCY and the GOSIA Code
The set of ^{72}Zn matrix elements connecting the low lying ^{72}Zn states have been determined using four different techniques which are based on two different Coulex codes: In sec. 6.3.1, a maximum likelihood analysis with the CLX/DCY code was presented using two different sets of ^{109}Ag matrix elements for normalization: previously measured ^{109}Ag matrix elements (c.f. appendix D.2) as well as the ^{109}Ag matrix elements which were determined in this work (c.f. tab. 6.5). Furthermore, a standard GOSIA analysis was conducted using the lifetime of the 2_1^+ state in ^{72}Zn as normalization. To also
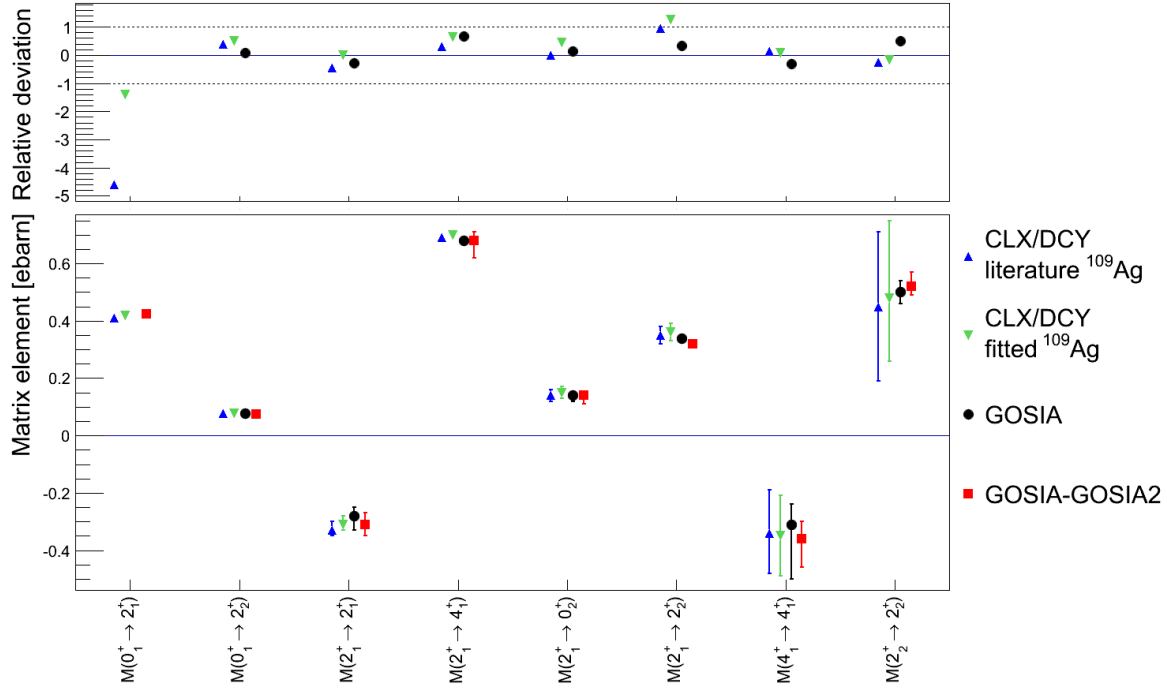
Fig. 6.26: A comparison of all extracted ^{72}Zn matrix elements using four different methods: The CLX/DCY analysis with two different sets of ^{109}Ag matrix elements as normalization (c.f. sec. 6.3.1), a standard GOSIA analysis with the lifetime of the ^{72}Zn 2_1^+ state as normalization (c.f. sec. 6.3.2) and a combined GOSIA-GOSIA2 analysis using the fitted ^{109}Ag matrix elements given in tab. 6.5 as normalization (c.f. sec. 6.3.3). The lower panel shows the absolute values obtained with each method. The upper pad visualizes the relative deviation to the GOSIA-GOSIA2 result, i.e. the deviation between the matrix elements to the GOSIA-GOSIA2 value divided by their total error. Nearly all values agree well within a 1σ confidence interval which is indicated by the dashed lines. Only the transitional matrix element $\mathcal{M}(0_1^+ \rightarrow 2_1^+)$ extracted from the CLX/DCY analysis and the literature ^{109}Ag values features a larger deviation which highlights the importance of a proper normalization.

extract the $\mathcal{M}(E2; 0_1^+ \rightarrow 2_1^+)$ matrix element with GOSIA, a combined GOSIA-GOSIA2 analysis has been performed using the lifetime $\tau(5/2_1^-)$ of the $5/2_1^+$ state at 415 keV of ^{109}Ag as normalization. All obtained results are summarized in fig. 6.26. The lower pad shows the absolute values while the upper pad shows the relative deviation to the matrix elements determined with the GOSIA-GOSIA2 analysis. All methods coincide well within or close to a 1σ confidence interval (indicated by the dashed lines in the upper pad of fig. 6.26). Only the transitional matrix element $\mathcal{M}(0_1^+ \rightarrow 2_1^+)$ determined with the CLX/DCY code and using the normalization to the previously known literature values of the ^{109}Ag matrix elements features a larger deviation. This emphasizes that a correct normalization is crucial for the obtained results. Note that the given uncertainties in fig. 6.26 correspond only to the given statistical errors, as the 5% systematic uncertainty, which is mainly attributed to the semi-classical treatment has the same effect in both Coulex codes. In case of the CLX/DCY analysis, the given uncertainties do not take correlations between all matrix elements into account. Furthermore, the uncertainties of the target matrix elements used for normalization are not included. In the standard GOSIA analysis, correlations are considered as well as the uncertainty of the lifetime data which is used for normalization. The matrix elements of the combined GOSIA-GOSIA2 analysis include all correlations and all uncertainties of all projectile and target normalization matrix elements. Hence, these matrix elements represent the final result of the Coulex experiment performed in this work.
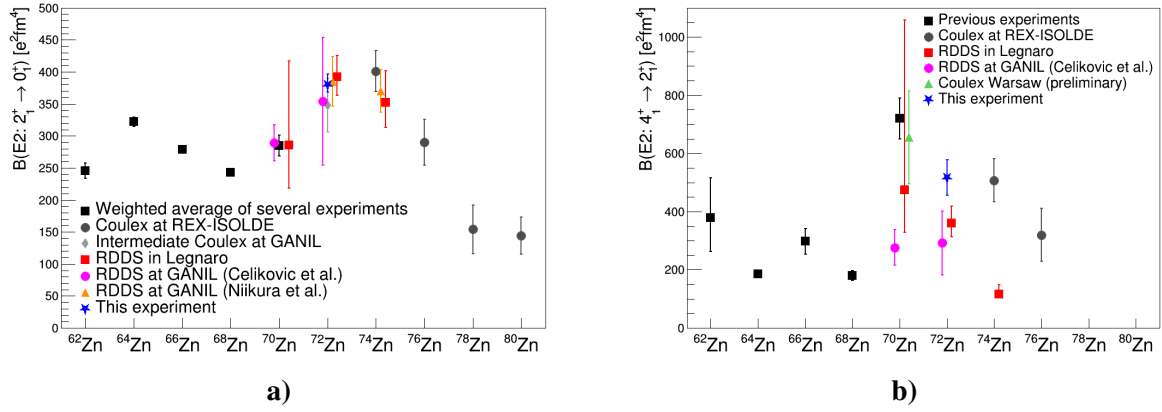
Fig. 6.27: The measured $B(E2)$ values of the neutron-rich zinc isotopes. The reduced transition strengths shown with the blue star have been obtained in this work. The dark gray dots represent previous Coulex experiments which were performed at ISOLDE [41]. The black squares for ^{70}Zn correspond to a DSAM measurement [35, 36]. In addition, lifetime measurements using the Recoil Distance Doppler Shift method (RDDS) are shown: The red squares are the results from a plunger measurement with AGATA in Legnaro [38], the orange triangles and magenta dots are lifetime measurements at GANIL from [39] and [40], respectively. **a)** shows the $B(E2; 2_1^+ \rightarrow 0_1^+)$-values where all results show a consistent picture. **b)** displays the $B(E2; 4_1^+ \rightarrow 2_1^+)$ values which feature discrepancies between the lifetime measurements and the Coulex experiments. With a green upper triangle a preliminary ^{70}Zn Coulex measurement at HIL Warsaw is visualized [42]. For details see text.

6.4   Discussion

The extracted ^{72}Zn matrix elements from tab. 6.4 can be translated into reduced transition probabilities (c.f. tab. 6.6) and spectroscopic quadrupole moments using eq. (2.18) and eq. (2.22), respectively. They are discussed in the following: Sec. 6.4.1 shows a comparison to the previously measured experimental data in the neutron-rich zinc chain. In sec. 6.4.2 the measured triaxiality of the ground state in ^{72}Zn is discussed and compared to the results of two mean field calculations. Last but not least, the obtained $B(E2)$ values and quadrupole moments are interpreted using three shell model calculations (c.f. sec. 6.4.3).

6.4.1   Comparison to Previous Experiments

Fig. 6.27 shows the evolution of the experimental $B(E2; 2_1^+ \rightarrow 0_1^+)$ and $B(E2; 4_1^+ \rightarrow 2_1^+)$ values of the neutron-rich zinc isotopes[24]. In ^{72}Zn, the $B(E2; 2_1^+ \rightarrow 0_1^+)$ measured in this thesis is in good agreement with the intermediate Coulex measurement as well as with the lifetime measurements [38, 39, 40] (c.f. fig. 6.27 a)). In general, the Coulex and the lifetime experiments coincide along the whole neutron-rich isotopic zinc chain.

The obtained $B(E2; 4_1^+ \rightarrow 2_1^+)$ value for ^{72}Zn in this work is significantly higher than the results from the lifetime measurements of the 4_1^+ state from Legnaro and GANIL (c.f. fig. 6.27 b). But it is close to the values of the previous safe Coulex experiments. The ^{70}Zn Coulex experiment was conducted at HIL Warsaw with a ^{32}S beam ($E_{beam} = 68$ MeV) impinging on a 0.7 mg/cm^2 thick ^{70}Zn target [42]. The Coulex experiments with the radioactive zinc beams were performed at ISOLDE using the same zinc beam energies of $E_{beam} \approx 2.85$ MeV/u like in this ^{72}Zn Coulex experiment (c.f. fig. 6.27 b)). Note that the discrepancy between the Coulex experiments and the lifetime measurements is even more dramatic in case of ^{74}Zn, since the data points from Coulex and RDDS are in disagreement by more

---

[24]Note that the error bars of this Coulex experiment in fig. 6.27 (and in fig. 6.29) include the statistical error as well as the 5% systematic error of the Coulex codes. They are comparable in size to the error bars of the other experiments although the statistics in the Coulex experiment of this thesis is much higher, since the 5% systematic error of GOSIA was neglected in the Coulex analysis of the $^{74-80}$Zn isotopes [49].

than 5σ. In the following possible reasons for this inconsistency in ^{72,74}Zn are discussed:

- From the point of view of high level physics analysis, the main difference between the lifetime measurements and the Coulex experiments is the different dependency of the analyzed γ-ray peak of the $4_1^+ \rightarrow 2_1^+$ transition: In the lifetime measurements, it is only sensitive to the transitional matrix element $\mathcal{M}(E2; 2_1^+ \rightarrow 4_1^+)$, while in Coulex experiments it also depends on the diagonal matrix element $\mathcal{M}(E2; 4_1^+ \rightarrow 4_1^+)$. In the latter case, both matrix elements are disentangled by exploiting the dependence of the Coulex cross section on the scattering angle (c.f. fig. 2.5).
  But in the Coulex analysis of ^{74,76}Zn the quadrupole moment of the 4_1^+ state could not be extracted, since the statistics was too low to divide the $4_1^+ \rightarrow 2_1^+$ γ-ray yield into several angular bins. However, its influence on the $\mathcal{M}(E2; 2_1^+ \rightarrow 4_1^+)$ strength was carefully evaluated [41, 49]. Even by assuming extreme values for the quadrupole moment, the $\mathcal{M}(E2; 2_1^+ \rightarrow 4_1^+)$ value of the lifetime measurement could not be reproduce at all [41] (c.f. sec. 1.2).
  In the present Coulex analysis of the ^{72}Zn data, both matrix elements have been determined from the differential cross section using 12 angular bins covering $\theta_{CM} \in [50°, 175°]$. As additional test, the obtained $B(E2; 4_1^+ \rightarrow 2_1^+)$ from the Legnaro lifetime measurement [38] has been used as input in the ^{72}Zn analysis: However, the ^{72}Zn Coulex data cannot be reproduced with any realistic quadrupole moment (c.f. sec. 6.3.2 and fig. 6.28). In addition, the lifetime does not even describe the data points with small scattering angles, where the influence of the quadrupole moment is smallest (c.f. fig. 6.28).

- A prerequisite for a correct extraction of the electromagnetic matrix elements in the Coulex analysis is, that the reaction is safe even for high scattering angles, i.e. the excitation process is purely electromagnetic and nuclear effects do not contribute. This condition was fulfilled for all ISOLDE experiments (c.f. fig. 2.3 for ^{72}Zn and [49] for $^{74-80}$Zn). Hence, the discrepancy between the Coulex and lifetime measurements cannot be attributed to the nuclear force which was not considered in the Coulex analyses.

- Feeding contributions from higher lying states such as the 6_1^+ state have to be fully taken into account in both experimental techniques to obtain reliable results for $\mathcal{M}(E2; 2_1^+ \rightarrow 4_1^+)$. In the determination of the 4_1^+ lifetime in ^{72,74}Zn, the feeding transition $6_1^+ \rightarrow 4_1^+$ was considered in [38] and [40]. In the ^{72}Zn Coulex experiment performed in this work, the influence of the 6_1^+ state was found to be negligible (c.f. fig. 6.16). Furthermore, an upper limit for the counts in the $6_1^+ \rightarrow 4_1^+$ transition has been determined which is in agreement with the measured lifetime of the 6_1^+ state (c.f. sec. 6.3.1). Other significant feeding contributions, like e.g. from the 5_1^- state discussed in [38], can be excluded: No further coincidences from higher lying states are visible in the Doppler corrected γ-ray spectra after a gate on the $4_1^+ \rightarrow 2_1^+$ transition despite their excellent statistics (c.f. fig. D.7).

- Another approach to explain the mismatch between the two experimental techniques is to postulate an $E4$ transition connecting the 4_1^+ state with the ground state. Such a transition has not been considered in the Coulex analysis, yet. To estimate its influence, the $\mathcal{M}(E2; 2_1^+ \rightarrow 4_1^+)$ matrix element has been fixed in the Coulex analysis to the lifetime of [38] and the strength of a possible $E4$ transition required to describe the experimental data has been determined (c.f. fig. 6.28). This results in an unrealistic high $B(E4 : 4_1^+ \rightarrow 0_1^+) \approx 710$ W.u. value. Consequently, the incorporation of a realistic $E4$ strength is not able to explain the discrepancy between the Coulex and the lifetime measurements.

- The influence of energetically close lying states has to be taken into account. This is especially important in the lifetime analysis, as the yields of the Doppler shifted and the unshifted component of the γ-ray peaks have to be determined (c.f. sec. 1.2). The extraction of the lifetime
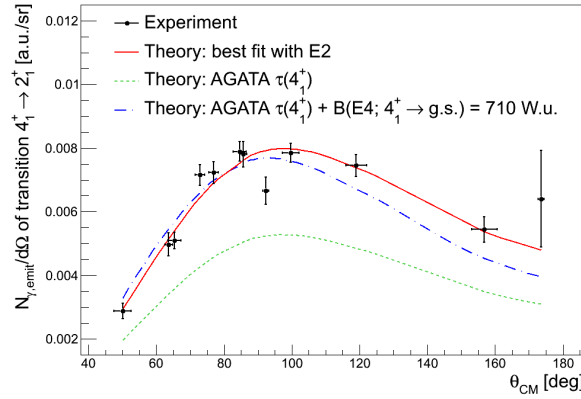
Fig. 6.28: The number of emitted γ-rays $N_{\gamma,emit}$ from the $4_1^+ \to 2_1^+$ transition in ^{72}Zn. To obtain a smooth curve, $N_{\gamma,emit}$ is divided by the solid angle $\Delta\Omega$ of the particle detector segment. In black, the experimental values calculated with eq. (6.6) are shown. In red (solid line) the result of the CLX/DCY calculation with the best fitted set of ^{72}Zn matrix elements are displayed. The green dotted curve represents a CLX/DCY calculation using the 4_1^+ lifetime measured with AGATA in Legnaro [38] which features a large discrepancy to the experimental data from this Coulex experiment. To achieve a qualitative agreement between the experimental yields and the predicted yields of the CLX/DCY calculation with the AGATA 4_1^+ lifetime a strong $E4$ transition strength $\mathcal{M}(E4; 4_1^+ \to 0_1^+)$ has been added (blue dotted-dashed curve). Due to its unrealistic high value ($\mathcal{M}(E4; 4_1^+ \to 0_1^+) = 710$ W.u.) the introduced $E4$ transition does not explain the discrepancy between the Coulex experiment and the lifetime measurement.

of the 4_1^+ state in ^{70}Zn from the GANIL data [40] is challenging as the unshifted $2_1^+ \to 0_1^+$ transition is superimposed by the shifted $4_1^+ \to 2_1^+$ transition [45]. For ^{72}Zn, it was found in the lifetime measurement of [45] that the γ-rays from the unshifted $4_1^+ \to 2_1^+$ transition cannot be clearly separated from the shifted γ-rays from the $0_2^+ \to 2_1^+$ transition. Hence, especially in ^{70}Zn and in ^{72}Zn a precise determination of the peak areas for the lifetime determination is challenging. The influence of the $0_2^+ \to 2_1^+$ transition on the 4_1^+ lifetime was not discussed in the lifetime measurement in Legnaro [38], since their spectra do not show a significant population of the 0_2^+ state. The superposition of γ-ray peaks does not occur in the present ^{72}Zn Coulex analysis, since the excellent performance of the Doppler correction allows to clearly separate the $4_1^+ \to 2_1^+$ transition and the $0_2^+ \to 2_1^+$ transition.

- In order to exclude systematic errors in the ^{72}Zn analysis of this thesis, various cross-checks were performed: The ^{72}Zn matrix elements were determined with four different methods using three Coulex codes (CLX/DCY, GOSIA and GOSIA2). Furthermore, the influence of different normalizations, (to the measured 2_1^+ lifetime, different sets of ^{109}Ag matrix elements) was evaluated. All methods are in good agreement with each other (c.f. sec. 6.3.5). Apart from that, the high statistics of the ^{72}Zn compared to the previous lifetime and Coulex experiments allows not only to extract a complete set of zinc matrix elements, but also to perform stringent test to exclude errors in the analysis (c.f. sec. 6.1).

In summary, the influence of the quadrupole moment of the 4_1^+ state in the Coulex analysis, unsafe Coulex processes, feeding contributions from higher lying states and a possible $E4$ transition from the 4_1^+ state to the ground state cannot explain the different $B(E2; 4_1^+ \to 2_1^+)$ strengths in both experimental methods. However, one advantage of the Coulex method is the absence of unresolved transitions.

$B(E2)$ **Values and Collectivity**
Despite their vicinity to the non-collective nickel isotopes, the evolution of the energy levels (except for the 0_2^+ state) and the measured g-factors in the neutron-rich zinc isotopes show a collective behavior (c.f. sec. 1.2). However, the collectivity is not fully supported by all measured zinc $B(E2)$
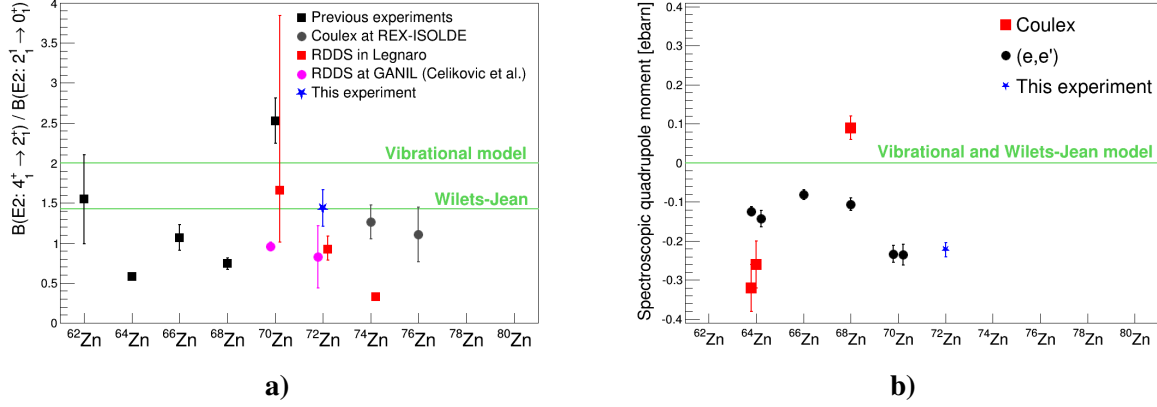
Fig. 6.29: a) The measured ratios $B(E2; 4_1^+ \rightarrow 2_1^+)/B(E2; 2_1^+ \rightarrow 0_1^+)$ of the neutron-rich zinc isotopes. The ratio shown with the blue star has been obtained in this work. The gray dots represent previous Coulex experiments which were performed at ISOLDE [41]. The black square for ^{70}Zn correspond to a DSAM measurement [35, 36]. In addition, lifetime measurements using the Recoil Distance Doppler Shift method (RDDS) are shown: The red squares are the results from a plunger measurement with AGATA in Legnaro [38], the magenta dots correspond lifetime measurements at GANIL [40], respectively. Additionally, the expectation of simple collective models are shown. In general, the neutron-rich zinc isotopes feature a lower collectivity than the vibrational model but are close to the Wilets-Jean model (c.f. fig. 1.6). **b)** Spectroscopic quadrupole moments of the 2_1^+ states of the neutron-rich zinc isotopes measured with (e,e') scattering and with Coulomb excitation. Values taken from [47] and [48]. Generally, negative spectroscopic quadrupole moments, i.e. prolate shapes are preferred in the zinc chain. Additionally, the Coulomb excitation experiments of ^{72}Zn (this thesis) and of ^{74}Zn [49] propose a prolate shape for the 2_1^+ state.

values: The lifetime measurements beyond $N = 40$ in Legnaro [38] and in GANIL [40] propose a non-collective $B_{42} = B(E2; 4_1^+ \rightarrow 2_1^+)/B(E2; 2_1^+ \rightarrow 0_1^+)$ ratio close to one which supports the $N = 40$ subshell closure, while the Coulex experiments are closer to the values predicted by simple collective models (c.f. fig. 6.29 a)). The $B_{42} = B(E2; 4_1^+ \rightarrow 2_1^+)/B(E2; 2_1^+ \rightarrow 0_1^+) = 1.44 \pm 0.23$ determined in this work is in excellent agreement with the γ-soft model of Wilets-Jean ($B_{42} = 1.43$, c.f. fig. 1.6 b)). Furthermore, the B_{42} values of ^{74,76}Zn are close to the prediction of Wilets-Jean.

Apart from the B_{42} ratio, the ^{72}Zn Coulex experiment allows to additionally study the collective behavior of the 2_2^+ and the 0_2^+ state in more detail. All $B(E2)$ values for the complete set of 2-phonon states $0_2^+, 2_2^+$ and 4_1^+ have been determined. This has been achieved only very rarely up to now in experiments with radioactive ion beams. Hence, the evolution of collective properties towards exotic nuclei can be investigated, where e.g. new modes of collective nuclear motion are expected. The obtained ratios $B(E2; 2_2^+ \rightarrow 2_1^+)/B(E2; 2_1^+ \rightarrow 0_1^+) = 0.57 \pm 0.08$ and $B(E2; 0_2^+ \rightarrow 2_1^+)/B(E2; 2_1^+ \rightarrow 0_1^+) = 0.57 \pm 0.08$ for ^{72}Zn are significantly below the predictions of collective models (c.f. fig. 1.6). This indicates that the 2_2^+ and the 0_2^+ state feature a different internal structure than the 0_1^+, the 2_1^+ and the 4_1^+ state of the yrast band (c.f. sec. 6.4.3).

Spectroscopic Quadrupole Moments: Shapes of the 2_1^+, 4_1^+ and 2_2^+ State in ^{72}Zn

Besides the $B(E2)$ values, the shape of the nucleus is coupled to its nuclear structure. The shape of a nuclear state in the laboratory frame is expressed with the spectroscopic quadrupole moment which is calculated from the measured diagonal matrix elements (c.f. eq. (2.22)). In the ^{72}Zn Coulex analysis performed in this work, the spectroscopic quadrupole moments of the 2_1^+, the 4_1^+ and the 2_2^+ state of ^{72}Zn were extracted (c.f. tab. 6.6), which represents the first measurement of quadrupole moments in

the radioactive neutron-rich zinc chain[25].

Similar to the stable zinc isotopes, a negative spectroscopic quadrupole moment $Q_s(2_1^+) = (-0.24 \pm 0.03(\text{stat}) \pm 0.01(\text{sys}))$ ebarn was determined for the 2_1^+ state which corresponds to a prolate shape. This is in agreement with the Coulex experiment of ^{74}Zn which features a tendency for a negative $Q_s(2_1^+)$ [41, 49]. However, combining the measured $B(E2; 2_1^+ \to 0_1^+)$ value of ^{74}Zn in the Coulex experiment [41, 49] with the lifetime measurement in Legnaro [38] an oblate shape of the 2_1^+ state in ^{74}Zn is predicted. Note that the oblate shape is in contradiction to the systematics of the zinc spectroscopic quadrupole moments and to the Coulex experiments of ^{72,74}Zn (c.f. fig. 6.29 b)).

In this experiment the quadrupole moment of the 4_1^+ state in ^{72}Zn was determined to be $Q_s(4_1^+) = (-0.27 \, {}^{+0.05}_{-0.07}(\text{stat}) \pm 0.01(\text{sys}))$ ebarn. This marks the first-ever measurement of a 4_1^+ quadrupole moment in any zinc isotope. Apart from the high beam intensity and the good MINIBALL efficiency, the excellent sensitivity of the newly built C-REX setup is an important ingredient for this measurement. The quadrupole moment $Q_s(4_1^+)$ is identical in sign and magnitude to $Q(2_1^+)$. This is the first experimental proof that the yrast band in ^{72}Zn shows robust collective features, in agreement to the non-vanishing $B(E2)$ values.

In contrast, the $B(E2)$ values of the states 0_2^+ and 2_2^+ are smaller and seem to be of different structure. This is supported by the first measurement of the quadrupole moment $Q(2_2^+) = (+0.39 \, {}^{+0.04}_{-0.03}(\text{stat}) \pm 0.02(\text{sys}))$ ebarn of the 2_2^+ state, which indicates an oblate deformation for the 2_2^+ state. Thus, on the one hand, a quasi 2-phonon triplet is observed in ^{72}Zn and, overall, $B(E2)$ values are not indicating large deformations. On the other hand, the yrast band is of a distinct and more collective structure than the low-lying off-yrast states. Such complicated behavior can be described e.g. by using more realistic collective models with e.g. triaxial deformation (c.f. sec. 6.4.2) or by using the nuclear shell model (c.f. sec. 6.4.3).

6.4.2   Shape and Triaxiality of the 0_1^+ State in ^{72}Zn

The nuclei close to ^{72}Zn feature a large variety of coexisting shapes in their 0^+ states. Two protons below ^{72}Zn, ^{70}Ni features a (nearly) spherical ground state, an oblate 0_2^+ state and a prolate 0_3^+ state [29]. ^{74}Ge with two protons more than ^{72}Zn has a deformed 0_1^+ state and a spherical 0_2^+ state (c.f. fig. 1.9 a)). Furthermore, a shell model calculation in the jj4c model space ($1f_{5/2}, 2p_{3/2}, 2p_{1/2}$ and $1g_{9/2}$ orbitals for protons and neutrons) with the jj4c interaction (c.f. sec. 6.4.3 predicts a more collective ground state and a spherical 0_2^+ state for ^{70}Zn [35, 130]. The large number of matrix elements obtained in this work allows to gain detailed information about the shape of the nucleus. As already demonstrated, the diagonal matrix elements of the 2_1^+, 4_1^+ and 2_2^+ state are related to spectroscopic quadrupole moments which define the shape of the nucleus. Additionally, the set of matrix elements of ^{72}Zn allows to determine the shape of the 0_1^+ state by applying quadrupole sum rules: The zero-coupled product of electromagnetic multipole operators ($E2$) are rotationally invariant and provide a model-independent way to extract shape parameters of the nucleus [61, 65]. Coupling two $E2$ quadrupole tensors to angular momentum zero allows to extract the expectation value of the quadrupole invariant $\langle Q^2 \rangle$ which is a measure for the over deformation of the state i [65]:

$$\frac{\langle Q^2 \rangle}{\sqrt{5}} = \langle i|[E2 \times E2]^0|i\rangle = \frac{1}{\sqrt{(2I_i + 1)}} \sum_t \langle i\|E2\|t\rangle\langle t\|E2\|i\rangle \begin{Bmatrix} 2 & 2 & 0 \\ I_i & I_i & I_t \end{Bmatrix}, \qquad (6.19)$$

with the expression in curly brackets being a Wigner 6-j symbol. The summation runs over all intermediate states t which can be reached via $E2$ transitions from the state i. The higher order invariant

---

[25]Note that in the Coulex analysis of $^{74-80}$Zn the quadrupole moment Q_s of all states were neglected as the statistics was too low to determine the angular dependence of the γ-ray yields. Hence, the stated $B(E2)$ values assume a zero quadrupole moment $Q_s = 0$. The uncertainties of the $B(E2)$ values include the influence of the quadrupole moment assuming extreme values for Q_s. [49]

$\langle\cos(3\delta)\rangle$ contains information about the triaxiality[26] of the state i [65]:

$$\sqrt{\frac{2}{35}}\langle Q^3\cos(3\delta)\rangle \quad = \quad \langle i|\{[E2\times E2]^2\times E2\}^0|i\rangle = \tag{6.20}$$

$$= \quad \frac{1}{(2I_i+1)}\sum_{t,u}\langle i\|E2\|u\rangle\langle u\|E2\|t\rangle\langle t\|E2\|i\rangle\begin{Bmatrix}2 & 2 & 0 \\ I_i & I_t & I_u\end{Bmatrix}.$$

According to eq. (6.19) and eq. (6.20) the evaluation of the quadrupole sum rules is only possible if a relatively complete set of matrix elements has been measured. For the ^{72}Zn Coulex experiment the invariants $\langle Q^2\rangle$ and $\langle\cos(3\delta)\rangle$ can only be calculated for the ground state [27]:

$$\langle Q^2\rangle = (0.19\pm0.01\,(\text{stat})\pm0.02\,(\text{sys}))e^2\text{barn}^2 \quad\text{and}\quad \langle\cos(3\delta)\rangle = 0.45\pm0.08\,(\text{stat})\pm0.09\,(\text{sys}), \tag{6.21}$$

involving the measured $E2$ matrix elements $\mathcal{M}(0_1^+\to2_1^+)$, $\mathcal{M}(0_1^+\to2_2^+)$, $\mathcal{M}(2_1^+\to2_2^+)$, $\mathcal{M}(2_1^+\to2_1^+)$ and $\mathcal{M}(2_2^+\to2_2^+)$. The invariants can be related to the deformation parameters β (deformation) and γ (triaxiality) of Bohr [131]:

$$\langle Q^2\rangle = q_0^2\langle\beta^2\rangle \quad\text{and}\quad \langle Q^3\cos(3\delta)\rangle = q_0^3\langle\beta^3\cos(3\gamma)\rangle \quad\text{with}\quad q_0^2 = \frac{3}{4\pi}ZR_0^3, \tag{6.22}$$

with Z being the atomic number of the nucleus and R_0 its radius. Using the rotational invariants of eq. (6.21), the shape parameters of the ^{72}Zn ground state reads in the Bohr nomenclature

$$\beta = 0.241 \pm 0.01\,(\text{stat}) \pm 0.01\,(\text{sys}) \quad\text{and}\quad \gamma = 21° \pm 2°\,(\text{stat}) \pm 2°\,(\text{sys}), \tag{6.23}$$

which corresponds to a moderate deformation and a triaxial shape with a tendency to a prolate deformation. This is in agreement with the measured prolate shapes of the 2_1^+ and the 4_1^+ state of the yrast band in ^{72}Zn, emphasizing again the moderate collective features of the yrast band. The $^{72}_{30}$Zn$_{42}$ ground state is with $\langle Q^2\rangle = (0.19 \pm 0.01\,(\text{stat}) \pm 0.02\,(\text{sys}))\,e^2\text{barn}^2$ in the transition region between the (nearly) spherical ground state of $^{70}_{28}$Ni$_{42}$ [29] and the deformed $^{74}_{32}$Ge$_{42}$ ground state with $\langle Q^2\rangle = (0.31 \pm 0.02)\,e^2\text{barn}^2$ [51] (c.f. fig. 1.9 a)).

Note, that this is one of the first measurements of triaxial behavior in nuclei using a radioactive beam. It represents a good benchmark test for theoretical models beyond stable isotopes. In the following, the measured triaxial shape of the ^{72}Zn ground state is used to validate two mean field calculations using the Hartree-Fock-Bogoliubov (HFB) theory with the Gogny D1S interaction:
The first calculation, presented in fig. 6.30, was performed by Jean-Paul Delaroche from the Bruyeres le Chatel group, CEA (France) using a five-dimensional collective Hamiltonian (5DCH) [132, 133]. Its minimum in the potential surface in the $\beta - \gamma$ plane coincides well with the experimental value. Furthermore, the predicted quadrupole moment of the 2_1^+ state and its reduced transition probability to the ground state is in agreement with the experiment (c.f. fig. 6.30, fig. 6.32 and tab. 6.6). However, the energies and the $B(E2)$ values of the higher lying states are overestimated in this theory. One possible reason is the tensor force (c.f. chap. 1) which is not included in the calculation, yet [133].
The second calculation corresponds to a beyond-mean-field calculation using the symmetry conserving configuration mixing approach (c.f. fig. 6.31) [46, 134]. It is in accordance to the measured g-factor of ^{72}Zn [46] and also features an energy minimum in its potential surface which is quite close to the experimental value (c.f. fig. 6.31). The beyond-mean-field theory predicts an evolution from a triaxial ^{70}Zn ground state to a more prolate ^{74}Zn ground state. Furthermore, going from ^{70}Zn to ^{74}Zn the γ-softness decreases. A similar behavior is seen in the neighboring germanium isotopes which features

---

[26]Here the following relation is applied: $\langle Q^3\cos(3\delta)\rangle \approx \langle Q^2\rangle^{3/2}\cdot\langle\cos(3\delta)\rangle$.

[27]The rotational invariants of the 0_2^+ state cannot be determined as the $\mathcal{M}(E2;0_2^+\to2_2^+)$ matrix element could not be extracted from the Coulex analysis.
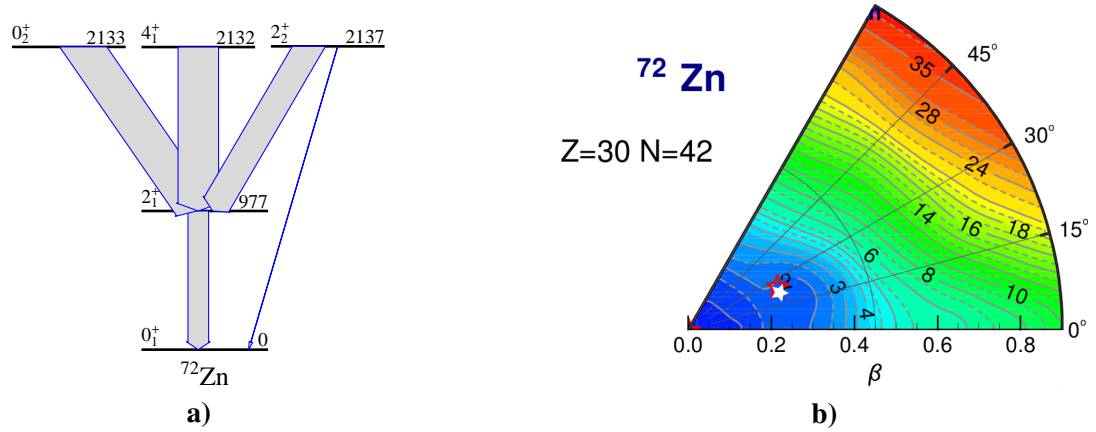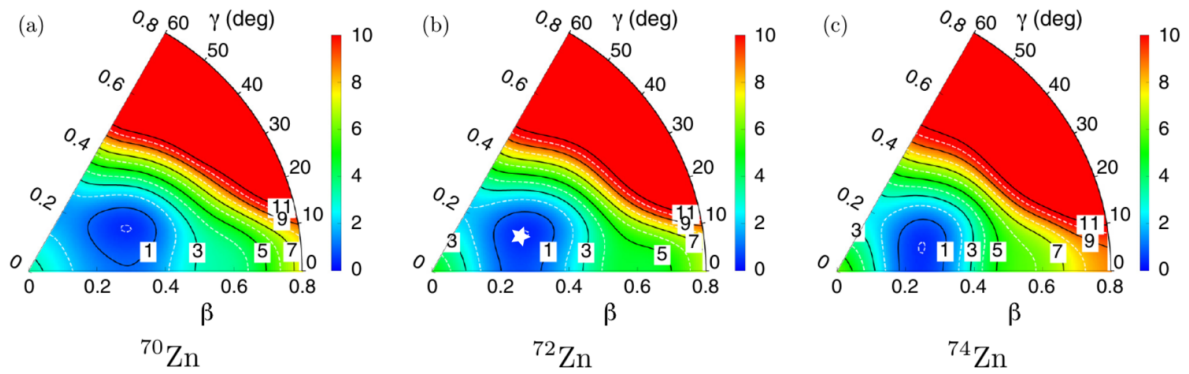
Fig. 6.30: The results for ^{72}Zn obtained from a mean field calculation with a five-dimensional collective Hamiltonian using the Gogny D1S force [132, 133]. **a)** shows the calculated level scheme. The width of the arrows represent the $E2$ reduced transition strengths (c.f. tab. 6.6). **b)** visualizes the potential surface of the ^{72}Zn ground state. Its energy minimum (at 0 MeV, red star) is in good agreement with the obtained experimental value in this thesis which is indicated with a white star. The shown dashed and solid contours are 1 MeV apart. For discussion see text.

Fig. 6.31: The potential energy surfaces of the ground states of ^{70,72,74}Zn obtained by a beyond-mean-field calculation [46, 134]. Their dashed white and solid black coutures are 1 MeV apart. The energy minimum (at 0 MeV) of the ^{72}Zn potential surface is in good agreement with the obtained experimental value in this thesis which is indicated with the white star. Picture adapted from [46].

an transition from a γ-soft nucleus ^{72}Ge to a ^{76}Ge γ-rigid nucleus [135].

In conclusion, both modern mean field calculations are able to describe the triaxiality of ^{72}Zn, while simple collective models such as the vibrational model or the Wilets-Jean model are not fully suitable (c.f. sec. 6.4.1).

6.4.3 Comparison with Shell Model Calculations

In this Coulex experiment, a complete set of reduced transition strengths and quadrupole moments of the low lying ^{72}Zn states were determined. This detailed experimental information is perfectly suited to extensively test effective interactions used in theoretical models. Due to the high number of experimental parameters ($B(E2)$ strengths, quadrupole moments) available, the results from this experiment allows for much more stringent tests of models than previous experiments providing only $B(E2; 2_1^+ \to 0_1^+)$ and, in some cases, $B(E2; 4_1^+ \to 2_1^+)$ values. Hence, in this section, the experimental reduced transition strengths and spectroscopic quadrupole moments are used as a good probe to test modern shell model calculations and to get information about the underlying ^{72}Zn wave functions. In tab. 6.6, the measured $B(E2, M1)$ values as well as the measured quadrupole moments of ^{72}Zn are

Transition strength in ^{72}Zn	This experiment [e^{2}fm^4]	jj4c [e^{2}fm^4]	jj44bpn [e^{2}fm^4]	JUN45 [e^{2}fm^4]	HFB+5DCH [e^{2}fm^4]
B(E2; $2_1^+ \to$ g.s.)	$360\ ^{+3}_{-3}$(stat) ±36(sys)	431	451	358	392
B(E2; $4_1^+ \to 2_1^+$)	$517\ ^{+9}_{-9}$(stat) ±52(sys)	575	582	377	768
B(E2; $0_2^+ \to 2_1^+$)	$204\ ^{+33}_{-73}$(stat) ±20(sys)	94.6	537	122	735
B(E2; $2_2^+ \to 2_1^+$)	$205\ ^{+12}_{-17}$(stat) ±21(sys)	336	338	471	542
B(E2; $2_2^+ \to$ g.s.)	$11.0\ ^{+1.4}_{-1.1}$(stat) ±1.1(sys)	1.70	4.75	8.88	8

Transition strength in ^{72}Zn	This experiment [μ_N^2fm^2]	jj4c [μ_N^2fm^2]	jj44bpn [μ_N^2fm^2]	JUN45 [μ_N^2fm^2]
B(M1; $2_2^+ \to 2_1^+$)	$0.84\ ^{+0.87}_{-0.87}$(stat) ±0.08(sys)	0.043	0.073	0.268

Quad. moment in ^{72}Zn	This experiment [efm^2]	jj4c [efm^2]	jj44bpn [efm^2]	JUN45 [efm^2]	HFB+5DCH [efm^2]
$Q_s(2_1^+)$	$-24\ ^{+3}_{-3}$(stat) ±1(sys)	-30.2	-32.5	-6.75	-26
$Q_s(4_1^+)$	$-27\ ^{+5}_{-7}$(stat) ±1(sys)	-48.9	-53.7	-45.0	-41
$Q_s(2_2^+)$	$39\ ^{+4}_{-3}$(stat) ±2(sys)	19.2	26.5	5.20	20

Tab. 6.6: A comparison of the ^{72}Zn experimental electric and magnetic reduced transition strengths as well as of the spectroscopic quadrupole moments to the values obtained by four theoretical calculations: The results of three shell model calculations in the jj44 model space ($1f_{5/2}$, $2p_{3/2}$, $2p_{1/2}$ and $1g_{9/2}$ orbitals for protons and neutrons) using the jj4c [136], the jj44bpn [110] and the JUN45 [137] interactions are listed. Furthermore, the results obtained from a mean field calculation using the Hartree-Fock-Bogoliubov (HFB) theory with a five-dimensional collective Hamiltonian (5DCH) and the Gogny D1S force are given [132, 133]. A visual comparison of the $B(E2)$ values is shown in fig. 6.30 and fig. 6.32. For a detailed discussion see text.

compared to three different shell model calculations. These calculations were performed by Alexander Lisetskiy [136] using the ANTOINE code (with the jj4c interaction [136]) and by Kathrin Wimmer using the NuShellX@MSU code [109] (with the jj44bpn [110] and the JUN45 [137] interaction).

Model Space and Interactions

All calculations were performed in the same active jj44 model space ($1f_{5/2}$, $2p_{3/2}$, $2p_{1/2}$ and $1g_{9/2}$ orbitals for protons and neutrons) and uses ^{56}Ni as a core. In the following, the interactions used in the three calculations are briefly described:

The Hamilton operator of the JUN45 [137] interaction is based on the realistic Bonn-C potential. It has been modified empirically by fitting 133 two-body-matrix elements and four single-particle energies[28] to reproduce 400 experimental binding and excitation energies of 69 nuclei with mass numbers $A = 63 - 96$. The predicted JUN45 level schemes of the zinc and germanium isotopes are in good agreement below $N = 40$, but show discrepancies above $N = 40$ which is due to the restricted model space [137]. Furthermore, in the Ge chain, JUN45 reproduces the evolution of the 0_2^+ state and predicts correctly the transition of a γ-soft nucleus to a γ-rigid nucleus at ^{74}Ge.

The jj44bpn interaction is an unpublished interaction from B. A. Brown (c.f. reference 28 in [110]). Its Hamiltonian is obtained with a method similar to the JUN45 interaction. 600 binding and excitation energies are fitted mainly from nuclei with $Z = 28 - 30$ and $N = 48 - 50$.

The jj4c interaction is an unpublished, modified version of the jj4b interaction by B. A. Brown which is optimized for the Ni, Cu, Zn and Ge isotopes [136]. It features the best description of ^{70}Zn [35, 36].

---

[28]The single-particle energies are included in the fit as the ^{56}Ni core is quite soft. Hence, low lying states in ^{57}Ni cannot be treated as single particle states and therefore their energy levels cannot be taken as single-particle energies.
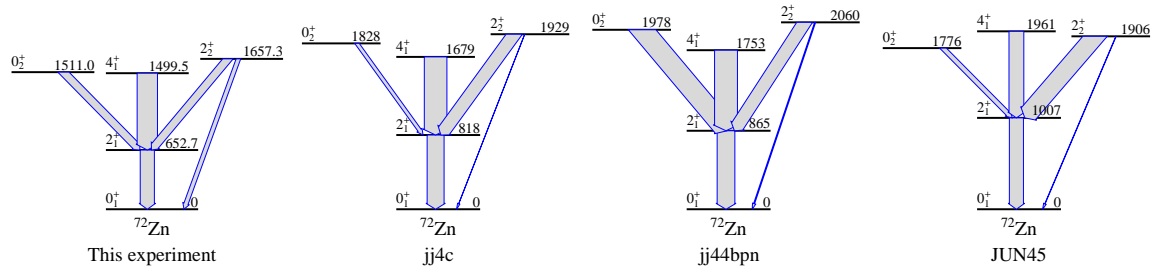
Fig. 6.32: A comparison of the experimental ^{72}Zn level scheme (left) to three shell model calculations in the jj44 model space ($1f_{5/2}$, $2p_{3/2}$, $2p_{1/2}$ and $1g_{9/2}$ orbitals for protons and neutrons) using the jj4c [136], the jj44bpn [110] and the JUN45 [137] interaction. The width of the arrows represent the E2 reduced transition strengths (c.f. tab. 6.6). For discussion see text.

Level Schemes, Reduced Transition Strengths and Quadrupole Moments

In the following, the experimental ^{72}Zn level schemes, reduced transition strengths and spectroscopic quadrupole moments are compared to the results of the shell model calculations (c.f. tab. 6.6). In the calculations of the $B(E2, M1)$ values and of the quadrupole moments, the same effective charges ($e_\pi = 1.76$, $e_\nu = 0.97$) and the same effective g-factors ($g_\pi = 5.586$, $g_\nu = -3.826$) are used for every interaction. These values are typical for the zinc isotopes [41, 35].

The experimental level sequence is well reproduced with the jj4c and the jj44bpn interaction, but not with the JUN45 interaction (c.f. fig. 6.32). Comparing the level energies, the shell model calculation using the jj4c interaction fits the data best.

Concerning the $B(E2)$ values, the absolute values of the calculated transition strengths are only consistent with the experimental data for the $2_1^+ \rightarrow 0_1^+$ transition in JUN45 and for the $4_1^+ \rightarrow 2_1^+$ transition in the jj4c and the jj44bpn interaction. However, the correct ordering for all $B(E2)$ values is predicted with the jj4c interaction, while the jj44bpn interaction incorrectly places the $0_2^+ \rightarrow 2_1^+$ transition and the JUN45 interaction misplaces the $2_2^+ \rightarrow 2_1^+$ transition. Furthermore, the $B(E2; 2_2^+ \rightarrow 0_1^+)$ strength is underestimated in all calculations, but, like in the experiment, it is always well below the $B(E2; 2_2^+ \rightarrow 2_1^+)$ strength. Moreover, the small $M1$ strength for the $2_2^+ \rightarrow 2_1^+$ transition is correctly reproduced by all theories. Apart from that, all shell model calculations correctly predict the signs of the measured quadrupole moments for all states. The magnitudes are best reproduced with the jj4c interaction and worst with the JUN45 interaction.

Wave Functions

In the following, the calculated wave functions of all interactions are discussed. The focus is set on the jj4c interaction, since it features the best description of the experimental data. The neutron wave functions are displayed in fig. 6.33. For the sake of completeness, the wave functions of all interactions are listed in tab. D.11, tab. D.12 and tab. D.13.

$0_1^+, 2_1^+$: Using the jj4c and the jj44bpn interaction, the ground state and the 2_1^+ state neutron wave function feature a similar structure: Configuration $|3\rangle = |\nu(2p_{3/2}^4 1f_{5/2}^4 2p_{1/2}^2 1g_{9/2}^4)\rangle = |\nu(1f_{5/2}^{-2} 1g_{9/2}^4)\rangle$ is with a fraction of about 30% most probable. In JUN45 the closed $N = 40$ configuration $|1\rangle = |\nu(2p_{3/2}^4 1f_{5/2}^6 2p_{1/2}^2 1g_{9/2}^2)\rangle = |\nu(1g_{9/2}^2)\rangle$ with a fraction of 22% is competing with configuration $|3\rangle = |\nu(1f_{5/2}^{-2} 1g_{9/2}^4)\rangle$ with a fraction of 21%.

4_1^+ : In the jj4c and the jj44bpn interaction the 2_1^+ and the 4_1^+ neutron wave functions have a large overlap which nicely reproduces the $B(E2; 4_1^+ \rightarrow 2_1^+)$ strength. The calculated smaller $B(E2; 4_1^+ \rightarrow 2_1^+)$ value in JUN45 originates from the reduced component of the closed $N = 40$ configuration $|1\rangle = |\nu(1g_{9/2}^2)\rangle$ in the 4_1^+ state (10%) compared to the 2_1^+ state (18%).
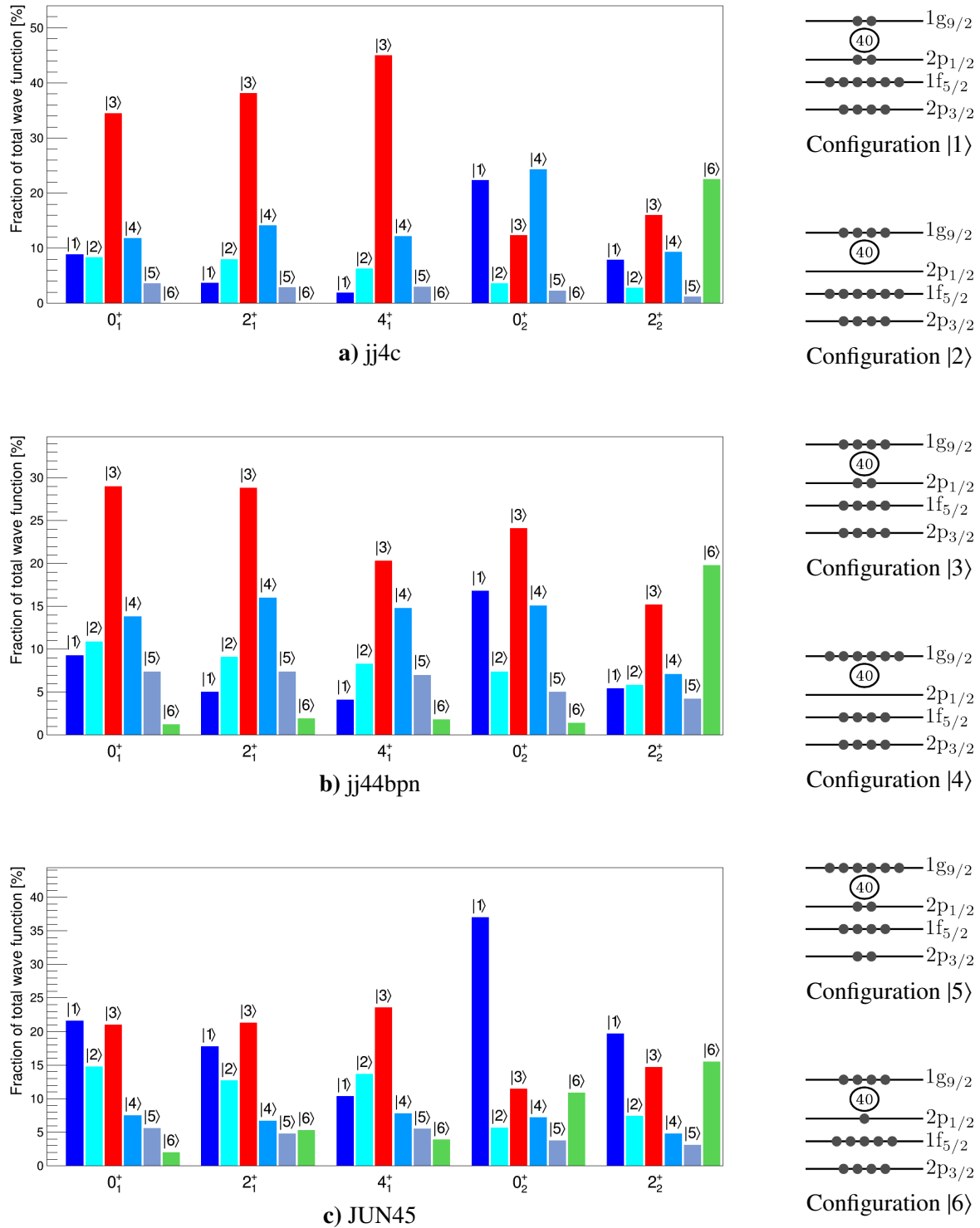
Fig. 6.33: The most dominant neutron wave functions of the low lying ^{72}Zn states calculated with the jj4c (**a**)), the jj44bpn (**b**)) and the JUN45 (**c**)) interaction. On the right the neutron configurations, shown in the bar charts, are visualized. For the discussion see text.

$\mathbf{0^+_2}$: Like in the experiment, the $B(E2; 0^+_2 \to 2^+_1)$ strength calculated with the jj4c interaction is smaller than the $B(E2; 2^+_1 \to 0^+_1)$ strength, although the effect is less dramatic in the experiment. This indicates that the 0^+_2 state features a different structure than the 0^+_1, 2^+_1 and 4^+_1 states of the yrast band. Indeed, this is reflected in the jj4c wave functions: The shell model predicts a 0^+_2 wave function featuring a reduced fraction of the $|3\rangle = |\nu(1f^{-2}_{5/2}1g^4_{9/2})\rangle$ component by about a factor of three compared to the yrast band, while the configurations $|1\rangle = |\nu(1g^2_{9/2})\rangle$ (closed $N = 40$ configuration) and $|4\rangle = |\nu(2p^4_{3/2}1f^4_{5/2}2p^0_{1/2}1g^6_{9/2})\rangle = |\nu(1f^{-2}_{5/2}2p^0_{1/2}1g^6_{9/2})\rangle$ are dominating with fractions of over 22% each. Moreover, in jj4c the proton wave function looks completely different for the 0^+_1 and the 0^+_2 state (c.f. tab. D.11).

A similar picture is present in the JUN45 interaction: The closed $N = 40$ configuration $|1\rangle = |\nu(1g^2_{9/2})\rangle$ is with 37% most probable in the 0^+_2 state. Furthermore, configuration $|3\rangle = |\nu(1f^{-2}_{5/2}1g^4_{9/2})\rangle$ is reduced and configuration $|6\rangle = |\nu(2p^4_{3/2}1f^{-1}_{5/2}2p^1_{1/2}1g^4_{9/2})\rangle = |\nu(1f^{-1}_{5/2}2p^1_{1/2}1g^4_{9/2})\rangle$ is enhanced in the 0^+_2 state compared to the yrast states.

Contrary, the jj44bpn interaction does not reproduce the $B(E2; 0^+_2 \to 2^+_1)$ strength, since its 0^+_2 state features a similar structure than the states of the yrast band with configuration $|3\rangle = |\nu(1f^{-2}_{5/2}1g^4_{9/2})\rangle$ being the most probable, although the closed $N = 40$ configuration $|1\rangle = |\nu(1g^2_{9/2})\rangle$ is enhanced.

$\mathbf{2^+_2}$: The 2^+_2 state features a different structure than the states of the yrast band, due to its low reduced transition probability to the 2^+_1 state (and even lower to the ground state). This trend is reproduced by the shell model calculations using the jj4c and the jj44bpn interaction. Both predict a 2^+_2 wave function in which the fraction of configuration $|3\rangle = |\nu(1f^{-2}_{5/2}1g^4_{9/2})\rangle$ drops by a factor of two compared to the yrast band, while configuration $|6\rangle = |\nu(1f^{-1}_{5/2}2p^1_{1/2}1g^4_{9/2})\rangle$ becomes the most probable configuration. Note that configuration $|6\rangle$ is negligible in all other states.

The same effect, albeit less pronounced, is present in the JUN45 interaction.

In summary, all interactions predicts similar wave functions in the yrast band $0^+_1 \to 2^+_1 \to 4^+_1$ which is confirmed by the measured $B(E2)$ values. Furthermore, the small reduced transition strength $B(E2; 0^+_2 \to 2^+_1)$ can be explained with the jj4c and the JUN45 interaction, since these interactions claim a different structure of the 0^+_2 state compared to the states in the yrast band: In the 0^+_2 state the closed $N = 40$ configuration is more probable than configuration $|3\rangle = |\nu(1f^{-2}_{5/2}1g^4_{9/2})\rangle$ which is much more dominant in the ground state. The smaller fraction of the closed $N = 40$ shell configuration $|1\rangle = |\nu(1g^2_{9/2})\rangle$ in the ground state is in good agreement with the collectivity (c.f. sec. 6.4.1) and the triaxiality (c.f. sec. 6.4.2) in the yrast band. Hence, combing the experimental data with the theoretical shell model and the mean field calculations indicates that the $N = 40$ subshell closure is not well established in the yrast band, whereas it is more present in the 0^+_2 state. A similar behavior was seen in ^{70}Zn: The 0^+_1 state in ^{70}Zn is collective, while the 0^+_2 state is spherical [35, 130]. However, the situation is more complicated in ^{72}Zn due to the two additional neutrons in the $1g_{9/2}$ shell. Especially, the jj4c interaction predicts a competing configuration $|4\rangle = |\nu(1f^{-2}_{5/2}2p^0_{1/2}1g^6_{9/2})\rangle$ in addition to the closed $N = 40$ shell configuration $|1\rangle = |\nu(1g^2_{9/2})\rangle$ for the 0^+_2 state. Furthermore, in all shell model calculations, the 2^+_2 state features a different structure compared to the yrast states and the 0^+_2 state. The dominant configuration $|3\rangle = |\nu(1f^{-2}_{5/2}1g^4_{9/2})\rangle$ of the yrast band is suppressed and instead configuration $|6\rangle = |\nu(1f^{-1}_{5/2}2p^1_{1/2}1g^4_{9/2})\rangle$ is with more than 15% significant for the first time[29]. This is consistent with the measured low reduced transition strengths of the 2^+_2 state to the prolate yrast band and the measured oblate quadrupole moment of the 2^+_2 state.

---

[29]Note, that from the data it can only be concluded that the 2^+_2 state has a different structure compared to the other states. Hence, the wave functions shown in fig. 6.33 are only one possibility to describe the data. Other solutions may be valid as well. Of course the same argument holds for the other states.

<div style="text-align: right; font-size: 3em; font-weight: bold;">7</div>

Summary and Outlook

In this thesis, the shell evolution around ^{68}Ni was studied experimentally. The nucleus ^{68}Ni features a magic proton number $Z = 28$, but despite many experimental and theoretical investigations, the stability of the subshell closure at its neutron number $N = 40$ is under discussion. ^{68}Ni mimics a doubly magic behavior corresponding to a high excitation energy for its first excited 2^+ state and a low reduced transition strength $B(E2; 2_1^+ \rightarrow 0_1^+))$. These magic features can be explained by neutron-pair scattering across $N = 40$ from the negative parity pf-shell to the positive parity $1g_{9/2}$ orbit. This statement is confirmed by the strongly increased collectivity of the neighboring isotopes, which is not expected close to doubly magic nuclei. In the neutron-rich zinc isotopes, which feature two protons more than the nickel isotopes, the degree and the nature of their collective properties is not fully understood. Especially, the measured reduced transition strengths $B(E2; 4_1^+ \rightarrow 2_1^+)$ in the neighboring zinc isotopes do not yield a consistent picture: On the one hand, lifetime measurements at Legnaro and GANIL yield low $B(E2; 4_1^+ \rightarrow 2_1^+)$ values which are expected close to magic nuclei. On the other hand, Coulomb excitation experiments propose higher $B(E2; 4_1^+ \rightarrow 2_1^+)$ values which are close to the predictions of collective models. Furthermore, the nature of the 0_2^+ states of the neutron-rich zinc isotopes is uncertain: The 0_2^+ energies in the even-even zinc isotopes show large deviations from any collective models. Additionally, the evolution of the two-neutron transfer cross sections to the 0_2^+ states with increasing neutron-number shows a strong increase while passing $N = 40$. This indicates a structural change in this region. Apart from that, it is likely that the 0_2^+ state represents a "second" ground state which has a different shape than the 0_1^+ ground state. This shape coexistence phenomenon has also been observed experimentally in the neighboring nickel ($Z = 28$) and germanium ($Z = 32$) isotopes.

In the course of this thesis, the measurements of the neutron-rich zinc isotopes are complemented with two additional experiments which address different aspects of the neutron-rich zinc isotopes. First, a two-neutron transfer experiment t(^{72}Zn, p)^{74}Zn was conducted to investigate transfer cross sections (c.f. sec. 7.1). Two-neutron transfer reactions are an excellent tool to populate and study 0^+ states. Second, a multiple Coulomb excitation (Coulex) experiment of ^{72}Zn was performed to determine the reduced transition strengths of all low lying ^{72}Zn levels (c.f. sec. 7.2). Coulex experiments have the advantage that also non-yrast states such as the 0_2^+ state are populated. Additionally, they allow to directly study the shape of nuclei in a model-independent way. The radioactive ^{72}Zn beams for both experiments were delivered by the REX-ISOLDE accelerator at CERN in Geneva, Switzerland. An outlook on future transfer and Coulex experiments at the new HIE-ISOLDE facility at CERN is given in sec. 7.3.

7.1 Transfer Experiments with a ^{72}Zn Beam

The two neutrons for the transfer experiment t(^{72}Zn, p)^{74}Zn were provided by a radioactive tritium target. The outgoing proton was detected using the position-sensitive silicon array T-REX. T-REX was surrounded by the MINIBALL γ-ray spectrometer to detect the γ-rays from the deexcitation of the ^{74}Zn nucleus.
Three different reaction channels have been disentangled using the particle identification capabilities

of T-REX: First, elastically scattered tritons have been identified. They allowed to determine the luminosity of the experiment as well as to extract optical model parameters which have been used as input for the calculation of transfer cross sections. Second, the one-neutron transfer reaction t(^{72}Zn, d)^{73}Zn has been studied by selecting events which feature a deuteron in the exit channel. Third, the two-neutron transfer reaction t(^{72}Zn, p)^{74}Zn has been analyzed by the detection and identification of the transfer proton. From the identified light reaction product (triton, deuteron or proton), the excited levels of the scattered Zn ions as well as the corresponding differential reaction cross sections could be determined using 4-momentum conservation. For (direct) transfer reactions, the shape of the differential cross section is characteristic for the total angular momentum transfer of the reaction. Hence, a spin assignment of the populated level is possible. To identify unambiguously a single populated state, coincidences of the light transfer products to γ-rays in MINIBALL have been investigated.

Due to the large Q-value ($Q = 5.24\,\mathrm{MeV}$), the two-neutron transfer reaction t(^{72}Zn, p)^{74}Zn dominantly populates levels around $5\,\mathrm{MeV}$ in ^{74}Zn. Hence, low lying levels with energies below $2\,\mathrm{MeV}$ feature a strong feeding contribution which flattens their angular distribution. Only the ground state and the 2_1^+ state of ^{74}Zn feature a direct population which could be isolated from the feeding component. Subsequently, their differential cross sections were determined. A comparison of the experimental cross section to a FRESCO calculation using shell model input reveals that the ground state can be described solely by the simultaneous transfer of the two neutrons (c.f. fig. 5.21). As input for the FRESCO calculation, the prediction of a shell model calculation using the jj44bpn interaction in the $1f_{5/2}$, $2p_{3/2}$, $2p_{1/2}$ and the $1g_{9/2}$ model space for protons and neutrons are used. According to the shell model the two neutrons are transferred with a probability of 60% to the $1g_{9/2}$ neutron orbit, although the large angular momentum transfer of $\Delta l = 4$ for each neutron kinematically suppresses the transfer cross section. However, the shell model calculation is not able to describe the measured cross section of the 2_1^+ state correctly. The agreement between experiment and theory was significantly improved by considering a larger model space, i.e. the full $fp - sdg$-shell, using a perturbation approximation (c.f. fig. 5.22). This is a weak indication that the $N = 50$ shell gap is not very pronounced for nuclei with $Z \approx 28$ and $N \approx 40$. Note that the theoretical FRESCO calculation is based on many input parameters, such as spectroscopic factors, which have not been confirmed with experiments, yet. Hence, it is still possible that the 2_1^+ cross section can be explained solely with the $f_{5/2}pg_{9/2}$-shell. Additionally, the obtained experimental cross section for the ^{74}Zn 2_1^+ state coincides well with the two-neutron transfer experiments dealing with the stable zinc isotopes. Apart from that, only an upper limit for the 0_2^+ state in ^{74}Zn could be determined, as the 0_2^+ state is neither identified in previous experiments nor in this transfer experiment. The low population of the 0_2^+ state is qualitatively in agreement with the shell model prediction. However, the obtained upper limit of the 0_2^+ state in ^{74}Zn is not sensitive enough to constrain the evolution of 0_2^+ cross sections in the neutron-rich zinc isotopes.

Besides the two-neutron transfer channel, the one-neutron transfer t(^{72}Zn, d)^{73}Zn was analyzed to complement the limited experimental information about the ^{73}Zn nucleus. Due to the lower Q-value ($Q = -0.74\,\mathrm{MeV}$) of the one-neutron transfer reaction, most states are populated directly. The extracted excitation energy from the transfer deuterons in combination with the γ-rays in MINIBALL allowed to construct the level scheme of ^{73}Zn which is, in general, in good agreement with previous β-decay experiments. Additionally, two new levels at $(1683 \pm 2)\,\mathrm{keV}$ and $(1832 \pm 2)\,\mathrm{keV}$ have been discovered unambiguously in ^{73}Zn. However, a clear spin assignment was not possible due to the limited angular range covered by the detectors. Apart from that, the one-neutron transfer reaction d(^{72}Zn, p)^{73}Zn with a deuterated polyethylene target has been studied. Despite the strong feeding contributions due to the high Q-value ($Q = 3.3\,\mathrm{MeV}$) and despite the low statistics, due to the short measurement time, the new levels at $1683\,\mathrm{keV}$ and $1832\,\mathrm{keV}$ have been confirmed.

7.2 Multiple Coulomb Excitation of ^{72}Zn and ^{109}Ag

In the Coulomb excitation experiment the ^{72}Zn beam (E_{beam} = 2.85 MeV/u) was impinged on a pure 1.17 mg/cm^2 thick ^{109}Ag target. The scattered ^{72}Zn and ^{109}Ag ions were detected with the new C-REX silicon array. C-REX represents a modified T-REX setup suited for Coulex experiments in normal kinematics. It has been designed and constructed in the scope of this thesis to cope with the high count rates of up to I_{Zn} = (3.5 ± 0.3) · 10^7 pps of the ^{72}Zn REX-ISOLDE beam. Compared to the traditional Coulex setup at ISOLDE, C-REX features an adjustable target forward-detector distance which allows to optimize the angular range covered, individually for each experiment. In addition, detectors in backward direction have been installed to increase the sensitivity for two-step excitation processes. Hence, by covering large scattering angles in the center-of-mass frame C-REX is well suited to extract quadrupole moments which are directly connected to the shape of the nucleus. Apart from that, C-REX is surrounded by the MINIBALL spectrometer to detect the γ-rays which are emitted by the excited ^{72}Zn and ^{109}Ag nuclei.

The high intensity of the ^{72}Zn beam in the safe Coulex experiment allows a detailed study of the multiple Coulomb excitation of ^{72}Zn as well as of the stable ^{109}Ag target. The Coulex analysis is centered around the Doppler corrected γ-ray spectra with respect to both nuclei. The counts in the γ-ray peaks can be related to the electromagnetic matrix elements of the beam and target nuclei. Hence, achieving a good Doppler correction is essential. It depends on a precise reconstruction of the reaction kinematics for each event, i.e. a full reconstruction of the Lorentz 4-vectors of all particles and γ-rays is required. This was achieved by an unambiguous particle identification, by an excellent energy reconstruction (resulting from a precise calibration of the C-REX detectors and MINIBALL) and by a detailed knowledge of the experimental setup. Based mainly on a newly developed technique to extract the position of the MINIBALL detectors from the data, the Doppler correction capabilities have been significantly increased from a peak width of ΔE = 10.6 keV (FWHM) to ΔE = 6.4 keV (FWHM) at E_γ = 653 keV γ-ray energy. This unprecedented resolution allowed to clearly resolve the $4_1^+ \rightarrow 2_1^+$ transition with E_γ = 847 keV from the $0_2^+ \rightarrow 2_1^+$ transition with E_γ = 858 keV in ^{72}Zn.

In the Doppler corrected γ-ray spectra with respect to ^{72}Zn, the following transitions could be identified in ^{72}Zn: $2_1^+ \rightarrow 0_1^+$, $4_1^+ \rightarrow 2_1^+$, $0_2^+ \rightarrow 2_1^+$ and $2_2^+ \rightarrow 2_1^+, 0_1^+$. Due to the excellent statistics of the γ-ray peaks, all corresponding transition matrix elements as well as the diagonal matrix elements (quadrupole moments) of the 2_1^+, the 4_1^+ and the 2_2^+ state could be determined. Note, that this is one of the first Coulex measurements of such a large set of matrix elements of a radioactive isotope. The matrix elements are extracted by fitting the experimental γ-ray yields to calculated yields which result from a given set of matrix elements. The latter are obtained by Coulex codes such as CLX/DCY or GOSIA. The calculation of the yields additionally requires a knowledge of the luminosity and the efficiencies of the detectors, which cannot be determined precisely. Hence, a relative measurement is performed, i.e. the yields are fitted relative to a known γ-ray transition with a known lifetime. In the course of this thesis, the normalization has been performed with the known lifetime of the 2_1^+ state in ^{72}Zn or with the known ^{109}Ag matrix elements and the $5/2_1^-$ (415 keV) state of the ^{109}Ag target. First, the ^{72}Zn matrix elements for each transition have been extracted successively using the CLX/DCY program and a maximum likelihood analysis. This technique has the advantage that only a small subset of matrix elements is fitted simultaneously which prevents the fit from being trapped in a local minimum. Of course the influence of higher lying transitions and their matrix elements, which feed into the current transition are taken into account. This allows to estimate correlations between the matrix elements. Furthermore, the literature as well as the obtained ^{109}Ag matrix elements in this thesis have been used as normalization. The drawback of this analysis method is that in the error calculation not all uncertainties of all projectile and target matrix elements are considered.

Therefore, a more sophisticated GOSIA analysis has been performed which fits all ^{72}Zn matrix elements simultaneously to the experimental yields using the lifetime of the 2_1^+ state as normalization. Thereby, the values and the uncertainties of all matrix elements, except the normalization matrix ele-

ment $\mathcal{M}(2_1^+ \rightarrow 0_1^+)$, are determined including all correlations. As start values for the GOSIA fit, the obtained matrix elements of the CLX/DCY analysis are used. A good set of start values is crucial to ensure that GOSIA does not get trapped in a local minimum instead of converging to the global minimum. The stability of the obtained final ^{72}Zn matrix elements was confirmed by using various measured lifetimes of 2_1^+ state in ^{72}Zn as normalization, by considering a possible $M1$ transition from the 2_2^+ state to the 2_1^+ state (which was found to be negligible) and by in- and excluding the branching ratio $BR = P(2_2^+ \rightarrow 0_1^+)/P(2_2^+ \rightarrow 2_1^+)$ in the fit and by assuming different relative signs of the matrix elements.

Moreover, a combined GOSIA-GOSIA2 analysis was performed to extract all ^{72}Zn matrix elements including $\mathcal{M}(2_1^+ \rightarrow 0_1^+)$. Thus, the $E_\gamma = 415\,$keV transition of ^{109}Ag is chosen for normalization. The Coulex code GOSIA2 allows to extract the $\mathcal{M}(2_1^+ \rightarrow 0_1^+)$ matrix element of ^{72}Zn while normalizing to a target transition by sharing the same normalization constants for both nuclei. Subsequently, the obtained ^{72}Zn $\mathcal{M}(0_1^+ \rightarrow 2_1^+)$ matrix element including its uncertainty is used as normalization in a standard GOSIA analysis to determine the higher lying matrix elements of ^{72}Zn.

In summary, the ^{72}Zn matrix elements have been determined with four different methods: two CLX/DCY analyses with different sets of ^{109}Ag matrix elements as normalization, a standard GOSIA analysis and a combined GOSIA-GOSIA2 analysis. Only the matrix element $\mathcal{M}(2_1^+ \rightarrow 0_1^+)$ of the CLX/DCY analysis with the previously known ^{109}Ag matrix elements shows a larger deviation of almost 5σ which is attributed to the huge uncertainties of the previous measurements of ^{109}Ag. All other obtained matrix elements with these techniques are in excellent agreement with a deviation less than 1σ (c.f. fig. 6.26).

Apart from that, the rich Coulex data set allows to determine ^{109}Ag matrix elements with a higher precision compared to previous measurements. In total 110 experimental yields could be extracted from the Doppler-corrected γ-ray spectra with respect to ^{109}Ag. They have been used to fit 26 matrix elements of ^{109}Ag with the GOSIA code. As a result, two unknown matrix elements could be determined in ^{109}Ag for the first time. Furthermore, the uncertainties of many known matrix elements could be reduced. As a few deviations to previous experiments have been observed, the obtained ^{109}Ag matrix elements have been used as input for the CLX/DCY code for an additional cross check of the result. Its calculated yields are in good agreement with the experimental data thus confirming the GOSIA fit. The obtained high-precision set of ^{109}Ag matrix elements is ideal to serve as an accurate normalization of future Coulex experiments.

The resulting nine ^{72}Zn matrix elements from the Coulex data set can be converted to six reduced transition strengths and three quadrupole moments. They have been compared to previous measurements in the chain of the neutron-rich zinc isotopes:

The $B(E2; 2_1^+ \rightarrow 0_1^+) = (20.2 \pm 0.2(\mathrm{stat}) \pm 2.1(\mathrm{sys}))\,$W.u. strength in ^{72}Zn is in excellent agreement with the previous Coulex data and lifetime measurements. Moreover, like the previous Coulex experiments dealing with zinc isotopes with $N \geqslant 40$, the obtained $B(E2; 4_1^+ \rightarrow 2_1^+) = (28.9 \pm 0.5(\mathrm{stat}) \pm 3.0\,(\mathrm{sys}))\,$W.u. value in this thesis is collective, whereas two lifetime experiments predict lower values which supports the $N = 40$ subshell closure. The discrepancy between these two experimental techniques could not be explained with a possible $E4$ transition between the ground state and the 4_1^+ state. Furthermore, feeding contributions from higher lying states such as the 6_1^+ state and the quadrupole moment of the 4_1^+ state have been considered carefully in the present Coulex analysis. Beside the yrast states, the 0_2^+ and the 2_2^+ state has been populated. Both feature a reduced transition strength to the 2_1^+ state which is much smaller than the $B(E2; 2_1^+ \rightarrow 0_1^+)$ value: $B(E2; 0_2^+ \rightarrow 2_1^+)/B(E2; 2_1^+ \rightarrow 0_1^+) = 0.57 \pm 0.08$ and $B(E2; 2_2^+ \rightarrow 2_1^+)/B(E2; 2_1^+ \rightarrow 0_1^+) = 0.57 \pm 0.08$. This low collectivity indicates that the 0_2^+ and the 2_2^+ state have a different structure than the 0_1^+, 2_1^+ and 4_1^+ states of the yrast band. The $E2$ transition from the $2_2^+ \rightarrow 2_1^+$ is the dominant depopulation path for the 2_2^+ state. The $M1$ strength of the $2_2^+ \rightarrow 2_1^+$ transition is negligible and the $E2$ strength to the ground state is suppressed by a factor of about 20. The resulting branching ratio

$BR = P(2_2^+ \rightarrow 0_1^+)/P(2_2^+ \rightarrow 2_1^+) = 0.66 \pm 0.09(\text{stat}) \pm 0.13(\text{sys})$ is consistent with the previously measured branching ratio $BR = 0.68 \pm 0.05$ from a β-decay study. Apart from that, thanks to the new C-REX setup covering a large solid angle and thanks to the highly efficient MINIBALL γ-ray spectrometer, the quadrupole moments Q_s of the states 2_1^+, 4_1^+ and 2_2^+ state have been determined exploiting the angular dependence of the Coulex cross sections: $Q_s(2_1^+) = (-24 \pm 3(\text{stat}) \pm 1(\text{sys}))\,\text{efm}^2$, $Q_s(4_1^+) = (-27\,_{-7}^{+5}(\text{stat}) \pm 1(\text{sys}))\,\text{efm}^2$ and $Q_s(2_2^+) = (+39\,_{-3}^{+4}(\text{stat}) \pm 2(\text{sys}))\,\text{efm}^2$. Note that the resulting $Q_s(4_1^+)$ and $Q_s(2_2^+)$ of the Coulex experiment discussed in this thesis are the only quadrupole moments of higher lying states which have been measured in the neutron-rich zinc isotopes so far. The obtained spectroscopic quadrupole moments of the 2_1^+ and the 4_1^+ state are both negative which corresponds to a prolate shape. This fits well in the systematics of previous measurements. Furthermore, the spectroscopic quadrupole moment of the non-yrast 2_2^+ state has an opposite sign reflecting an oblate shape.

An additional method to study the shape of a nucleus are quadrupole sum rules: Using the fact that zero-coupled $E2$ operators are rotationally invariant, allows to extract the deformation β and the triaxiality parameter γ of the ^{72}Zn ground state. With $\beta = 0.241 \pm 0.01(\text{stat}) \pm 0.01(\text{sys})$ and $\gamma = 21° \pm 2°(\text{stat}) \pm 2°(\text{sys})$ the ground state is moderately deformed and quite triaxial. This result confirms the predictions of two mean-field calculations which are based on the Hartree-Fock-Bogoliubov (HFB) theory and use the Gogny D1S interaction. One of the calculation predicts an evolution from a triaxial ^{70}Zn nucleus to a prolate ^{74}Zn nucleus. Furthermore, the γ-softness decreases going to higher neutron-numbers. This is in agreement with the experimentally proved evolution of the neighboring germanium isotopes which show an evolution from the γ-soft nucleus ^{72}Ge to the ^{76}Ge γ-rigid nucleus.

The large set of ^{72}Zn matrix elements was compared to three different shell model calculations. This allows to test the used effective interactions (jj4c, jj44bpn and JUN45) in detail and to gain information on the microscopic structure of ^{72}Zn. The calculations have been performed in the jj44 model space ($1f_{5/2}$, $2p_{3/2}$, $2p_{1/2}$ and $1g_{9/2}$ orbitals for protons and neutrons) using a ^{56}Ni core. The jj4c interaction describes the experimental data of ^{72}Zn (level scheme, reduced transition strengths and quadrupole moments) best, but some features are reproduced by all interactions (c.f. fig. 6.33): All shell model calculations predict a collective yrast-band with a strong $|3\rangle = |\nu(2p_{3/2}^4 1f_{5/2}^4 2p_{1/2}^2 1g_{9/2}^4)\rangle = |\nu(1f_{5/2}^{-2} 1g_{9/2}^4)\rangle$ configuration in its neutron-wave function. This is in agreement with the measured $B(E2)$ values and the measured moderately deformed triaxial shape of the ^{72}Zn ground state. Moreover, the 0_2^+ state seems to have a different structure than the states of the yrast band, since the measured reduced transition strength $B(E2; 0_2^+ \rightarrow 2_1^+)$ is quite small. This is reproduced by the shell model calculations using the jj4c and the JUN45 interaction. The 0_2^+ state features a reduced $|3\rangle = |\nu(1f_{5/2}^{-2} 1g_{9/2}^4)\rangle$ component and an increased closed $N = 40$ configuration $|1\rangle = |\nu(2p_{3/2}^4 1f_{5/2}^6 2p_{1/2}^2 1g_{9/2}^2)\rangle = |\nu(1g_{9/2}^2)\rangle$. Furthermore, the 2_2^+ state has a different structure compared to the yrast states in all interactions: The fraction of the configuration $|3\rangle = |\nu(1f_{5/2}^{-2} 1g_{9/2}^4)\rangle$ in the total wave function is decreased compared to the yrast band, while the configuration $|6\rangle = |\nu(2p_{3/2}^4 1f_{5/2}^{-1} 2p_{1/2}^1 1g_{9/2}^4)\rangle = |\nu(1f_{5/2}^{-1} 2p_{1/2}^1 1g_{9/2}^4)\rangle$ approaches more than 15-20%. This is confirmed by the measured quadrupole moment of the 2_2^+ state and the low reduced transition strengths from the 2_2^+ state to the yrast band.

In summary, the multiple Coulomb excitation experiment of ^{72}Zn yielded a deep insight into the nuclear structure of the low-lying ^{72}Zn states: The measured reduced transition strengths $B(E2; 2_1^+ \rightarrow 0_1^+) = (20.2 \pm 2.3)\,\text{W.u.}$ and $B(E2; 4_1^+ \rightarrow 2_1^+) = (28.9 \pm 3.5)\,\text{W.u.}$ in the yrast band of ^{72}Zn are moderately collective instead of showing single-particle character like the neighboring nickel isotopes ($Z = 28$). This is consistent with the measured quadrupole moments $Q_s(2_1^+) = (-24 \pm 4)\,\text{efm}^2$ and $Q_s(4_1^+) = (-27 \pm 8)\,\text{efm}^2$, which both correspond to a moderate, prolate deformation of the yrast states 2_1^+ and 4_1^+. In addition, by applying quadruple sum rules, it was found that the ^{72}Zn ground state is

moderately deformed. Hence, it was experimentally shown that the yrast band of ^{72}Zn inhabits some collectivity which emphasizes that the zinc isotopes are located in a transitional region between the nickel isotopes ($Z = 28$) featuring single-particle character and the collective germanium isotopes ($Z = 32$). This underlined the locality of the $N = 40$ subshell closure, as it is not strong enough to stabilize the (nearly) spherical shapes, present in the ground state of the nickel isotopes at $N = 40, 42$, not even if only two protons are added to $Z = 28$. Instead, the 0^+_2 state in ^{72}Zn features a stronger closed $N = 40$ configuration in its wave functions compared to the ground state. This is predicted by two shell model calculations, which are in agreement with the measured low reduced transition strength $B(E2; 0^+_2 \rightarrow 2^+_1) = 11.0 \pm 5.4$ W.u. in ^{72}Zn compared to the larger reduced transition strengths of the yrast band.

7.3   Future Transfer and Coulomb Excitation Experiments at HIE-ISOLDE

The multiple Coulomb excitation experiment at the end of 2012 was one of the last experiments conducted at REX-ISOLDE, before the main construction of the ISOLDE upgrade, the High Intensity and Energy ISOLDE (HIE-ISOLDE) project, was started. The main improvements of HIE-ISOLDE compared to ISOLDE are an energy increase of the delivered radioactive beams which enhances the cross section of many reaction channels, an intensity upgrade by about a factor of four and better beam properties especially concerning beam purity, ionization efficiency and optical quality [138, 139]. In a first stage, the energy upgrade from $E_{beam} = 3$ MeV/u to $E_{beam} = 5.5$ MeV/u is realized by replacing the normal conducting REX-LINAC with a superconducting LINAC featuring two cryomodules [138, 139]. In a second phase, two more cryomodules are added to reach a beam energy of $E_{beam} = 10$ MeV/u [138, 139]. The first phase is almost completed to start physics runs in autumn 2015. Due to the higher beam energy and the increased beam intensities the HIE-ISOLDE project poses new challenges to the detector arrays.

Transfer Experiments

Transfer reactions at HIE-ISOLDE benefit from the higher available beam energies which result in more pronounced transfer cross sections. As the angular momentum transfer depends strongly on the shape of the differential cross section, the experiments are more sensitive to the spins of newly discovered states. Furthermore, the intensity upgrade of HIE-ISOLDE allows to study more exotic nuclei, far away from the valley of stability. For these nuclei, a common feature is the higher level density. Therefore, it is crucial to achieve a high energy resolution with the detector setup to disentangle closely lying states.

The T-REX silicon array was used very successfully from 2007 to 2012 at ISOLDE to study one- and two-neutron transfer reactions. To cope also with the experimental conditions available at HIE-ISOLDE, an upgrade of T-REX is planned. The main improvements of T-REX focus on a better energy resolution and a reduction of the detection threshold for low energetic particles, especially in backward direction. The energy resolution is limited by the segmentation of the silicon detectors and, in case of high Z beams, by the energy straggling of the beam and the light transfer product in the target. To quantitatively determine the different contributions to the energy resolution, a realistic Geant4 simulation has been implemented and performed within this work. As show case, the one-neutron transfer reaction d(^{132}Sn, p)^{133}Sn of a HIE-ISOLDE ^{132}Sn beam ($E_{beam} = 10$ MeV/u) impinging on a 0.1 mg/cm^2 thick deuterated PE target is used. A significant improvement of the energy resolution[1] is gained by increasing the number of strips in the Barrel part of T-REX from 16 to 64 or 128 (c.f. fig. 7.1 a), b) and c)). The influence of the target thickness on the energy resolution was studied as well: Assuming 64 Barrel strips, the energy resolution of the ground state deteriorates from $\Delta E \approx 86$ keV (FWHM) to $\Delta E \approx 265$ keV (FWHM) for an increase of the target thickness from

---

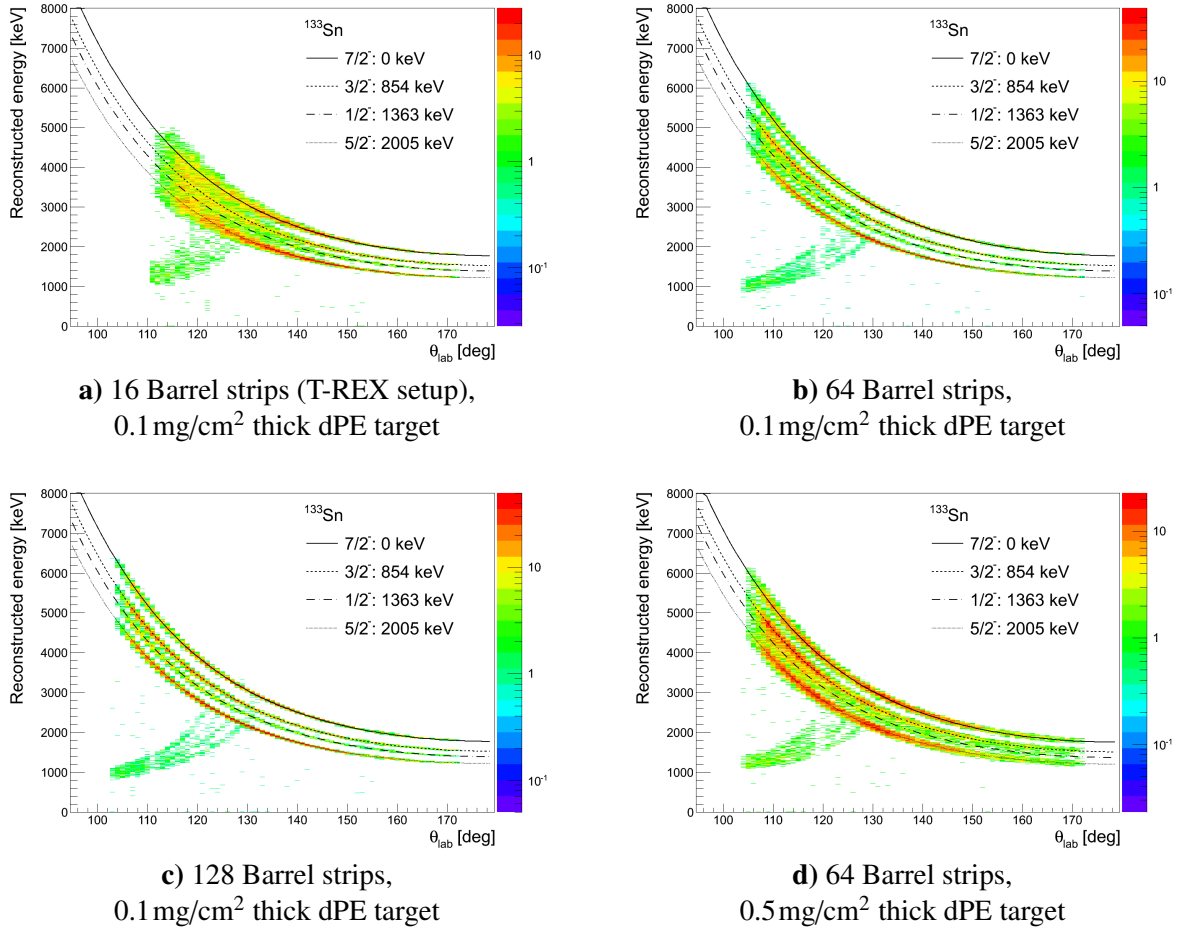[1]Exact numbers for the energy resolution are not given since, it strongly depends on the scattering angle θ_{lab}.

a) 16 Barrel strips (T-REX setup),
0.1 mg/cm² thick dPE target

b) 64 Barrel strips,
0.1 mg/cm² thick dPE target

c) 128 Barrel strips,
0.1 mg/cm² thick dPE target

d) 64 Barrel strips,
0.5 mg/cm² thick dPE target

Fig. 7.1: The reconstructed particle energy as a function of the scattering angle θ_{lab} in the laboratory frame for the d(^{132}Sn, p)^{133}Sn reaction with $E_{beam} = 10$ MeV/u. The spectra are obtained by a detailed Geant4 simulation using various Barrel segmentations and various thicknesses of the deuterated PE target. For comparison the kinematic predictions for the first four states of ^{133}Sn are visualized. Note that only the transfer protons in backward direction are shown. Fig. **a)**, **b)** and **c)** demonstrate that the energy resolution is improved by increasing the segmentation of the Barrel detectors from 16 strips to 128 strips. The comparison of fig. **b)** with fig. **d)** shows that the energy resolution deteriorates if the thickness of the deuterated PE target is increased. The resolution for the ground state declines from $\Delta E \approx 86$ keV (FWHM) to $\Delta E \approx 265$ keV (FWHM) going from 0.1 mg/cm² dPE to 0.5 mg/cm² dPE.

0.1 mg/cm² to 0.5 mg/cm² (c.f. fig. 7.1 b) and d)). Without the use of gas targets, the energy straggling on the target carrier material and thus the energy resolution can only be improved by decreasing the target thickness. Hence, a compromise between energy resolution and maximizing the statistics with a thicker target has to be found individually for each experiment.

In summary, for the T-REX upgrade, the resistive strip Barrel detectors will be replaced by double sided strip detectors which additionally feature a higher segmentation. Due to the higher segmentation and to reduce the detection threshold, a long term plan for the T-REX upgrade is to process and multiplex the detector signals with an ASIC based readout. This allows a more precise measurement of differential cross sections over a large angular range which is mandatory to study exotic nuclei.

Coulomb Excitation Experiments

HIE-ISOLDE also provides new opportunities for the MINIBALL Coulex campaign. The higher beam energies increase the cross sections for multiple Coulomb excitation processes significantly which allows a more detailed study of nuclear structure by testing theoretical calculations more accurately.

However, it has to be considered that the Coulex reactions are not safe, i.e. purely electromagnetic, over the whole scattering range anymore. In the case of the ^{72}Zn Coulex experiment with the ^{109}Ag target, the Coulex reaction is only safe for scattering angles below $\theta_{CM} = 41°$ in the center-of-mass frame for a beam energy of $E_{beam} = 5.5\,\text{MeV/u}$. If a ^{208}Pb target is used, the critical angle $\theta_{CM} = 62°$ increases only slightly. The data beyond the critical angle cannot be used to determine reduced transition strengths and quadrupole moments. One advantage of the unsafe Coulex reaction is that the effect of the strong nuclear force can be studied if, like in ^{72}Zn, the electromagnetic matrix elements are known. Furthermore, in case of very exotic nuclei with low beam intensities, higher lying states can be identified for the first time, since their population is increased due to the additional reaction channels. The big advantage of HIE-ISOLDE is that the beam energy can be adjusted. Hence, either the safe Coulex cross sections can be maximized to measured electromagnetic transition probabilities or the unsafe Coulex reactions can be studied to efficiently populate and identify higher-lying states. One of the approved day-one experiments at HIE-ISOLDE is the multiple Coulomb excitation of $^{74-80}$Zn with a $2\,\text{mg/cm}^2$ thick ^{196}Pt target or a 4 or $5\,\text{mg/cm}^2$ thick ^{208}Pb target to study the evolution of the shell structure between the harmonic subshell closure $N = 40$ and the magic number $N = 50$ [140]. This experiment also addresses the inconsistencies between lifetime measurements from Legnaro / GANIL and Coulex experiments at REX-ISOLDE. With a beam energy of $E_{beam} = 4.0\,\text{MeV/u}$ the Coulex reactions are safe for all scattering angles covered by the standard CD setup at MINIBALL. In a second step, the delivery of the second cryomodule in spring 2016 allows to investigate ^{80}Zn with a higher, unsafe beam energy to study the 4_1^+ state in ^{80}Zn in more detail [140].

A

T-REX and C-REX Electronics

In this chapter, the electronics of the transfer setup T-REX and the Coulex setup C-REX is presented in detail.

T-REX

A schematic of the readout electronics of T-REX is shown in fig. A.1. It is based on standard Mesytec modules [141] which are visualized with yellow boxes. As already mentioned in sec. 3.3, the electronics is split into two identical chains: the "Top-Left" trigger group and the "Bottom-Right" trigger group. For simplification fig. A.1 only displays the Top-Left trigger group as the Bottom-Right trigger group works in the same manner. Due to the different detector types in T-REX their signals have to be treated separately:

The 64 = 2×2×16 Top and Left signals of the Forward and Backward resistive Barrel strips are first preamplified with a MPR-64 module[1], then shaped with four STM-16 modules[2] and finally digitized using two 32 channel peak sensing ADCs (MADC-32)[3].

The four rear ΔE signals of all four Top-Left Barrel detectors as well as their four E_{rest} signals are preamplified and shaped separately with one MSI-8 module[4]. Each of the eight outgoing energy signals of the MSI-8 are digitized in another MADC-32. Furthermore, the MSI-8 module offers a fast timing signal for each channel which is sent to a constant fraction discriminator to create a trigger. Analogously to the energy signals of the Barrel detectors, the four E_{rest} signals of the Forward and Backward Top and Left CD pad detectors are treated.

Contrary to the Barrel detectors and the CD pad detectors, the ring and strip signals of the Forward and Backward ΔE-CD detectors are processed differently. Their 128 signals[5] are multiplexed with four MUX-32 modules[6] to reduce the total number of channels. As an example, the FCD top rings and FCD left rings are feed in one MUX-32 module which consists of 2 MUX-16 submodules. Each submodule has five main output signals: a trigger, the energy signal of the first and the second hit and the position signal of the first and the second hit which is connected to the fired ring number (c.f. sec. 4.2). As the two submodules of one MUX-32 are connected to the same bus, the signals are combined to further reduce the number of channels by a factor of two. As a result, two energy and two position signals are send to a MADC-32 while the trigger signal is send to a coincidence unit.

In the coincidence unit a common logical OR of all trigger signals of all Top-Left detectors is created, defining the global Top-Left trigger, which is distributed to the three Top-Left MADCs. Thus, the trigger ensures that all detectors in the Top-Left trigger group are read out.

The MADCs are operated in the multi-event readout mode, i.e. the events which occur during one spill of the beam (in the so called "On-Beam" Window) are all stored in the MADC to avoid dead-time of the data acquisition while writing the events to disk. After the "On-Beam" Window the MADC is read out. Subsequently, data is recorded in an additional "Off-Beam" window without the presence of the radioactive beam. Again, it is followed by a readout time window. The "Off-Beam" window allows to perform a background subtraction, e.g. of natural background sources and of the β-decay of

---

[1]MPR-64: 64-fold charge sensitive preamplifier from Mesytec
[2]STM-16: 16-fold shaper with timing and multiplicity trigger from Mesytec
[3]MADC-32: Fast 32 channel VME peak sensing ADC from Mesytec
[4]MSI-8: 8 channel preamplifier, shaper and timing filter amplifier
[5]128 = 4 ΔE-CD quadrants × (16 rings + 16 strips each)
[6]MUX-32: 32 fold preamplifier, shaper and timing filter with multiplexed output from Mesytec
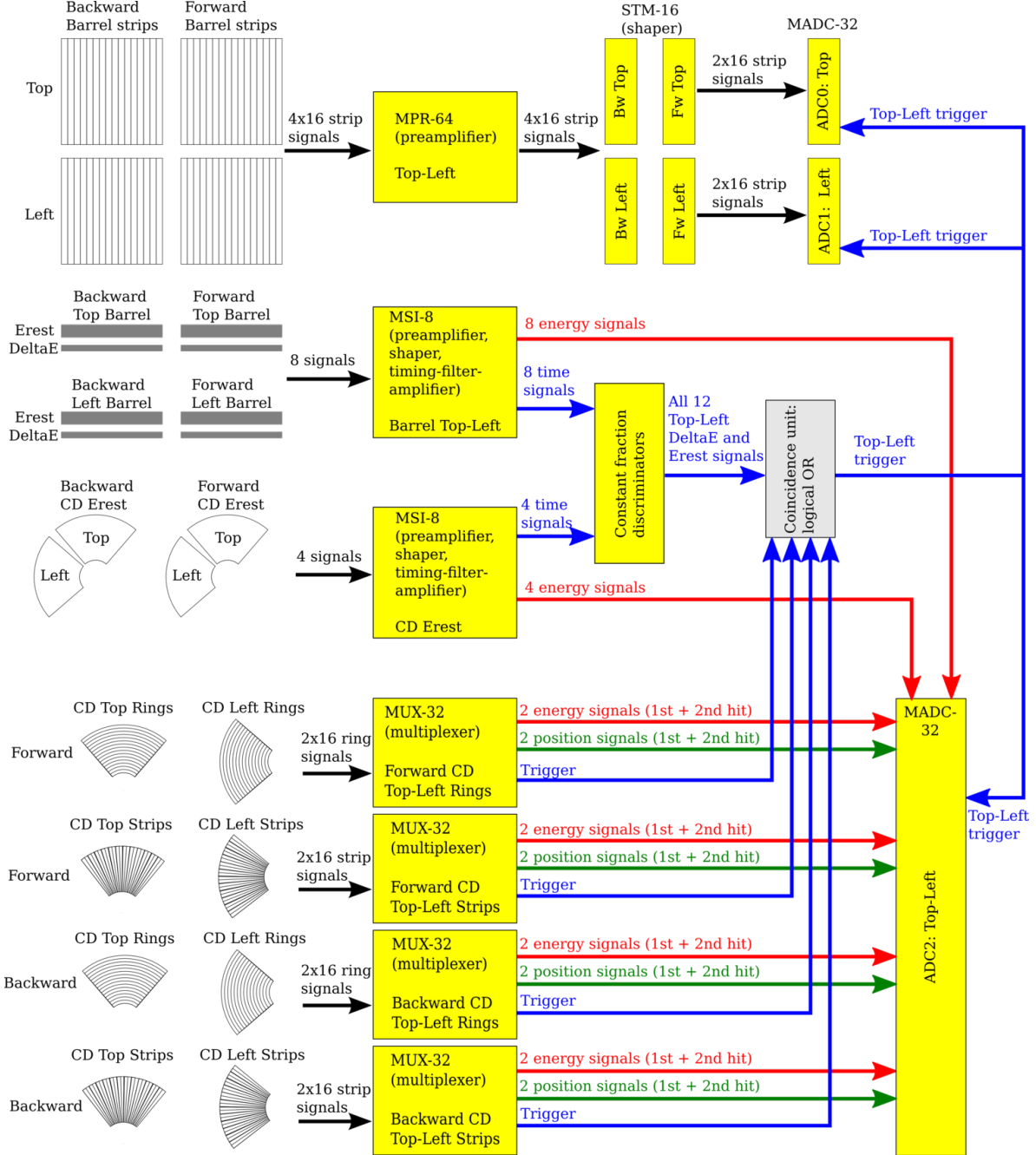
Fig. A.1: A schematic drawing of the T-REX readout electronics as it was used in the transfer experiment in 2011. Only the Top-Left trigger group is shown here, as the Bottom-Right trigger group has exactly the same layout. Hence, the T-REX electronics feature two independent trigger groups.
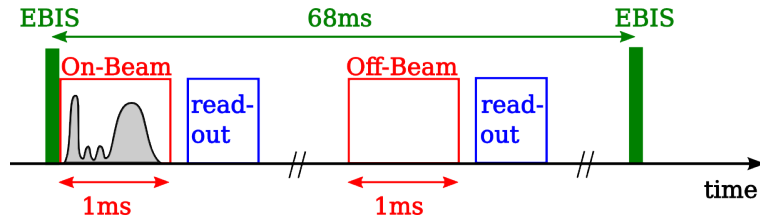

Fig. A.2: Time relation of the beam and the readout electronics. Due to the pulsed structure of the beam, a buffered readout is possible which reduces the dead-time of the data acquisition significantly.
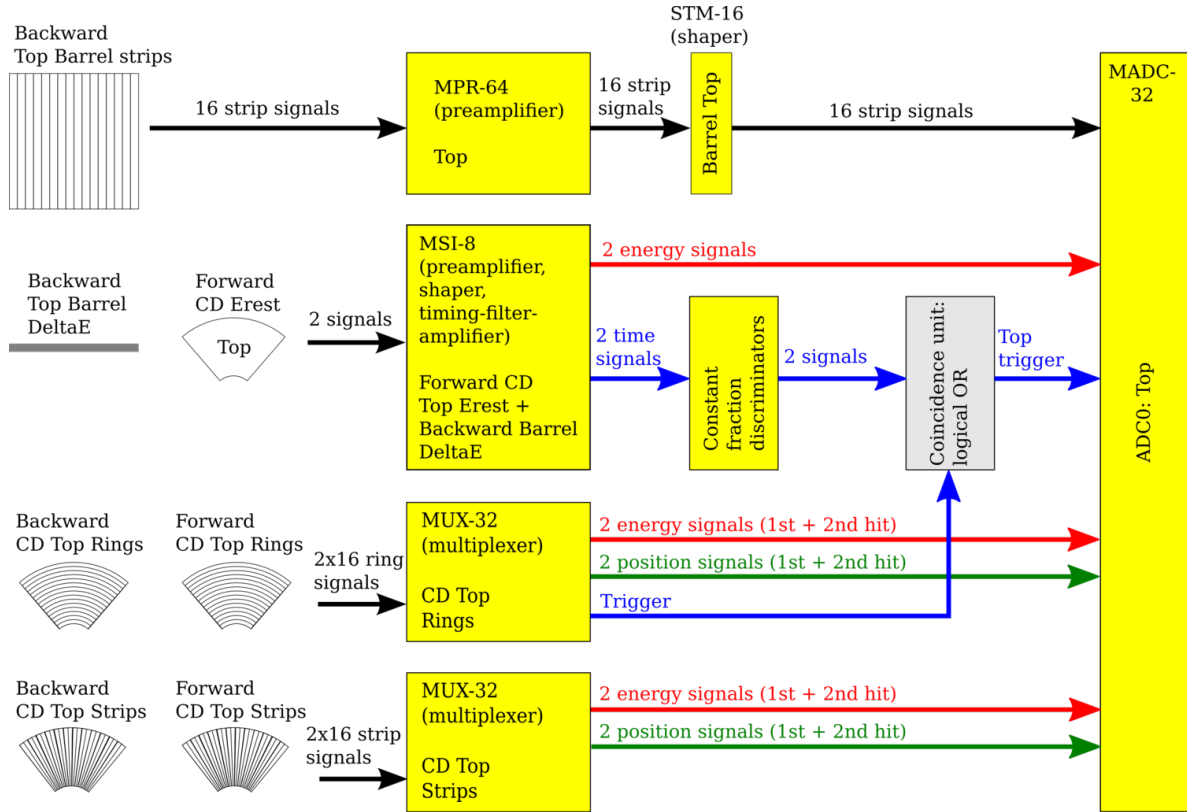
Fig. A.3: A schematic drawing of the Coulex readout electronics. As an example only the Top trigger group is shown here. All the other quadrants Left, Bottom and Right have the same electronic layout. Hence, the C-REX electronics feature four independent trigger groups.

the beam. The time relation of the readout of the data acquisition and the EBIS pulse which defines the beginning of the "On-Beam" window is visualized in fig. A.2.

C-REX

Due to the higher expected count rates in C-REX experiments, the two trigger groups Top-Left and Bottom-Right from the T-REX electronics have been replaced by four independent trigger groups, i.e. one trigger for each quadrant: Top, Left, Bottom and Right. As an example fig. A.3 shows the readout chain for all Top detectors. Like the T-REX electronics, the readout of C-REX is based on Mesytec modules. The Barrel strips, the rear ΔE signal of the Barrel detector as well as the E_{rest} signal of the FCD pad detector are processed in the same way as in the T-REX electronics. Moreover, the FCD and BCD ring and strip signals are also read out with the MUX-32 multiplexers from Mesytec. However, contrary to the T-REX electronics in fig. A.1 the BCD and FCD rings are processed with one MUX-bus. The strip signals of the trigger group are combined on a second MUX-bus. Like in the transfer electronics this reduces the number of channels without losing information as it is e.g. physically impossible that two top detectors are hit in one physical event in two-body reactions. Furthermore, due to the reaction kinematics (c.f. sec. 6.1.1), MUX PCBs with a 1 GeV range are used for the FCD whereas the BCD used MUX PCBs with a 100 MeV range.

Details of the Particle Detector Calibration

This section gives a more detailed insight into the calibration of all silicon detectors of T-REX and C-REX compared to sec. 4.2. Sec. B.1 and sec. B.2 describe the calibration steps of the ΔE and E_{rest} Barrel detectors, while sec. B.3 and sec. B.4 deal with the ΔE and E_{rest} CD detectors.

B.1 ΔE Barrel Detectors

The calibration of the Barrel ΔE detectors is performed using a standard quadruple calibration α-source which is installed on the target ladder. Fig. B.1 a) shows a typical uncalibrated E_{rear}^{raw} energy spectrum of the unsegmented backside of the Barrel ΔE detector. The lowest peak in energy is the noise peak which is removed by an energy cut for further analysis. This cut defines the energy threshold of the detector. The four remaining peaks in fig. B.1 a) belong to the four strongest α-lines of the isotopes ^{148}Gd (3.18 MeV), ^{239}Pu (5.16 MeV), ^{214}Am (5.49 MeV) and ^{244}Cm (5.81 MeV). However, their resolution is deteriorated as the energy signal is dependent on the position of the hit along the strip (c.f. fig. B.1 b)). As explained in sec. 3.3, the position along the strip is calculated from the ratio between the signal of one side of the resistive strip and the E_{rear} signal. As both signals are not calibrated yet, this ratio is not in the physical range [0, 1] but in the interval [0, x_0]. Hence, to get a physical position information between 0 and 1 the maximal uncalibrated position x_0 is determined by fitting the position spectrum of each Barrel strip with a Fermi-function (c.f. fig. B.1 c)). After the position calibration, the tilt of the α-lines in fig. B.1 b) is corrected: The spectrum is divided into 10 position slices. For each slice, the positions of the four α-peaks are fitted. As a result, the mean α-peak positions can be shown as a function of the slice position (c.f. B.1 d)). In this plot each α-line can be well fitted with a straight line showing the linearity of the tilt. Subsequently, their slopes are plotted as a function of the α-energy in fig. B.1 e) indicating that the tilt t features a simple linear energy dependency:

$$t(E_{rear}^{cal}) = t_{\text{offset}} + t_{\text{gain}} \cdot E_{rear}^{cal}. \tag{B.1}$$

Hence, the tilt corrected E_{rear}^{corr} energy of the Barrel ΔE detector is given by

$$E_{rear}^{corr} = t(E_{rear}^{cal}) \cdot (1 - x) + E_{rear}^{raw}, \tag{B.2}$$

where x is the calibrated position along the strip and E_{rear}^{raw} the uncorrected energy of the rear detector side. Note, that E_{rear}^{corr} and E_{rear}^{raw} are not energy calibrated yet, i.e. they still have the dimensions "channels". However, to calculate the tilt correction factor $t(E_{rear}^{cal})$ in (B.2) an energy calibration is needed as the tilt correction factor is given as a function of calibrated energies E_{rear}^{cal} in eq. (B.1). Therefore, a rough linear energy calibration using the four α-peaks is performed. It considers only events close the the readout side of the strips, i.e. in the last position bin as these events are almost not affected by the tilt effect. Finally, after applying the tilt correction with eq. (B.2), the energy spectrum of the rear side has a much better energy resolution compared to fig. B.1 a). Hence, the energy calibration of the Barrel ΔE detector can be done more precisely using all hits along the resistive strips: The fitted peak positions in the corrected E_{rear}^{raw} energy spectrum are fitted to the literature
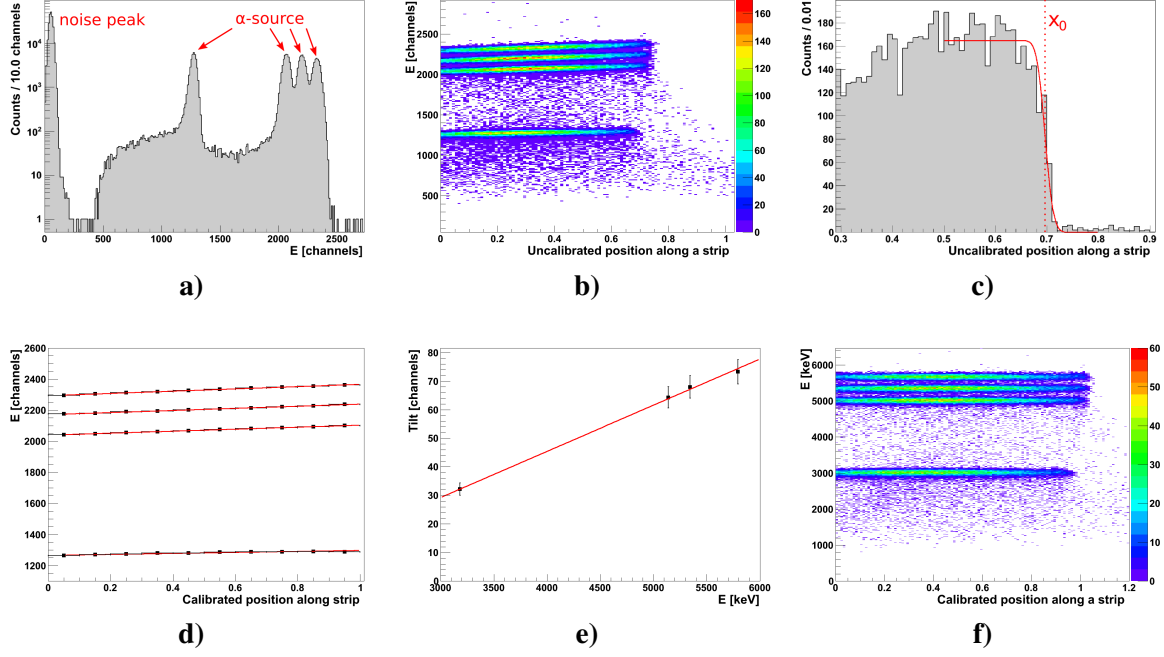
Fig. B.1: The calibration steps of a Barrel ΔE detector using a standard quadruple calibration α-source. **a)** An uncalibrated energy E_{rear} spectrum of the rear side of a T-REX BBarrel ΔE detector. It shows the noise peak as well as the four α-peaks from the source. **b)** The uncalibrated E_{rear} signal vs. the uncalibrated position along the strip which has been hit. The tilt of the α-lines visualizes the dependence of the E_{rear} signal of the hit position along a resistive Barrel strip. **c)** Histogram of the uncalibrated hit positions along a BBarrel strip which is used for the position calibration. A fit (in red) of a Fermi-function is included which defines the maximal hit position x_0 along the strip. **d)** The fitted position of the α-peaks as a function of the calibrated position along the strip. To determine the α-peak positions, E_{rear} spectra are plotted for 10 different position slices. The error bars in x-direction visualizes the width of the position slices. **e)** The slope of the straight lines in d) as a function of the α-energies in keV. **f)** The final calibrated E_{rear} energy including the tilt correction as a function of the calibrated position along the strip.

values of the α-energies using a linear channel-energy dependence:

$$E_{cal} = a_1 \cdot (E_{raw} - a_0), \tag{B.3}$$

with a_0 and a_1 being the offset and the gain of the linear calibration, respectively. E_{cal} represents the calibrated energy in keV, while E_{raw} is the uncalibrated raw energy in ADC channels. As a result, the final calibrated Barrel spectrum in fig. B.1 f) is obtained.

Calibration of Barrel ΔE Detectors with a Mylar Foil in Front

The above described calibration procedure have been performed for all BBarrel ΔE detectors in the T-REX setup as well as in the C-REX setup. However, the FBarrel ΔE detectors in T-REX feature an additional mylar foil (c.f. sec. 3.3). Hence, the energy loss of the α-particles in the foil has to be taken into account. To calculate the energy loss, a detailed Geant4 simulation [142, 143] of the T-REX setup and a quadruple α-source is performed. The Geant4 simulation is preferred compared to a simple energy loss calculation e.g. with SRIM [144], as the effective foil thickness and therefore the energy loss of the α-particles does not only depend on the strip number, but also on the position along the strip. This effect is not negligible as the difference in energy deposition of the α-particles between the edges and the middle of the strips can exceed 500 keV (c.f. fig. B.2 a)). A second effect of the mylar foil which has to be considered, is the energy straggling in the foil. As a result, the energy resolution deteriorates with increasing effective foil thickness. Hence, the α-peaks can only be distinguished in about the first four strips which are closest to the target (c.f. fig. B.2 b)). Furthermore, the foil is thick

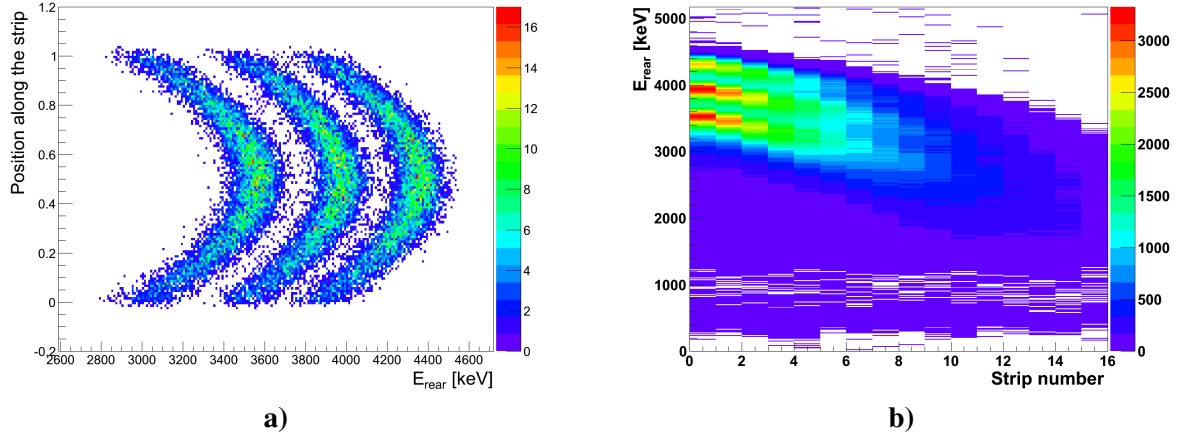**a)**   **b)**

Fig. B.2: Energy calibration of a T-REX FBarrel ΔE detector using a quadruple α-source. The FBarrel features a $11.75\,\mu$m thick aluminized mylar foil in front. **a)** A result of a Geant4 simulation with a quadruple α-source. It shows the energy deposition of strip zero of the FBarrel which is closest to the target. As the effective foil thickness changes along the strip, the α-lines are bended. **b)** Calibrated energy E_{rear} as a function of the strip number. The energy resolution deteriorates with increasing strip number as the effective thickness of the foil and therefore the energy straggling in the foil increases. Moreover, the energy deposition in the detector decreases with the strip number due to the increasing foil thickness. Furthermore, in both figures the lowest α-line is not visible as these α-particles don't have enough energy to penetrate the mylar foil.

enough that the lowest α-line is never visible.

Hence, due to these effects of the mylar foil, the energy calibration procedure of the T-REX FBarrel ΔE detectors has to be slightly modified: First, energy spectra of the E_{rear} signal are plotted for the first four strips and their three α-peaks are fitted. Subsequently, their peak positions are compared to the results of the Geant4 simulation. As the energy loss of the α-particles depends on the strip number, four strips lead to $4 \cdot 3 = 12$ calibration points which allow to perform a linear calibration of the unsegmented rear side using eq. (B.3).

B.2 Barrel Pad Detectors

In contrast to the Barrel ΔE detectors, the Barrel pad detectors cannot be calibrated with an α-source as it is not possible to mount the source directly before the detector[1]. Thus, two complementary calibration techniques have been developed: A low energy calibration for the BBarrel pad detectors and a high energy calibration method for the FBarrel detectors, where higher energy depositions are expected due to the reaction kinematics. Both techniques are presented in the following.

Low Energy Calibration: Compton Scattering of an ^{152}Eu Source

The first method for the calibration of the Barrel pad detectors exploits γ-rays from an ^{152}Eu source which is installed at the MINIBALL target position. The emitted γ-rays can easily penetrate the Barrel ΔE detector. Hence, they can undergo Compton scattering in the Barrel pad detector and can subsequently be absorbed in a MINIBALL crystal via photo effect. These events are identified as an anti-correlation line in fig. B.3 a) which shows the detected energy in MINIBALL versus the detected energy in the Barrel pad detector. As the energy of each emitted γ-ray from the ^{152}Eu is known and due to the good energy resolution of MINIBALL, the energy deposition in the pad detector is well defined. Thus, a fit of the anti-correlation line allows a precise energy calibration. Its slope and offset

---

[1]The front of the pad is shielded by the Barrel ΔE detector and at the back the vacuum chamber is too close. This is a problem as the α-particles from the source do not have enough energy to penetrate through the ΔE detector or the vacuum chamber.

a)   **b)**
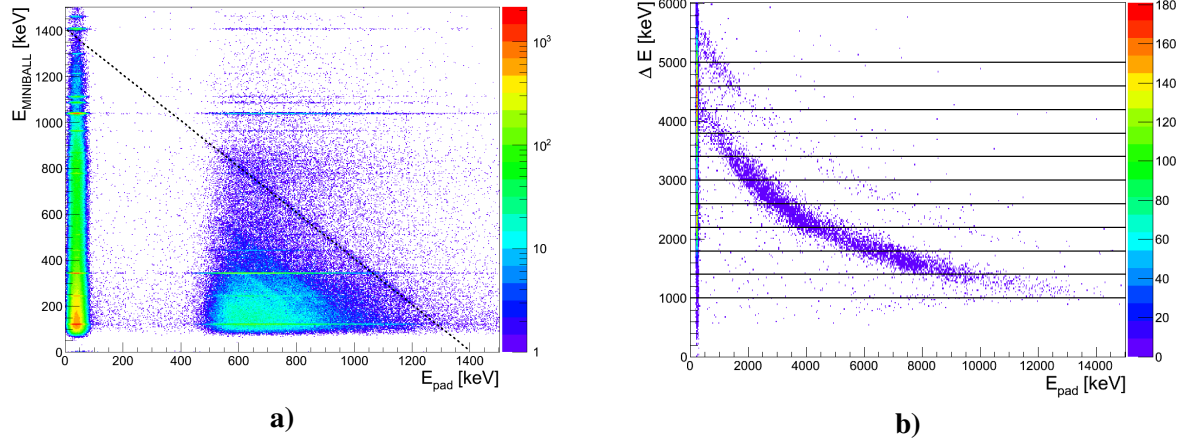
Fig. B.3: a) Low energy Barrel pad calibration with a ^{152}Eu source mounted at the MINIBALL target position. The energy deposition in MINIBALL vs. the energy deposition in a Barrel pad detector is shown. The strong vertical structure at low pad energies is related to the noise peak of the pad detector. The thin dominant horizontal lines corresponds to photopeaks of γ-rays in MINIBALL. Furthermore, the dotted anti-correlation line results from the strong $E_\gamma = 1.408$ MeV line of the ^{152}Eu source. It represents the Compton scattering of the $E_\gamma = 1.408$ MeV γ-rays in the Barrel pad detector and its final photo absorption in a MINIBALL crystal. The dotted fit of the Compton-line allows a low energy calibration of the pad detectors as the MINIBALL energy and the total γ-ray energy are well defined. **b)** High energy calibration of a Barrel pad detector using a ^{22}Ne beam impinging on a deuterated PE target. The ΔE-E spectrum of a single strip of a FBarrel telescope is shown. The strong vertical line corresponds to stopped particles in the ΔE detector which feature only noise in the pad detector. The upper branch at higher pad energies is related to elastically scattered deuterons, whereas the lower branch corresponds to transfer protons. The position of theses branches is well defined by the reaction kinematics. Thus, a calibrated ΔE detector allows an energy calibration of the Barrel pad detector. The black horizontal lines define the energy bins which are used in the calibration procedure (for details see text).

can be used to calculate the linear energy calibration parameters (gain and offset) of the pad detector. However, this calibration method is limited to the low energy regime, since the highest γ-ray-line of an ^{152}Eu source is about $E_\gamma = 1.4$ MeV.

High Energy Calibration: Stable Beam Experiment

Complementary to the low energy Barrel pad calibration, a stable beam experiment allows to cover pad energies up to 12 MeV, which is the typical range for transfer reactions with T-REX. At ISOLDE the well known transfer reaction d(^{22}Ne,p)^{23}Ne with a deuterated PE target is used for the pad calibration. A stable ^{22}Ne beam ($E_{beam} = 2.7$ MeV/u) can be easily produced at high intensities since ^{22}Ne is a buffer gas in the REXEBIS. The known reaction kinematics in combination with the previously calibrated Barrel ΔE detector allow to predict the energy deposition in the pad detector which is essential for a pad calibration[2]. Fig. B.3 b) shows a typical ΔE-E spectrum for a FBarrel ΔE-E telescope. The upper branch corresponds to elastically scattered deuterons, whereas the lower branch is related to the transfer protons resulting from the d(^{22}Ne,p)^{23}Ne reaction. This 2D spectrum is divided into 400 keV thick vertical slices (c.f. fig. B.3 b)). The projection on the E_{pad}-axis of each slice features a strong peak for the transfer protons and a less dominant peak at higher energies for elastic deuterons. Their peak positions are characteristic for the strip number (scattering angle) and can be calculated exploiting the reaction kinematics. To take also the effect of the finite opening angle of each Barrel strip and of the beam spot size into account, the same spectra are produced with a realistic Geant4 simulation of the setup and the reaction. The comparison experiment-Geant4 allows to determine the

---

[2]For the calibration of the FBarrel pad detectors, besides the energy loss in the target, the energy loss in the mylar foils has to be considered, too.
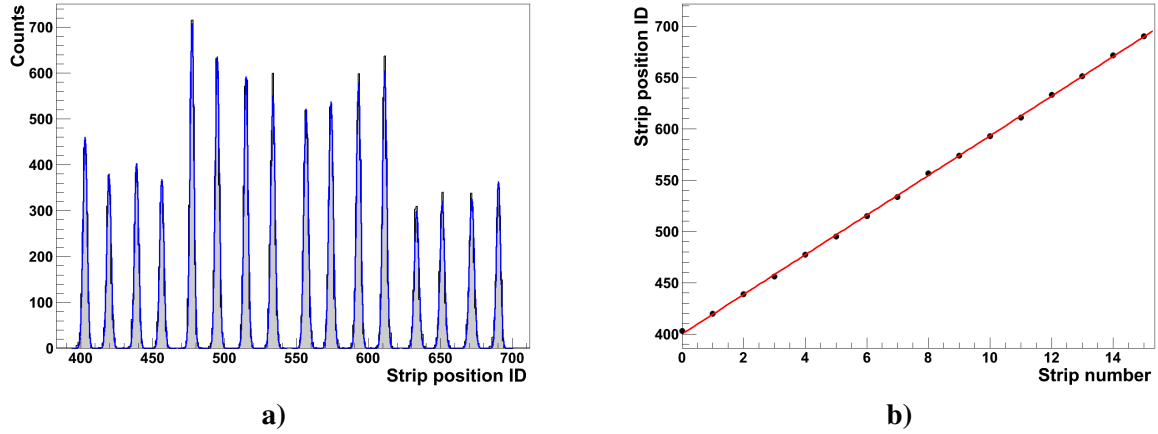
Fig. B.4: a) A typical strip position signal of a FCD ΔE quadrant. Each peak represents a strip number. As the inner eight strips are combined in the electronic chain their count rate is twice as high as the rate for the four strips at the outer edges of the detector. **b)** The peak positions of a) as a function of the strip number. The red line shows the result of a linear fit.

energy calibration parameters for the Barrel pad detectors[3].

B.3 ΔE CD Detectors

As mentioned in the description of the T-REX and C-REX electronics in sec. 3.3, sec. 3.4 and appendix A, the ring and strip signals of the ΔE CD detectors are multiplexed. Hence, their calibration is done in two steps: First, a de-multiplexing has to be performed to decode which ring or strip has been hit. Second, the energy of each CD ring and of each strip is calibrated. Dependent on the experiment, a low energy calibration with an α-source is performed or a high energy calibration with a (stable) beam is necessary.

De-Multiplexing of the ΔE CD Detector Signals
The multiplexed position signal of a ΔE CD quadrant is directly related to the ring or strip number, respectively. An example for a strip position signal is shown in fig. B.4 a): Each peak represents one strip of the ΔE CD quadrant. The peak positions are in good approximation directly proportional to the strip number (c.f. fig. B.4 b))[4]. Hence, the peak which is closest to the measured position signal defines the strip number. As the multiplexers are not stable during the whole experiments, this results in a time dependent shift of the position spectrum. Therefore, in both, the transfer and the Coulex [72]Zn experiment, it has been mandatory to determine the peak positions for each run separately.

Low Energy Calibration with an α-Source
After the de-multiplexing, an energy calibration of each ΔE CD ring and strip can be performed. If the CD detector is used for transfer experiments, the expected energy depositions are in the order of a few MeV. Hence, a calibration with a quadruple α-source is conducted by fitting the α-peaks and assuming a linear calibration according to eq. (B.3).

---

[3]In the present implementation only transfer protons and only the first four strips close to the target are considered. Higher strips with scattering angles close to the beam line feature a larger energy straggling e.g. in the mylar foil and the ΔE detector which results in much broader peak shapes.

[4]A closer look at fig. B.4 a) and b) reveals that always four peaks are grouped together, i.e. after four peaks the distance to the next peak is a little bit larger. Thus, it is possible to identify broken rings / strips even if they are located at the edge of the detector. If e.g. the first strip is broken, the first group consists of only three peaks instead of four.
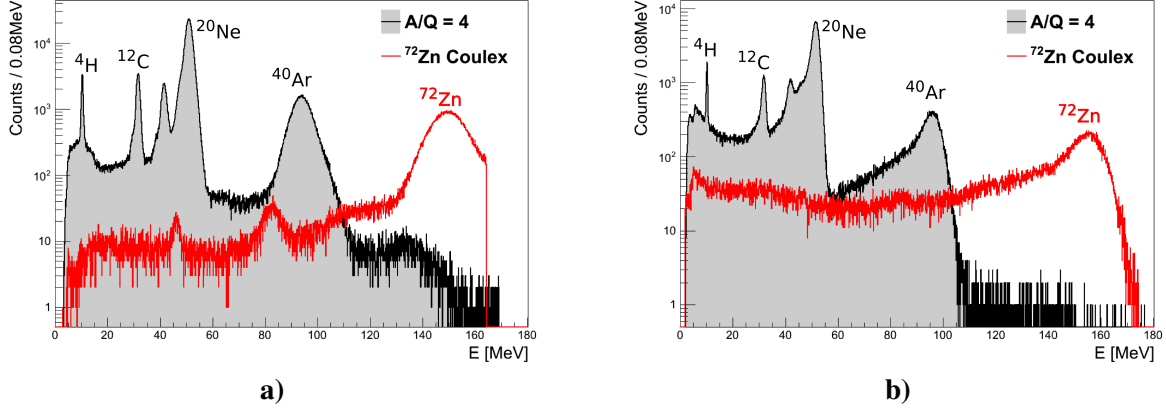
Fig. B.5: The energy spectra of a FCD ring in **a)** and of a FCD strip in **b)** are shown. The filled gray spectrum results from an $A/Q = 4$ EBIS beam (E_{beam} = 2.85 MeV/u) which is impinging on a 1.17 mg/cm^2 thick ^{109}Ag target, while the red spectrum results from the scattering of a ^{72}Zn beam (E_{beam} = 2.85 MeV/u) by the same target. The EBIS beam contains the following ions: ^{4}He$^+$, ^{12}C^{3+}, ^{16}O^{4+}, ^{20}Ne^{5+} and ^{40}Ar^{10+}. The marked peaks are used for the energy calibration of the ΔE FCD detector. The small peak between ^{12}C^{3+} and ^{20}Ne^{5+} belongs to ^{16}O^{4+} which is not used for calibration as it is not seen in all ring and strip spectra. Furthermore, the first two peaks at around 45 MeV and 85 MeV of the red ^{72}Zn ring spectrum correspond to a beam contaminant from the EBIS rest gas (c.f. sec. 6.1.6). Due to their low intensity both are not used for the energy calibration.

High Energy Calibration with a High Intensity Beam

In contrast, if the ΔE CD detector is used for a Coulomb excitation experiment, a calibration with solely an α-source is not very precise due to the extrapolation to Coulex energies which can be in the order of 100 MeV and more. In this case, the energy calibration is performed with a high intensity REX-ISOLDE beam exploiting the kinematics of the elastically scattered particles. For the ^{72}Zn Coulex experiment, an $A/Q = 4$ beam from the buffer gas of the REXEBIS is used which impinges on the 1.17 mg/cm^2 ^{109}Ag Coulex target. This beam consists mainly of the isotopes ^{4}He$^+$, ^{12}C^{3+}, (^{16}O^{4+}), ^{20}Ne^{5+} and ^{40}Ar^{10+} [87]. Fig. B.5 a) and b) show examples of a ring and a strip FCD ΔE spectrum of the elastically scattered $A/Q = 4$ beam particles. The beam energy of the $A/Q = 4$ beam is E_{beam} = 2.85 MeV/u, resulting in a maximal energy deposition of about 100 MeV in the FCD (c.f. ^{40}Ar peak). However, the beam energy of the ^{72}Zn Coulex experiment is 205.2 MeV. Therefore, to avoid an imprecise extrapolation to the ^{72}Zn energies, the elastically scattered ^{72}Zn particles of the Coulex experiments have also been considered in the energy calibration (c.f. red spectra in fig. B.5). To achieve a high accuracy and a linear channel-energy dependence in the calibration, also the thicknesses of the dead layers of the ΔE detectors have been taken into account. The dead layers consists of $0.4 - 0.5 \mu$m of silicon due to implantation and $0.2 - 0.3 \mu$m aluminum due to metalization [86]. In a Coulomb excitation analysis, they play a crucial role as the deposited energy in the dead layers are about $6 - 10$ MeV for the scattered ^{72}Zn particles and about $6 - 14$ MeV for the scattered ^{109}Ag particles. The calibration was done by comparing the fitted experimental peak positions with a realistic Geant4 simulation and applying eq. B.3. The Geant4 simulation features a detailed setup of the CD detector including the dead layers and considers a finite beam spot size of 3 mm diameter. Furthermore, the analysis of the ^{72}Zn Coulex data has shown that not only the position signal is shifted over the time, but also the energy calibration is not time-stable and produces a shift of about 10 MeV (c.f. fig. B.6 a)). To correct this shift, the energy is scaled with a time-dependent correction factor (c.f. fig. B.6 b)). As a result, including all these small effects, a high accuracy for the energy calibration is gained, which is one important ingredient for a precise Doppler correction (c.f. sec. 4.4 and sec. 6.1.5).
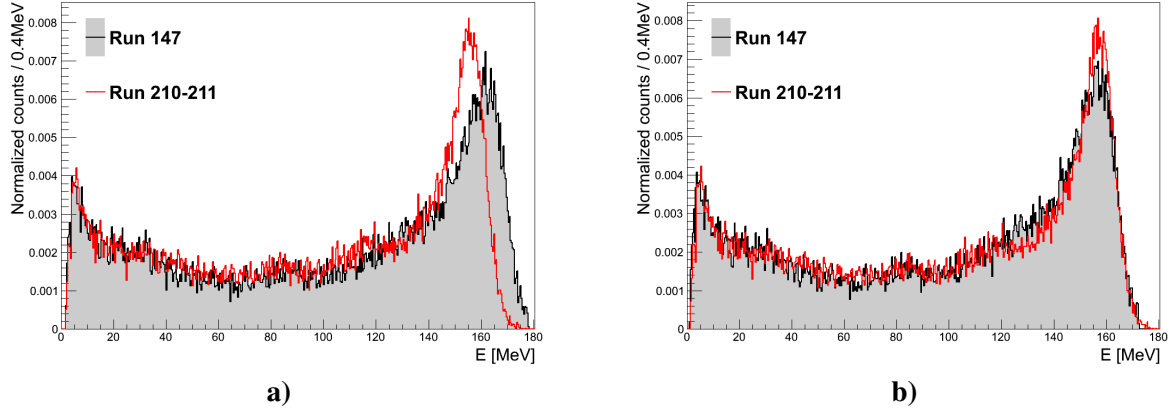
Fig. B.6: a) A comparison of a FCD strip spectrum after energy calibration between the first run 147 and the last two runs 210-211 of the Coulex experiment. Here, exactly the same calibration parameters have been used. The shift between the spectra indicates that the calibration is not stable in time. **b)** The same spectra, but corrected with a time-dependent calibration factor which cancels the relative shift of the two spectra.

B.4 CD Pad Detectors

The energy calibration of the CD pad detectors is done using a quadruple α-source. This is sufficient as the CD pad detector is only needed in the transfer experiments. Here, the deposited energy in the E_{rest} detector is in the same order of magnitude as the energy deposition of the α-particles. During the calibration run, the α-source is directly mounted behind the CD pad detector and not, like in the other α-calibration runs, at the target position.

C

Additional Information about the Transfer Experiments

C.1 Elastically Scattered Protons

Besides the elastically scattered tritons, which are mainly used to determine the luminosity of the experiment, also the elastically scattered protons contain important information. The elastic proton data is suitable to evaluate e.g. optical model parameterizations (c.f. sec. 2.1). This parameter set is mandatory for the description of transfer reactions which feature a proton in their exit channel (c.f. sec. 2.2.1).

Kinematics and Excitation Energies
The identification of protons is done with the ΔE-E telescope of the FBarrel detector. Additionally, to discriminate between transfer and elastic protons, a cut on the elastic reaction kinematics (c.f. fig. 5.2 a)) is mandatory. The kinematics of the identified elastic scattered protons, which are contained in the tritium target, is shown in fig. C.1 a).
After the particle identification, the excitation energy of the elastics protons can be calculated using the approach described in sec. 5.1.1. Its distributions is visualized in fig. C.1 b). As expected for elastic scattering data, the mean value coincidences with zero. A resolution of $\Delta E = (257 \pm 1)\,\mathrm{keV}$ (FWHM) is achieved. The proton excitation energy distribution is narrower compared to the distribution of the elastic tritons (c.f. fig. 5.4 b)), as the absolute energy resolution of the protons is, due to the lower deposited energies, better than the absolute energy resolution of the tritons. Furthermore, the identified protons cover a smaller θ_{lab} range. Hence, small deviations from the expected kinematic line (shown in black in fig. 5.4 and in fig. C.1) deteriorate the resolution of the excitation energy spectrum less for protons than for tritons.

Differential Cross Section
The differential cross section of the elastic scattered protons can be calculated by slicing its excitation energy spectrum into small scattering angle bins. According to eq. 5.2, the counts in the slices are subsequently divided by the solid angle $\Delta\Omega$ and the particle detection efficiency ϵ_{T-REX}. The latter is shown in fig. C.2 a). The obtained cross section for the elastically scattered protons is displayed in fig. C.2 b). In its calculation only the scattering angles which do not feature a large variation in their particle detection efficiency are considered. Thus, the influence of systematic errors is reduced. The drawback of this method is that the cross section covers only a small θ_{CM} range. Hence, in contrast the triton cross section (c.f. fig. 5.6), this limited range does not allow for performing a reliable fit of the optical model parameters. Nevertheless, the cross section can be compared to the calculated cross section with FRESCO using global optical model parameters. For the protons, the Perey-Perey parameterization is chosen [98]. Fig. C.2 b) indicates that the Perey-Perey parameters (c.f. tab. C.1) describes the experimental data well. Therefore, the Perey-Perey parameterization of the optical model is used in the calculation of the 1n and 2n transfer cross sections which feature protons in one of their channels.
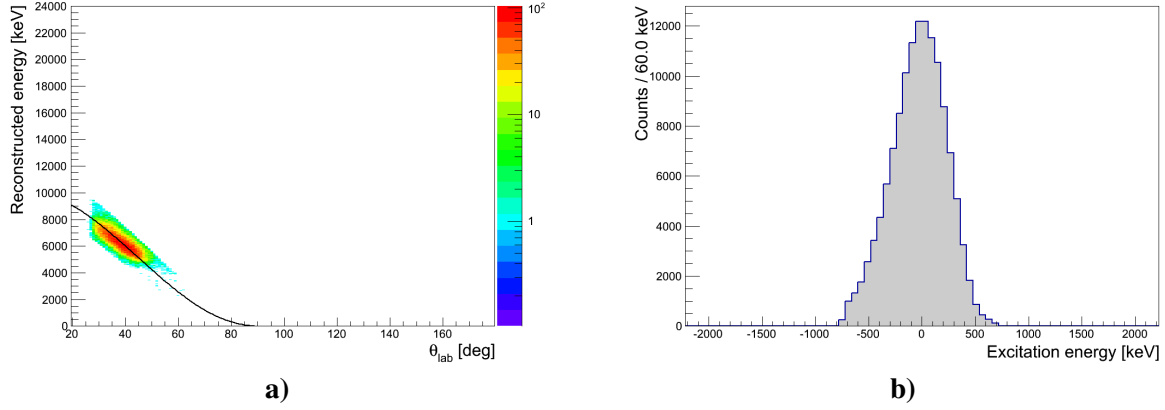
Fig. C.1: a) Reconstructed energy vs. θ_{lab} spectrum of all elastic protons which have been identified with the ΔE-E telescope of the FBarrel detector and the kinematic identification cut shown in fig. 5.2 a). The additional kinematic cut is necessary to discriminate the elastic scattered protons from the transfer protons. **b)** The excitation energy of the identified protons shown in fig. a). Due to the selection of the elastic scattering channel, the excitation energy is distributed around zero.
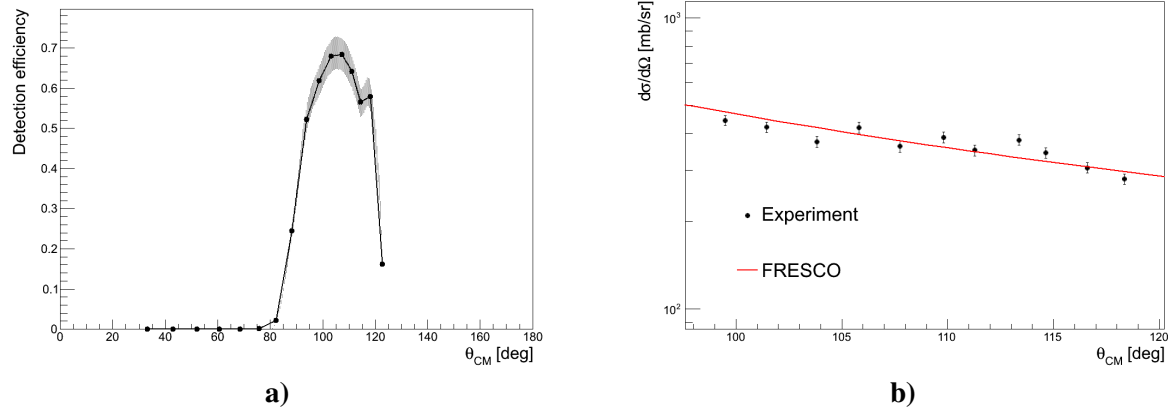
Fig. C.2: a) Detection efficiency of the FBarrel detector for identified elastic protons. The particle identification has been done with the ΔE-E telescope of the Barrel detector and with the kinematic splines shown in fig. 5.2 a). **b** Differential cross section of the elastic scattered protons. The experimental data points are compared to a FRESCO calculation using the global optical model parameterization of Perey-Perey [98]. The parameters are summarized in tab. C.1.

r_c [fm]	V [MeV]	r_0 [fm]	a_0 [fm]	W_D [MeV]	r_D [fm]	a_D [fm]
1.25	59.2	1.25	0.65	13.5	1.25	0.47

Tab. C.1: The global optical parameters for the p(^{72}Zn, p)^{72}Zn reaction at 2.7 MeV/u ^{72}Zn beam energy (i.e. 2.7 MeV proton energy in normal kinematics) from Perey-Perey [98]. In contrast to the triton optical model parameters, the proton parameterization features a surface absorption term instead of a volume absorption term. The potential formula of the optical model is given in eq. (2.2).

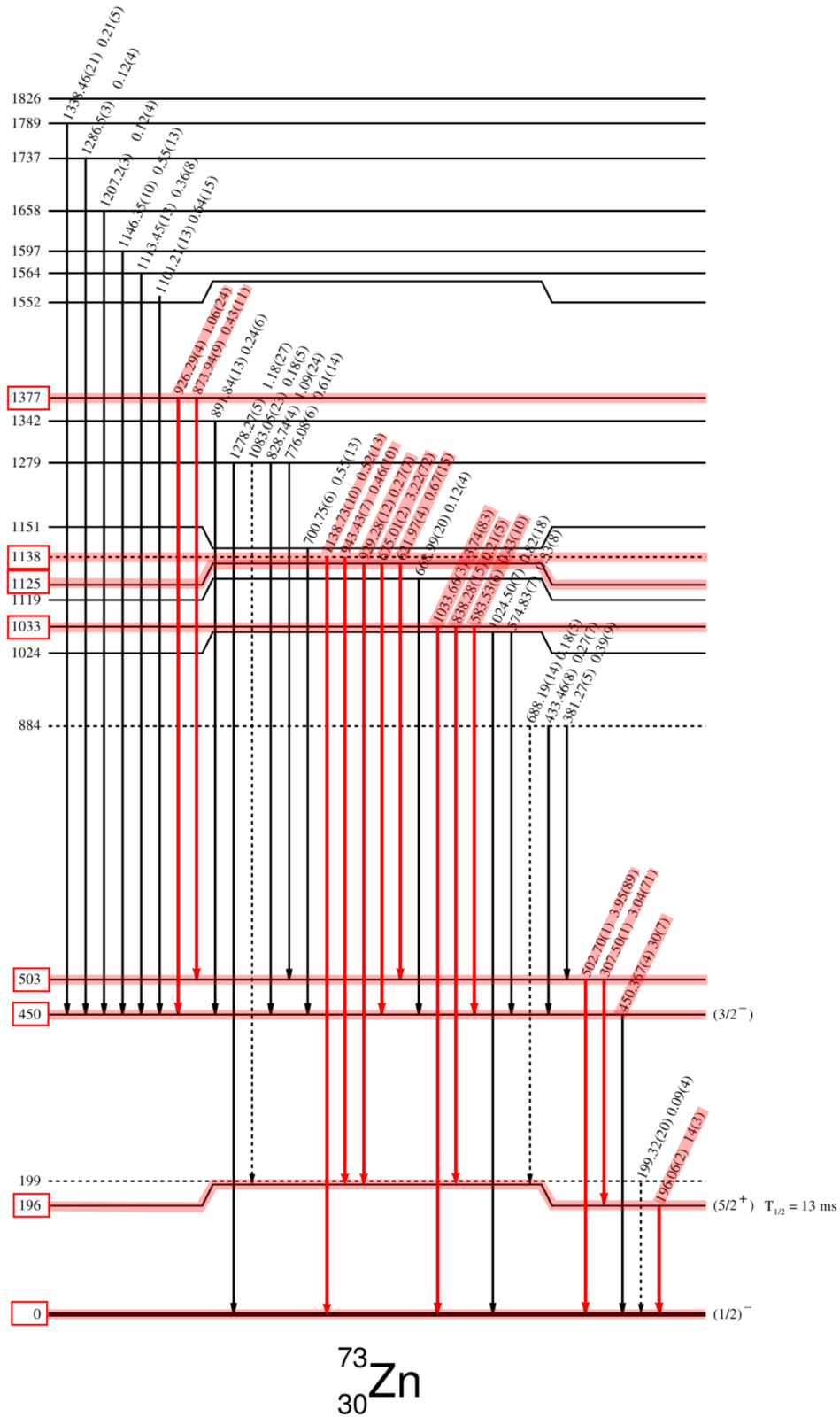## C.2 Previously Measured Level Scheme of ^{73}Zn

Fig. C.3: Level scheme of ^{73}Zn measured in a ^{73}Cu β-decay experiment which was performed at ISOLDE. The red marked levels and transitions are discussed in sec. 5.3.3. Adapted from [107].

C.3 Deuteron γ-ray γ-ray Coincidences in the t(^{72}Zn, d)^{73}Zn Channel

a) Cut on $E_\gamma = 450$ keV

b) Cut on $E_\gamma = 926$ keV

c) Cut on $E_\gamma = 943$ keV

d) Cut on $E_\gamma = 1033$ keV

e) Cut on $E_\gamma = 1382$ keV

f) Cut on $E_\gamma = 1683$ keV
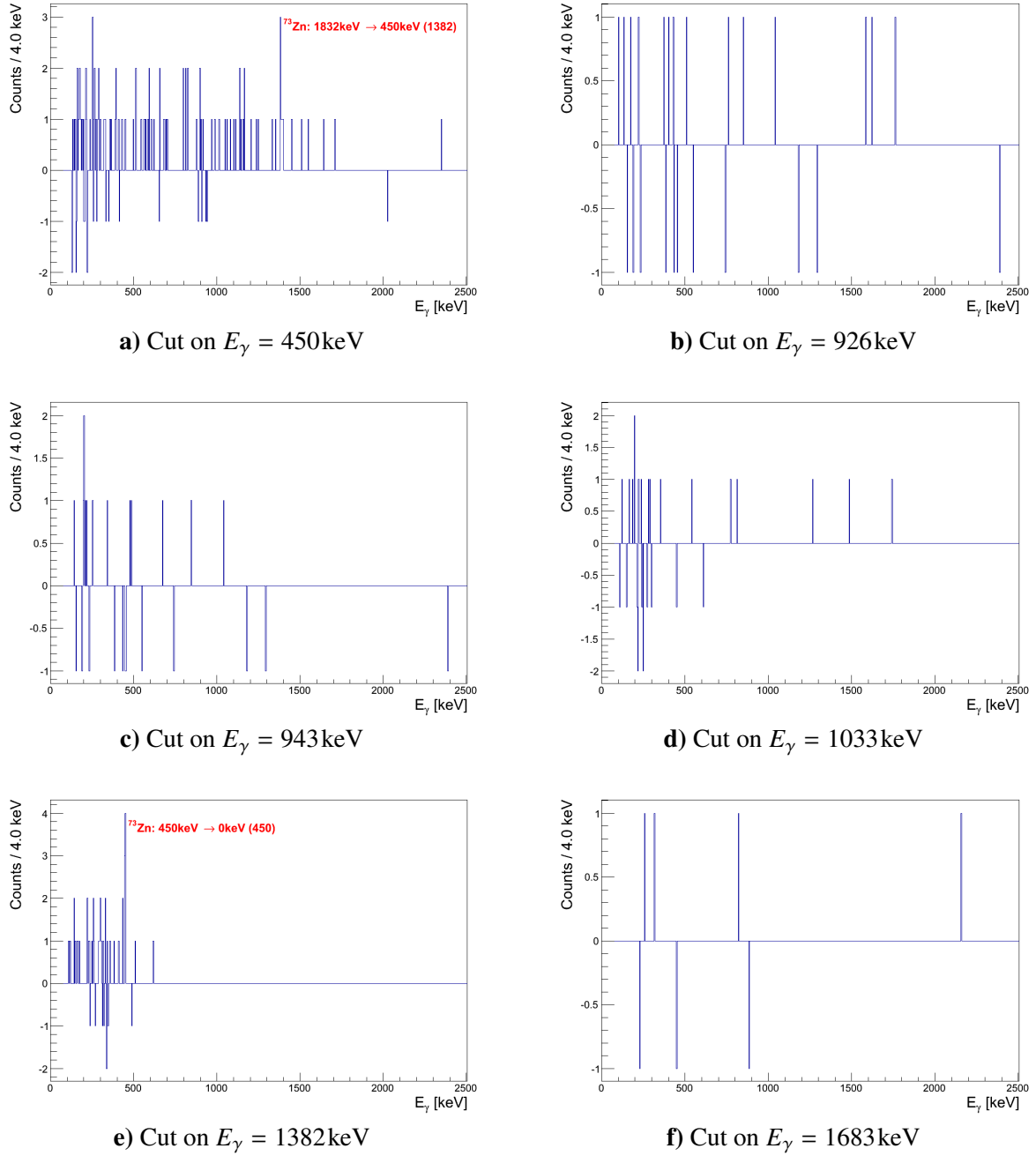
Fig. C.4: Doppler corrected γ-ray spectra of the t(^{72}Zn, d)^{73}Zn ($Q = -0.74$ MeV) reaction using different cuts on the most dominant γ-rays and gating on an identified transfer deuteron. The negative counts results from a background subtraction. For details, see sec. 5.3.3.

D

Additional Information about the Coulex Experiment

D.1 Precise Determination of the Beam Purity

Before the beam purity can be determined, a dedicated dead time analysis of the C-REX detectors is mandatory due to the high beam intensity (c.f. appendix D.1.1). Based on the results of this study, the beam composition is extracted in appendix D.1.2.

D.1.1 Dead Time Study of the Silicon Detectors

Due to the high intensity of the ^{72}Zn beam of $I = (3.5 \pm 0.3) \cdot 10^7$ pps, a significant amount of dead time cannot be excluded. The influence of the high count rate on the MINIBALL clusters has already been discussed in sec. 4.3.2. It has been shown that the MINIBALL detectors do not show any dead time effects. The dead time of the silicon detectors was monitored using events which should feature a simultaneous detection of the ejectile and the recoil (c.f. sec. 6.1.1): According to the reaction kinematics, for each event containing an identified ^{109}Ag ion in a FCD ring with ring number in [5, 15] there should be a detected ^{72}Zn ion, too. Fig. D.1 shows the fraction of the number of detected and identified ^{72}Zn ions (fulfilling the requirements given in sec. 6.1.1) from the number of all detected ^{109}Ag ions in a FCD ring with ring numbers equal or greater than five[1]. The fraction strongly depends on the beam intensity which is visualized with the red shaded area in fig. D.1 a). High particle count rates result in a drop of the detection efficiency for a simultaneous detection of both reaction products ^{72}Zn and ^{109}Ag. Hence, this effect shows the influence of the dead time of the FCD. At lower count rates, the detection efficiency is constant, but does not reach the ideal value 1. This results from the fact that the used identification cuts (c.f. sec. 6.1.1) are not 100% efficient. Additionally, the efficiency decreases due to the dead layers in the detector which are caused by the two-dimensional segmentation. Furthermore, due to the finite beam spot size, it is possible that one particle is detected at the edge of a FCD quadrant, while the second particle hits the PCB instead of the active area of the detector (c.f. fig. D.1 b)). This results in a further reduction of the mean detection efficiency. If the edges of the FCD quadrants and the areas featuring broken strips or rings are not included in the calculation, the efficiency increases significantly (c.f. fig. D.1 a)).
The obtained detection efficiency is an important ingredient for the determination of the beam composition (c.f. sec. 6.1.6).

D.1.2 Beam Purity

Along the production chain of the beam, different sources of beam contaminations can occur: First, isobaric contaminates such as ^{72}Ga can pass the HRS mass-separator at a significant amount due to their small mass difference to ^{72}Zn. Ga atoms are directly produced in the ISOLDE primary target with high intensity. Although the Ga atoms are not ionized with RILIS laser system, which is tuned to the ionization scheme of Zn, Ga can be surface ionized in the hot cavities of the transfer line and

---

[1] As all FCD rings in one quadrant belong to the same trigger group, the found dead time is representative for the whole quadrant, despite the event selection.
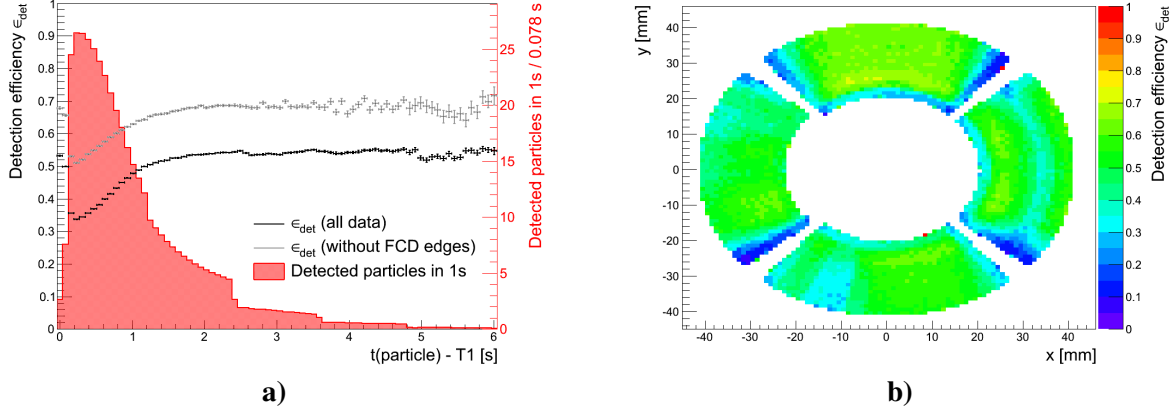
Fig. D.1: a) The detection efficiency ϵ_{det} for a simultaneous detection of a scattered ^{72}Zn ion and ^{109}Ag ion originating from the same reaction. It is shown as a function of the time difference between the particle detection and the last proton pulse on the primary ISOLDE target at $t = T1$. For comparison, the red shaded area displays the count rate in the FCD detector. Its time dependence is ideal to demonstrate the rate dependence of the detection efficiency due to the dead time of the FCD. The steps in the rate histogram appear as the proton pulses occur in multiples of $1.2\,$s. **b)** The detection efficiency of the FCD as a function of the x and y position of the detected ^{109}Ag ion. A deterioration of the efficiency is visible in the areas close to the detector edges as well as in areas corresponding to broken rings or strips.

the RILIS source, as the ionization potential of Ga is much lower compared to the ionization potential of Zn. Hence, both the ^{72}Zn beam and a small amount of ^{72}Ga ions are guided to the MINIBALL target position. Another source of beam contaminants is the buffer gas of the charge breeding system REXTRAP and REXEBIS. All buffer gas ions which have the same $A/Q = 3.6$ ratio as the ^{72}Zn^{20+} beam can pass the subsequent mass-separator and are finally accelerated in the REX-LINAC. This is the case for the gases ^{36}Ar^{10+} and ^{18}O^{5+}. Furthermore, it is possible that the beam undergoes β-decay during its production. This would result in an additional beam contaminant. However, this effect can be neglected here as the half-life of ^{72}Zn is $T_{1/2} = 46.5\,$hours [13] which is orders of magnitude higher than the time to deliver the beam from the primary target to the MINIBALL setup which is in the order of $10\,$ms. In summary, the ^{72}Zn REX-ISOLDE beam is composed of ^{72}Zn with a small admixture of ^{72}Ga, ^{36}Ar and ^{18}O.

Methods to Determine the Beam Composition

The beam composition can be determined with several methods. First, the different release time profiles of the elements from the primary target can be used to extract the amount of the isobaric contaminants (c.f. fig. 3.6). However, this methods was not successful here as the ^{72}Ga fraction in the beam is too small. Thus, the release curves of each isobar could not be fitted with the required precision. Another possibility to determine the beam content is the signal of the ionization chamber which is installed as beam dump behind the MINIBALL target (c.f. sec. 3.3). Nevertheless, due to the high ^{72}Zn beam intensity, it could not be used in this experiment to avoid damage to the ionization chamber. Finally, the beam composition can be determined from the comparison of laser On and laser Off runs which is detailed in the next paragraph.

Analysis of the Laser On and Laser Off Runs

A few hours of the beam time were dedicated to run in the laser Off mode, i.e. with the RILIS lasers being blocked (c.f. sec. 3.1.1). Thus, the beam in the laser Off mode does not feature any ^{72}Zn as the high ionization potential of Zn ensures that ^{72}Zn is not (surface) ionized. Hence, the ^{72}Zn stays inside the hot cavities of the ionization source. Contrary, the low ionization potential of Ga enables the ^{72}Ga to be surface ionized and thus being accelerated towards the MINIBALL target. Due to the
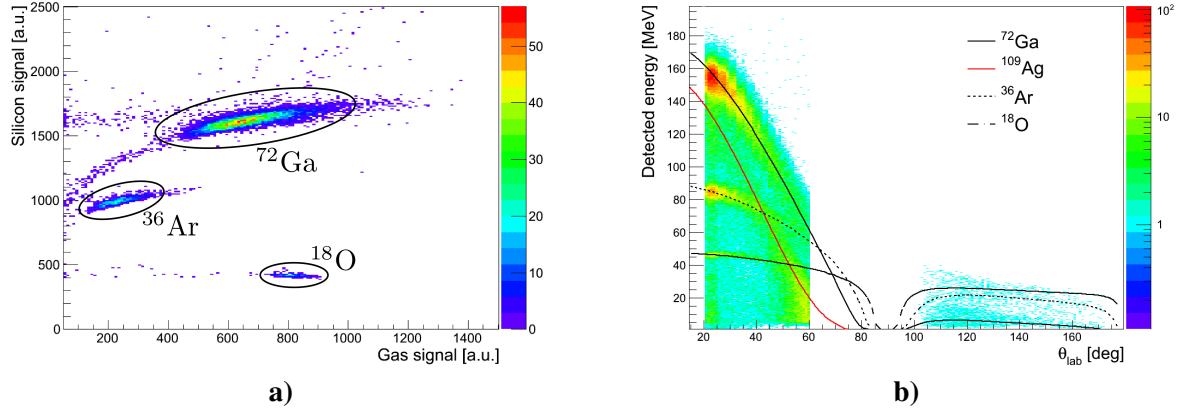
Fig. D.2: a) The ionization chamber spectrum of the laser Off runs which is used to determine the beam composition. Three beam contaminants could be identified: ^{72}Ga and the gases ^{36}Ar and ^{18}O originating from the charge-breeding system REXTRAP and REXEBIS. For details about the ionization chamber see sec. 3.3. **b)** The detected particle energy in the C-REX detectors as a function of the scattering angle θ_{lab} in the laboratory frame of all events from the laser Off runs. Additionally, the kinematic predictions for the ^{72}Ga, ^{36}Ar and ^{18}O beam contaminants are displayed. The red kinematic line of the ^{109}Ag target corresponds to the elastic scattering with the ^{72}Ga ions. As the mass of the ^{72}Zn and the ^{72}Ga ions is approximately identical, the kinematic lines of both ions coincide.

blocked ^{72}Zn beam, the beam intensity with laser Off was low enough to perform a measurement with the ionization chamber. Fig. D.2 a) shows its spectrum. The three peaks corresponds to ^{72}Ga as well as the contaminations ^{36}Ar and ^{18}O originating from the charger breeder. A cross check of the contribution of the gaseous contaminants can be done using their correct kinematic behavior of the elastic scattering on the ^{109}Ag target which is shown in fig. D.2 b). The number of counts in the peaks of the ionization chamber spectrum allows to determine the ratios of the gases ^{36}Ar and ^{18}O to ^{72}Ga:

$$\frac{I_{Ar}}{I_{Ga}} = (13.41 \pm 0.43)\% \quad \text{and} \quad \frac{I_O}{I_{Ga}} = (3.69 \pm 0.22)\% \tag{D.1}$$

The reminder of this paragraph is dedicated to the determination of the ratio of the ^{72}Ga and the ^{72}Zn ions in the beam. This is done by a direct comparison of the counts passing the ^{72}Zn identification cut of the FCD in the laser On and the laser Off runs, following [49]. The number of events fulfilling the identification condition is directly proportional to the beam intensity I_{Zn}, I_{Ga} of each isobar. For the laser On runs, the total number of counts $N_{det}^{ON}(tot)$ in the identification cut is the sum of the detected Zn ions $N_{det}^{ON}(Zn)$ and Ga ions $N_{det}^{ON}(Ga)$:

$$N_{det}^{ON}(tot) = N_{det}^{ON}(Zn) + N_{det}^{ON}(Ga) \quad \text{with} \quad N_{det}^{ON}(Zn) \propto I_{Zn} \cdot \sigma_{Zn} \cdot t_{ON}$$
$$\text{and} \quad N_{det}^{ON}(Ga) \propto I_{Ga} \cdot \sigma_{Ga} \cdot t_{ON}. \tag{D.2}$$

$\sigma_{Zn} = 74.68$ mbarn and $\sigma_{Ga} = 80.17$ mbarn are the cross sections for the scattering of the ^{72}Zn and the ^{72}Ga ions on the ^{109}Ag target integrated over the FCD range[2], respectively. t_{ON} is the measurement time in the laser On mode. In the laser Off runs the detected counts N_{det}^{OFF} is equal to the number $N_{det}^{OFF}(Ga)$ of scattered ^{72}Ga ions.

$$N_{det}^{OFF}(Ga) \propto I_{Ga} \cdot \sigma_{Ga} \cdot t_{OFF}. \tag{D.3}$$

Furthermore, it is assumed that the beam intensity I_{Ga} of the ^{72}Ga contaminant is the same in the laser On and in the laser Off runs:

$$N_{det}^{OFF}(Ga) = N_{det}^{ON}(Ga) \cdot \frac{t_{OFF}}{t_{ON}}. \tag{D.4}$$

---

[2]The calculation of the cross sections σ_{Zn} and σ_{Ga} has been done using the CLX/DCY code [69, 70].

Combining eq. (D.2), (D.3) and (D.4) the intensity ratio I_{Ga}/I_{Zn} in the laser On runs can be calculated:

$$\frac{I_{Ga}}{I_{Zn}} = \frac{N_{det}^{ON}(Ga)/\sigma_{Ga}}{N_{det}^{ON}(Zn)/\sigma_{Zn}} = \frac{N_{det}^{OFF}(Ga)}{N_{det}^{ON}(Zn)} \cdot \frac{t_{ON}}{t_{OFF}} \cdot \frac{\sigma_{Zn}}{\sigma_{Ga}} = \frac{1}{\frac{N_{det}^{ON}(tot)}{N_{det}^{OFF}(Ga)\cdot\frac{t_{ON}}{t_{OFF}}} - 1} \cdot \frac{\sigma_{Zn}}{\sigma_{Ga}}. \qquad (D.5)$$

However, before the ratio I_{Ga}/I_{Zn} can be evaluated, the dead time of the C-REX detectors has to be taken into account (c.f. sec. D.1.1). Due to the huge difference in beam intensity of the laser On and laser Off runs, the mean detection efficiencies $\epsilon_{det}^{ON,OFF}$ differ. In contrast to the laser On runs, the laser Off runs show no dead time losses in the detection efficiency. Thus, the ratio I_{Ga}/I_{Zn} reads

$$\frac{I_{Ga}}{I_{Zn}} = \frac{1}{\frac{N_{det}^{ON}(tot)/\epsilon_{det}^{ON}}{N_{det}^{OFF}(Ga)/\epsilon_{det}^{OFF}\cdot\frac{t_{ON}}{t_{OFF}}} - 1} \cdot \frac{\sigma_{Zn}}{\sigma_{Ga}}. \qquad (D.6)$$

The precision of the ratio I_{Ga}/I_{Zn} depends not only on the statistics in the identification cuts in the laser On and laser Off runs, but also on the validity of the assumption, that the beam composition is stable in time. Furthermore, it has to be assured that the proton beam intensity of the PS booster and the rate of proton pulses on the primary ISOLDE target is the same in the laser On and in the laser Off runs. Otherwise, the rate of the ^{72}Ga in the laser On and laser Off runs it not the same, i.e. the equality $N_{det}^{ON}(Ga) = N_{det}^{OFF}(OFF)\cdot\frac{t_{ON}}{t_{OFF}}$ which is used to derive eq. (D.6) does not hold. Hence, the ratio I_{Ga}/I_{Zn} is not calculated from all laser On runs, but only from the laser On runs which are close in time to the laser Off runs featuring the same proton current and the same proton PS booster supercycle. In this case, the resulting ratio is

$$\left(\frac{I_{Ga}}{I_{Zn}}\right)_{\text{Laser ON, OFF}} = (8.42 \pm 0.07)\%. \qquad (D.7)$$

To monitor the variation of the beam composition during the whole ^{72}Zn Coulex experiment, the ratio $R_\gamma = N_\gamma(^{72}Ga)/N_\gamma(^{72}Zn)$ of the counts in the strongest ^{72}Ga and the strongest ^{72}Zn γ-ray lines in the Doppler corrected γ-ray spectrum can be used, as the number of counts in the γ-ray peaks is directly proportional to the intensity of the corresponding beam component[3]. The resulting ratios are

$$R_\gamma^{\text{Laser ON,OFF}} = 0.103 \pm 0.008 \quad \text{and} \quad R_\gamma^{\text{all runs}} = 0.091 \pm 0.002. \qquad (D.8)$$

Hence, the mean ratio $(I_{Ga}/I_{Zn})_{\text{all runs}}$ over the whole Coulex experiment is given by

$$\left(\frac{I_{Ga}}{I_{Zn}}\right)_{\text{all runs}} = \left(\frac{I_{Ga}}{I_{Zn}}\right)_{\text{Laser ON, OFF}} \cdot \frac{R_\gamma^{\text{all runs}}}{R_\gamma^{\text{Laser ON,OFF}}} = (7.51 \pm 0.60)\%. \qquad (D.9)$$

The total beam composition, including the EBIS buffer gases, is summarized in tab. 6.1.

D.2   Available Spectroscopic Data of ^{109}Ag

In the following tables the available spectroscopic data of ^{109}Ag is summarized. The relative signs of the transition matrix elements is defined by the multipole mixing ratios δ.

---

[3]The ^{72}Ga peak at $E_\gamma = 165\,\text{keV}$ was not fitted with the background model (step function + straight line) of eq. (D.10). Instead the background left and right of the peak was fitted with two linear functions with different slopes and offsets. The background in the peak region was assumed to be a cubic interpolation of the two linear background functions.

Method	State	τ [ps]	Reference
RDDS	$3/2_1^-$ at 311 keV	8.5 ± 1.0	[145]
		9.1 ± 2.6	[124]
RDDS	$5/2_1^-$ at 415 keV	50 ± 3	[145]
		47.0 ± 2.3	[146]
		58 ± 4	[124]
RDDS	$3/2_2^-$ at 702 keV	0.7 ± 0.3	[124]
RDDS	$5/2_2^-$ at 863 keV	1.9 ± 0.6	[124]
RDDS	$3/2_3^-$ at 1324 keV	0.5 ± 0.1	[124]

Tab. D.1: Previously measured lifetimes of ^{109}Ag. The valued were obtained by applying the Recoil Distance Doppler Shift method (RDDS). The lifetimes measured by [145], [146] and the lifetime of the $3/2_3^-$ state are included in the ^{109}Ag GOSIA analysis of this thesis.

Method	P_2	P_1	$BR = P_2/P_1$	Reference
Coulex	$5/2_1^- \to 3/2_1^-$	$5/2_1^- \to 1/2_1^-$	0.069 ± 0.016	[125]
			0.049 ± 0.005	[124]
β-decay	$3/2_2^- \to 3/2_1^-$	$3/2_2^- \to 1/2_1^-$	0.30 ± 0.07	[147]
Coulex			0.20 ± 0.04	[124]
β-decay	$3/2_2^- \to 5/2_1^-$	$3/2_2^- \to 1/2_1^-$	0.05 ± 0.01	[147]
Coulex			0.05 ± 0.05	[124]
β-decay	$5/2_2^- \to 3/2_1^-$	$5/2_2^- \to 1/2_1^-$	4.6 ± 1.6	[147]
Coulex			4.6 ± 0.6	[124]
β-decay	$5/2_2^- \to 5/2_1^-$	$5/2_2^- \to 1/2_1^-$	6.3 ± 2.2	[147]
Coulex			5.6 ± 0.7	[124]
Coulex	$7/2_1^- \to 5/2_1^-$	$7/2_1^- \to 3/2_1^-$	4.0 ± 0.6	[124]
Coulex	$3/2_3^- \to 3/2_1^-$	$3/2_3^- \to 1/2_1^-$	6 ± 1	[124]
Coulex	$3/2_3^- \to 5/2_1^-$	$3/2_3^- \to 1/2_1^-$	0.5 ± 0.3	[124]

Tab. D.2: Previously measured branching ratios of ^{109}Ag. In the ^{109}Ag GOSIA of this thesis, all given branching ratios are included in the fit.

Method	Transition	δ	Reference
β-decay	$3/2_1^- \to 1/2_1^-$	0.193 ± 0.010	[148]
Coulex		0.196 ± 0.027	[124]
Coulex	$5/2_1^- \to 3/2_1^-$	0.039 ± 0.017	[124]
Coulex	$3/2_2^- \to 1/2_1^-$	0.029 ± 0.007	[124]
Coulex	$3/2_2^- \to 3/2_1^-$	0.241 ± 0.016	[149]
Coulex	$5/2_2^- \to 3/2_1^-$	0.28 ± 0.04	[124]
Coulex	$5/2_2^- \to 5/2_1^-$	0.16 ± 0.04	[124]
Coulex	$3/2_3^- \to 3/2_1^-$	0.09 ± 0.03	[124]

Tab. D.3: Previously measured multipole mixing ratios δ of ^{109}Ag. In the Coulex analysis the multipole mixing ratio have been determined from the angular distributions. In the ^{109}Ag GOSIA, performed in this thesis, all given multipole mixing ratios are included in the fit.

Method	Transition	$E2$-Matrix element [eb]	Reference
Coulex	$1/2_1^- \rightarrow 3/2_1^-$	$\pm 0.648 \pm 0.025$	[125]
		$\pm 0.666 \pm 0.029$	[124]
Plunger		$\pm 0.672 \pm 0.010$	[122]
Coulex	$1/2_1^- \rightarrow 5/2_1^-$	$\pm 0.80 \pm 0.04$	[125]
		$\pm 0.801 \pm 0.032$	[124]
Plunger		$\pm 0.843 \pm 0.043$	[122]
Coulex	$1/2_1^- \rightarrow 3/2_2^-$	$\pm 0.0415 \pm 0.0046$	[124]
		$-0.098 \, ^{+0.006}_{-0.015}$	[123]
Coulex	$3/2_1^- \rightarrow 5/2_1^-$	$\pm 0.155 \pm 0.087$	[124]
Plunger		$\pm 0.304 \pm 0.020$	[122]
Coulex	$3/2_1^- \rightarrow 3/2_2^-$	$0.27 \, ^{+0.04}_{-0.03}$	[123]
Coulex	$5/2_1^- \rightarrow 3/2_2^-$	-0.17 ± 0.08	[123]
Coulex	$1/2_1^- \rightarrow 5/2_2^-$	$\pm 0.1866 \pm 0.0091$	[124]
		$0.175 \, ^{+0.005}_{-0.015}$	[123]
Coulex	$3/2_1^- \rightarrow 5/2_2^-$	$\pm 0.23 \pm 0.04$	[124]
		0.36 ± 0.09	[123]
Coulex	$3/2_1^- \rightarrow 7/2_1^-$	$1.16 \, ^{+0.09}_{-0.10}$	[123]
Coulex	$5/2_1^- \rightarrow 5/2_2^-$	$\pm 0.363 \pm 0.091$	[124]
		$-0.38 \, ^{+0.16}_{-0.17}$	[123]
Coulex	$5/2_1^- \rightarrow 9/2_1^-$	$1.64 \, ^{+0.05}_{-0.07}$	[123]
Coulex	$1/2_1^- \rightarrow (3/2)_3^-$	$\pm 0.156 \pm 0.012$	[124]
Coulex	$3/2_1^- \rightarrow (3/2)_3^-$	$\pm 0.05 \pm 0.02$	[124]

Tab. D.4: Previously measured $E2$ matrix elements of ^{109}Ag. The ^{109}Ag GOSIA analysis used only the measured lifetimes of the transitions $1/2_1^- \rightarrow 3/2_1^-$ and $1/2_1^- \rightarrow 5/2_1^-$ as additional data points for the fit. In contrast to the other matrix elements, these lifetimes measurements are independent of the quadrupole moment.

D.3   Division of the Coulex Data Set into Angular Ranges

The whole Coulex data set is divided into several angular ranges. This has the advantage that transitional matrix elements and diagonal matrix elements can be determined with a higher precision as the Coulex cross section feature a strong dependence on the scattering angle θ_{CM}: One step processes dominate at low scattering angles where the interaction time between the beam and the target nucleus is smallest. Contrary, two step processes such as the quadrupole moment or the excitation of higher lying states in multiple steps have a higher cross section at large θ_{CM}. Tab. D.7 shows the division of the γ-ray counts into several θ_{CM} ranges of the particle detectors which are used in the Coulex analysis in chap. 6. Dependent on the statistics in the γ-ray peak a broader or a finer subdivision in the FCD detector is used.

D.4   Doppler Corrected γ-ray Spectra if ^{109}Ag is Detected in C-REX

In sec. 6.1.5 the Doppler corrected γ-ray spectra for the case that the scattered ^{72}Zn ions are detected in C-REX are shown. Additionally, in fig. D.3 show the Doppler corrected γ-ray spectra if the scattered ^{109}Ag particles are identified in the FCD of C-REX. For a detailed discussion of the spectra see sec. 6.1.5.

Method	Transition	$M1$-Matrix element [μb]	Reference
Coulex	$1/2_1^- \rightarrow 3/2_1^-$	$\pm 0.63 \pm 0.09$	[124]
		$0.92\,^{+0.11}_{-0.08}$	[123]
Plunger		$\pm 0.871 \pm 0.013$	[122]
Coulex	$1/2_1^- \rightarrow 3/2_2^-$	$\pm 0.60\,^{+0.20}_{-0.08}$	[124]
		$-0.74\,^{+0.11}_{-0.18}$	[123]
Coulex	$3/2_1^- \rightarrow 5/2_1^-$	$\pm 0.29 \pm 0.03$	[124]
Plunger		$\pm 0.656 \pm 0.040$	[122]
Coulex	$3/2_1^- \rightarrow 3/2_2^-$	$\pm 0.89\,^{+0.31}_{-0.16}$	[124]
		$0.37\,^{+0.06}_{-0.04}$	[123]
Coulex	$5/2_1^- \rightarrow 3/2_2^-$	$\pm 0.92 \pm 0.46$	[124]
		$-1.4\,^{+0.3}_{-0.4}$	[123]
Coulex	$3/2_1^- \rightarrow 5/2_2^-$	$\pm 0.44 \pm 0.04$	[124]
		0.60 ± 0.04	[123]
Coulex	$5/2_1^- \rightarrow 5/2_2^-$	$\pm 0.85 \pm 0.07$	[124]
		-0.91 ± 0.07	[123]
Coulex	$1/2_1^- \rightarrow (3/2)_3^-$	< 0.7	[124]
Coulex	$3/2_1^- \rightarrow (3/2)_3^-$	$\pm 0.63 \pm 0.09$	[124]

Tab. D.5: Previously measured $M1$ matrix elements of ^{109}Ag.

Method	State	$E2$-Diagonal matrix element [μb]	Reference
Coulex	$3/2_1^-$	-0.8 ± 0.1	[126]
		-1.3 ± 0.1	[126][4]
		-1.3 ± 0.35	[123]
Coulex	$5/2_1^-$	-0.21 ± 0.17	[126]
		-0.56 ± 0.17	[126][5]

Tab. D.6: Previously measured $E2$ diagonal matrix elements of ^{109}Ag.

Data set	Description	θ_{lab} range	θ_{CM} range
1	^{72}Zn detected in FCD ring 1-3	$25.08° - 35.88°$	$41.37° - 58.69°$
2	^{72}Zn detected in FCD ring 4-6	$35.88° - 44.38°$	$58.69° - 71.94°$
3	^{72}Zn detected in FCD ring 7-9	$44.38° - 50.98°$	$71.94° - 81.89°$
4	^{72}Zn detected in FCD ring 10-12	$50.98° - 56.12°$	$81.89° - 89.41°$
5	^{72}Zn detected in FCD ring 13-15	$56.12° - 60.18°$	$89.41° - 95.18°$
6	^{109}Ag detected in FCD ring 1-3	$25.08° - 35.88°$	$108.21° - 129.81°$
7	^{109}Ag detected in FCD ring 4-6	$35.88° - 44.38°$	$91.21° - 108.21°$
8	^{109}Ag detected in FCD ring 7-9	$44.38° - 50.98°$	$78.01° - 91.21°$
9	^{109}Ag detected in FCD ring 10-12	$50.98° - 56.12°$	$67.73° - 78.01°$
10	^{109}Ag detected in FCD ring 13-15	$56.12° - 60.18°$	$59.62° - 67.73°$
11	^{72}Zn detected in FCD	$25.08° - 60.18°$	$41.37° - 95.18°$
12	^{109}Ag detected in FCD	$25.08° - 60.18°$	$59.62° - 129.81°$
13	^{72}Zn detected in BBarrel	$104.0° - 151.4°$	$143.88° - 169.84°$
14	^{72}Zn detected in BCD	$153.3° - 172.0°$	$170.57° - 176.66°$

Tab. D.7: The angular ranges which are used to divide the whole Coulex data set into several small subsets.
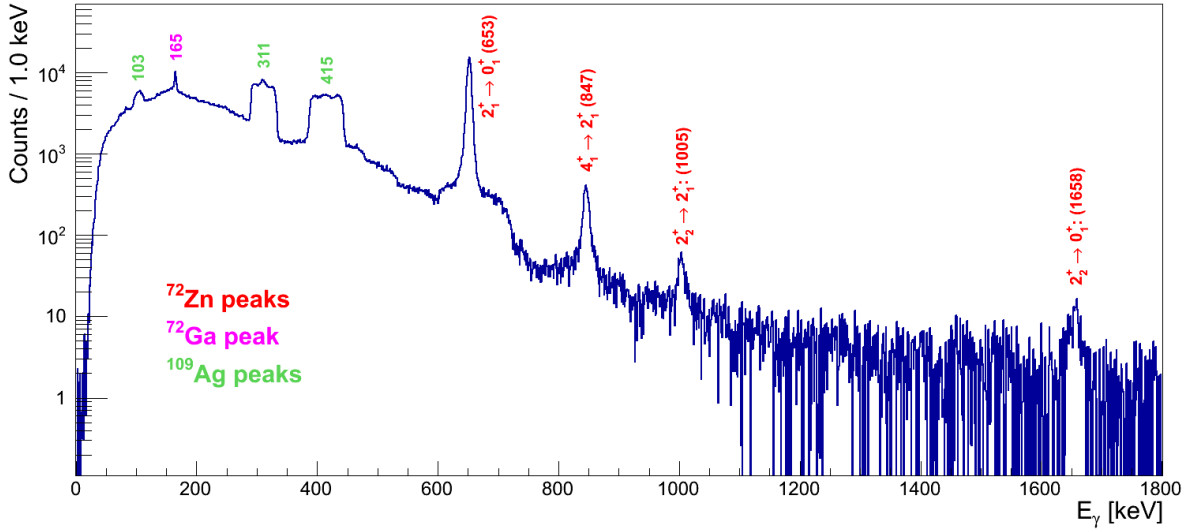
a) Forward CD
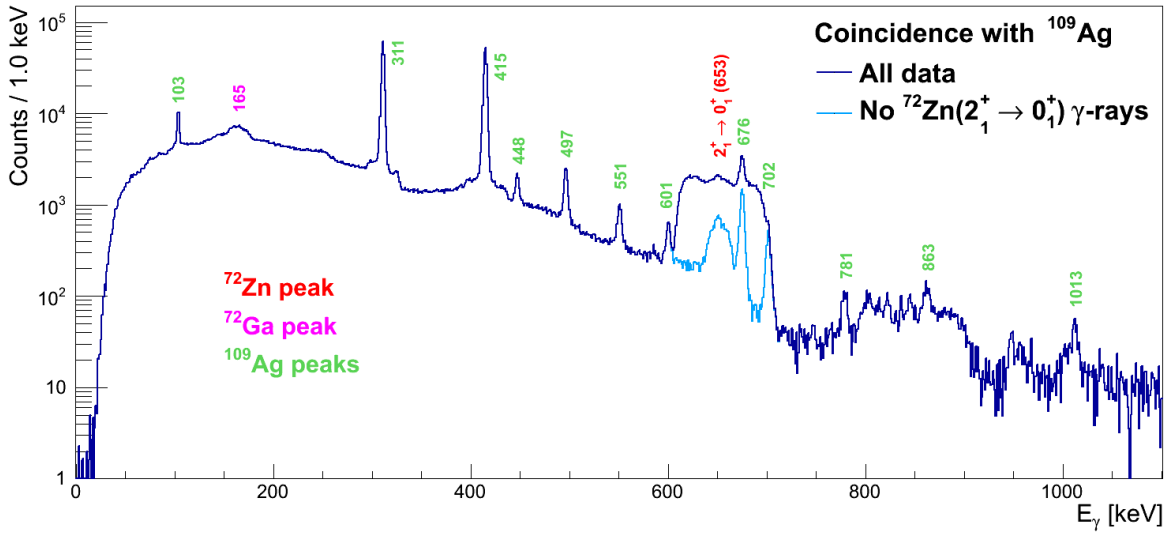
b) Forward CD

Fig. D.3: Doppler corrected γ-ray spectra for the case that the recoil ^{109}Ag is detected in the FCD. The Doppler correction has been done with respect to ^{72}Zn in a) and with respect to ^{109}Ag in b). These spectra show the same peaks as in fig. 6.8 a) and fig. 6.10 a).

D.5   Determination of the Counts in the γ-ray Peaks and the Calculation of Upper Limits of Unobserved Peaks

Determination of the Counts in the γ-ray Peaks

The counts in the γ-ray peaks are directly connected to the Coulex cross section and, therefore, to the matrix elements containing the nuclear structure information. Thus, a precise determination of the counts in the γ-ray peaks is essential. The high number of events in the peaks allows to test different models for the peak and the background shape. Due to the charge collection processes and the electronics of HPGe detectors like MINIBALL as well as due to the Doppler correction, small deviations of the peak shapes from a normal distribution have been found. Hence, in this analysis, the counts in the peak are determined by fitting a Gaussian and a background function. Instead, to take all effects which can change the peak shape into account, only the background was fitted and the counts
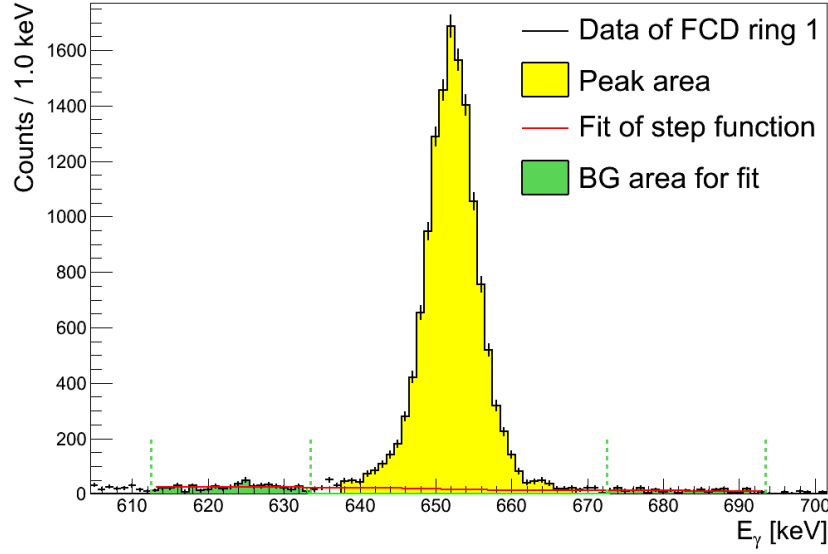
Fig. D.4: The Doppler corrected γ-ray peaks are fitted with a step function as background. The green area left and right of the peak defines the fit region for the background model. The counts in the peak corresponds to the integral of the yellow histogram minus the integrated counts of the background function in the yellow peak region.

in the peak have been assigned by integrating the counts in the spectrum over a defined peak area. The background in the peak area is subtracted by integrating the background function over the peak area. The experience has shown, that a step function which is is superimposed with a polynomial function of order one as a background model, gives the best results:

$$f_{BG}(E) = \underbrace{a_0 + a_1 \cdot E}_{\text{linear function}} + \underbrace{\frac{h}{\left(1 + \exp\left(\frac{E - E_\gamma^{rest}}{\sigma}\right)\right)^2}}_{\text{step function}} , \tag{D.10}$$

with E_γ^{rest} being the energy of the transition in the rest-mass frame, σ the standard deviation of an approximated Gaussian of the peak and h the height of the step function. a_0 and a_1 corresponds to the offset and the slope of the linear function. The parameters a_0, a_1 and h of the background function f_{BG} are fixed by a fit combined fit of two background regions left and right of the peak[6]. The parameter σ corresponds to the obtained standard deviation of a Gaussian fit to the peak[7]. An example of a fitted peak is shown in fig. D.4. The error of the counts in the γ-ray peak is given by the statistical error of the counts in the peak area and the fit error of the background function.

Determination of Upper Limits of Unobserved γ-ray Transitions

In the Coulex analysis which is detailed in sec. 6.2, it is sometimes essential to include γ-ray transitions which are too weak to feature a significant signal in the experimental. This is e.g. the case for the 0_2^+ state which is only visible in the BBarrel, but not in the FCD. Hence, including an upper limit for its counts in the FCD can impose an additional constrain on the $\mathcal{M}(2_1^+ \rightarrow 0_2^+)$ matrix element. Therefore, this paragraph deals with the determination of the maximal possible counts, i.e. the upper limit in an unobserved transition. It follows the idea of [150]: The probability density function of an

---

[6]In case of low statistics in the peak, the height h of the background model f_{BG} is fixed to zero, i.e. the background is approximated by a linear function.

[7]This approximation is sufficient as its value does not change the area under the background function due to the symmetry of the setp function.

unobserved peak with area a is given by[8]

$$g(a) = \mathcal{N}\frac{\exp[-(a - \overline{a})^2/(2\sigma^2)]}{\sqrt{2\pi}\sigma}, \tag{D.11}$$

with $\mathcal{N}$ being a normalization constant, $\overline{a}$ is the estimate of the peak area and σ its error. They are given by the counts C in the peak area and the counts B in the background area

$$\overline{a} = C - B \quad \text{and} \quad \sigma^2 = \sqrt{B}^2 + \sqrt{C}^2. \tag{D.12}$$

The number of background counts B is estimated from two regions positioned symmetrically around the peak area. Subsequently, the upper limit A at a confidence level $C.L.$ is defined by the probability that the peak area a is smaller than A

$$C.L. = 1 - \int_A^\infty g(a)\, da. \tag{D.13}$$

This equation can be solved using the error function. For the upper limits A which are used in this thesis (c.f. appendix D.3), a confidence level of 2σ, i.e. of 95.45% is applied.

D.6   Tables of Measured γ-ray Yields and Upper Limits

The measured γ-ray yields of ^{72}Zn and ^{109}Ag in each subdivision are given in tab. D.8 and tab. D.9, respectively. Tab. D.10 summarized the upper limits of the unobserved γ-ray transitions which have been considered in the analysis.

Data set	Description	Transition	E_γ [keV]	Counts
1	^{72}Zn detected in FCD ring 1-3	$2_1^+ \rightarrow 0_1^+$	652.7	38833 ± 342
		$4_1^+ \rightarrow 2_1^+$	846.8	265 ± 22
		$2_2^+ \rightarrow 2_1^+$	1004.7	53 ± 10
2	^{72}Zn detected in FCD ring 4-6	$2_1^+ \rightarrow 0_1^+$	652.7	31432 ± 283
		$4_1^+ \rightarrow 2_1^+$	846.8	458 ± 24
		$2_2^+ \rightarrow 2_1^+$	1004.7	63 ± 10
3	^{72}Zn detected in FCD ring 7-9	$2_1^+ \rightarrow 0_1^+$	652.7	23185 ± 227
		$4_1^+ \rightarrow 2_1^+$	846.8	566 ± 27
		$2_2^+ \rightarrow 2_1^+$	1004.7	68 ± 10
4	^{72}Zn detected in FCD ring 10-12	$2_1^+ \rightarrow 0_1^+$	652.7	16560 ± 177
		$4_1^+ \rightarrow 2_1^+$	846.8	498 ± 25
		$2_2^+ \rightarrow 2_1^+$	1004.7	86 ± 11
5	^{72}Zn detected in FCD ring 13-15	$2_1^+ \rightarrow 0_1^+$	652.7	11370 ± 143
		$4_1^+ \rightarrow 2_1^+$	846.8	328 ± 20
		$2_2^+ \rightarrow 2_1^+$	1004.7	50 ± 9
6	^{109}Ag detected in FCD ring 1-3	$2_1^+ \rightarrow 0_1^+$	652.7	21694 ± 222
		$4_1^+ \rightarrow 2_1^+$	846.8	993 ± 45
		$2_2^+ \rightarrow 2_1^+$	1004.7	158 ± 17

Continued on next page . . .

[8]The Gaussian approximation is only valid if the counts in the peak area is large, i.e. $C > 0$. This is the case for all unobserved Coulex transitions which are discussed in this thesis. In the transfer experiments the upper limits are determined using the Feldman-Cousins method due to the low statistics [114].

Data set	Description	Transition	E_γ [keV]	Counts
7	^{109}Ag detected in FCD ring 4-6	$2^+_1 \to 0^+_1$	652.7	28072 ± 263
		$4^+_1 \to 2^+_1$	846.8	1055 ± 39
		$2^+_2 \to 2^+_1$	1004.7	145 ± 15
8	^{109}Ag detected in FCD ring 7-9	$2^+_1 \to 0^+_1$	652.7	32130 ± 295
		$4^+_1 \to 2^+_1$	846.8	960 ± 37
		$2^+_2 \to 2^+_1$	1004.7	145 ± 15
9	^{109}Ag detected in FCD ring 10-12	$2^+_1 \to 0^+_1$	652.7	29925 ± 278
		$4^+_1 \to 2^+_1$	846.8	677 ± 31
		$2^+_2 \to 2^+_1$	1004.7	80 ± 12
10	^{109}Ag detected in FCD ring 13-15	$2^+_1 \to 0^+_1$	652.7	21316 ± 214
		$4^+_1 \to 2^+_1$	846.8	291 ± 21
		$2^+_2 \to 2^+_1$	1004.7	34 ± 9
11	^{72}Zn detected in FCD	$2^+_1 \to 0^+_1$	652.7	11946 ± 918
		$4^+_1 \to 2^+_1$	846.8	2094 ± 55
		$2^+_2 \to 2^+_1$	1004.7	320 ± 28
		$2^+_2 \to 0^+_1$	1657.6	134 ± 14
12	^{109}Ag detected in FCD	$2^+_1 \to 0^+_1$	652.7	132041 ± 1020
		$4^+_1 \to 2^+_1$	846.8	4405 ± 83
		$2^+_2 \to 2^+_1$	1004.7	568 ± 36
		$2^+_2 \to 0^+_1$	1657.6	220 ± 17
13	^{72}Zn detected in BBarrel	$2^+_1 \to 0^+_1$	652.7	4889 ± 81
		$4^+_1 \to 2^+_1$	846.8	240 ± 17
		$2^+_2 \to 2^+_1$	1004.7	66 ± 10
		$2^+_2 \to 0^+_1$	1657.6	30 ± 6
		$0^+_2 \to 2^+_1$	858.3	38 ± 8
14	^{72}Zn detected in BCD	$2^+_1 \to 0^+_1$	652.7	371 ± 20
		$4^+_1 \to 2^+_1$	846.8	21 ± 5

Tab. D.8: The measured yield in the ^{72}Zn γ-ray peaks of the Coulex experiment. The yields are not corrected for the MINIBALL efficiency, but the efficiency error is included in the error of the counts.

Data set	Description	Transition	E_γ [keV]	Counts	Corrected counts
1	^{72}Zn detected in FCD ring 1-3	$3/2^-_1 \to 1/2^-_1$	311	61463 ± 422	57021 ± 504
		$5/2^-_1 \to 1/2^-_1$	415	60300 ± 382	55980 ± 470
		$5/2^-_1 \to 3/2^-_1$	103	5139 ± 130	4770 ± 124
		$5/2^-_2 \to 5/2^-_1$	448	829 ± 68	773 ± 64
		$7/2^-_1 \to 5/2^-_1$	497	644 ± 54	603 ± 51
		$5/2^-_2 \to 3/2^-_1$	551	517 ± 49	482 ± 46
		$7/2^-_1 \to 3/2^-_1$	601	127 ± 39	119 ± 36
		$9/2^-_1 \to 5/2^-_1$	676	432 ± 35	405 ± 33
		$3/2^-_2 \to 1/2^-_1$	702	164 ± 18	153 ± 17

Data set	Description	Transition	E_γ [keV]	Counts	Corrected counts
2	^{72}Zn detected	$3/2_1^- \to 1/2_1^-$	311	47478 ± 340	44017 ± 400
	in FCD ring 4-6	$5/2_1^- \to 1/2_1^-$	415	46896 ± 305	43504 ± 372
		$5/2_1^- \to 3/2_1^-$	103	$3846 \pm, 108$	3567 ± 102
		$5/2_2^- \to 5/2_1^-$	448	804 ± 61	749 ± 57
		$7/2_1^- \to 5/2_1^-$	497	993 ± 53	929 ± 50
		$5/2_2^- \to 3/2_1^-$	551	618 ± 44	575 ± 41
		$7/2_1^- \to 3/2_1^-$	601	165 ± 34	155 ± 32
		$9/2_1^- \to 5/2_1^-$	676	871 ± 38	816 ± 35
		$3/2_2^- \to 1/2_1^-$	702	237 ± 18	220 ± 17
3	^{72}Zn detected	$3/2_1^- \to 1/2_1^-$	311	34669 ± 272	32120 ± 310
	in FCD ring 7-9	$5/2_1^- \to 1/2_1^-$	415	34150 ± 249	31657 ± 290
		$5/2_1^- \to 3/2_1^-$	103	2987 ± 97	2769 ± 91
		$5/2_2^- \to 5/2_1^-$	448	754 ± 57	702 ± 53
		$7/2_1^- \to 5/2_1^-$	497	1055 ± 51	987 ± 48
		$5/2_2^- \to 3/2_1^-$	551	496 ± 42	461 ± 39
		$7/2_1^- \to 3/2_1^-$	601	305 ± 34	285 ± 32
		$9/2_1^- \to 5/2_1^-$	676	985 ± 38	923 ± 36
		$3/2_2^- \to 1/2_1^-$	702	295 ± 22	274 ± 20
4	^{72}Zn detected	$3/2_1^- \to 1/2_1^-$	311	25063 ± 218	23204 ± 240
	in FCD ring 10-12	$5/2_1^- \to 1/2_1^-$	415	24358 ± 202	22566 ± 226
		$5/2_1^- \to 3/2_1^-$	103	2052 ± 80	1901 ± 75
		$5/2_2^- \to 5/2_1^-$	448	564 ± 48	525 ± 44
		$7/2_1^- \to 5/2_1^-$	497	1009 ± 47	944 ± 44
		$5/2_2^- \to 3/2_1^-$	551	353 ± 37	328 ± 34
		$7/2_1^- \to 3/2_1^-$	601	272 ± 30	254 ± 28
		$9/2_1^- \to 5/2_1^-$	676	897 ± 36	840 ± 34
		$3/2_2^- \to 1/2_1^-$	702	270 ± 20	251 ± 18
5	^{72}Zn detected	$3/2_1^- \to 1/2_1^-$	311	17299 ± 168	16008 ± 180
	in FCD ring 13-15	$5/2_1^- \to 1/2_1^-$	415	16995 ± 162	15737 ± 174
		$5/2_1^- \to 3/2_1^-$	103	1517 ± 67	1405 ± 63
		$5/2_2^- \to 5/2_1^-$	448	420 ± 41	391 ± 38
		$7/2_1^- \to 5/2_1^-$	497	778 ± 39	727 ± 37
		$5/2_2^- \to 3/2_1^-$	551	246 ± 30	229 ± 28
		$7/2_1^- \to 3/2_1^-$	601	190 ± 25	177 ± 23
		$9/2_1^- \to 5/2_1^-$	676	671 ± 31	628 ± 30
		$3/2_2^- \to 1/2_1^-$	702	245 ± 18	227 ± 17

Data set	Description	Transition	E_γ [keV]	Counts	Corrected counts
6	^{109}Ag detected	$3/2^-_1 \to 1/2^-_1$	311	31929 ± 267	29499 ± 298
	in FCD ring 1-3	$5/2^-_1 \to 1/2^-_1$	415	32180 ± 245	29769 ± 282
		$5/2^-_1 \to 3/2^-_1$	103	2804 ± 106	2594 ± 100
		$5/2^-_2 \to 5/2^-_1$	448	958 ± 72	892 ± 68
		$7/2^-_1 \to 5/2^-_1$	497	2162 ± 66	2020 ± 62
		$5/2^-_2 \to 3/2^-_1$	551	718 ± 42	668 ± 39
		$7/2^-_1 \to 3/2^-_1$	601	362 ± 33	339 ± 31
		$9/2^-_1 \to 5/2^-_1$	676	1736 ± 50	1623 ± 47
		$3/2^-_2 \to 1/2^-_1$	702	778 ± 35	721 ± 33
7	^{109}Ag detected	$3/2^-_1 \to 1/2^-_1$	311	42744 ± 321	39534 ± 371
	in FCD ring 4-6	$5/2^-_1 \to 1/2^-_1$	415	41852 ± 286	38746 ± 342
		$5/2^-_1 \to 3/2^-_1$	103	3553 ± 116	3289 ± 109
		$5/2^-_2 \to 5/2^-_1$	448	1001 ± 77	931 ± 72
		$7/2^-_1 \to 5/2^-_1$	497	2281 ± 66	2131 ± 63
		$5/2^-_2 \to 3/2^-_1$	551	729 ± 43	678 ± 40
		$7/2^-_1 \to 3/2^-_1$	601	502 ± 33	469 ± 31
		$9/2^-_1 \to 5/2^-_1$	676	1816 ± 48	1698 ± 46
		$3/2^-_2 \to 1/2^-_1$	702	735 ± 31	682 ± 29
8	^{109}Ag detected	$3/2^-_1 \to 1/2^-_1$	311	48205 ± 369	44620 ± 424
	in FCD ring 7-9	$5/2^-_1 \to 1/2^-_1$	415	47245 ± 324	43766 ± 387
		$5/2^-_1 \to 3/2^-_1$	103	4116 ± 126	3812 ± 119
		$5/2^-_2 \to 5/2^-_1$	448	1057 ± 80	984 ± 74
		$7/2^-_1 \to 5/2^-_1$	497	1808 ± 66	1689 ± 62
		$5/2^-_2 \to 3/2^-_1$	551	701 ± 44	652 ± 41
		$7/2^-_1 \to 3/2^-_1$	601	451 ± 33	421 ± 31
		$9/2^-_1 \to 5/2^-_1$	676	1610 ± 56	1506 ± 53
		$3/2^-_2 \to 1/2^-_1$	702	501 ± 28	465 ± 26
9	^{109}Ag detected	$3/2^-_1 \to 1/2^-_1$	311	44549 ± 333	41258 ± 385
	in FCD ring 10-12	$5/2^-_1 \to 1/2^-_1$	415	43946 ± 299	40727 ± 357
		$5/2^-_1 \to 3/2^-_1$	103	3693 ± 117	3422 ± 110
		$5/2^-_2 \to 5/2^-_1$	448	936 ± 67	871 ± 62
		$7/2^-_1 \to 5/2^-_1$	497	1187 ± 57	1109 ± 53
		$5/2^-_2 \to 3/2^-_1$	551	555 ± 41	516 ± 38
		$7/2^-_1 \to 3/2^-_1$	601	282 ± 29	264 ± 27
		$9/2^-_1 \to 5/2^-_1$	676	1062 ± 45	994 ± 42
		$3/2^-_2 \to 1/2^-_1$	702	318 ± 22	296 ± 21

Continued on next page . . .

Data set	Description	Transition	E_γ [keV]	Counts	Corrected counts
10	^{109}Ag detected	$3/2_1^- \to 1/2_1^-$	311	31699 ± 259	29367 ± 290
	in FCD ring 13-15	$5/2_1^- \to 1/2_1^-$	415	31345 ± 236	29058 ± 271
		$5/2_1^- \to 3/2_1^-$	103	2587 ± 97	2397 ± 90
		$5/2_2^- \to 5/2_1^-$	448	640 ± 58	596 ± 54
		$7/2_1^- \to 5/2_1^-$	497	625 ± 45	584 ± 42
		$5/2_2^- \to 3/2_1^-$	551	381 ± 33	354 ± 31
		$7/2_1^- \to 3/2_1^-$	601	136 ± 23	128 ± 21
		$9/2_1^- \to 5/2_1^-$	676	520 ± 37	487 ± 34
		$3/2_2^- \to 1/2_1^-$	702	144 ± 17	134 ± 16
11	^{72}Zn detected	$3/2_1^- \to 1/2_1^-$	311	184277 ± 1092	170928 ± 1392
	in FCD	$5/2_1^- \to 1/2_1^-$	415	178059 ± 918	165270 ± 1250
		$5/2_1^- \to 3/2_1^-$	103	14175 ± 236	13156 ± 231
		$5/2_2^- \to 5/2_1^-$	448	3515 ± 167	3276 ± 156
		$7/2_1^- \to 5/2_1^-$	497	4507 ± 128	4218 ± 122
		$5/2_2^- \to 3/2_1^-$	551	2226 ± 98	2075 ± 92
		$7/2_1^- \to 3/2_1^-$	601	1095 ± 71	1025 ± 67
		$9/2_1^- \to 5/2_1^-$	676	3866 ± 83	3622 ± 80
		$3/2_2^- \to 1/2_1^-$	702	1243 ± 44	1157 ± 42
		$5/2_2^- \to 1/2_1^-$	863	301 ± 30	281 ± 28
		$(3/2)_3^- \to 3/2_1^-$	1013	326 ± 23	306 ± 22
12	^{109}Ag detected	$3/2_1^- \to 1/2_1^-$	311	195028 ± 1151	180475 ± 1471
	in FCD	$5/2_1^- \to 1/2_1^-$	415	190127 ± 977	176097 ± 1335
		$5/2_1^- \to 3/2_1^-$	103	15624 ± 267	14469 ± 260
		$5/2_2^- \to 5/2_1^-$	448	4568 ± 173	4249 ± 162
		$7/2_1^- \to 5/2_1^-$	497	7861 ± 155	7345 ± 149
		$5/2_2^- \to 3/2_1^-$	551	3172 ± 122	2951 ± 114
		$7/2_1^- \to 3/2_1^-$	601	1759 ± 78	1643 ± 73
		$9/2_1^- \to 5/2_1^-$	676	6592 ± 113	6166 ± 110
		$3/2_2^- \to 1/2_1^-$	702	2405 ± 61	2233 ± 58
		$5/2_2^- \to 1/2_1^-$	863	385 ± 40	358 ± 37
		$(3/2)_3^- \to 3/2_1^-$	1013	359 ± 28	337 ± 27
13	^{72}Zn detected	$3/2_1^- \to 1/2_1^-$	311	7553 ± 115	6896 ± 112
	in BBarrel	$5/2_1^- \to 1/2_1^-$	415	7246 ± 105	6633 ± 103
		$5/2_1^- \to 3/2_1^-$	103	593 ± 49	543 ± 45
		$5/2_2^- \to 5/2_1^-$	448	387 ± 36	358 ± 33
		$7/2_1^- \to 5/2_1^-$	497	712 ± 35	663 ± 33
		$5/2_2^- \to 3/2_1^-$	551	229 ± 23	212 ± 21
		$7/2_1^- \to 3/2_1^-$	601	91 ± 19	85 ± 17
		$9/2_1^- \to 5/2_1^-$	676	521 ± 34	485 ± 31
		$3/2_2^- \to 1/2_1^-$	702	290 ± 21	265 ± 19

Continued on next page . . .

Data set	Description	Transition	E_γ [keV]	Counts	Corrected counts
14	^{72}Zn detected	$3/2_1^- \to 1/2_1^-$	311	506 ± 26	458 ± 24
	in BCD	$5/2_1^- \to 1/2_1^-$	415	521 ± 25	473 ± 23
		$5/2_1^- \to 3/2_1^-$	103	43 ± 11	39 ± 10
		$5/2_2^- \to 5/2_1^-$	448	25 ± 7	23 ± 7
		$7/2_1^- \to 5/2_1^-$	497	54 ± 9	51 ± 9
		$9/2_1^- \to 5/2_1^-$	676	41 ± 8	38 ± 7
		$3/2_2^- \to 1/2_1^-$	702	29 ± 6	26 ± 5

Tab. D.9: The measured yield in the ^{109}Ag γ-ray peaks of the Coulomb excitation experiment. Note, that the yields are not corrected for the MINIBALL efficiency. The corrected counts correspond to the yields which are attributed to the excitation of ^{109}Ag by the ^{72}Zn beam and not by the beam contaminants. These latter yields are used in the Coulex analysis involving ^{109}Ag.

Data set	Description	Transition	E_γ [keV]	Upper limit
11	^{72}Zn detected in FCD	^{72}Zn: $0_2^+ \to 2_1^+$	858.3	100
		^{72}Zn: $6_1^+ \to 4_1^+$	1153.3	16
		^{109}Ag: $(3/2)_3^- \to 1/2_1^-$	1324.2	60
12	^{109}Ag detected in FCD	^{72}Zn: $0_2^+ \to 2_1^+$	858.3	272
		^{72}Zn: $6_1^+ \to 4_1^+$	1153.3	9
		^{109}Ag: $(3/2)_3^- \to 1/2_1^-$	1324.2	14
13	^{72}Zn detected in BBarrel	^{72}Zn: $6_1^+ \to 4_1^+$	1153.3	5

Tab. D.10: The upper limits of the unobserved ^{72}Zn and ^{109}Ag γ-ray transitions. They are not corrected for the MINIBALL efficiency. However, only one upper limit can be defined in the GOSIA input file per data set. Hence, the smaller upper limits $UPL(6_1^+ \to 4_1^+)$ are chosen. The larger $UPL(0_2^+ \to 2_1^+)$ values are considered by estimating the counts in the $0_2^+ \to 2_1^+$ transitions with "peak area - background area" in the yield file and by imposing a huge error on this yield.

D.7 Influence of the Deorientation Effect on ^{72}Zn and ^{109}Ag Yields

Fig. D.5 and fig. D.6 shows the influence of the deorientation effect in GOSIA for the ^{72}Zn and the ^{109}Ag yields. A discussion of the figures can be found in sec. 6.3.5.

D.8 Feeding to the 4_1^+ State in ^{72}Zn

For the determination of the $B(E2; 4_1^+ \to 2_1^+)$ value and the quadrupole moment of the 4_1^+ state in ^{72}Zn, feeding from higher lying states has to be investigated in detail. A good method to identity possible feeding contributions to the 4_1^+ state are the Doppler corrected γ-ray spectra with respect to ^{72}Zn which additional feature a gate on the $4_1^+ \to 2_1^+$ transition (c.f. fig. D.7). Candidates to feed the 4_1^+ state is manly the 6_1^+ state from the yrast band and the (5_1^-) state [38, 151] from a neighboring band. A significant feeding contribution originating from the 6_1^+ state would be visible in the gated γ-ray spectra as a peak at $E_\gamma(6_1^+ \to 4_1^+) = 1151\,\text{keV}$. Feeding from the (5_1^-) state would be visible as a broad structure around the γ-ray energy $E_\gamma((5_1^-) \to 4_1^+) = 1527\,\text{keV}$, since its lifetime is quite short. As none
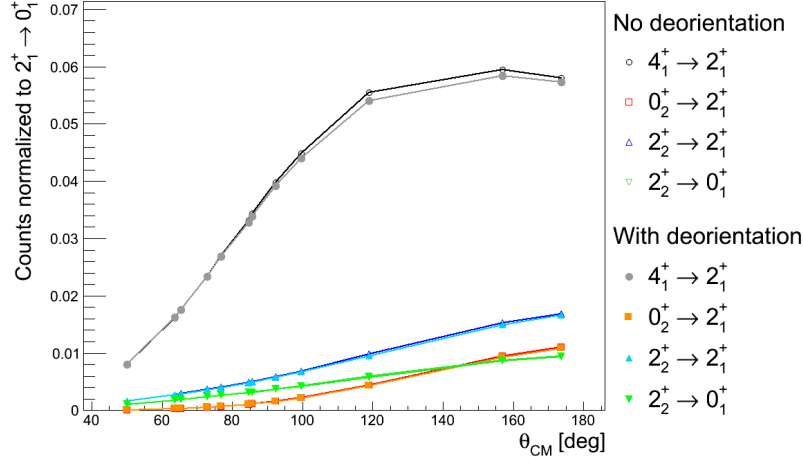
Fig. D.5: The influence of the deorientation effect on the calculated ^{72}Zn yield using the GOSIA code. In both calculations the same set of matrix elements resulting from sec. 6.3.2 are used.
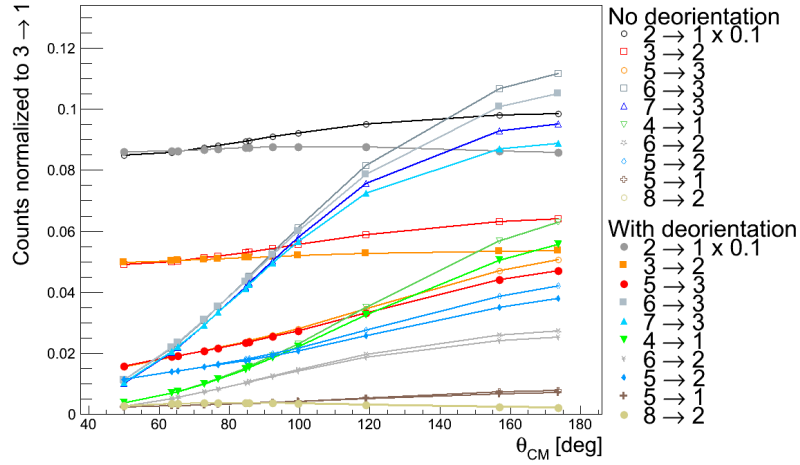
Fig. D.6: The influence of the deorientation effect on the calculated ^{109}Ag yield using the GOSIA code. In both calculations the same set of matrix elements resulting from sec. 6.3.4 are used.

of these signatures has been observed in the gated γ-ray spectra of fig. D.7, feeding from the 6_1^+ and the (5_1^-) state is negligible at the available statistics.

D.9   Shell Model Calculations: Wave Functions of ^{72}Zn

The neutron wave functions of the low lying ^{72}Zn states obtained by a shell model calculation in the jj44 model space using the jj4c, the jj44bpn and the JUN45 interaction are shown in tab. D.11, tab. D.12 and tab. D.13, respectively. For a detailed discussion see sec. 6.4.3.
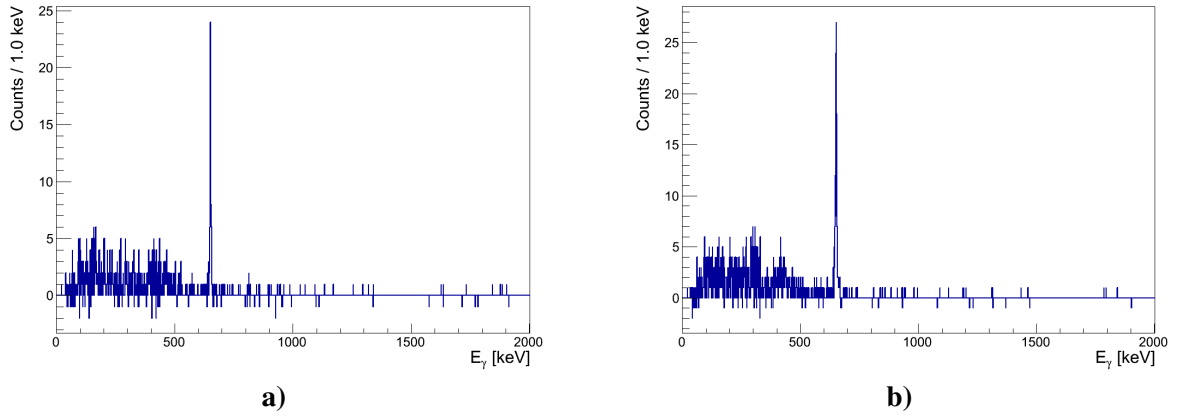
Fig. D.7: The Doppler corrected γ-ray spectrum with respect to ^{72}Zn for the detection of ^{72}Zn in C-REX (**a**)) and for the detection of ^{109}Ag in C-REX (**b**)), respectively. Only the $2_1^+ \rightarrow 0_1^+$ transition is visible, but no feeding from higher lying states such as the 6_1^+ state ($E_\gamma(6_1^+ \rightarrow 4_1^+) = 1151$ keV) or the (5_1^-) state ($E_\gamma((5_1^-) \rightarrow 4_1^+) = 1527$ keV) is observed.

$\nu(1g_{9/2})$ $\nu(2p_{1/2})$ $\nu(1f_{5/2})$ $\nu(2p_{3/2})$						
Configuration	$\|1\rangle$	$\|2\rangle$	$\|3\rangle$	$\|4\rangle$	$\|5\rangle$	$\|6\rangle$
0_1^+	8.9%	8.3%	34.5%	11.8%	3.6%	-
$\pi(2p_{3/2})^2$	6.2%	2.6%	12.9%	2.1%	1.4%	-
$\pi(1f_{5/2})^2$	2.7%	5.7%	10.2%	6.0%	2.2%	-
2_1^+	3.7%	8.0%	38.1%	14.1%	2.9%	-
$\pi(2p_{3/2})^2$	2.6%	1.6%	11.2%	1.8%	1.0%	-
$\pi(1f_{5/2})^2$	1.1%	4.0%	9.3%	5.9%	1.9%	-
0_2^+	22.3%	3.6%	12.3%	24.3%	2.3%	-
$\pi(2p_{3/2})^2$	10.0%	<1%	11.1%	<1%	<1%	-
$\pi(1f_{5/2})^2$	1.0%	3.6%	<1%	14.2%	2.3%	-
4_1^+	1.9%	6.3%	45.0%	12.2%	3.0%	-
$\pi(2p_{3/2})^2$	-	-	10.2%	1.0%	-	-
$\pi(1f_{5/2})^2$	-	3.2%	9.2%	4.3%	1.4%	-
$\pi(2p_{3/2}1f_{5/2})$	1.9%	3.1%	13.1%	3.4%	1.6%	-
$\pi(1f_{5/2}2p_{1/2})$	-	-	4.9%	2.3%	-	-
$\pi(2p_{3/2}2p_{1/2})$	-	-	5.9%	1.2%	-	-
2_2^+	7.9%	2.8%	16.0%	9.3%	1.2%	22.5%
$\pi(2p_{3/2})^2$	6.0%	-	5.8%	-	-	5.2%
$\pi(1f_{5/2})^2$	1.9%	2.8%	5.8%	4.1%	1.2%	9.3%

Tab. D.11: The most dominant wave functions of the low lying ^{72}Zn states calculated with the jj4c interaction [136]. In black the fractions of the neutron configurations are shown, whereas in gray the fractions of the proton configuration are given. Comparing the wave functions, the 0_2^+ and the 2_2^+ state feature a different structure than the yrast states 0_1^+, 2_1^+ and 4_1^+. For detailed discussion see sec. 6.4.3.

	$|1\rangle$	$|2\rangle$	$|3\rangle$	$|4\rangle$	$|5\rangle$	$|6\rangle$	$|7\rangle$	$|8\rangle$	$|9\rangle$	$|10\rangle$
$\nu(1g_{9/2})$										
$\nu(2p_{1/2})$										
$\nu(1f_{5/2})$										
$\nu(2p_{3/2})$										
Configuration	$|1\rangle$	$|2\rangle$	$|3\rangle$	$|4\rangle$	$|5\rangle$	$|6\rangle$	$|7\rangle$	$|8\rangle$	$|9\rangle$	$|10\rangle$
0_1^+	9.3%	10.9%	29.0%	13.8%	7.4%	1.2%	5.6%	4.4%	3.3%	4.7%
2_1^+	5.0%	9.1%	28.8%	16.0%	7.4%	1.9%	4.0%	6.5%	3.9%	4.0%
0_2^+	16.8%	7.4%	24.1%	15.1%	5.0%	1.4%	3.7%	7.8%	3.2%	3.1%
4_1^+	4.1%	8.3%	30.3%	14.8%	7.0%	1.8%	3.9%	6.3%	3.8%	3.5%
2_2^+	5.4%	5.8%	15.2%	7.1%	4.2%	19.8%	3.6%	8.0%	6.8%	1.8%

Tab. D.12: The most dominant neutron wave functions of the low lying ^{72}Zn states calculated with the jj44bpn interaction [110]. For detailed discussion see sec. 6.4.3.

	$|1\rangle$	$|2\rangle$	$|3\rangle$	$|4\rangle$	$|5\rangle$	$|6\rangle$	$|7\rangle$	$|8\rangle$	$|9\rangle$	$|10\rangle$
$\nu(1g_{9/2})$										
$\nu(2p_{1/2})$										
$\nu(1f_{5/2})$										
$\nu(2p_{3/2})$										
Configuration	$|1\rangle$	$|2\rangle$	$|3\rangle$	$|4\rangle$	$|5\rangle$	$|6\rangle$	$|7\rangle$	$|8\rangle$	$|9\rangle$	$|10\rangle$
0_1^+	21.6%	14.8%	21.0%	7.5%	5.6%	2.0%	10.5%	0.8%	2.0%	2.1%
2_1^+	17.8%	12.7%	21.3%	6.7%	4.8%	5.3%	8.4%	1.0%	2.3%	1.8%
0_2^+	37.0%	5.7%	11.5%	7.2%	3.8%	10.9%	4.6%	0.9%	2.4%	1.5%
4_1^+	10.4%	13.7%	23.6%	7.8%	5.5%	3.9%	7.8%	1.1%	2.0%	2.1%
2_2^+	19.7%	7.4%	14.7%	4.8%	3.1%	15.5%	6.0%	1.6%	3.4%	1.1%

Tab. D.13: The most dominant neutron wave functions of the low lying ^{72}Zn states calculated with the JUN45 interaction [137]. For detailed discussion see sec. 6.4.3.

Bibliography

[1] R. F. Casten, *Nuclear Structure from a Simple Perspective (Oxford Studies in Nuclear Physics)*. Oxford University Press, 2001.

[2] R. D. Woods and D. S. Saxon, "Diffuse surface optical model for nucleon-nuclei scattering," *Phys. Rev.*, vol. 95, pp. 577–578, Jul 1954.

[3] M. G. Mayer, "On closed shells in nuclei. ii," *Phys. Rev.*, vol. 75, pp. 1969–1970, Jun 1949.

[4] O. Haxel, J. H. D. Jensen, and H. E. Suess, "On the "magic numbers" in nuclear structure," *Phys. Rev.*, vol. 75, pp. 1766–1766, Jun 1949.

[5] T. Mayer-Kuckuk, *Kernphysik: Ein Einführung (German Edition)*. Vieweg+Teubner Verlag, 2013.

[6] O. Sorlin and M.-G. Porquet, "Nuclear magic numbers: New features far from stability," *Progress in Particle and Nuclear Physics*, vol. 61, no. 2, pp. 602 – 673, 2008.

[7] A. Ozawa, T. Kobayashi, T. Suzuki, K. Yoshida, and I. Tanihata, "New magic number, $N = 16$, near the neutron drip line," *Phys. Rev. Lett.*, vol. 84, pp. 5493–5495, Jun 2000.

[8] C. Hoffman, T. Baumann, D. Bazin, J. Brown, G. Christian, D. Denby, P. DeYoung, J. Finck, N. Frank, J. Hinnefeld, S. Mosby, W. Peters, W. Rogers, A. Schiller, A. Spyrou, M. Scott, S. Tabor, M. Thoennessen, and P. Voss, "Evidence for a doubly magic ^{24}O," *Physics Letters B*, vol. 672, no. 1, pp. 17 – 21, 2009.

[9] R. Kanungo, C. Nociforo, A. Prochazka, T. Aumann, D. Boutin, D. Cortina-Gil, B. Davids, M. Diakaki, F. Farinon, H. Geissel, R. Gernhäuser, J. Gerl, R. Janik, B. Jonson, B. Kindler, R. Knöbel, R. Krücken, M. Lantz, H. Lenske, Y. Litvinov, B. Lommel, K. Mahata, P. Maierbeck, A. Musumarra, T. Nilsson, T. Otsuka, C. Perro, C. Scheidenberger, B. Sitar, P. Strmen, B. Sun, I. Szarka, I. Tanihata, Y. Utsuno, H. Weick, and M. Winkler, "One-Neutron Removal Measurement Reveals ^{24}O as a New Doubly Magic Nucleus," *Phys. Rev. Lett.*, vol. 102, p. 152501, Apr 2009.

[10] T. Otsuka, T. Suzuki, R. Fujimoto, H. Grawe, and Y. Akaishi, "Evolution of nuclear shells due to the tensor force," *Phys. Rev. Lett.*, vol. 95, p. 232502, Nov 2005.

[11] P. T. Hosmer, H. Schatz, A. Aprahamian, O. Arndt, R. R. C. Clement, A. Estrade, K.-L. Kratz, S. N. Liddick, P. F. Mantica, W. F. Mueller, F. Montes, A. C. Morton, M. Ouellette, E. Pellegrini, B. Pfeiffer, P. Reeder, P. Santi, M. Steiner, A. Stolz, B. E. Tomlin, W. B. Walters, and A. Wöhr, "Half-life of the doubly magic *r*-process nucleus ^{78}Ni," *Phys. Rev. Lett.*, vol. 94, p. 112501, Mar 2005.

[12] The ISOLDE yield database. `https://oraweb.cern.ch/pls/isolde/query_tgt/`, August 2015.

[13] National Nuclear Data Center at Brookhaven National Laboratory, "Evaluated Nuclear Structure Data File (ENSDF) online database." `http://www.nndc.bnl.gov/ensdf/`, February 2015.

[14] R. Broda, B. Fornal, W. Królas, T. Pawłat, D. Bazzacco, S. Lunardi, C. Rossi-Alvarez, R. Menegazzo, G. de Angelis, P. Bednarczyk, J. Rico, D. De Acuña, P. J. Daly, R. H. Mayer, M. Sferrazza, H. Grawe, K. H. Maier, and R. Schubart, "$N = 40$ Neutron Subshell Closure in the ^{68}Ni Nucleus," *Phys. Rev. Lett.*, vol. 74, pp. 868–871, Feb 1995.

[15] O. Sorlin, S. Leenhardt, C. Donzaud, J. Duprat, F. Azaiez, F. Nowacki, H. Grawe, Z. Dombrádi, F. Amorini, A. Astier, D. Baiborodin, M. Belleguic, C. Borcea, C. Bourgeois, D. M. Cullen, Z. Dlouhy, E. Dragulescu, M. Górska, S. Grévy, D. Guillemaud-Mueller, G. Hagemann, B. Herskind, J. Kiener, R. Lemmon, M. Lewitowicz, S. M. Lukyanov, P. Mayet, F. de Oliveira Santos, D. Pantalica, Y.-E. Penionzhkevich, F. Pougheon, A. Poves, N. Redon, M. G. Saint-Laurent, J. A. Scarpaci, G. Sletten, M. Stanoiu, O. Tarasov, and C. Theisen, "$^{68}_{28}$Ni$_{40}$: Magicity versus Superfluidity," *Phys. Rev. Lett.*, vol. 88, p. 092501, Feb 2002.

[16] N. Bree, I. Stefanescu, P. A. Butler, J. Cederkäll, T. Davinson, P. Delahaye, J. Eberth, D. Fedorov, V. N. Fedosseev, L. M. Fraile, S. Franchoo, G. Georgiev, K. Gladnishki, M. Huyse, O. Ivanov, J. Iwanicki, J. Jolie, U. Köster, T. Kröll, R. Krücken, B. A. Marsh, O. Niedermaier, P. Reiter, H. Scheit, D. Schwalm, T. Sieber, J. V. de Walle, P. V. Duppen, N. Warr, D. Weisshaar, F. Wenander, and S. Zemlyanoy, "Coulomb excitation of $^{68}_{28}$Ni$_{40}$ at "safe" energies," *Phys. Rev. C*, vol. 78, p. 047301, Oct 2008.

[17] M. Bernas, P. Dessagne, M. Langevin, J. Payet, F. Pougheon, and P. Roussel, "Magic features of ^{68}Ni," *Physics Letters B*, vol. 113, no. 4, pp. 279 – 282, 1982.

[18] S. Rahaman, J. Hakala, V.-V. Elomaa, T. Eronen, U. Hager, A. Jokinen, A. Kankainen, I. Moore, H. Penttilä, S. Rinta-Antila, J. Rissanen, A. Saastamoinen, C. Weber, and J. Äystö, "Masses of neutron-rich Ni and Cu isotopes and the shell closure at Z = 28 , N = 40," *The European Physical Journal A*, vol. 34, no. 1, pp. 5–9, 2007.

[19] C. Guénaut, G. Audi, D. Beck, K. Blaum, G. Bollen, P. Delahaye, F. Herfurth, A. Kellerbauer, H.-J. Kluge, J. Libert, D. Lunney, S. Schwarz, L. Schweikhard, and C. Yazidjian, "High-precision mass measurements of nickel, copper, and gallium isotopes and the purported shell closure at $N = 40$," *Phys. Rev. C*, vol. 75, p. 044303, Apr 2007.

[20] K. Heyde and J. L. Wood, "Shape coexistence in atomic nuclei," *Rev. Mod. Phys.*, vol. 83, pp. 1467–1521, Nov 2011.

[21] Y. Tsunoda, T. Otsuka, N. Shimizu, M. Honma, and Y. Utsuno, "Novel shape evolution in exotic Ni isotopes and configuration-dependent shell structure," *Phys. Rev. C*, vol. 89, p. 031301, Mar 2014.

[22] S. Suchyta, S. N. Liddick, Y. Tsunoda, T. Otsuka, M. B. Bennett, A. Chemey, M. Honma, N. Larson, C. J. Prokop, S. J. Quinn, N. Shimizu, A. Simon, A. Spyrou, V. Tripathi, Y. Utsuno, and J. M. VonMoss, "Shape coexistence in ^{68}Ni," *Phys. Rev. C*, vol. 89, p. 021301, Feb 2014.

[23] K. Kaneko, M. Hasegawa, T. Mizusaki, and Y. Sun, "Magicity and occurrence of a band with enhanced $B(E2)$ in neutron-rich nuclei ^{68}Ni and ^{90}Zr," *Phys. Rev. C*, vol. 74, p. 024321, Aug 2006.

[24] D. Pauwels, J. L. Wood, K. Heyde, M. Huyse, R. Julin, and P. Van Duppen, "Pairing-excitation versus intruder states in ^{68}Ni and ^{90}Zr," *Phys. Rev. C*, vol. 82, p. 027304, Aug 2010.

[25] A. Dijon, E. Clément, G. de France, G. de Angelis, G. Duchêne, J. Dudouet, S. Franchoo, A. Gadea, A. Gottardo, T. Hüyük, B. Jacquot, A. Kusoglu, D. Lebhertz, G. Lehaut, M. Martini, D. R. Napoli, F. Nowacki, S. Péru, A. Poves, F. Recchia, N. Redon, E. Sahin, C. Schmitt, M. Sferrazza, K. Sieja, O. Stezowski, J. J. Valiente-Dobón, A. Vancraeyenest, and Y. Zheng, "Discovery of a new isomeric state in ^{68}Ni: Evidence for a highly deformed proton intruder state," *Phys. Rev. C*, vol. 85, p. 031301, Mar 2012.

[26] S. M. Lenzi, F. Nowacki, A. Poves, and K. Sieja, "Island of inversion around ^{64}Cr," *Phys. Rev. C*, vol. 82, p. 054301, Nov 2010.

[27] J. Elseviers, *Probing the Semi-Magicity of ^{68}Ni via the ^{66}Ni(t,p)^{68}Ni Two-Neutron Transfer Reaction in Inverse Kinematics*. PhD thesis, Instituut voor Kern- en Stralingsfysica,Katholieke Universiteit Leuven, 2014.

[28] J. Elseviers, R. Flavigny, A. N. Andreyev, V. Bildstein, B. A. Brown, J. Diriken, V. N. Fedosseev, S. Franchoo, R. Gernhauser, M. Huyse, S. Ilieva, S. Klupp, T. Kröll, R. Lutter, B. A. Marsh, D. Mücher, K. Nowak, J. Pakarinen, N. Patronis, R. Raabe, F. Recchia, T. Roger, S. Sambi, M. D. Seliverstov, P. Van Duppen, M. Von Schmid, R. Voulot, N. Warr, R. Wenander, and K. Wimmer, "Probing the 0^+ States in ^{68}Ni via the two-Neutron Transfer Reaction ^{66}Ni(t,p)," *to be submitted*, June 2015.

[29] C. J. Chiara, D. Weisshaar, R. V. F. Janssens, Y. Tsunoda, T. Otsuka, J. L. Harker, W. B. Walters, F. Recchia, M. Albers, M. Alcorta, V. M. Bader, T. Baugher, D. Bazin, J. S. Berryman, P. F. Bertone, C. M. Campbell, M. P. Carpenter, J. Chen, H. L. Crawford, H. M. David, D. T. Doherty, A. Gade, C. R. Hoffman, M. Honma, F. G. Kondev, A. Korichi, C. Langer, N. Larson, T. Lauritsen, S. N. Liddick, E. Lunderberg, A. O. Macchiavelli, S. Noji, C. Prokop, A. M. Rogers, D. Seweryniak, N. Shimizu, S. R. Stroberg, S. Suchyta, Y. Utsuno, S. J. Williams, K. Wimmer, and S. Zhu, "Identification of deformed intruder states in semi-magic ^{70}Ni," *Phys. Rev. C*, vol. 91, p. 044309, Apr 2015.

[30] D. Pauwels, O. Ivanov, N. Bree, J. Büscher, T. E. Cocolios, J. Gentens, M. Huyse, A. Korgul, Y. Kudryavtsev, R. Raabe, M. Sawicka, I. Stefanescu, J. Van de Walle, P. Van den Bergh, P. Van Duppen, and W. B. Walters, "Shape isomerism at $N = 40$: Discovery of a proton intruder state in ^{67}Co," *Phys. Rev. C*, vol. 78, p. 041307, Oct 2008.

[31] M. Hannawald, T. Kautzsch, A. Wöhr, W. B. Walters, K.-L. Kratz, V. N. Fedoseyev, V. I. Mishin, W. Böhmer, B. Pfeiffer, V. Sebastian, Y. Jading, U. Köster, J. Lettry, H. L. Ravn, and the ISOLDE Collaboration, "Decay of Neutron-Rich Mn Nuclides and Deformation of Heavy Fe Isotopes," *Phys. Rev. Lett.*, vol. 82, pp. 1391–1394, Feb 1999.

[32] J. Ljungvall, A. Görgen, A. Obertelli, W. Korten, E. Clément, G. de France, A. Bürger, J.-P. Delaroche, A. Dewald, A. Gadea, L. Gaudefroy, M. Girod, M. Hackstein, J. Libert, D. Mengoni, F. Nowacki, T. Pissulla, A. Poves, F. Recchia, M. Rejmund, W. Rother, E. Sahin, C. Schmitt, A. Shrivastava, K. Sieja, J. J. Valiente-Dobón, K. O. Zell, and M. Zielińska, "Onset of collectivity in neutron-rich Fe isotopes: Toward a new island of inversion?," *Phys. Rev. C*, vol. 81, p. 061301, Jun 2010.

[33] W. Rother, A. Dewald, H. Iwasaki, S. M. Lenzi, K. Starosta, D. Bazin, T. Baugher, B. A. Brown, H. L. Crawford, C. Fransen, A. Gade, T. N. Ginter, T. Glasmacher, G. F. Grinyer, M. Hackstein, G. Ilie, J. Jolie, S. McDaniel, D. Miller, P. Petkov, T. Pissulla, A. Ratkiewicz, C. A. Ur, P. Voss, K. A. Walsh, D. Weisshaar, and K.-O. Zell, "Enhanced Quadrupole Collectivity at $N = 40$: The Case of Neutron-Rich Fe Isotopes," *Phys. Rev. Lett.*, vol. 106, p. 022502, Jan 2011.

[34] I. Stefanescu, G. Georgiev, D. L. Balabanski, N. Blasi, A. Blazhev, N. Bree, J. Cederkäll, T. E. Cocolios, T. Davinson, J. Diriken, J. Eberth, A. Ekström, D. Fedorov, V. N. Fedosseev, L. M. Fraile, S. Franchoo, K. Gladnishki, M. Huyse, O. Ivanov, V. Ivanov, J. Iwanicki, J. Jolie, T. Konstantinopoulos, T. Kröll, R. Krücken, U. Köster, A. Lagoyannis, G. Lo Bianco, P. Maierbeck, B. A. Marsh, P. Napiorkowski, N. Patronis, D. Pauwels, G. Rainovski, P. Reiter, K. Riisager, M. Seliverstov, G. Sletten, J. Van de Walle, P. Van Duppen, D. Voulot, N. Warr, F. Wenander, and K. Wrzosek, "Interplay between Single-Particle and Collective Effects in the Odd-A Cu Isotopes beyond $N = 40$," *Phys. Rev. Lett.*, vol. 100, p. 112502, Mar 2008.

[35] D. Mücher, *Dynamische Symmetrien von Atomkernen an Unterschalenabschlüssen*. PhD thesis, Universität zu Köln, Mathematisch-Naturwissenschaftliche Fakultät, 2009.

[36] D. Mücher, G. Gürdal, K.-H. Speidel, G. J. Kumbartzki, N. Benczer-Koller, S. J. Q. Robinson, Y. Y. Sharon, L. Zamick, A. F. Lisetskiy, R. J. Casperson, A. Heinz, B. Krieger, J. Leske, P. Maier-Komor, V. Werner, E. Williams, and R. Winkler, "Nuclear structure studies of ^{70}Zn from g-factor and lifetime measurements," *Phys. Rev. C*, vol. 79, p. 054310, May 2009.

[37] C. Fransen, A. Dewald, T. Baumann, D. Bazin, A. Blazhev, B. A. Brown, A. Chester, A. Gade, T. Glasmacher, P. T. Greenlees, M. Hackstein, S. Harissopulos, U. Jakobsson, J. Jolie, P. M. Jones, R. Julin, S. Juutinen, S. Ketelhut, T. Konstaninopoulos, A. Lagoyannis, M. Leino, P. Nieminen, M. Nyman, P. Petkov, P. Peura, T. Pissulla, P. Rahkila, W. Rother, P. Ruotsalainen, J. Saren, C. Scholey, J. Sorri, K. Starosta, A. Stolz, J. Uusitalo, P. Voss, and D. Weisshaar, "New developments on the recoil distance Doppler-shift method," *Journal of Physics: Conference Series*, vol. 205, no. 1, p. 012043, 2010.

[38] C. Louchart, A. Obertelli, A. Görgen, W. Korten, D. Bazzacco, B. Birkenbach, B. Bruyneel, E. Clément, P. J. Coleman-Smith, L. Corradi, D. Curien, G. de Angelis, G. de France, J.-P. Delaroche, A. Dewald, F. Didierjean, M. Doncel, G. Duchêne, J. Eberth, M. N. Erduran, E. Farnea, C. Finck, E. Fioretto, C. Fransen, A. Gadea, M. Girod, A. Gottardo, J. Grebosz, T. Habermann, M. Hackstein, T. Huyuk, J. Jolie, D. Judson, A. Jungclaus, N. Karkour, S. Klupp, R. Krücken, A. Kusoglu, S. M. Lenzi, J. Libert, J. Ljungvall, S. Lunardi, G. Maron, R. Menegazzo, D. Mengoni, C. Michelagnoli, B. Million, P. Molini, O. Möller, G. Montagnoli, D. Montanari, D. R. Napoli, R. Orlandi, G. Pollarolo, A. Prieto, A. Pullia, B. Quintana, F. Recchia, P. Reiter, D. Rosso, W. Rother, E. Sahin, M.-D. Salsac, F. Scarlassara, M. Schlarb, S. Siem, P. P. Singh, P.-A. Söderström, A. M. Stefanini, O. Stézowski, B. Sulignano, S. Szilner, C. Theisen, C. A. Ur, J. J. Valiente-Dobón, and M. Zielinska, "Collective nature of low-lying excitations in ^{70,72,74}Zn from lifetime measurements using the AGATA spectrometer demonstrator," *Phys. Rev. C*, vol. 87, p. 054302, May 2013.

[39] M. Niikura, B. Mouginot, S. Franchoo, I. Matea, I. Stefan, D. Verney, F. Azaiez, M. Assie, P. Bednarczyk, C. Borcea, A. Burger, G. Burgunder, A. Buta, L. Cáceres, E. Clément, L. Coquard, G. de Angelis, G. de France, F. de Oliveira Santos, A. Dewald, A. Dijon, Z. Dombradi, E. Fiori, C. Fransen, G. Friessner, L. Gaudefroy, G. Georgiev, S. Grévy, M. Hackstein, M. N. Harakeh, F. Ibrahim, O. Kamalou, M. Kmiecik, R. Lozeva, A. Maj, C. Mihai, O. Möller, S. Myalski, F. Negoita, D. Pantelica, L. Perrot, T. Pissulla, F. Rotaru, W. Rother, J. A. Scarpaci, C. Stodel, J. C. Thomas, and P. Ujic, "First direct lifetime measurement of the 2_1^+ state in ^{72,74}Zn: New evidence for a shape transition between $N = 40$ and $N = 42$ close to $Z = 28$," *Phys. Rev. C*, vol. 85, p. 054321, May 2012.

[40] I. Čeliković, A. Dijon, E. Clément, G. De France, P. Van Isacker, J. Ljungvall, C. Franzen, G. Georgiev, A. Görgen, A. Gottardo, M. Hackstein, T. Hagen, C. Louchart, P. Napiorkowski, A. Obertelli, F. Recchia, W. Rother, S. Siem, B. Sulignano, P. Ujić, J. Valiente-Dobón, and

M. Zielińska, "Lifetime measurements of Zn isotopes around N = 40," in *Zakopane Conference on Nuclear Physics "Extremes of the Nuclear Landscape"*, vol. 44, (Zakopane, Poland), pp. 375–380, Aug. 2012. Expérience GANIL/EXOGAM/VAMOS.

[41] J. Van de Walle, F. Aksouh, T. Behrens, V. Bildstein, A. Blazhev, J. Cederkäll, E. Clément, T. E. Cocolios, T. Davinson, P. Delahaye, J. Eberth, A. Ekström, D. V. Fedorov, V. N. Fedosseev, L. M. Fraile, S. Franchoo, R. Gernhauser, G. Georgiev, D. Habs, K. Heyde, G. Huber, M. Huyse, F. Ibrahim, O. Ivanov, J. Iwanicki, J. Jolie, O. Kester, U. Köster, T. Kröll, R. Krücken, M. Lauer, A. F. Lisetskiy, R. Lutter, B. A. Marsh, P. Mayet, O. Niedermaier, M. Pantea, R. Raabe, P. Reiter, M. Sawicka, H. Scheit, G. Schrieder, D. Schwalm, M. D. Seliverstov, T. Sieber, G. Sletten, N. Smirnova, M. Stanoiu, I. Stefanescu, J.-C. Thomas, J. J. Valiente-Dobón, P. V. Duppen, D. Verney, D. Voulot, N. Warr, D. Weisshaar, F. Wenander, B. H. Wolf, and M. Zielińska, "Low-energy Coulomb excitation of neutron-rich zinc isotopes," *Phys. Rev. C*, vol. 79, p. 014309, Jan 2009.

[42] M. Zielinska, "Collectivity of the 4_1^+ states in heavy Zn isotopes," *ISOLDE Workshop*, 2013.

[43] B. Kotliński, T. Czosnyka, D. Cline, J. Srebrny, C. Wu, A. Bäcklin, L. Hasselgren, L. Westerberg, C. Baktash, and S. Steadman, "Heavy-ion Coulomb excitation of ^{72}Ge," *Nuclear Physics A*, vol. 519, no. 3, pp. 646 – 658, 1990.

[44] D. J. Rowe, *Fundamentals of nuclear models : foundational models*. Singapore Hackensack, NJ: World Scientific, 2010.

[45] I. Celikovic, *Nuclear structure around doubly-magic nuclei: lifetime measurements in the vicinity of ^{68}Ni and search for isomers around ^{100}Sn*. PhD thesis, Universite de Caen Basse-Normandie - Esplanade de la Paix, CS 14032, 14032 Caen cedex 5 (France); CEA, DSM-GANIL (France), 2013.

[46] A. Illana, A. Jungclaus, R. Orlandi, A. Perea, C. Bauer, J. A. Briz, J. L. Egido, R. Gernhäuser, J. Leske, D. Mücher, J. Pakarinen, N. Pietralla, M. Rajabali, T. R. Rodriguez, D. Seiler, C. Stahl, D. Voulot, F. Wenander, A. Blazhev, H. De Witte, P. Reiter, M. Seidlitz, B. Siebeck, M. J. Vermeulen, and N. Warr, "Low-velocity transient-field technique with radioactive ion beams: g-factor of the first excited 2^+ state in ^{72}Zn," *Phys. Rev. C*, vol. 89, p. 054316, May 2014.

[47] N. Stone, "Table of nuclear magnetic dipole and electric quadrupole moments," *Atomic Data and Nuclear Data Tables*, vol. 90, no. 1, pp. 75 – 176, 2005.

[48] M. Koizumi, A. Seki, Y. Toh, A. Osa, Y. Utsuno, A. Kimura, M. Oshima, T. Hayakawa, Y. Hatsukawa, J. Katakura, M. Matsuda, T. Shizuma, T. Czosnyka, M. Sugawara, T. Morikawa, and H. Kusakari, "Multiple Coulomb excitation experiment of ^{68}Zn," *Nuclear Physics A*, vol. 730, no. 1–2, pp. 46 – 58, 2004.

[49] J. V. de Walle, *Coulomb excitation of neutron rich Zn isotopes*. PhD thesis, Instituut voor Kern-en Stralingsfysica,Katholieke Universiteit Leuven, 2006.

[50] S. L. Rice, Y. Y. Sharon, N. Benczer-Koller, G. J. Kumbartzki, and L. Zamick, "Systematics of low-lying state transition probabilities and excitation energies in the region $30 \leq Z \leq 38$ and $30 \leq N \leq 50$," *Phys. Rev. C*, vol. 88, p. 044334, Oct 2013.

[51] Y. Toh, T. Czosnyka, M. Oshima, T. Hayakawa, Y. Hatsukawa, M. Matsuda, J. Katakura, N. Shinohara, M. Sugawara, and H. Kusakari, "Shape Coexistence in Even-Even Ge Isotopes - Complete Spectroscopy with Coulomb Excitation -," *Journal of Nuclear Science and Technology*, vol. 39, no. sup2, pp. 497–499, 2002.

[52] F. Hudson and R. Glover, "The (t, p) reaction on the zinc isotopes," *Nuclear Physics A*, vol. 189, no. 2, pp. 264 – 284, 1972.

[53] K. Wimmer, T. Kröll, R. Krücken, V. Bildstein, R. Gernhäuser, B. Bastin, N. Bree, J. Diriken, P. Van Duppen, M. Huyse, N. Patronis, P. Vermaelen, D. Voulot, J. Van de Walle, F. Wenander, L. M. Fraile, R. Chapman, B. Hadinia, R. Orlandi, J. F. Smith, R. Lutter, P. G. Thirolf, M. Labiche, A. Blazhev, M. Kalkühler, P. Reiter, M. Seidlitz, N. Warr, A. O. Macchiavelli, H. B. Jeppesen, E. Fiori, G. Georgiev, G. Schrieder, S. Das Gupta, G. Lo Bianco, S. Nardelli, J. Butterworth, J. Johansen, and K. Riisager, "Discovery of the Shape Coexisting 0^+ State in ^{32}Mg by a Two Neutron Transfer Reaction," *Phys. Rev. Lett.*, vol. 105, p. 252501, Dec 2010.

[54] K. Wimmer, *Discovery of the shape coexisting 0^+ state in ^{32}Mg*. PhD thesis, Technische Universität München, Lehrstuhl E12 für Experimentalphysik, 2010.

[55] A. K. Nowak, *Untersuchungen zur Formkoexistenz durch die ^{44}Ar(t,p)^{46}Ar-Reaktion in inverser Kinematik*. PhD thesis, Technische Universität München, Lehrstuhl E12 für Experimentalphysik, 2015.

[56] P. E. Hodgson, *The nucleon optical model*. Singapore New Jersey: World Scientific, 1994.

[57] R. Stock, *Encyclopedia of applied high energy and particle physics*. Weinheim: Wiley-VCH, 2009.

[58] Ian J. Thompson, Filomena M. Nunes, *Nuclear Reactions for Astrophysics: Principles, Calculation and Applications of Low-Energy Reactions*. Cambridge University Press, 1 ed., 2009.

[59] M. Tsang, J. Lee, and W. Lynch, "Survey of ground state neutron spectroscopic factors from Li to Cr isotopes," *Phys.Rev.Lett.*, vol. 95, p. 222501, 2005.

[60] C. Bertulani, "Theory and Applications of Coulomb Excitation," 2009.

[61] D. Cline, "Nuclear shapes studied by Coulomb excitation," *Ann.Rev.Nucl.Part.Sci.*, vol. 36, pp. 683–716, 1986.

[62] N. Glendenning, *Direct nuclear reactions*. River Edge, N.J: World Scientific, 2004.

[63] K. Alder and A. Winther, *Coulomb Excitation*. New York: Academic Press, 1966.

[64] K. Alder, A. Bohr, T. Huus, B. Mottelson, and A. Winther, "Study of nuclear structure by electromagnetic excitation with accelerated ions," *Rev. Mod. Phys.*, vol. 28, pp. 432–542, Oct 1956.

[65] D. Cline, T. Czosnyka, A. Hayes, P. Napiorkowski, N. Warr, and C. Wu, *GOSIA user manual for simulation and analysis of Coulomb excitation experiments*, May 2012.

[66] M. Zielińska, L. P. Gaffney, K. Wrzosek-Lipska, E. Clément, T. Grahn, N. Kesteloot, P. Napiorkowski, J. Pakarinen, P. V. Duppen, and N. Warr, "Analysis methods of safe Coulomb-excitation experiments with radioactive ion beams using the GOSIA code," 2015.

[67] W. S. M. Samuel, *Introductory Nuclear Physics*. New Jersey: Prentice-Hall Of India Pvt. Limited, 1st ed., 2002.

[68] D. Kean, "Measurement of quadrupole moments through Coulomb excitation," in *Nuclear Interactions* (B. Robson, ed.), vol. 92 of *Lecture Notes in Physics*, pp. 80–94, Springer Berlin Heidelberg, 1976.

[69] H. Ower, *The Coulex code CLX/DCY (unpublished)*.

[70] A. Winther and J. de Boer, "A Computer Program for Multiple Coulomb Excitation, in Coulomb Excitation," (New York / London), Academic Press, edited by K. Alder and A. Winther, 1966.

[71] A. Görgen, "Shapes and collectivity of exotic nuclei via low-energy Coulomb excitation," *Journal of Physics G: Nuclear and Particle Physics*, vol. 37, no. 10, p. 103101, 2010.

[72] K. S. Krane, "$\frac{E2}{M1}$ Multipole Mixing Ratios of γ Transitions in Even-Even Deformed Nuclei," *Phys. Rev. C*, vol. 8, pp. 1494–1499, Oct 1973.

[73] The official REX-ISOLDE website. `http://rex-isolde.web.cern.ch/`, 2014.

[74] The official ISOLDE website. `http://isolde.web.cern.ch/`, October 2014.

[75] The official website of the CERN Engineering: Sources, Targets and Interactions - Lasers and Photocathodes group. `https://en-sti-lp.web.cern.ch/en-sti-lp/`, October 2014.

[76] M. Seidlitz, *Nuclear shell effects in neutron-rich nuclei around N = 20 and N = 32, 34*. PhD thesis, IKP Köln, 2012.

[77] P. V. Duppen and K. Riisager, "Physics with REX-ISOLDE: from experiment to facility," *Journal of Physics G: Nuclear and Particle Physics*, vol. 38, no. 2, p. 024005, 2011.

[78] The official website of the RILIS ISOLDE group. `http://rilis.web.cern.ch/`, October 2014.

[79] "Cian O'Luanaigh: A fundamental property of the rarest element on Earth." `http://home.web.cern.ch/about/updates/2013/05/fundamental-property-rarest-element-earth`, October 2014.

[80] U. Köster, T. Behrens, C. Clausen, P. Delahaye, V. Fedosseev, L. M. Fraile-Prieto, R. Gernhäuser, T. J. Gilles, A. Ionan, T. Kröll, H. Mach, B. Marsh, D. M. Seliverstov, T. Sieber, E. Siesling, E. Tengborn, F. Wenander, and J. Van de Walle, "ISOLDE beams of neutron-rich zinc isotopes: yields, release, decay spectroscopy," *AIP Conf. Proc.*, vol. 798, pp. 315–326. 9 p, Jul 2005.

[81] N. Warr, J. Van de Walle, M. Albers, F. Ames, B. Bastin, C. Bauer, V. Bildstein, A. Blazhev, S. Bönig, N. Bree, B. Bruyneel, P. Butler, J. Cederkäll, E. Clément, T. Cocolios, T. Davinson, H. De Witte, P. Delahaye, D. DiJulio, J. Diriken, J. Eberth, A. Ekström, J. Elseviers, S. Emhofer, D. Fedorov, V. Fedosseev, S. Franchoo, C. Fransen, L. Gaffney, J. Gerl, G. Georgiev, R. Gernhäuser, T. Grahn, D. Habs, H. Hess, A. Hurst, M. Huyse, O. Ivanov, J. Iwanicki, D. Jenkins, J. Jolie, N. Kesteloot, O. Kester, U. Köster, M. Krauth, T. Kröll, R. Krücken, M. Lauer, J. Leske, K. Lieb, R. Lutter, L. Maier, B. Marsh, D. Mücher, M. Münch, O. Niedermaier, J. Pakarinen, M. Pantea, G. Pascovici, N. Patronis, D. Pauwels, A. Petts, N. Pietralla, R. Raabe, E. Rapisarda, P. Reiter, A. Richter, O. Schaile, M. Scheck, H. Scheit, G. Schrieder, D. Schwalm, M. Seidlitz, M. Seliverstov, T. Sieber, H. Simon, K.-H. Speidel, C. Stahl, I. Stefanescu, P. Thirolf, H.-G. Thomas, M. Thürauf, P. Van Duppen, D. Voulot, R. Wadsworth, G. Walter, D. Weißhaar, F. Wenander, A. Wiens, K. Wimmer, B. Wolf, P. Woods, K. Wrzosek-Lipska, and K. Zell, "The Miniball spectrometer," *The European Physical Journal A*, vol. 49, no. 3, 2013.

[82] N. Warr, "The MINIBALL clusters 2011." `http://www.ikp.uni-koeln.de/~warr/doc/photos_17May2011/index.html`, November 2014.

[83] J. Simpson, J. Nyberg, and W. Korten, "AGATA Technical Design Report," 2008. `http://www-w2k.gsi.de/agata/publications.htm`.

[84] X-ray instrumentation associates (XIA). `http://www.xia.com/`, November 2014.

[85] Bildstein, Vinzenz, Gernhäuser, Roman, Kröll, Thorsten, Krücken, Reiner, Wimmer, Kathrin, Van Duppen, Piet, Huyse, Mark, Patronis, Nikolas, Raabe, Riccardo, and T-REX Collaboration, "T-REX: A new setup for transfer experiments at REX-ISOLDE," *Eur. Phys. J. A*, vol. 48, no. 6, p. 85, 2012.

[86] V. Bildstein, *Exploring the Island of Inversion with the d(^{30}Mg,p)^{31}Mg Reaction.* PhD thesis, Technische Universität München, Lehrstuhl E12 für Experimentalphysik, 2010.

[87] N. Warr, "Ionization chamber." `http://www.ikp.uni-koeln.de/~warr/doc/ion_chamber.pdf`, April 2012.

[88] J. Lichtinger, "private communication," 2013.

[89] J. Lichtinger, *Quantitative Untersuchungen der lokalen Lithiumkonzentration im menschlichen Gehirn und ihr Bezug zu affektiven Störungen.* PhD thesis, Technische Universität München, Lehrstuhl E12 für Experimentalphysik, 2015.

[90] R. Lutter, O. Schaile, K. Schöffel, K. Steinberger, and C. Broude, *MARaBOU data aquisition system*, 2003. `http://www.bl.physik.uni-muenchen.de/marabou/html/`.

[91] I. Antcheva, M. Ballintijn, B. Bellenot, M. Biskup, R. Brun, N. Buncic, P. Canal, D. Casadei, O. Couet, V. Fine, L. Franco, G. Ganis, A. Gheata, D. G. Maline, M. Goto, J. Iwaszkiewicz, A. Kreshuk, D. M. Segura, R. Maunder, L. Moneta, A. Naumann, E. Offermann, V. Onuchin, S. Panacek, F. Rademakers, P. Russo, and M. Tadel, "ROOT – A C++ framework for petabyte data storage, statistical analysis and visualization," *Computer Physics Communications*, vol. 180, no. 12, pp. 2499 – 2512, 2009. 40 YEARS OF CPC: A celebratory issue focused on quality software for high performance, grid and novel computing architectures.

[92] S. Hellgartner (former Klupp), *Documentation of the Calibration of the T-REX Detectors and of MINIBALL*, Oct 2012. contact: `stefanie.hellgartner@tum.de`.

[93] S. Hellgartner (former Klupp), *Documentation of the Calibration of the C-REX Detectors and of MINIBALL*, Oct 2012. contact: `stefanie.hellgartner@tum.de`.

[94] I. Kim, C. Park, and H. Choi, "Absolute calibration of ^{60}Co by using sum-peak method and an {HPGe} detector," *Applied Radiation and Isotopes*, vol. 58, no. 2, pp. 227 – 233, 2003.

[95] S. Baruah, *Precision mass measurements on neutron-rich Zn isotopes and their consequences on the astrophysical r-process.* PhD thesis, Ernst-Moritz-Arndt-Universität Greifswald, Mathematisch-Naturwissenschaftliche Fakultät, 2008.

[96] S. Baruah, G. Audi, K. Blaum, M. Dworschak, S. George, C. Guénaut, U. Hager, F. Herfurth, A. Herlert, A. Kellerbauer, H.-J. Kluge, D. Lunney, H. Schatz, L. Schweikhard, and C. Yazidjian, "Mass Measurements beyond the Major *r*-Process Waiting Point ^{80}Zn," *Phys. Rev. Lett.*, vol. 101, p. 262501, Dec 2008.

[97] C. Bertulani and P. Danielewicz, *Introduction to Nuclear Reactions (Graduate Student Series in Physics).* CRC Press, 2004.

[98] C. Perey and F. Perey, "Compilation of phenomenological optical-model parameters 1954–1975," *Atomic Data and Nuclear Data Tables*, vol. 17, no. 1, pp. 1 – 101, 1976.

[99] X. Li, C. Liang, and C. Cai, "Global triton optical model potential," *Nuclear Physics A*, vol. 789, no. 1–4, pp. 103 – 113, 2007.

[100] I. Thompson, *Sfresco is an additional version of Fresco, to provide Chi-squared searches of potential and coupling parameters*, 2006. `http://www.fresco.org.uk/index.htm`.

[101] F. James, *MINUIT-Function minimization and error analysis*. CERN, Computing and Networks division. CERN Program Library Long Writeup D506.

[102] I. Thompson, *Fresco, coupled reaction channels calculations*, 2006. `http://www.fresco.org.uk`.

[103] I. J. Thompson, "Coupled reaction channels calculations in nuclear physics," *Computer Physics Reports*, vol. 7, no. 4, pp. 167 – 212, 1988.

[104] I. Thompson, *Nuclear reactions for astrophysics: principles, calculation and applications of low-energy reactions*. Cambridge New York: Cambridge University Press, 2009.

[105] M. Huhta, P. F. Mantica, D. W. Anthony, P. A. Lofy, J. I. Prisciandaro, R. M. Ronningen, M. Steiner, and W. B. Walters, "New evidence for deformation in ^{73}Zn," *Phys. Rev. C*, vol. 58, pp. 3187–3194, Dec 1998.

[106] M. Bernas, P. Dessagne, M. Langevin, J. Payet, F. Pougheon, P. Roussel, W.-D. Schmidt-Ott, P. Tidemand-Petersson, and M. Girod, "Mass and excited levels of the neutron-rich nuclei ^{73}Zn and ^{74}Zn studied with the ^{76}Ge(^{14}C, ^{17}O) and (^{14}C, ^{16}O) reactions," *Nuclear Physics A*, vol. 413, no. 2, pp. 363 – 374, 1984.

[107] T. Faul, *Etude de la Structure des Noyaux Riches en Neutrons autour du Noyau Doublement Magique ^{78}Ni*. Theses, Université Louis Pasteur - Strasbourg I, Dec. 2007.

[108] K. Wimmer, "private communication," 2014, 2015.

[109] B. Brown and W. Rae, "The Shell-Model Code NuShellX@MSU," *Nuclear Data Sheets*, vol. 120, pp. 115 – 118, 2014.

[110] B. Cheal, E. Mané, J. Billowes, M. L. Bissell, K. Blaum, B. A. Brown, F. C. Charlwood, K. T. Flanagan, D. H. Forest, C. Geppert, M. Honma, A. Jokinen, M. Kowalska, A. Krieger, J. Krämer, I. D. Moore, R. Neugart, G. Neyens, W. Nörtershäuser, M. Schug, H. H. Stroke, P. Vingerhoets, D. T. Yordanov, and M. Žáková, "Nuclear Spins and Moments of Ga Isotopes Reveal Sudden Structural Changes between $N = 40$ and $N = 50$," *Phys. Rev. Lett.*, vol. 104, p. 252502, Jun 2010.

[111] J. Van Roosbroeck, H. De Witte, M. Gorska, M. Huyse, K. Kruglov, D. Pauwels, J.-C. Thomas, K. Van de Vel, P. Van Duppen, S. Franchoo, J. Cederkall, V. N. Fedoseyev, H. Fynbo, U. Georg, O. Jonsson, U. Köster, L. Weissman, W. F. Mueller, V. I. Mishin, D. Fedorov, A. De Maesschalck, N. A. Smirnova, and K. Heyde, "Evolution of the nuclear structure approaching ^{78}Ni : β decay of $^{74-78}$Cu," *Phys. Rev. C*, vol. 71, p. 054307, May 2005.

[112] J. A. Winger, J. C. Hill, F. K. Wohn, E. K. Warburton, R. L. Gill, A. Piotrowski, and D. S. Brenner, "Structure of neutron-rich ^{74}Zn from ^{74}Cu decay and shell-model calculations for even-A zn nuclei," *Phys. Rev. C*, vol. 39, pp. 1976–1984, May 1989.

[113] G. Cowan, *Statistical data analysis*. Oxford New York: Clarendon Press Oxford University Press, 1998.

[114] G. J. Feldman and R. D. Cousins, "Unified approach to the classical statistical analysis of small signals," *Phys. Rev. D*, vol. 57, pp. 3873–3889, Apr 1998.

[115] B. A. Brown, "private communication," July 2015.

[116] K. Sieja and F. Nowacki, "Three-body forces and persistence of spin-orbit shell gaps in medium-mass nuclei: Toward the doubly magic ^{78}Ni," *Phys. Rev. C*, vol. 85, p. 051301, May 2012.

[117] J.-C. Thomas, H. D. Witte, M. Gorska, M. Huyse, K. Kruglov, Y. Kudryavtsev, D. Pauwels, N. V. S. V. Prasad, K. V. d. Vel, P. V. Duppen, J. V. Roosbroeck, S. Franchoo, J. Cederkall, H. O. U. Fynbo, U. Georg, O. Jonsson, U. Köster, L. Weissman, W. F. Mueller, V. N. Fedosseev, V. I. Mishin, D. Fedorov, A. D. Maesschalck, and N. A. Smirnova, "β-decay properties of ^{72}Ni and ^{72}Cu," *Phys. Rev. C*, vol. 74, p. 054309, Nov 2006.

[118] S. Leenhardt, O. Sorlin, M.G. Porquet, F. Azaiez, J.C. Angélique, M. Belleguic, C. Borcea, C. Bourgeois, J.M. Daugas, C. Donzaud, I. Deloncle, J. Duprat, A. Gillibert, S. Grévy, D. Guillemaud-Mueller, J. Kiener, M. Lewitowicz, S.M. Lukyanov, F. Marie, N.A. Orr, Yu.-E. Penionzhkevich, F. de Oliveira Santos, F. Pougheon, M.G. Saint-Laurent, W. Shuying, Yu. Sobolev, and J.S. Winfield, "Coulomb excitation of $^{72}_{30}$Zn$_{42}$," *Eur. Phys. J. A*, vol. 14, no. 1, pp. 1–5, 2002.

[119] E. S. Bönig, *Quadrupole Collectivity in ^{128}Cd.* PhD thesis, Technische Universität Darmstadt, 2014.

[120] G. Cowan, *Statistical data analysis.* Oxford New York: Clarendon Press Oxford University Press, 1998.

[121] N. Kesteloot, "private communication," April 2014.

[122] M. Seidlitz, *Coulomb-Anregung von instabilen, ungeraden Mg-Isotopen.* PhD thesis, IKP Köln, 2008.

[123] M. Zielinska, A. Görgen, A. Bürger, W. Catford, E. Clement, C. Dossat, J. Iwanicki, W. Korten, J. Ljungvall, P. Napiorkowski, D. Pietak, G. Sletten, J. Srebrny, C. Theisen, and K. Wrzosek-Lipska, "Coulomb excitation of ^{109}Ag," *HIL Annular Report*, 2009.

[124] R. Robinson, P. McGowan, P. Stelson, and W. Milner, "Coulomb excitation of ^{107,109}Ag," *Nuclear Physics A*, vol. 150, no. 2, pp. 225 – 246, 1970.

[125] C. Cottrell, "Transitions, with change in parity, produced in ^{107,109}Ag by Coulomb excitation," *Nuclear Physics A*, vol. 204, no. 1, pp. 161 – 171, 1973.

[126] M. Throop, I. Hall, I. Naqib, D. Thomas, and B. Waefield, "Quadrupole moments of the first $3/2^-$ and $5/2^-$ states of ^{109}Ag and the particle-vibrator coupling model," *Physics Letters B*, vol. 41, no. 5, pp. 585 – 587, 1972.

[127] A. Abragam and R. V. Pound, "Influence of electric and magnetic fields on angular correlations," *Phys. Rev.*, vol. 92, pp. 943–962, Nov 1953.

[128] F. Bosch and H. Spehl, "Asymptotic attenuation coefficients in random perturbations of angular correlations," *Zeitschrift für Physik A Atoms and Nuclei*, vol. 280, no. 4, pp. 329–339, 1977.

[129] R. Brenn, H. Spehl, A. Weckherlin, H. Doubt, and G. van Middelkoop, "Nuclear deorientation for heavy ions recoiling in vacuum and low pressure gas," *Zeitschrift für Physik A Atoms and Nuclei*, vol. 281, no. 3, pp. 219–227, 1977.

[130] D. Mücher, "private communication," 2014.

[131] K. Wrzosek-Lipska, L. Próchniak, M. Zielińska, J. Srebrny, K. Hadyńska-Klęk, J. Iwanicki, M. Kisieliński, M. Kowalczyk, P. J. Napiorkowski, D. Piętak, and T. Czosnyka, "Electromagnetic properties of ^{100}Mo: Experimental results and theoretical description of quadrupole degrees of freedom," *Phys. Rev. C*, vol. 86, p. 064305, Dec 2012.

[132] J. P. Delaroche, M. Girod, J. Libert, H. Goutte, S. Hilaire, S. Péru, N. Pillet, and G. F. Bertsch, "Structure of even-even nuclei using a mapped collective Hamiltonian and the D1S Gogny interaction," *Phys. Rev. C*, vol. 81, p. 014303, Jan 2010.

[133] J. P. Delaroche, "private communication," September 2015.

[134] T. R. Rodríguez and J. L. Egido, "Triaxial angular momentum projection and configuration mixing calculations with the Gogny force," *Phys. Rev. C*, vol. 81, p. 064323, Jun 2010.

[135] J. Sun, Z. Shi, X. Li, H. Hua, C. Xu, Q. Chen, S. Zhang, C. Song, J. Meng, X. Wu, S. Hu, H. Zhang, W. Liang, F. Xu, Z. Li, G. Li, C. He, Y. Zheng, Y. Ye, D. Jiang, Y. Cheng, C. He, R. Han, Z. Li, C. Li, H. Li, J. Wang, J. Liu, Y. Wu, P. Luo, S. Yao, B. Yu, X. Cao, and H. Sun, "Spectroscopy of ^{74}Ge: From soft to rigid triaxiality," *Physics Letters B*, vol. 734, pp. 308 – 313, 2014.

[136] A. Lisetskiy, "private communication," September 2009.

[137] M. Honma, T. Otsuka, T. Mizusaki, and M. Hjorth-Jensen, "New effective interaction for f_5pg_9-shell nuclei," *Phys. Rev. C*, vol. 80, p. 064323, Dec 2009.

[138] Borge, María José G., "ISOLDE highlights and the HIE-ISOLDE project," *EPJ Web of Conferences*, vol. 66, p. 11005, 2014.

[139] The official HIE-ISOLDE website. `https://hie-isolde.web.cern.ch/hie-isolde/`, September 2015.

[140] E. Rapisarda, D. Voulot, F. Wenander, P. Van Duppen, M. Huyse, R. Raabe, H. De Witte, K. Wrzosek-Lipska, M. Zielinska, T. Duguet, L. Grente, C. Louchart, W. Korten, M.D. Salsac, T. Davinson, P. Woods, R. Gernhäuser, K. Nowak, K. Wimmer, D. Mücher, Th. Kröll, N. Pietralla, G. Rainovski, P. Napiorkowski, J. Srebrny, A. Blazhev, J. Jolie, N. Warr, P. Reiter, M. Seidlitz, B. Siebeck, T. Grahn, P.T. Greenlees, J. Pakarinen, P. Rahkila, E. Clément, A.N. Andreyev, S. Harissopulos, A. Lagoyannis, M. Axiotis, T. J. Mertzimekis, A. Pakou, N. Patronis, G. Georgiev, D.L. Balabanski, J. Cederkäll, D. Di Julio, C. Fahlander, K. Sieja, F. Nowacki, "Coulomb excitation ^{74}Zn-^{80}Zn (N=50): probing the validity of shell-model descriptions around ^{78}Ni," *Proposal to the ISOLDE and Neutron Time-of-Flight Committee.*

[141] mesytec GmbH und Co. KG. `http://www.mesytec.com/`, December 2014.

[142] The Geant4 Collaboration, "G4 — A simulation toolkit," *Nuclear Instruments and Methods in Physics Research Section A*, vol. 506, pp. 250–303, July 2003.

[143] The Geant4 Collaboration, "Geant4 developments and applications," *IEEE Transactions on Nuclear Science*, vol. 53, no. 1, pp. 270–278, 2006.

[144] J. F. Ziegler, M. Ziegler, and J. Biersack, "{SRIM} – the stopping and range of ions in matter (2010)," *Nuclear Instruments and Methods in Physics Research Section B: Beam Interactions with Materials and Atoms*, vol. 268, no. 11–12, pp. 1818 – 1823, 2010. 19th International Conference on Ion Beam Analysis.

[145] T. Miller and M. Takeda, "Lifetimes in ^{103}Rh, ^{107}Ag and ^{109}Ag measured by the recoil-distance technique," *Nuclear Physics A*, vol. 221, no. 2, pp. 392 – 402, 1974.

[146] M. Loiselet, O. Naviliat-Cuncic, and J. Vervier, "Measurements of reduced {E2} transition probabilities in the nuclei ^{102}Ru, ^{103}Rh, ^{106,108}Pd and ^{107,109}Ag," *Nuclear Physics A*, vol. 496, no. 3, pp. 559 – 588, 1989.

[147] W.C. Schick Jr. and W.L. Talbert Jr., "Gamma-ray decay schemes of ^{109g}Pd, ^{111g}Pd and ^{111m}Pd," *Nuclear Physics A*, vol. 128, no. 2, pp. 353 – 387, 1969.

[148] W. M. Roney, "Proc. Intern. Conf. Nucl. Reactions Induced by Heavy Ions, Heidelberg, Germany," 1969.

[149] H. E. Bosch, V. M. Silbergleit, M. Davidson, and J. Davidson, "Determination of mixing ratios for some cascades corresponding to ^{109}Ag," *Canadian Journal of Physics*, vol. 55, no. 2, pp. 175–179, 1977.

[150] O. Helene, "Upper limit of peak area," *Nuclear Instruments and Methods in Physics Research*, vol. 212, no. 1–3, pp. 319 – 322, 1983.

[151] A. Wilson, C. Beausang, N. Amzal, D. Appelbe, S. Asztalos, P. Butler, R. Clark, P. Fallon, and A. Macchiavelli, "High-spin states following multi-nucleon transfer," *The European Physical Journal A - Hadrons and Nuclei*, vol. 9, no. 2, pp. 183–189, 2000.

Danke !!